NELSON MANDELA UNIVERSITY

SYNTHESIS, CHARACTERISATION AND ANTITUMOUR ACTIVITIES OF LANTHANIDE COMPLEXES WITH HYDRAZONES AND CARBOXYLIC ACID LIGANDS

By

Tatenda Madanhire

Submitted in fulfilment of the requirements for the degree of Philosophiae Doctor (Chemistry) to be awarded at the Nelson Mandela University

April 2020

Promoter: **Dr Abubak'r Abrahams**

Co-promoter: **Dr Hajierah Davids**

DECLARATION BY CANDIDATE

NAME: Tatenda Madanhire

STUDENT NUMBER: 210154810

QUALIFICATION: PhD Chemistry

TITLE OF PROJECT: Synthesis, characterisation and antitumour activities of lanthanide complexes with hydrazones and carboxylic acid ligands

DECLARATION:

In accordance with Rule G5.6.3, I hereby declare that the above-mentioned thesis is my own work and that it has not previously been submitted for assessment to another University or for another qualification.

SIGNATURE: _____

DATE: ____05/12/2019____

TABLE OF CONTENTS

CHAPTER 1

Introduction

CHAPTER 2

Materials and Methods

CHAPTER 3

Lanthanide(III) acetate complexes with benzohydrazone and nicotinohydrazone ligands

CHAPTER 4

Synthesis, characterisation and cytotoxic activity of Ln(III) complexes with N-(2,6-dimethylphenyl)oxamate in cancer cell lines

CHAPTER 5

Lanthanide complexes with N-(2,6-dimethylphenyl)oxamate and 1,10-phenanthroline

CHAPTER 6

Mixed-ligand complexes of lanthanides derived from an α-hydroxycarboxylic acid (benzilic acid) and 1,10-phenanthroline

CHAPTER 7

Conclusions and Future prospects

LIST OF PUBLICATIONS

ACKNOWLEDGEMENTS

First and foremost, I am most thankful to my promoters Dr Abubak'r Abrahams and Dr Hajierah Davids for their patience, help, encouragement and guidance throughout the studies. I am forever grateful. Their knowledge, encouragement and commitment is motivating and was instrumental in defining the path of my research, and I could not have succeeded in this project without their contribution. Words are not enough to fully express my gratitude.

I wish to express my sincere gratitude to Dr Eric Hosten for his contribution in X-ray crystallography and Mr Henk Schalekamp for technical support. Dr Melanie Pereira deserves special recognition not only for her assistance in biological studies, but also for her helpful advice. Throughout my research I have been greatly aided by lab mates: Mr Cameron Matthews, Mr Cyprian Moyo, Mr Kwakhanya Mkwakwi and Miss Sibongile Pikoli, and it is here that I acknowledge their assistance as well as helpful discussions. I have great appreciation for Mr Matthews' and Mr Moyo's contribution, especially in computational chemistry.

Financial support from the Nelson Mandela University Postgraduate Research Scholarship (PGRS) and National Research Foundation (NRF) is gratefully appreciated. My deepest gratitude also goes to the Centre for High Performance Computing (CHPC) of CSIR, in South Africa, for allowing access to usage of computational resources to execute this research. This achievement would not have been possible without these institutes.

I would like to give a special thanks to my family and friends for all of the incredible support and love they offered. Thank you for being the pillar of strength and the driving force behind my doctoral studies. God Almighty gave me an opportunity, knowledge and strength to persevere as I undertook this research study. I am extremely grateful for His blessings. My sincere apologies if I have unintentionally omitted anyone who helped me with this research and to whom acknowledgement is due.

DEDICATION

This thesis is dedicated to my beloved mother Mavis Mashinya and my grandmother Aloisia Sibukani Ndabambi, who always stressed the importance of education throughout my life.

ABBREVIATIONS

Abbreviation	Meaning
Ln	lanthanide
Solvents	
DMSO	dimethyl sulfoxide
DMF	dimethylformamide
MeOH	methanol
EtOH	ethanol
THF	tetrahydrofuran
Ligands	
H$_2$phen	(*E*)-*N'*-(2-hydroxybenzylidene)benzohydrazide
H$_2$Nic	(*E*)-*N'*-(2-hydroxybenzylidene)nicotinohydrazide
OAc$^-$	acetate
Hdmp	ethyl (2,6-dimethylphenylcarbamoyl)formate
Hpma$^-$	*N*-(2,6-dimethylphenyl)oxamate
Phen	1,10-phenanthroline
H$_2$ben	benzilic acid
Hben$^-$	benzilate
Spectroscopic and crystallographic characterisation techniques	
FT-IR	Fourier-transform infrared
	• signal intensities are defined as w = weak, m = medium, s = strong and b = broad
NMR	nuclear magnetic resonance
UV-Vis-NIR	ultraviolet-visible-near infrared
XRD	X-ray diffraction

Abbreviation	Meaning
Coordination geometries	
C.N.	coordination number
CShM	continuous shape measure
vOC-5	vacant octahedron
OC-6	octahedron
SAPR-8	square antiprism
TDD-8	triangular dodecahedron
CSAPR-9	spherical capped square antiprism
TCTPR-9	spherical tricapped trigonal prism
MFF-9	muffin
JSPC-10	sphenocorona J87
Molecular modelling	
DFT	Density Functional Theory
B3LYP	Becke3-Lee-Yang-Parr
SCRF	self-consistent reaction field
CPCM	conductor-like polarisable continuum model
NBO	natural bond orbital
NPA	natural population analysis
MEP	molecular electrostatic potential
FMO	frontier molecular orbital
HOMO	highest occupied molecular orbital
LUMO	lowest unoccupied molecular orbital
Anticancer tests	
MCF-7	breast cancer cell line
HEC-1A	endometrial carcinoma cell line
THP-1	leukemic monocytic cell line
MTT	3-(4,5-dimethylthiazol-2-yl)-2,5-diphenyltetrazolium bromide
S.D.	standard deviation

Periodic Table of the Elements

Key

11	Atomic number
Na	Element symbol
Sodium	Element name
22.990	Atomic weight

Legend:
- Alkali metals
- Alkaline earth metals
- Lanthanides
- Actinides
- Transition metals
- Unknown properties
- Post-transition metals
- Metalloids
- Other nonmetals
- Halogens
- Noble gases

Group	1 1A	2 2A	3 3B	4 4B	5 5B	6 6B	7 7B	8 8B	9 8B	10 8B	11 1B	12 2B	13 3A	14 4A	15 5A	16 6A	17 7A	18 8A
Period 1	1 H Hydrogen 1.0078																	2 He Helium 4.0026
2	3 Li Lithium 6.938	4 Be Beryllium 9.0122											5 B Boron 10.806	6 C Carbon 12.009	7 N Nitrogen 14.006	8 O Oxygen 15.999	9 F Fluorine 18.998	10 Ne Neon 20.180
3	11 Na Sodium 22.990	12 Mg Magnesium 24.305											13 Al Aluminum 26.982	14 Si Silicon 28.084	15 P Phosphorus 30.974	16 S Sulfur 32.059	17 Cl Chlorine 35.446	18 Ar Argon 39.948
4	19 K Potassium 39.098	20 Ca Calcium 40.078	21 Sc Scandium 44.956	22 Ti Titanium 47.867	23 V Vanadium 50.942	24 Cr Chromium 51.996	25 Mn Manganese 54.938	26 Fe Iron 55.845	27 Co Cobalt 58.933	28 Ni Nickel 58.693	29 Cu Copper 63.546	30 Zn Zinc 65.38	31 Ga Gallium 69.723	32 Ge Germanium 72.63	33 As Arsenic 74.922	34 Se Selenium 78.96	35 Br Bromine 79.904	36 Kr Krypton 83.798
5	37 Rb Rubidium 85.468	38 Sr Strontium 87.62	39 Y Yttrium 88.906	40 Zr Zirconium 91.224	41 Nb Niobium 92.906	42 Mo Molybdenum 95.96	43 Tc Technetium 98.9062	44 Ru Ruthenium 101.07	45 Rh Rhodium 102.91	46 Pd Palladium 106.42	47 Ag Silver 107.87	48 Cd Cadmium 112.41	49 In Indium 114.82	50 Sn Tin 118.71	51 Sb Antimony 121.76	52 Te Tellurium 127.60	53 I Iodine 126.90	54 Xe Xenon 131.29
6	55 Cs Cesium 132.91	56 Ba Barium 137.33	57 La Lanthanum 138.91	72 Hf Hafnium 178.49	73 Ta Tantalum 180.95	74 W Tungsten 183.84	75 Re Rhenium 186.21	76 Os Osmium 190.23	77 Ir Iridium 192.22	78 Pt Platinum 195.08	79 Au Gold 196.97	80 Hg Mercury 200.59	81 Tl Thallium 204.38	82 Pb Lead 207.2	83 Bi Bismuth 208.98	84 Po Polonium (209)	85 At Astatine (210)	86 Rn Radon (222)
7	87 Fr Francium (223)	88 Ra Radium (226)	89 Ac Actinium (227)	104 Rf Rutherfordium (261)	105 Db Dubnium (262)	106 Sg Seaborgium (266)	107 Bh Bohrium (264)	108 Hs Hassium (269)	109 Mt Meitnerium (268)	110 Ds Darmstadtium (268)	111 Rg Roentgenium (268)	112 Cn Copernicium (268)	113 Uut Ununtrium (268)	114 Fl Flerovium (268)	115 Uup Ununpentium (268)	116 Lv Livermorium (268)	117 Uus Ununseptium (268)	118 Uuo Ununoctium (268)

Lanthanides

57 La Lanthanum 138.91	58 Ce Cerium 140.12	59 Pr Praseodymium 140.91	60 Nd Neodymium 144.24	61 Pm Promethium (145)	62 Sm Samarium 150.36	63 Eu Europium 151.96	64 Gd Gadolinium 157.25	65 Tb Terbium 158.93	66 Dy Dysprosium 162.50	67 Ho Holmium 164.93	68 Er Erbium 167.26	69 Tm Thulium 168.93	70 Yb Ytterbium 173.04	71 Lu Lutetium 174.97

Actinides

89 Ac Actinium (227)	90 Th Thorium 232.04	91 Pa Protactinium 231.04	92 U Uranium 238.03	93 Np Neptunium (237)	94 Pu Plutonium (244)	95 Am Americium (243)	96 Cm Curium (247)	97 Bk Berkelium (247)	98 Cf Californium (251)	99 Es Einsteinium (252)	100 Fm Fermium (257)	101 Md Mendelevium (258)	102 No Nobelium (259)	103 Lr Lawrencium (262)

LIST OF FIGURES

CHAPTER 2

Experimental

CHAPTER 3

Lanthanide(III) acetate complexes with benzohydrazone and nicotinohydrazone ligands

CHAPTER 4

Synthesis, characterisation and cytotoxic activity of Ln(III) complexes with N-(2,6-dimethylphenyl)oxamate in cancer cell lines

CHAPTER 5

Lanthanide complexes with N-(2,6-dimethylphenyl)oxamate and 1,10-phenanthroline

CHAPTER 6

Mixed-ligand complexes of lanthanides derived from an α-hydroxycarboxylic acid (benzilic acid) and 1,10-phenanthroline

LIST OF REACTION SCHEMES

CHAPTER 5

Lanthanide complexes with N-(2,6-dimethylphenyl)oxamate and 1,10-phenanthroline

CHAPTER 6

Mixed-ligand complexes of lanthanides derived from an α-hydroxycarboxylic acid (benzilic acid) and 1,10-phenanthroline

LIST OF TABLES

CHAPTER 4

Synthesis, characterisation and cytotoxic activity of Ln(III) complexes with N-(2,6-dimethylphenyl)oxamate in cancer cell lines

CHAPTER 5

Lanthanide complexes with N-(2,6-dimethylphenyl)oxamate and 1,10-phenanthroline

CHAPTER 6

Mixed-ligand complexes of lanthanides derived from an α-hydroxycarboxylic acid (benzilic acid) and 1,10-phenanthroline

ABSTRACT

The tridentate hydrazone ligands, (*E*)-*N'*-(2-hydroxybenzylidene)benzohydrazide (**H₂phen**) and (*E*)-*N'*-(2-hydroxybenzylidene)nicotinohydrazide (**H₂Nic**), were synthesised and complexed to Ln(III) acetates. The centrosymmetric, acetato-bridged dinuclear coordination compounds with the formulae, [La₂(Hphen)₂(OAc)₄(H₂O)₂]·DMF·H₂O (**1**), [Ln₂(HNic)₂(OAc)₄(H₂O)₂]·DMF·H₂O (Ln = La (**2**) and Nd (**3**)) and [Ln₂(HNic)₂(OAc)₄(H₂O)₂]·DMF (Ln = Er (**4**) and Yb (**5**)) were isolated and characterised by elemental analyses, IR spectroscopy, UV-Vis spectroscopy, X-ray diffraction studies and *SHAPE 2.1*. The nine-coordinate complexes **1**–**3** crystallise in the triclinic space group *P-1*, with the metal centres having the distorted spherical capped square antiprism geometry (C_{4v}), while the eight-coordinate Er(III) and Yb(III) complexes (monoclinic system, space group *P*21/c) display the geometry of distorted triangular dodecahedron (D_{2d}). Geometry optimisation of the monoanionic forms of the hydrazone ligands (**Hphen⁻** and **HNic⁻**) were performed using Density Functional Theory (DFT) with Becke's three parameter hybrid method and correlation functional of Lee, Yang and Parr (B3LYP) with aug-cc-pVTZ basis set. Natural population analysis (NPA) and molecular electrostatic potential (MEP) maps indicated that the most preferred sites for electrophilic attack in the anionic ligands are the phenolate and carbonyl oxygens, and the azomethine nitrogens. The evaluation of the cytotoxic activity of the compounds on breast cancer (MCF-7), the endometrial carcinoma (HEC-1A) and the human monocytic (THP-1) cell lines using the 3-(4,5-dimethyl-2-thiazolyl)-2,5-diphenyl tetrazolium bromide (MTT) assay revealed that the hydrazone ligands and complexes **1**–**4** are partially cytotoxic against MCF-7 cells, while the Schiff bases and complexes **3**–**5** significantly inhibit cell growth in HEC-1A cells.

The complexation reactions of Ce(III), Nd(III), Gd(III) and Er(III) with the chelating/ bridging monoanionic ligand *N*-(2,6-dimethylphenyl)oxamate (**Hpma⁻**) in basic media were performed in view of the potential applications of oxamate derivatives as cytotoxic agents. The coordination compounds were characterised by different

physico-chemical techniques: elemental analysis, conductivity measurements, IR, ^{1}H NMR and UV-Vis-NIR spectroscopy. The anionic **Hpma**$^-$ was obtained through conversion of the proligand ethyl (2,6-dimethylphenylcarbamoyl)formate (**Hdmp**). The reactions afforded lanthanide(III)–oxamate coordination polymers of formulae: $\{[Ln(Hpma)_3(MeOH)(H_2O)]\cdot 2MeOH\}_n$ (Ln = Ce (**1**) and Nd (**2**)), $\{[Gd_2(Hpma)_6(MeOH)_4]\cdot 6MeOH\}_n$ (**3**), $\{[Er_2(Hpma)_6(MeOH)(H_2O)_3]\cdot 2MeOH\}_n$ (**4**) and $[Ln_2Na_2(Hpma)_8(EtOH)(H_2O)_6]_n$ (Ln = Nd (**5**) and Gd (**6**)). The polymeric complexes feature Ln-Hpma moieties bridged by $\mu_2\text{-}\eta^1{:}\eta^1{:}\eta^1$ **Hpma**$^-$, giving one-dimensional zig-zag chains of the –Ln–O–C–O–Ln– type. Atomic charge analysis and the MEP map of the **Hpma**$^-$ moiety done using the DFT/B3LYP method were found to be consistent with the chelating and bridging modes of the anionic ligand through all the oxygen atoms. The evaluation of the cytotoxic activities of the metal salts, the proligand and the novel lanthanide complexes on MCF-7, HEC-1A and THP-1 cell lines revealed that only the rare-earth metal salts $[Ce(NO_3)_3\cdot 6H_2O]$ and $[Nd(NO_3)_3\cdot 6H_2O]$ showed modest cytotoxicity against MCF-7 and HEC-1A cells, respectively.

Seven novel mixed-ligand complexes, $[Ln(Hpma)_2(phen)_2(OAc)]\cdot 2H_2O$ (Ln = La (**1**), Ce (**2**) and Nd (**3**)), $[Er(Hpma)_2(phen)(OAc)(H_2O)]\cdot EtOH\cdot H_2O$ (**4**), $[Yb(Hpma)_3(phen)]\cdot 2EtOH$ (**5**) and $[Ln(Hpma)_3(phen)(H_2O)]\cdot 4H_2O$ (Ln = Nd (**6**) and Gd (**7**)) (**Hpma** = *N*-(2,6-dimethylphenyl)oxamate; **phen** = 1,10-phenanthroline) were prepared in the presence of NaOH. Complexes **1**–**3** are isostructural and each metal ion is ten-coordinate adopting a distorted sphenocorona geometry, with continuous shape measures of 2.702, 2.677 and 2.592, respectively. In contrast, the nona-coordinate complexes **4**, **6** and **7** display spherical capped square antiprism molecular geometry, while the Yb(III) complex is bonded to three bidentate **Hpma**$^-$ ligands and one phen, forming a square antiprism structure (coordination number = 8). Besides the strong Ln(III)-ligand bonds as the main driving force for coordination, the relatively weak hydrogen bonds (O-H···O and N-H···O), C-H···O contacts, C-H···π, N-H···π and offset π-π interactions between the aromatic rings play a key role in crystal packing. The UV-Vis-NIR absorption spectra of the metal complexes are associated with the $\pi\to\pi^*$ transitions of phen and the Laporte-forbidden *f-f* transitions of the Nd(III),

Er(III) and Gd(III) ions from the $^4I_{9/2}$, $^4I_{15/2}$ and $^8S_{7/2}$ ground states, respectively, to the various excited J-levels. Cytotoxicity studies revealed antiproliferative activity in MCF-7 cells ($p<0.05$) after treatment with phen and coordination compounds **1**–**7**. Statistically significant cytotoxic effects were also exerted by [Nd(NO$_3$)$_3$·6H$_2$O], phen, **3**, **6** and **7** in HEC-1A cells ($p<0.05$). No cytotoxic effects were observed in THP-1 cells ($p>0.05$) for all the compounds, except for the positive control curcumin; indicating that the target compounds do not exert adverse effects on the immune system monocytes.

The reactions of [Ln(NO$_3$)$_3$·6H$_2$O] (Ln = Pr and Sm), [SmCl$_3$·6H$_2$O] and [Nd(OAc)$_3$·xH$_2$O] with benzilic acid (**H$_2$ben**) and 1,10-phenanthroline (**phen**) as an auxiliary ligand in basic media yielded isostructural nine-coordinate complexes (monoclinic system, space group *P*2$_1$/n) of the type [Ln(Hben)$_3$(phen)$_2$(H$_2$O)]·DMF·H$_2$O (where Ln = Pr(III), Nd(III) and Sm(III)). In the structures, the monodeprotonated **Hben$^-$** ligand connects the metal centres monodentately through the deprotonated carboxylate oxygen, and bidentately *via* the hydroxy oxygen and the carboxylate group oxygen. Additional stability of the crystal structures is provided by intra- and intermolecular O-H···O interactions, C-H···O contacts, parallel-displaced aromatic π···π and C-H···π interactions. The electronic absorption spectra of the complexes show $\pi \rightarrow \pi^*$ transitions of the bidentate aromatic phen, as well as 4*f*-4*f* transitions. Anticancer screen indicated that **phen**, and the Pr(III) and Nd(III) complexes reduced MCF-7 cell proliferation significantly ($p<0.05$). 1,10-Phenanthroline also exerted cytotoxic effects in HEC-1A cells ($p<0.05$).

Keywords: Lanthanide(III), lanthanide complexes, hydrazone, carboxylic acid, oxamate, 1,10-phenanthroline, monodentate, bidentate, tridentate, bridging, crystal structure, geometry, shape analysis, natural charge, anticancer

CRYSTALLOGRAPHIC AND MOLECULAR MODELLING DATA

Supplementary data for all the crystal structures reported herein are stored on the compact disc that is attached to the inside back cover of this dissertation.

The crystallographic data include:

- Final crystal data and details of the structure determinations
- Final coordinates and equivalent isotropic displacement parameters of the non-hydrogen atoms
- Hydrogen atom positions
- Isotropic displacement parameters
- All bond distances and bond angles
- Torsion angles
- Contact distances
- Hydrogen bonds

In addition, the *Gaussian 16* molecular modelling data for all geometry optimisations performed for the ligands have been included. For the ligands, Hphen⁻, HNic⁻, Hpma⁻, phen and Hben⁻, the geometry optimisation and NBO calculations' .log and .com files (output and input files, respectively) are found on the disc.

CHAPTER 1

Introduction

1.1   Motivation of study

Cancer is a range of diseases characterised by the uncontrolled growth and metastases of abnormal cells to different organs and other parts of the body [1]. The disease is caused by inherited genetic mutations, immune and hormonal factors, as well as external factors, such as an unhealthy diet, infectious organisms, exposure to toxic chemicals or radiation and consumption of alcohol or tobacco [1-3]. The International Agency for Research on Cancer (IARC) reported approximately 14.1 million new cancer cases in 2012 worldwide, with 5.3 million deaths related to cancer occurring in economically developing countries, and 2.9 million fatalities in developed countries [1].

The most prevalent types of cancers in females are breast, cervical, uterine, lung and colorectal, while those of the opposite sex are prostate, lung, colorectal, liver and stomach cancer [1,3]. Breast cancer is the most prevalent cancer amongst women globally and the second most common cancer overall [3]. About 1.7 million breast cancer cases were reported in 2012, with 521 900 cancer-related deaths (Table 1.1 summarises the estimated cancer cases and deaths in 2012) [1]. It is notable that cancer types vary by geographical area: adenocarcinoma of the endometrium (uterine cancer) is the fourth leading cause of death in females in developed countries, and the sixth most common type of cancer in women worldwide [4]. Three main methods are applied in the treatment of diverse classes of cancers, namely chemotherapy, surgical therapy and radiotherapy. At advanced stages, the disease responds poorly to chemotherapy, resulting in poor clinical outcomes [4].

Table 1.1: Estimated cancer statistics on leukemia, breast, cervical, and uterine cancer (2012) [1].

	Estimated new cases			Estimated deaths		
	Female			Female		
	Breast	Cervix uteri	Corpus uteri	Breast	Cervix uteri	Corpus uteri
Worldwide	1 676 600	527 600	319 600	521 900	265 700	-
Developed countries	793 700	-	167 900	197 600	35 500	34 700
Developing countries	882 900	444 500	151 700	324 300	230 200	-
	Male			Male		
	Leukemia			Leukemia		
Worldwide	200 700			151 300		
Developed countries	-			51 300		
Developing countries	120 400			100 000		

The first platinum-based anticancer drug to be used in chemotherapy, cisplatin (*cis*-[PtCl$_2$(NH$_3$)$_2$]), was discovered in 1969 by Rosenberg [5]. The drug proved useful in the treatment of different kinds of cancers including ovarian carcinoma, advanced cervical cancer and testicular cancer. Cisplatin, however, presents with adverse effects, such as renal toxicity, neurotoxicity, nausea, alopecia and vomiting [5]. These adverse effects emerge from lack of selectivity, as well as the undesirable reactions of the platinum-based drug with proteins and biological nucleophiles [5]. It is therefore necessary to design and synthesise more selective (towards cancer cells) metal complexes with different kinetic and thermodynamic properties, and with different metal ions for efficient tumour treatment.

Hydrazones have received a lot of attention in the past few decades because of their potentially beneficial antitumour activities [6-11]. Two isostructural La(III) and Ce(III) complexes with a *N,N,O*-donor tridentate hydrazone ligand (*E*)-*N'*-[1-(2-pyridinyl)ethylidene]isonicotinohydrazone (Figure 1.1) have been isolated. The antitumour effects in the human lung cancer cell line, A549, and the human gastric cancer cell lines, SGC7901 and BGC823, were investigated [12]. The 3-(4,5-dimethyl-2-thiazolyl)-2,5-diphenyl tetrazolium bromide (MTT) assay and Annexin V/propidium iodide staining were applied in determining the effect on proliferation

and apoptosis, respectively, on the tumour cell lines [12,13]. The 50 % inhibitory concentration (IC_{50}) values of the complexes were significantly lower than that of the uncoordinated ligand.

Antitumour activities of the Ln(III) complexes are possibly a result of the *N,O*-donor bidentate systems [12]. Western blotting was applied to explore the possible antitumour mechanisms of the metal complexes. The Ce(III) complex induced apoptosis in A549 cells by enhancing the expression of caspase 3 and B cell lymphoma (Bcl)-2-associated X protein (Bax), and downregulation of Bcl-2, all key regulators of the apoptotic pathway. This research promotes the study of lanthanide-hydrazone complexes with great potential in biomedical applications [12].
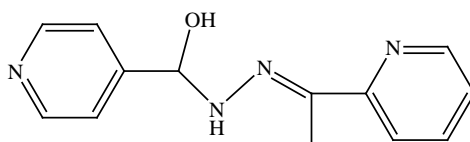
Figure 1.1: The structure of (*E*)-*N*'-[1-(2-pyridinyl)ethylidene]isonicotinohydrazone [12].

Mixed ligand complexes of metals with carboxylic acid ligands and 1,10-phenanthroline are of interest because of their ability to prevent tumour growth [14]. An example of a coordination compound that has been reported to play an important role in the inhibition of proliferation of LA795 lung adenocarcinoma cells is depicted in Figure 1.2. The inhibitory effect occurred in a dose-dependent and time-dependent manner, associated with enhanced expression of apoptotic proteins p53 and Bax, and a reduction in the expression of Bcl-2 [14].

The mixed ligand ruthenium complex prepared from 1,10-phenanthroline and its derivative 2′-(2″-nitro-3″,4″-methylenedioxyphenyl)imidazo[4′,5′-f]phenanthroline) (NMIP), [Ru(phen)$_2$(NMIP)](ClO$_4$)$_2$ (Figure 1.3a) was evaluated for its *in vitro* cytotoxicity on the human hepatocellular carcinoma cell line, BEL-7402 [5,15]. The IC_{50} value, indicative of effectivity of the coordination compound, was 39 ± 2 µM. Flow cytometry illustrated 5.87 % of apoptotic cells when BEL-7402 cells were exposed to 25 µM of the metal complex [15].
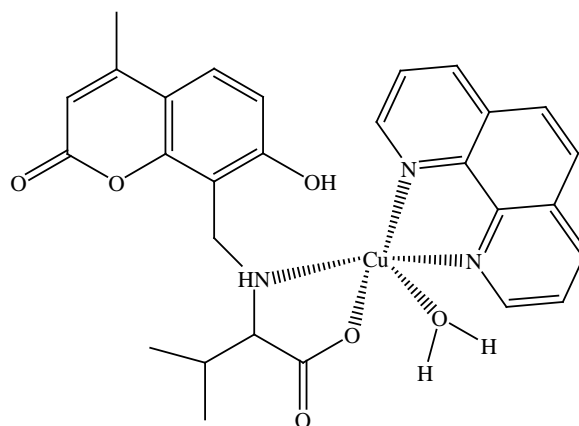
Figure 1.2: The structure of a copper(II) complex of a carboxylic acid and phenanthroline [14].

Some Cu(I) complexes of 1,10-phenanthroline and its derivatives were synthesised and their interaction with extracted DNA investigated [5,16]. The four-coordinate complex, $[Cu(phen)_2]^+$, interacted and cleaved the extracted DNA. A cuprous bis-phenanthroline complex (Figure 1.3b) showed *in vitro* photocytotoxicity on the A549 and human malignant melanoma (A375) cell lines. This cuprous-phenanthroline complex, with a long excited state lifetime, could potentially be exploited in photochemotherapy (PCT) [16].

a

b
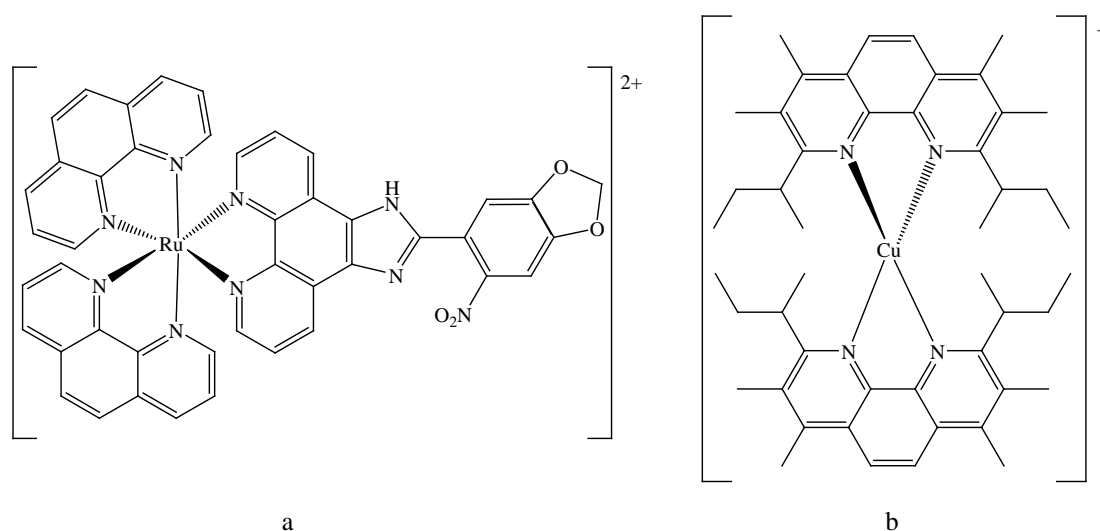
Figure 1.3: The ruthenium (a) and the copper (b) complexes, derived from 1,10-phenanthroline [15,16].

In addition to their broader structural diversity, lanthanides are useful in medicinal chemistry due to their accessible redox states [17]. Redox reactions and ligand-exchange reactions can thus occur in the body, making it possible for specific mechanisms of action to occur [17-19]. The unique metal-ligand interactions impart usefulness in biology by binding to DNA, thus influencing expression levels of proteins [20]. Inorganic molecules may also impede protein function and alter membrane integrity through interaction with proteins and lipids, respectively [20].

The rare-earth compounds are a better alternative as therapeutic agents compared to organic molecules because of the existence of lanthanide radioisotopes with tumour-targeting properties [21]. Rare-earth compounds can be linked to nucleic acids or proteins, making them more specific in inhibiting proteins and more efficient in imaging applications [22]. Lanthanides can adopt a wide range of coordination numbers and coordination geometries, allowing them to gain access to chemical spaces that are otherwise inaccessible to organic compounds [17]. Lanthanide complexes may thus provide a lead into the design of new metal-based therapeutics with a broader spectrum of antitumour activity and improved pharmacological properties, to overcome the development of resistance [12,23,24]. This work will focus on the study of lanthanide metal complexes with hydrazones, carboxylic acids and 1,10-phenanthroline as an auxiliary ligand, as well as the anticancer screen of these compounds [5,12,25].

1.2   Lanthanides and their chemistry

1.2.1   Introduction to the elements

The lanthanides (Lns) refer to the group of fifteen metal elements in the Periodic Table from lanthanum (Z = 57) to lutetium (Z = 71), with electronic configurations from $[Xe]4f^0$ to $[Xe]4f^{14}$ [26-28]. The elements scandium and yttrium have similar chemical properties to the lanthanides and are usually studied together with the $4f$ elements, although they do not have $4f$ electrons [27]. The two types of electronic configurations adopted by the rare-earth elements are $[Xe]4f^n6s^2$ and $[Xe]4f^{n-1}5d^16s^2$,

where [Xe] denotes the electronic configuration of xenon, and *n* is a number from 1 to 14. The elements La, Ce and Gd adopt the former configuration, while Pr, Nd, Pm, Sm, Eu, Tb, Dy, Ho, Er, Tm, Yb and Lu belong to the latter electronic configuration [26,29].

1.2.2   Oxidation states

The $4f$ electrons are not involved in bonding, making the elements electropositive with +3 as their prime oxidation state, although the +2 and +4 oxidation states do exist for some lanthanides [26,29,30]. For example, Sm, Eu and Yb can lose two electrons and therefore exhibit oxidation states of +2 due to the stability of the nearly half-filled $4f^6$ shell, the half-filled $4f^7$ shell, and the completely filled $4f^{14}$ shell, respectively [26,30]. The +4 state is energetically favourable for Ce and Tb according to Hund's rule, since an empty $4f$ orbital is obtained for Ce and a half-filled $4f^7$ configuration is achieved for Tb on the loss of four electrons [26,30].

1.2.3   Lanthanide contraction and element electronegativities

The decrease in ionic radius as the atomic number increases, is an outcome of an increase in strength of attraction of $4f$ orbital electrons by the increasing positive charge of the nucleus; a phenomenon called the lanthanide contraction [26,27,31]. From lanthanum to lutetium, there is a decrease in the Ln(III) ionic radii as the atomic number increases, with larger effective ionic radii leading to higher coordination numbers [26,27,29]. The increase in the effective ionic radii is attributed to the lanthanide contraction diminishing with an increase in the coordination number. The correlation between the atomic numbers, electronegativities, coordination numbers and bond lengths of the lanthanides and oxygen- and nitrogen-donor ligands is that the electronegativity increases from La to Lu [26,29,31]. The Ln-O and Ln-N bond lengths decrease as the atomic number of $4f$ elements increases due to the lanthanide contraction. This relationship between electronegativities and the ionic radii of rare-earth ions is depicted in Figure 1.4 [26,29].
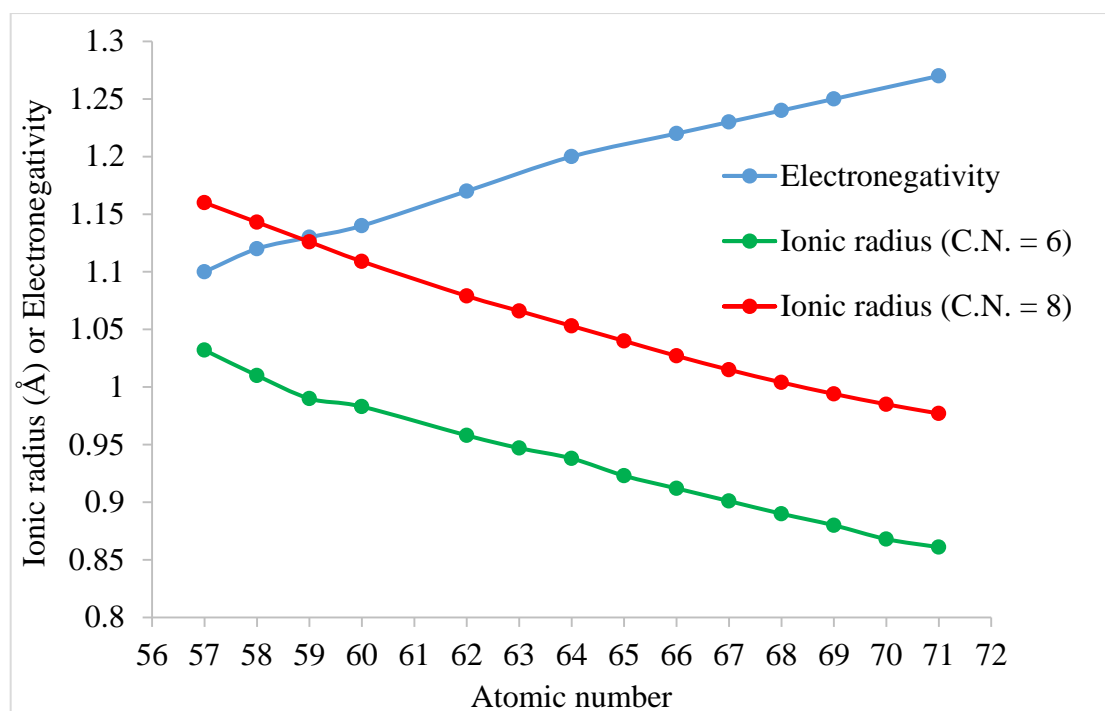
Figure 1.4: The relationship between electronegativities and ionic radii of Ln(III) ions (electronegativity values of Eu, Tb and Yb not indicated) [26, 29].

1.2.4   Chemical properties of the elements

Lanthanides are hard bases due to their small size and high positive charge density [28]. This gives the elements the ability to form chemical bonds with hard acid group atoms, such as fluorine, oxygen, nitrogen and chlorine that are highly electronegative. There is a wide range of ligands that are applied in complexation studies, including Schiff bases, alcohols, carboxylic acids, nitrates, crown ethers, phosphates and amines [28,31-34]. Sulfur is not anticipated to complex well with the 4f elements due to its soft donor properties, although lanthanide complexes with sulfur-donor ligands have been reported [35]. These materials may possess a wide range of geometries, as well as unique and fascinating traits that are not present in easily accessible oxygen- and nitrogen-donor ligand complexes. Examples of these complexes include the distorted dodecahedral dithiocarbamate $Et_4N[Eu(S_2CNEt_2)_4]$, and the trigonal prismatic dithiophosphate $Pr[S_2P(cyclohexyl)_2]_3$ complex [35]. The chemical bonds are ionic, with the main contribution of the 5d and 6s orbitals of the rare-earth elements. The poor shielding of the 4f electrons means that their contribution to covalent interactions

with the coordinating ligands are non-existent [28,31-34]. Unlike many transition metals or some actinides, lanthanides do not form double (Ln=O) or triple (Ln≡N) bonds [35].

1.2.5 Coordination numbers and stereochemistry

The coordination numbers of their complexes formed range from 3 to 12, and are dependent on steric effects and the size of the Ln(III) ion [28,31]. The most common coordination numbers of 8 or 9 are expected with smaller ligands, such as water and perchlorate, while bulky ligands such as bis(trimethylsilyl) amide give lower coordination numbers (typically less than 8) to minimise electronic repulsion. The coordination numbers also appear to decrease from light lanthanides to heavy lanthanides due to the decrease in the Ln(III) ionic size [28].

These elements are known to have diverse and fascinating coordination geometries that are useful in the stereochemical description of molecular structures, or the coordination environment around the metal ions [36,37]. Their diverse geometries is due to their large ionic radii, allowing them to accommodate more ligands than transition metals. Some of the techniques used in the elucidation of their coordination geometries or polyhedra are single crystal X-ray diffraction studies and continuous shape measurement (CShM) calculations [36,37]. Although the former has been used extensively in all fields of science, continuous shape measurements provide a novel way of predicting the geometries [36]. Continuous shape measurements of a molecular fragment(s) with a central atom refers to its deviation or distance to the ideal shape, independent of orientation and size of the vertices. The distance of the structure Q to the ideal (perfect) polyhedron P is indicated by Equation 1, where the position vector $\vec{Q}_k$ ($k = 1, 2,..., N$) gives the coordinates of N atoms (donor atoms and the central atom) of the investigated structure and $\vec{P}_k$ ($k = 1, 2,..., N$) indicates the coordinates of the corresponding vertices in the reference (ideal) polyhedron. The position vector of the geometrical centre of the investigated structure is indicated by $\vec{Q}_0$. The shape measures $S_Q(P)$ are in the range 0 – 100, with 0 suggesting an exact

match to the reference polyhedron, with increasing values indicating an increase in deviation or distortion from the ideal shape [36].

$$S_Q(P) = \min \frac{\sum_{k=1}^{N} |\vec{Q}_k - \vec{P}_k|^2}{\sum_{k=1}^{N} |\vec{Q}_k - \vec{Q}_0|^2} \times 100 \qquad \text{(Equation 1)}$$

Examples of coordination geometries and their respective CShMs are listed in Table 1.2 [25,38-40]. The structures of the ligands abbreviated in Table 1.2 are indicated in Figure 1.5.

Table 1.2: Geometry analysis of some lanthanide complexes with C.N. 8 and 9 [25,38-40].

Complex	C.N.	Geometry	Symmetry	CShM
[Eu(MBTF)$_3$(DMSO)(H$_2$O)]	8	Trigonal-dodecahedral (8-TDH)	D_{2d}	0.828
[Eu$_2$(BTPE)$_3$(DMSO)$_4$]	8	Square antiprism (8-SAP)	D_{4d}	1.254
[Dy$_2$(FDA)$_3$(DMF)$_2$(CH$_3$OH)]$_n$	8	Biaugmented trigonal prism (BTPR-8)	C_{2v}	0.671
[Gd$_4$(L)$_4$(μ_4-OH)(μ_3-OH)$_2$(NO$_3$)$_4$]·(NO$_3$)	9	Capped square antiprism (CSAPR-9)	C_{4v}	~2

C.N. = coordination number
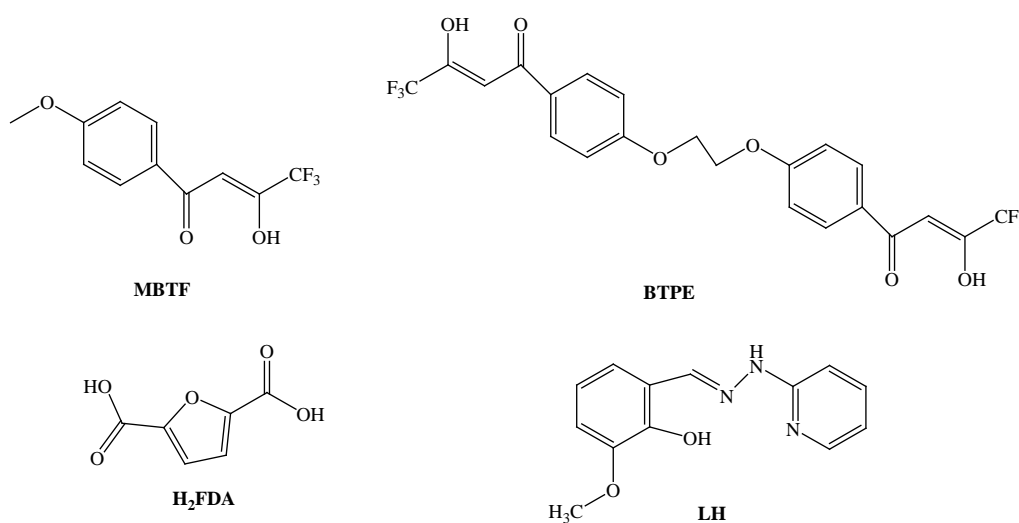
Figure 1.5: The structures of the ligands abbreviated in Table 1.2 [25,38-40].

1.3   Toxicity of lanthanide complexes

As with most therapeutic agents, side effects and the monitoring thereof, plays an important role in whether the drug reaches clinical trials or not [41]. It is thus vital to monitor potential toxicities in promising anticancer agents, such as repeated dose toxicity, genotoxicity and general toxicity [41,42]. This improves the efficiency of drug development, and ensures safe use of medicines. In addition to protecting the patients, the study of toxicological effects also reduces development costs in conducting clinical trials [41].

Once the metal compound has served its purpose, the stability of the complex plays an important role in the removal of chelated lanthanides from the body [27,43]. There is rapid renal excretion of coordinated lanthanides in urine, whereas the uncoordinated ionic Ln(III) form colloids in the blood, resulting in the uptake of the colloidal particles by phagocytes of the spleen and liver [27,43]. This leads to hepatic necrosis, characterised by morphological changes such as proliferation of smooth endoplasmic reticulum (ER), and disordering, dilation and degranulation of hepatic rough ER on intravenous injection [27]. Accumulation complications may include effects on metabolic processes such as enzymatic activities and blockage of some membrane receptors in neurons [27]. The biological changes observed at the cellular level are a result of the fact that the ionic radii of lanthanides resemble that of calcium, allowing competition with Ca^{2+} for calcium channels [27,44,45]. For example, a Gd-DTPA (DTPA = diethylenetriaminepentaacetic acid) chelate, which is useful as a nuclear magnetic resonance (NMR) contrast imaging agent, is rapidly cleared such that over 80 % is excreted within 3 hours in the urine [45]. This chelate is therefore 50 times less toxic compared to $GdCl_3$, with only 2 % excreted after 7 days, when administered intravenously [45].

Metal toxicity is not only dependent on the stability of the complex or the chemical form, but also on the route of exposure such as oral ingestion or intravenous administration, exposure time, the administered dosage and the nature of the organism affected [45,46]. The lanthanides are generally non-toxic if ingested orally, as the rare-earths cannot cross cell membranes, but are toxic when intravenously

administered, where they access calcium channels [45]. Coordination, especially to hydrophilic ligands, can be applied to improve permeability of lanthanides into cells and overcome solubility challenges within the body [47]. Toxicity studies have revealed that non-radioactive lanthanides are less toxic compared to other chemical elements, with some intravenously injected and intraperitoneal injected rare-earth compounds having the median lethal dose (LD_{50}) values higher than those of transition metals (Table 1.3) [48-50].

Table 1.3: LD_{50} of intravenously and intraperitoneal administered lanthanides obtained from material safety data sheets [49,50].

Compound	Animal	Administration method	LD_{50} (mg/kg)
Sodium chloride	Rat	Oral	3000
	Rabbit	Dermal	>10000
Chromium trioxide	Rat	Oral	80
Platinum(IV) chloride	Rat	Oral	276
Lanthanum oxide	Rat	Oral	>8500
	Mouse	Intraperitoneal	530
Cerium(IV) oxide	Rat	Oral	5000
	Rat	Dermal	1000 – 2000
Europium chloride	Mouse	Intraperitoneal	550
	Mouse	Oral	5000
Europium nitrate	Rat	Intraperitoneal	320
	Rat	Oral	>5000
[Eu(PIC)$_3$(NMK)$_3$]	Mouse	Oral	1000

Notes: (i) [Eu(PIC)$_3$(NMK)$_3$]: PIC = picric acid, NMK = *n*-methyl-caprolactam [50].

(ii) "**Toxicity Rating:** Highly toxic = 1 – 50 mg/kg, Moderately toxic = 50 – 500 mg/kg, Slightly toxic = 500 – 5000 mg/kg, Practically non-toxic = 5000–15000 mg/kg" [46].

1.4   Applications of the lanthanides

1.4.1   Therapeutic applications

Metal complexes have attracted attention due to their potential therapeutic use in different types of cancers [5]. The utility of lanthanide complexes in clinical radiology as contrast agents for cancer imaging allows for the acquisition of high resolution images in clinical magnetic resonance imaging (MRI) scans, making monitoring of organ functions possible [22,51,52]. Gadolinium complexes, such as $[Gd(DOTA)(H_2O)]^-$ and $[Gd(DTPA)(H_2O)]^{2-}$ (DOTA = 1,4,7,10-tetraazacyclododecane-1,4,7,10-tetraacetate and DTPA = diethylenetriaminepentaacetate), are the most useful in MRI [22,51,52].

Luminescent lanthanide compounds are an important tool in photodynamic therapy due to their optical emission on activation by X-rays, resulting in activation of sensitisers, which as a result, produces cytotoxic reactive oxygen species [22,51,52]. Porphyrin-conjugated terbium(III) oxide (Tb_2O_3) nanoparticles applied in photodynamic therapy have been reported [22].

The cytotoxic activity of Ln(III) coordination compounds can be ascribed to the ability of the complex to interact with DNA, inhibit calcium transport in the mitochondria (due to similar ionic radii) and hinder enzyme activities (for example thioredoxin reductase action). This subsequently inhibits replication and repair of cancer cell DNA. The photo-stability, redox stability, magnetic properties and luminescent properties, as well as the ability to interact with DNA, makes the coordination chemistry of lanthanides a key area in cancer research [22,51,52].

Recently, lanthanide complexes with oxoglaucine (Scheme 1.1) were synthesised and their *in vitro* cytotoxicity evaluated against breast cancer (MCF-7), human gastric cancer (SGC7901), liver cancer (BEL-7404), cervical carcinoma (HeLa) and A549 cell lines [13,22]. Anticancer activities against these five cancer cell lines were determined by the MTT assay [13]. It was found that the free oxoglaucine and the

corresponding lanthanide salts showed low or no inhibitory action on the cell lines tested. All three complexes were active and exhibited enhanced cytotoxicity *versus* lanthanide salts and the free ligand. The IC_{50} values of coordination compounds were determined, and it was shown that the Eu(III) and Er(III) complexes had lower IC_{50} values than cisplatin on exposure to MCF-7 cells, indicating that the lanthanide complexes are more effective [13].
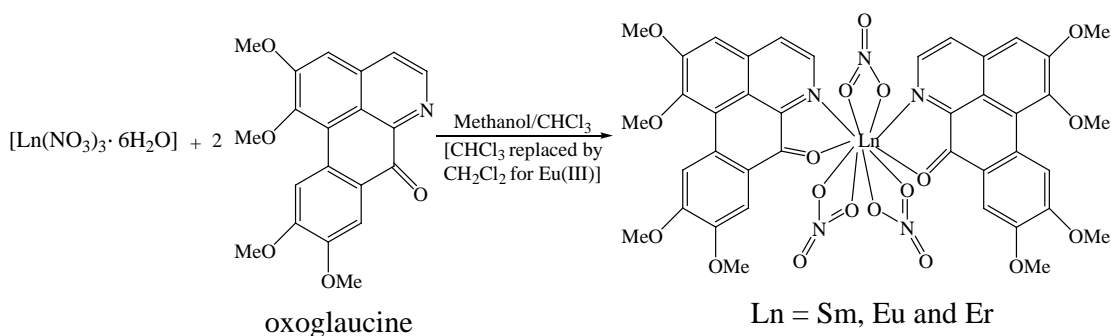
Scheme 1.1: Synthetic route for lanthanide-oxoglaucine complexes (complexes have different co-crystallised solvent molecules) [13].

1.4.2 Antimicrobial agents

Globally, high mortality rates are resultant of bacterial infections, most of which are resistant to available antibiotics [53]. This defines the urgent need for the design of novel antibacterial agents with different and more efficient mechanisms of action towards bacteria. The biological properties of the compounds like hydrazones and their Ln(III) compounds have been targeted as promising antibacterial agents [54].

Lanthanide complexes with a hydrazone ligand 2-[2-hydroxy-3-methoxyphenyl]-3-[hydroxyl-3-methoxybenzylamino]-1,2-dihydroquinazoline-4(3H)-one   (**Hmpbaq**, Figure 1.6) have been synthesised and screened for their antifungal and antibacterial activities [55]. The antimicrobial activity tests were determined against *Aspergillus niger*, *Penicillium notatum*, *Pseudomonas aeruginosa* and *Bacillus cirroflagellosus*, using the cup-plate method [55]. It was observed that the complexes exhibited higher antibacterial activity compared to the ligands and metal salts. Improved antibacterial

activity of the metal complexes is a result of the synergistic effect that enhances the lipophilicity of the complex. The more lipophilic Ln(III) coordination compounds are better able to penetrate into and through the microorganism membranes or cell wall and deactivate enzymatic activity. Structural characterisation of the complexes revealed that the Hmpbaq coordinates in a tridentate fashion through the deprotonated phenolic oxygen, the amine nitrogen and the carbonyl oxygen, to produce complexes with the formula [Ln(mpbaq)$_2$(H$_2$O)$_2$]·(NO$_3$) [55].
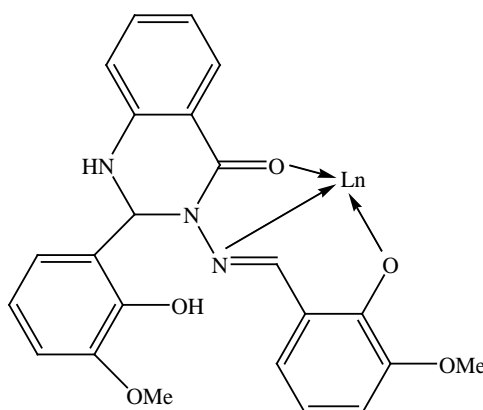
Figure 1.6: The structure of deprotonated **Hmpbaq** and its coordination mode to lanthanides [Ln = La(III), Pr(III), Nd(III), Sm(III), Eu(III), Gd(III), Tb(III), Dy(III) and Y(III)] [55].

1.4.3   Magnetic properties

Homometallic rare-earth complexes with varying nuclearities and conformations have excited researchers due to their abundant structures that have applications in magnetism and MRI contrast agents [40,56]. Mono-, di-, tri- and polynuclear lanthanide complexes have sparked enormous attention in recent years because some have been found to display single-molecule magnetic (SMM), single-chain magnetic (SCM) and single-ion magnetic (SIM) behaviour [40,56]. Slow magnetisation relaxation of polynuclear Ln(III) complexes at low temperatures enables their application in making spintronic devices [40,56].

Some research on the magnetic tetranuclear metal complexes prepared from the hydrazone Schiff base ligand, 2-methoxy-6-(pyridin-2-ylhydrazonomethyl)phenol (**LH**), (Figure 1.7), have been conducted [40]. For the gadolinium complex, the presence of weak antiferromagnetic exchange within the Gd_4 core was confirmed using an isotropic spin Hamiltonian. The alternating current susceptibility measurements performed on the dysprosium analogue, as a function of temperature and frequency, revealed a slow magnetic relaxation at low temperatures. The hydrazone ligand **LH** is suitable for the synthesis of polynuclear metal complexes due to the potential coordination sites provided through the phenolic and the methoxy oxygens, and the pyridyl and imine nitrogens [40]. The complexes produced have the formula, $[Ln_4(L)_4(\mu_4\text{-OH})(\mu_3\text{-OH})_2(NO_3)_4]\cdot(NO_3)$ (where Ln = Gd, Tb, Dy and Ho), in which the metal ions are held together by four L^- ligands, one μ_4-OH and two μ_3-OH, and a single η^2-nitrate ligand on each Ln(III) ion. The nitrate counterion balances the overall charge of the complex [40].
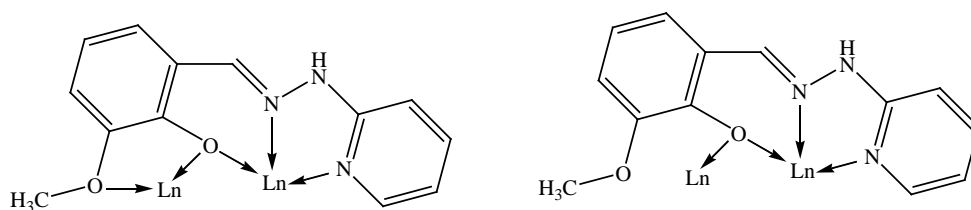
Figure 1.7: The structure of the mono-deprotonated hydrazone ligand **LH** and its coordination modes (Ln = Gd, Tb, Dy and Ho) [40].

1.4.4   Luminescence

Luminescent lanthanide compounds are generating increased attention because of their diverse applications in telecommunications, displays, lighting, lasers, pressure sensors, security inks and marking, and in a range of bioanalytical applications, such as in probing enzyme activity [28,57]. Their long luminescence lifetimes and high detection sensitivities enable utilisation of Ln(III) complexes in studying enzyme action, to gain more knowledge on enzyme activation or inhibition. This is important in curbing diseases [58].

Most lanthanide ions are luminescent due to *d-f* transitions, or the weak and faint Laporte forbidden *f-f* transitions [57]. The more intense and energetic, inter-configurational *d-f* transitions are common for Ce(III), Pr(III), Tb(III), Sm(II), Eu(II), Tm(II) and Yb(II) in the UV-Visible spectroscopic range. Since it is difficult to produce luminescence by direct excitation of the Ln(III) ion due to its poor light absorption capacity, luminescence is sensitised by energy transfer from an antenna chromophore that is strongly absorbing [26,59,60]. Efficient light absorption by the chelating ligands is achieved by light-absorbing aromatic fragments that exhibit high extinction coefficients for absorption in the ultraviolet range [26,60]. The sensitisation of Ln(III) luminescence is initiated by excitation of the ligand into the singlet excited state, followed by generation of a ligand-based triplet state after fast inter-system crossing (Figure 1.8) [26,57,61]. Distance-dependent energy transfer will then occur from the photosensitiser triplet state to the Ln(III) centre through a Dexter double electron-exchange mechanism, resulting in a luminescent *f-f* state [26,61,62].
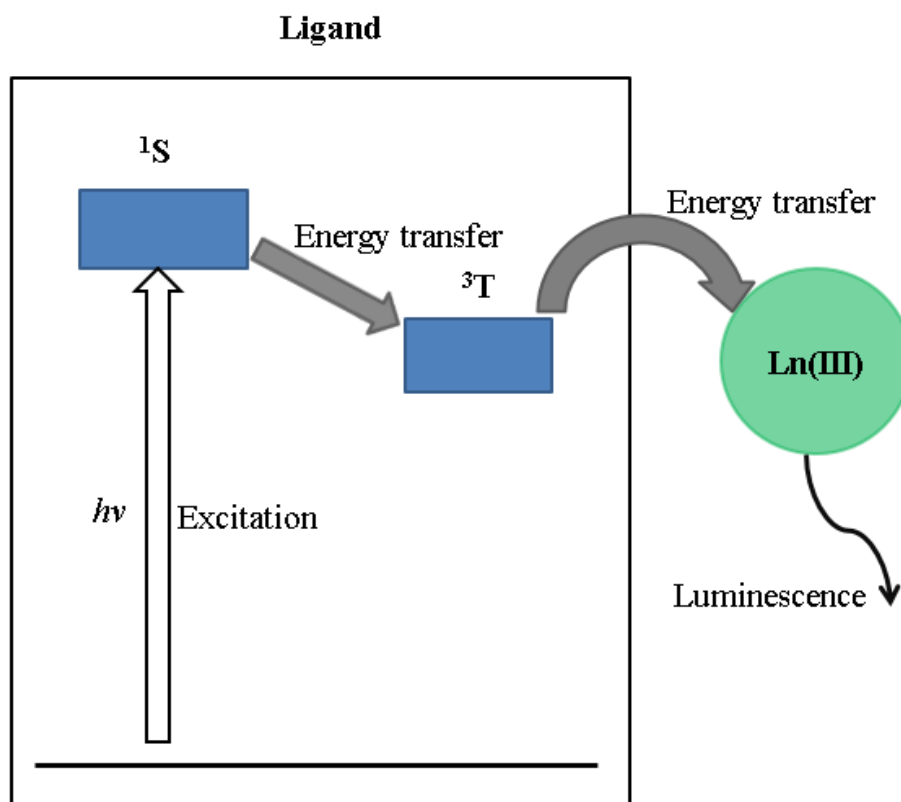
Figure 1.8: An illustration of the antenna effect on sensitisation of Ln(III) luminescence [57].

Polydentate ligands with anionic donor sites, such as carboxylates, strongly coordinate to hard Ln(III) cations to form luminescent Ln(III) complexes [28]. Europium(III) and terbium(III) complexes of the ligands featured in Figure 1.9 display high quantum yields, as well as long emission lifetimes [28,63]. The ligands shield the metal centres from water molecules, effectively eliminating these from the first coordination sphere, thereby preventing the quenching effect. Nitrogen atoms of heterocyclic moieties, such as pyridine, provide additional binding sites, and act as antennae towards the rare-earth cation [28].
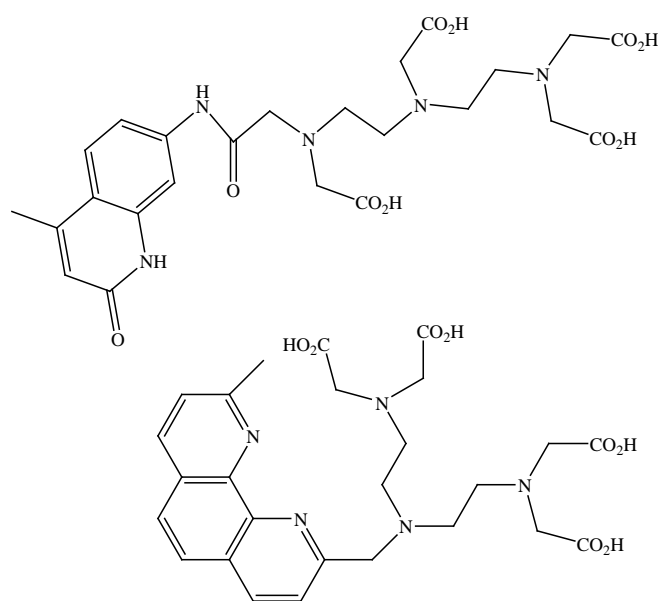
Figure 1.9: Ligands used in the preparation of Eu(III) and Tb(III) complexes displaying highly luminescent properties [28].

1.4.5   Catalysis

Lanthanides and their complexes form an important class of catalysts used in biological systems, refining petroleum, polymerisation, hydroboration, amidation, to name a few [64]. The catalytic properties that make lanthanide complexes promising candidates for catalysis, include their large ionic radii and little or no covalent bond character with the ligands. This means that the complex is not confined to a single geometry, facilitating intramolecular and intermolecular ligand exchange [26,65].

In biological systems, lanthanide complexes with hydroxide-containing ligands have potential use in the catalysis of hydrolytic cleavage of RNA and DNA [26]. These Ln(III) complexes are able to mimic the role of natural nucleases through the coordination of the Ln(III) cation to the phosphate group, proceeded by nucleophilic attack by the Ln-bonded hydroxide group [26]. The result is cleavage of the biozide-type phenyl phosphate esters of DNA or related oligonucleotides [26].

Metal complexes with 1,10-phenanthroline or its derivatives have been exploited due to their catalytic and redox properties [66]. For example, nickel(II) complexes with 2-(benzimidazol-2-yl)-1,10-phenanthroline derivatives, are used as catalysts for oligomerisation of ethylene [66]. Homoleptic lanthanide amido complexes, Ln[N(SiMe$_3$)$_2$]$_3$ (Ln = La, Sm and Y) are an important class of efficient catalysts that mediate amidation of aldehydes with amines (Scheme 1.2) [67]. This is a vital process in the formation of aromatic and aliphatic amides that are useful in the synthesis of pharmaceuticals and natural products, and polymers. Generally, most amidation processes reported were catalysed by transition metal complexes, such as palladium, copper and nickel, with an added oxidant, whilst lanthanide-catalysed reactions reached high yields at room temperature in the absence of heat, light, oxidants and bases [67].
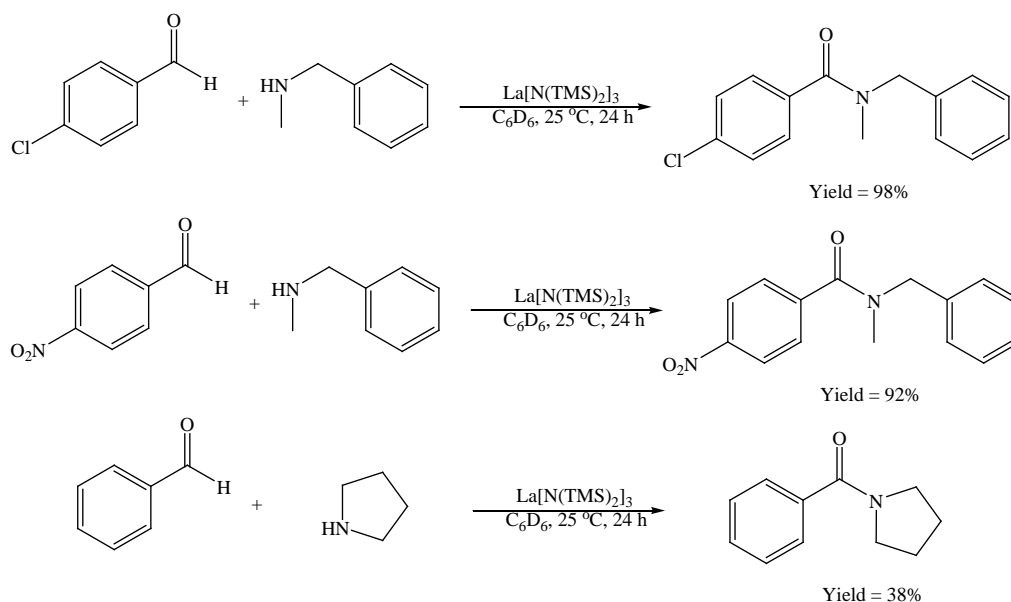
Scheme 1.2: Catalytic amidation of aldehydes with amines by lanthanide complexes (Yields are based on amines) [67].

1.4.6   Plant growth regulators

Low concentrations of lanthanides enhance plant growth, while exposure to high concentrations leads to toxicity, a process referred to as the Hormesis effect [68,69]. In view of this, rare-earth-based fertilisers containing the appropriate concentration of lanthanides are used in agriculture to promote plant growth or seed germination by minimising water loss (due to the high affinity of the metal for the hard *O*-atoms), increasing chlorophyll content, and improving nitrogen fixation [68,70,71]. Rare-earth complexes can augment respiration and photosynthesis rates through enhancement of hydrolytic enzymes and plant hormone activities [68,70].

Carboxylic acids, such as indole-3-acetic acid, naphthyl-1-acetic acid and benzimidazole-2-acetic acid and their Ln(III) complexes, form an important class of plant growth promoters [69]. Lanthanum(III) has been coordinated to benzimidazole-2-acetic acid (**H₂bza**) to yield a complex that displays improved activity on the germination of wheat, compared to the free ligand and the metal salt (Scheme 1.3). This chelation resulted in a synergistic effect: the interaction of two or more substances to give a combined effect that is greater than the sum of their separate effects [69]. Studies on the biological action of the La(III) complex with the hydrazono-acetic acid ligand, 2-{[2-(2,4-dichloro-phenoxy)-acetyl]-hydrazonomethyl}-phenoxy acetic acid (**H₂L**) (Figure 1.10) on the wheat seeds, *Triticum durum*, revealed enhanced auxin activity upon coordination to lanthanum, that is essential for plant growth processes [72]. Lanthanum nitrate was found to increase the rate of germination of rice seeds [70].

$[La(NO_3)_3]$ + 2 [Benzimidazole-2-acetic acid structure] $-CH_2-COOH$ $\xrightarrow[\text{Methanol}]{\text{NaOH}}$ $[La_3(Hbza)_2(NO_3)_7(H_2O)_4]\cdot 3H_2O$

Benzimidazole-2-acetic acid (H₂bza)
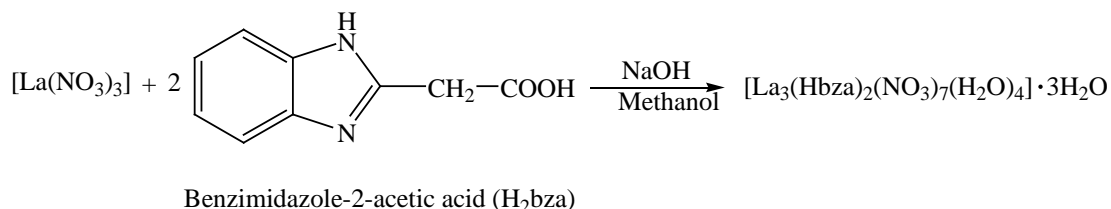
Scheme 1.3: Synthesis of the La(III) complex with **H₂bza** [69].
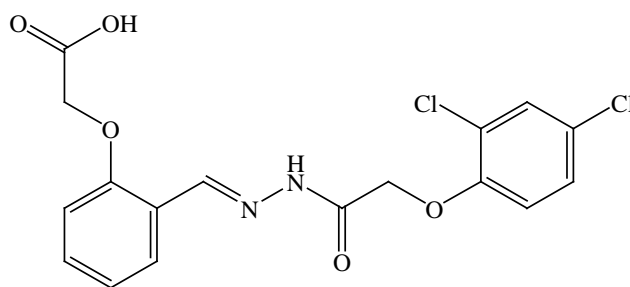
Figure 1.10: The structure of **H₂L** [72].

1.5   Schiff bases and their metal complexes

Schiff bases are organic compounds with the general structure $R^1R^2C=NR^3$ ($R^3 \neq H$) containing an imine or azomethine (>C=N-) moiety that connects two or more heterocyclic or aromatic groups to form biologically active and structurally diverse compounds [53,73-75]. The organic compounds are synthetically attainable under specific conditions by the condensation of a primary amine and a ketone or an aldehyde. Schiff bases are useful *d*-block and lanthanide chelating agents due to the presence of oxygen, nitrogen or sulphur atoms. The various biological uses of this distinctive category of compounds and their metal complexes include anticancer, antimicrobial, antidiabetic, antimalarial, antioxidant, and anti-inflammatory activities [53,73-75].

Unique biological properties are conferred by the electrophilic carbon and the nucleophilic nitrogen atom of the >C=N- functional group allowing interaction with nucleophiles and electrophiles, thus impeding enzyme action and DNA replication [76]. Consequently, the progression of targeted diseases can be halted or limited. The mechanism of action of the Schiff bases might also involve the azomethine *N*-atom that can potentially form hydrogen bonds with active components of the cell, for example, nucleic acids or proteins, thereby interfering with cellular processes [75]. Their metal complexes exhibit fluorescence characteristics that are useful in diuretic and DNA-binding research [73,74]. Apart from their therapeutic uses, Schiff bases are also used in industry as catalysts, pigments, dyes, corrosion inhibiting agents, as well as polymer stabilisers [75].

Praseodymium(III) and erbium(III) complexes with the neutral bidentate Schiff base ligand N^2,N^3-bis(anthracen-9-ylmethylene)pyridine-2,3-diamine (**SBL**), were tested as anticancer against MCF-7 and HeLa cell lines [77]. The neutral ligand coordinates to the metal ions in a bidentate fashion *via* two azomethine nitrogen atoms. *In vitro* cytotoxicity and induced DNA cleavage activities of Pr-SBL and Er-SBL complexes against MCF7 and HeLa cells were confirmed using the MTT and propidium iodide (PI) staining assays [77]. Another intriguing facet of research involved a distorted octahedron copper(II) complex with a bidentate *N,O*-donor ligand derived from sulfamethoxazole and 5-nitrosalicylaldehyde that was screened for antifungal and antibacterial activity against *Candida albicans, Aspergillus niger, Bacillus subtilis, Klebsiella aerogenes, Escherichia coli* and *Staphylococcus aureus* [78]. Significant antimicrobial activities were detected. The *in vitro* cytotoxicity of the free ligand and the metal complex was investigated on human cancer cell lines: breast cancer (MDA-MB-231) and colon cancer (HCT-116). It was discovered that the metal complex displayed higher activity (IC$_{50}$ = 6.48 µm) compared to the platinum-based drugs cisplatin (IC$_{50}$ = 13.98 µm) and carboplatin (IC$_{50}$ = 68.26 µm) against MDA-MB-231 cells [78].

A bioactive Schiff base *N*-(salicylidene)-2-hydroxyaniline is a promising antibacterial agent against *Mycobacterium tuberculosis* [79]. The La(III), Pr(III), Nd(III), Sm(III) and Gd(III) complexes with a tetradentate chelating agent (*N,N'*-bis(1-naphthaldimine)-*o*-phenylenediamine) were prepared and subjected to antimicrobial activity tests using the agar well diffusion and the micro-broth dilution methods [80]. It was concluded that various pathogenic bacterial species, such as *S. aureus*, *E. coli*, *Shigella dysenteriae* and *Pseudomonas aeruginosa*, were susceptible to the metal complexes [80].

The currently available vaccines or viral agents used in the treatment of viral infections, such as polio, smallpox and influenza, are not satisfactorily effective due to mutations that lead to antiviral drug-resistant strains [73]. The Schiff bases are a good platform for the construction of new antiviral agents, providing an effective therapeutic alternative for viral infections [73]. The compound, 3-[(2-hydroxy-

benzylidine)-amino]-2-phenyl-3*H*-quinazolin-4-one, showed antiviral activity towards a number of viruses, including herpes simplex virus-1 (KOS), herpes simplex virus-2(G) and vaccinia virus, in HEL, vero, CRFK, HeLa and MDCK cell cultures [81]. The Schiff base showed more potent inhibitory action than related compounds on the replication of the reovirus, Coxsackie virus B4, Sindbis virus and Punta Toro virus, with cytotoxicity indicated at 100 mg/mL using the colorimetric formazan-based MTS (3-(4,5-dimethylthiazol-2-yl)-5-(3-carboxymethoxyphenyl)-2-(4-sulfophenyl)-2H-tetrazolium) assay [81].

Schiff bases and their lanthanide complexes are thus favourite candidates for gaining knowledge on the structure of biomolecules and cellular processes, facilitating cancer treatment, immobilisation of enzymes and effectively treating infectious diseases such as tuberculosis [73,76,79].

1.6   Hydrazones and their metal complexes

Hydrazones are Schiff bases of the type $R_1R_2C=N–NR_3R_4$ [82,83]. The two connected nitrogen atoms are of different chemical nature, and conjugation of the >C=N- bond occurs with the lone pair electrons of the terminal *N*-atom [82]. It is these structural fragments that are mainly responsible for the physico-chemical properties of hydrazones. Both the hydrazone group *N*-atoms are known to be nucleophilic due to their high electronegativity and lone electron pairs, and their reactivities are dependent on the chemical traits of the electrophiles. The compounds are of great significance in inorganic and synthetic chemistry due to their ability to react with nucleophilic and electrophilic compounds, producing compounds with a broad range of biological and pharmaceutical activities, such as antimicrobial, anticancer, antimalarial, as well as antioxidative, activities [6-11]. Hydrazones also find applications as rodenticides, insecticides, plant-growth regulators and herbicides, to name a few [83]. Some of the desirable characteristics of these compounds include increased hydrolytic stability compared to imines, ease of preparation and tendency toward crystallinity [82]. Due to these positive characteristics, hydrazones are ideal candidates as ligands for metal complexes in drug design.

These special class of Schiff bases are generally prepared by the reactions of carbonyl compounds with hydrazines in the presence of an acid, such as acetic acid (AcOH) (Scheme 1.4) [82]. Modifications to molecules can be attained by the introduction of functional groups, such as thioamide, amide and amidine groups, leading to unique physico-chemical properties (Figure 1.11) [82].
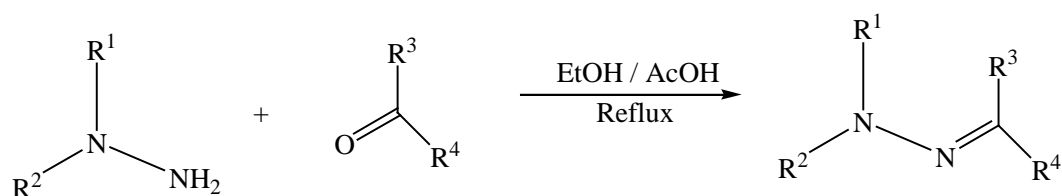
Scheme 1.4: General synthesis of hydrazones [82].

Hydrazono-thioamide   Hydrazono-amide   Hydrazono-amidine

R^1, R^2, R^3, R^4, R^5 = H, alkyl or aryl
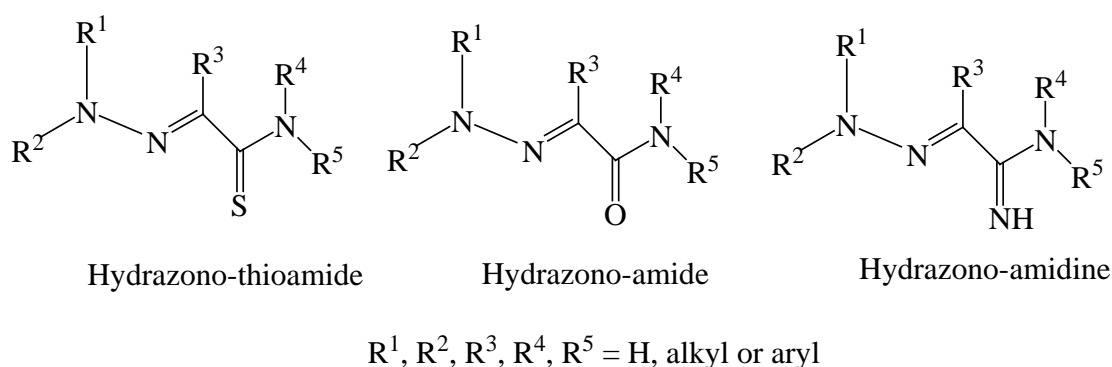
Figure 1.11: Hydrazones bearing thioamide, amide and amidine moieties [82].

This class of compounds have potential use in the development of new antitubercular drugs that are effective against resistant strains of *Mycobacterium tuberculosis*, thereby reducing public health problems caused by tuberculosis [8-10]. The evaluation of the antibacterial activity of hydrazone ligands, such as (*E*)-*N*-(2,5-dichlorophenyl)-*N'*-(1*H*-indol-3-ylmethylene)hydrazine and (*E*)-*N'*-(2-methyl-1*H*-indol-3-ylmethylene)-*N*-phenylhydrazine (Figure 1.12), was performed against *Mycobacterium tuberculosis H37Rv* at a concentration of 6.25 μg/mL using the Microplate Alamar Blue Assay (MABA) [8]. It was concluded that the compounds were active, with IC$_{50}$ values of 5.40 and 5.96 μg/mL, respectively [8].

a   b
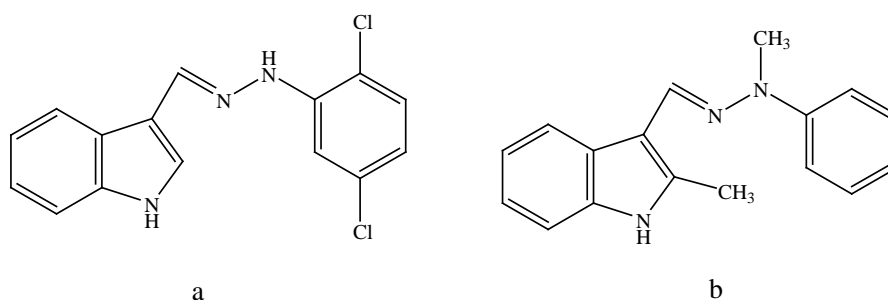
Figure 1.12: The structures of: (a) (*E*)-*N*-(2,5-dichlorophenyl)-*N*′-(1*H*-indol-3-ylmethylene)hydrazine, (b) (*E*)-*N*′-(2-methyl-1*H*-indol-3-ylmethylene)-*N*-phenylhydrazine [8].

The tridentate hydrazone ligand derived from 2-hydrazinopyridine and pyridine-2-carbaldehyde (Figure 1.13) was prepared and successfully complexed to Nd(III) and Sm(III) [11]. X-ray diffraction studies indicated that the binuclear complexes are nine-coordinate, obeying a distorted tricapped trigonal prism geometry [11]. Each unit of the centrosymmetric dimeric structure has the Ln(III) ion bonded to the tridentate hydrazone (two pyridyl and one azomethine *N*-atoms), one bidentately coordinated acetate group (*O,O*-donor), one bidentate bridging acetate group, two water molecules and one uncoordinated nitrate anion to counteract the charge [11].

The radical scavenging ability of the ligand (Figure 1.13) and its complexes on 2,2-diphenyl-1-picrylhydrazyl (DPPH·) were screened [11]. The ligand was found to exhibit significant antioxidant activities against the DPPH· radicals, with more efficient radical quenching upon complexation. It was reported that the the free radical scavenging ability of hydrazones arises from polarisation of the N-H bond, hence allowing abstraction and donation of the hydrogen atom to form DPPH-H [11,84]. Complexation to the lanthanides increases the polarisation of the N-H bond, thereby significantly increasing scavenging activity [11].
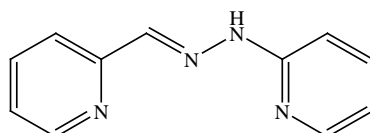
Figure 1.13: The structure of 1-(pyridin-2-yl)-2-(pyridine-2-ylmethylene)hydrazine [11].

Conjugated hydrazones possess antimalarial activity by inhibiting *Plasmodium falciparum* growth *in vitro* and *in vivo* [85,86]. An example of an antimalarial hydrazone that displayed antiplasmodial activity towards *P. falciparum* (K1) strain, resistant to pyrimethamine and chloroquine, is shown in Figure 1.14 [85]. The hydrazone mechanism of action involved interaction with free heme and inhibition of heme polymerisation by parasite lysate. The sulfur- and nitrogen-substituted aromatic rings play an important role in facilitating the iron chelator ability of hydrazones, thus limiting the activity of iron-containing enzymes in the parasite [85].
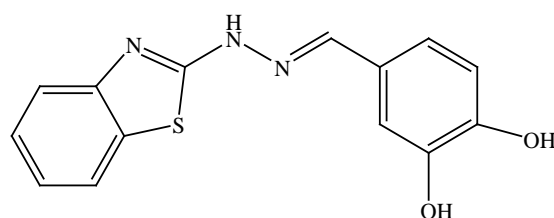
Figure 1.14: The structure of a hydrazone ligand with antiplasmodial activity [85].

Another biological advantage that makes hydrazones a unique class of organic compounds is the anti-urease activity [87]. Generally, hydrazone derivatives bearing electron-withdrawing groups (*e.g.* -NO$_2$) strongly inhibit urease action. Urease is an enzyme found in bacteria (such as *H. pylori* and *P. mirabilis*), plants, fungi, and man that converts urea to NH$_3$ and CO$_2$, making the environment ideal for bacterial development and growth. Focusing on the chemistry of hydrazones and their coordination compounds is therefore of tremendous importance in fighting gastrointestinal and urinary tract infections caused by ureolytic bacteria [87].

Hydrazones play a role as pesticides in combating pests (especially anthropods and nematodes) that cause huge economic losses to farmers, as well as fighting pest resistance [76]. The hydrazone compounds featured in Figure 1.15 exhibit anti-pesticidal action against anthropod pests and nematodes [76].
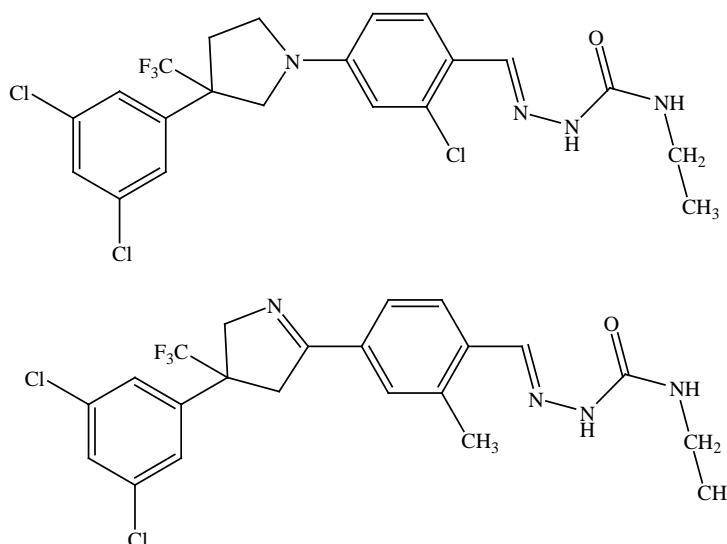
Figure 1.15: Bioactive hydrazone derivatives with potential use against pests [76].

1.7   Carboxylic acids and their metal complexes

Aromatic carboxylic acids have a high affinity for rare-earth ions, due to the presence of their hard, anionic donor atoms [28,88]. The hydroxyl group can be deprotonated to form a carboxylate anion, producing various binding modes, or provide extra coordination sites in addition to the carboxyl groups, to form more complex structures, like polymers [89]. The carboxylates are resonance stabilised, where the excess charge on the carboxylate anion can be stabilised upon complexation through interaction with the cation [28]. Molecular stability in carboxylic acids and their coordination compounds can be enhanced by formation of C/O–H···π, C/O–H···O and π···π interactions [89].

In light of the intriguing properties of carboxylic acids, lanthanide carboxylate compounds have generated interest in the past due to their use as luminescence and magnetic materials [89]. The aromatic carboxylic acid ligands, such as benzoic acid and its derivatives like 3,4,5-triethoxybenzoic acid, play an important role in fine-tuning the geometric properties and functionality of lanthanide complexes [88,89]. The ligand, 3,4,5-triethoxybenzoic acid, was used for the preparation of a highly luminescent Eu(III) complex [88]. Typical Eu(III) luminescence and the antenna effect of the aromatic ligand were observed in the photoluminescence spectra [88].

The dimeric coordination compound $[Eu_2L_2(\mu\text{-}OH)_2]$ (where L = 1,7-diaza-4,10, 13-trioxacyclopentadecane-*N,N'*-diacetic acid) cleaves the RNA analogue, phosphodiester 2-hydroxypropyl-6-nitrophenyl phosphate [26]. A search of the literature indicated the catalytic activity of $[EuEDDA]^+$ (where EDDA is ethylenediamine-*N,N'*-diacetic acid) on the efficient hydrolysis of the phosphodiester bond of sodium bis(4-nitrophenyl)-phosphate (BNPP), pH 8.4 [90]. The reaction rates are dependent on the Ln(III) ionic radius, charge on the complex, coordination number and the number of bound water molecules. Effective BNPP hydrolysis is achieved with a smaller metal ionic radius, maximum amount of bonded water molecules (in the inner coordination sphere) and a higher positive charge on the complex [90]. Lanthanide-carboxylic acid chelates are preferable in the preparation of these artificial nucleases and ribonucleases because of their Lewis acidity, high coordination numbers, increased flexibility, and most importantly, high thermal and kinetic stabilities of the complexes. Understanding the behaviour of lanthanide compounds as artificial nucleases or ribonucleases is of paramount importance in the development of biomedical applications, as DNA is one of the most vital targets of several anticancer agents [90].

In search of anticancer drugs that can counter drug resistance, toxicity and adverse effects, platinum(IV) complexes with the carboxylic acid ligands indole-3-acetic acid and indole-3-propionic acid were of significant interest [91]. Two of the ten Pt(IV)-carboxylic acid complexes reported by Tolan *et al.* are shown in Figure 1.16. The Pt(IV)-carboxylic acid pro-drugs encouraged reactive oxygen species (ROS) generation in cells, promoting apoptosis of cancer cells. It was also observed that the Pt(IV) complexes had the ability to overcome resistance associated with the use of cisplatin [91]. The coordination chemistry of carboxylic acids and the 4*f* elements may therefore lead to the development of new therapeutic strategies in the treatment of cancer [91,92].
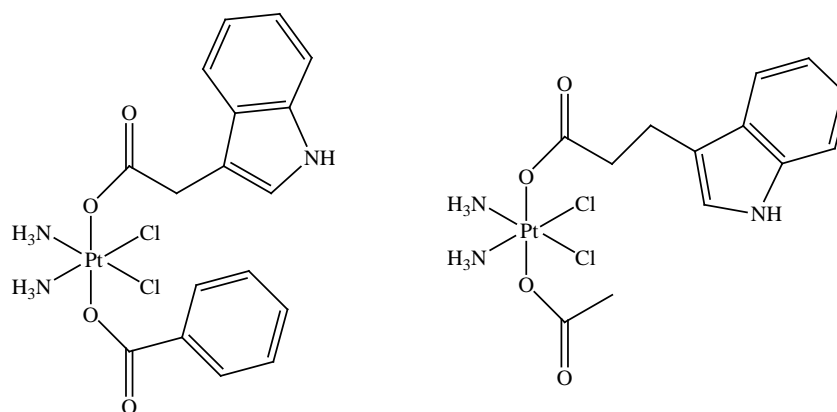
Figure 1.16: Structures of Pt(IV) complexes of indole-3-acetic acid and indole-3-propionic acid [91].

1.8   Phenanthrolines and their metal complexes

The coordination chemistry of the 4*f* metals is dominated by *O*-donor ligands [48]. Nitrogen-donors, such as 1,10-phenanthroline, however, have the ability to form stable Ln(III) complexes, that are further stabilised with nitrates. This bidentate aromatic *N*-donor ligand is hydrophobic, basic, planar and has a rigid structure due to the presence of the central ring, leading to the two *N*-atoms being in juxtaposition [48,66]. The rigidity, high dipole moment, bidenticity, as well as the π-π stacking interaction of the 1,10-phenanthroline rings, provide stability upon coordination [48,93]. The chemical properties of the auxiliary ligands like 1,10-phenanthroline in metal complexes thus play a vital role in the kinetic and thermodynamic properties of the coordination compounds [17].

These heterocyclic aromatic diazaphenanthrene analogues are found in sex hormones, sterols, morphine alkaloids and bile acids [94]. Phenanthrolines and their derivatives have attracted enormous attention in medicinal and synthetic chemistry due to their use in the preparation of biologically active molecules, and the ability to form strong complexes with metal ions [28,88,95]. These ligands can be synthesised through the Friedländer condensation from aminoquinolines and enolisable ketones as displayed in Scheme 1.5 [66].
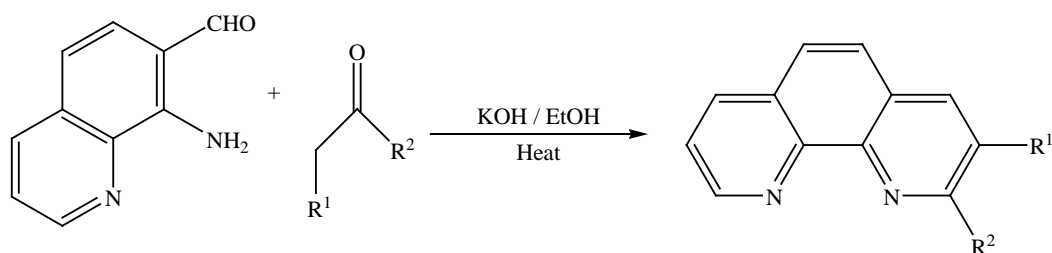
Scheme 1.5: Preparation of phenanthrolines [62,66].

Phenanthroline metal complexes interacts with DNA and can thus be used as therapeutic agents and DNA nucleases [66]. A tris(phen)-La(III) trithiocyanate complex has been found to exhibit anticancer properties [96]. The compound comprise of the lanthanum centre bonded to three rigid planar 1,10-phenanthroline ligands, to give a coordination number of six [96]. A tris-(1,10-phenanthroline) complex with cobalt(III) was prepared and characterised [97]. Antimicrobial evaluation of the Co(III) complex against *S. aureus*, *Proteus vulgaris* and *A. flavus* indicated good antibacterial and antifungal activities [97].

Phenanthroline-based compounds may act in the synthesis of luminescent materials, stabilising agents in nanoparticle synthesis, ligands for the formation of catalytic complexes and separation of actinides from lanthanides [48,66,89,98]. For example, a phenanthroline-derived bis-triazine ligand (**BTPhen**) proved to be highly efficient and selective in the separation of the trivalent actinides Am(III) and Cm(III), from the trivalent lanthanides Eu(III) and Yb(III), in nitric acid solutions [98]. The ligand forms very stable complexes and displays high selectivity towards Eu(III) and Yb(III) [99]. The ligand 1,10-phenanthroline and its derivatives significantly increase the luminescence quantum yield of lanthanide complexes, for example in Ln(III)-carboxylate complexes [63]. The ligand enhances luminescence by exclusion of water and solvent molecules from the coordination sphere that may trigger the quenching effect [63,100].

1.9   Mixed-ligand   complexes   of   carboxylic   acids   and phenanthrolines

Carboxylic acids, such as benzoic acid and its derivatives, have interesting chemical properties and therefore play a major role in pharmaceutical industries and the construction of polymers [101]. In addition to a carboxylic acid, 1,10-phenanthroline is usually used as an auxiliary or secondary ligand to enhance biological and luminescence properties, as well as complex stability. The aromatic ligands, such as 1,10-phenanthroline, benzoate, salicylic acid and benzoate derivatives, have been applied in the sensitisation of lanthanide luminescence by the antenna effect [66,89].

Four mixed ligand coordination compounds of 2-bromine-5-methoxybenzoic acid and 1,10-phenanthroline with the trivalent rare-earths Nd(III), Sm(III), Ho(III) and Er(III), have been constructed and screened for bacteriostatic activities against *C. albicans*, *E. coli* and *S. aureus* [101]. The dinuclear isostructural coordination compounds are nine coordinate, and the geometry around the metal ion is distorted mono-capped square antiprism [101]. The complexes comprise bidentately chelating 1,10-phenanthroline and bidentately coordinating carboxylic acid ligands, as well as the bridging carboxylic acid molecules in a tridentate fashion. All the complexes have significant action against the yeast, *C. albicans* [101].

Researchers also reported the synthesis and characterisation of luminescent/magnetic trinuclear and binuclear lanthanide complexes derived from salicylic acid (**H$_2$SA**) and 1,10-phenanthroline (**phen**) [89]. The compounds have the formulae, [Ln$_3$(HSA)$_5$(SA)$_2$(phen)$_3$] (Ln = Ho and Er) and [Sm$_2$(HSA)$_2$(SA)$_2$(phen)$_3$], and feature salicylate in coordination modes (Figure 1.17). At excitation, the Sm(III) and Er(III) complexes display luminescence in the visible and the near-infrared regions, respectively [89].
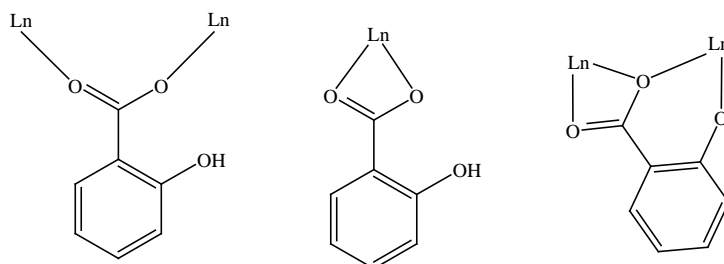
Figure 1.17: The coordination mode of **HSA$^-$** and **SA^{2-}** to Ho(III), Er(III) and Sm(III) ions [89].

1.10   Research aims and objectives

Aim:

The aim of this study was to develop efficient synthetic routes for the total synthesis of novel lanthanide complexes with hydrazones, carboxylates (or oxamates) and 1,10-phenanthroline (as an auxiliary ligand); and to further undertake theoretical, spectroscopic and structural studies of these compounds. A screen for anticancer activity was conducted to determine potential anticancer effects of the compounds.

The objectives of the study are as follows:

1. Chemical synthesis of hydrazone and carboxylic acid complexes were performed under varying reaction conditions including varying temperatures, different solvents (e.g. methanol and H_2O) and reactant ratios, and with or without the use of base catalysts, such as NaOH. Lanthanide(III) acetate, nitrate and chloride salts were used as starting materials.

2. Physico-chemical techniques, such as melting points, elemental analyses, FT-IR, NMR, UV/Vis spectroscopy and X-ray crystallography were used in characterisation. *SHAPE 2.1* and *VESTA* softwares were used in determining the geometries around the 4*f* metal ions.

3. In order to obtain information about the structure in solution (DMSO) and the gaseous phase of the neutral and monoanionic ligands, DFT calculations were performed using the *Gaussian 16* program package (Rev. B01), based on the B3LYP model and aug-cc-pVTZ basis set. Natural population analysis (NPA) and visual representations from molecular electrostatic potential (MEP) maps were used to show the charge distributions of the molecules, thus providing insights into electrophilic and nucleophilic reactivity.

4. Investigate cancer cell cytotoxicity of the target compounds on MCF-7, HEC-1A and THP-1 cell lines using the MTT assay. The MCF-7 and HEC-1A cells are estrogen responsive cells, while THP-1 cells are used to represent the normal cell population. Selectivity towards cancer cells is an advantage as it appears that the compounds would selectively target cancerous cells without adversely affecting the functioning of the normal cells.

1.11   References

[1]   American Cancer Society. *Global Cancer Facts & Figures*, 3rd Edition, Atlanta: American Cancer Society; 2015, pp 1–61.

[2]   R. Shah, K. Rosso and S.D. Nathanson, "Pathogenesis, prevention, diagnosis and treatment of breast cancer", *World J. Clin. Oncol.*, **5** (2014) 283–284.

[3]   M.I. Nounou, F. ElAmrawy, N. Ahmed, K. Abdelraouf, S. Goda and H. Syed-Sha-Qhattal, "Breast Cancer: Conventional diagnosis and treatment modalities and recent patents and technologies", *Breast Cancer: Basic and Clinical Research*, **9** (2015) 17–34.

[4]   A. Talhouk and J.N. McAlpine, "New classification of endometrial cancers: The development and potential applications of genomic-based classification in research and clinical care", *Gynecologic Oncology Research and Practice,* **3** (2016) 1–12.

[5]   P. Jia, R. Ouyang, P. Cao, X. Tong, X. Zhou, T. Lei, Y. Zhao, N. Guo, H. Chang, Y. Miao and S. Zhou, "Review: Recent advances and future development of metal complexes as anticancer agents", *J. Coord. Chem.*, **70** (2017) 2175–2201.

[6]   B. Moksharagni and K. Hussain Reddy, "A review on pharmaceutical applications of lanthanide complexes with nicotinoyl and isonicotinoyl hydrazones", *EJBPS*, **5** (2018) 810–817.

[7]   J. Easmon, G. Pürstinger, K.-S. Thies, G. Heinisch and J. Hofmann, "Synthesis, structure–activity relationships, and antitumor studies of 2-benzoxazolyl hydrazones derived from alpha-(*N*)-acyl heteroaromatics", *J. Med. Chem.*, **49** (2006) 6343–6350.

[8]   V.N. Sonar and P.A. Crooks, "Synthesis and antitubercular activity of a series of hydrazone and nitrovinyl analogs derived from heterocyclic aldehydes", *J. Enzyme Inhib. Med. Chem.*, **24** (2009) 117–124.

[9]   F.R. Pavan, P.I. da S. Maia, S.R.A. Leite, V.M. Deflon, A.A. Batista, D.N. Sato, S.G. Franzblau and C.Q.F. Leite, "Thiosemicarbazones, semicarbazones, dithiocarbazates and hydrazide/hydrazones: Anti–mycobacterium tuberculosis activity and cytotoxicity", *Eur. J. Med. Chem.*, **45** (2010) 1898–1905.

[10]   A. De Logu, V. Onnis, B. Saddi, C. Congiu, M.L. Schivo and M.T. Cocco, "Activity of a new class of isonicotinoylhydrazones used alone and in combination with isoniazid, rifampicin, ethambutol, para-aminosalicylic acid and clofazimine against *Mycobacterium tuberculosis*", *J. Antimicrob. Chemother.*, **49** (2002) 275–282.

[11]   M.N. Gueye, M. Dieng, I.E. Thiam, D. Lo, A.H. Barry, M. Gaye and P. Retailleau, "Lanthanide(III) complexes with tridentate Schiff base ligand, antioxidant activity and X-ray crystal structures of the Nd(III) and Sm(III) complexes", *S. Afr. J. Chem.,* **70** (2017) 8–15.

[12]   J. Xie, S. Shen, R. Chen, J. Xu, K. Dong, J. Huang, Q. Lu, W. Zhu, T. Ma, L. Jia, H. Cai and T. Zhu, "Synthesis, characterization and antitumor activity of Ln(III) complexes with hydrazone Schiff base derived from 2-acetylpyridine and isonicotinohydrazone", *Oncol. Lett.,* **13** (2017) 4413–4418.

[13]   Y.-C. Liu, Z.-F. Chen, Y.-F. Shi, K.-B. Huang, B. Geng and H. Liang, "Oxoglaucine-lanthanide complexes: synthesis, crystal structure and cytotoxicity", *Anticancer Res.,* **34** (2014) 531–536.

[14]   T. Zhu, R. Chen, H. Yu, Y. Feng, J. Chen, Q. Lu, J. Xie, W. Ding and T. Ma, "Antitumor effect of a copper(II) complex of a coumarin derivative and phenanthroline on lung adenocarcinoma cells and the mechanism of action", *Mol. Med. Rep.*, **10** (2014) 2477–2482.

[15]   S.-H. Liu, J.-W. Zhu, H.-H. Xu, Y. Wang, Y.-M. Liu, J.-B. Liang, G.-Q. Zhang, D.-H. Cao, Y.-Y. Lin, Y. Wu and Q.-F. Guo, "Protein-binding, cytotoxicity in vitro and cell cycle arrest of ruthenium(II) polypyridyl complexes", *Spectrochim. Acta, Part A: Molecular and Biomolecular Spectroscopy*, **161** (2016) 77–82.

[16]   C. Al Hageh, M. Al Assaad, Z. El Masri, N. Samaan, M. El-Sibai, C. Khalil and R.S. Khnayzer, "Long-lived cuprous bis-phenanthroline complex for the photodynamic therapy of cancer", *Dalton Trans.*, **47** (2018) 4959–4967.

[17]   C.-H. Leung, S. Lin, H.-J. Zhong and D.-L. Ma, "Metal complexes as potential modulators of inflammatory and autoimmune responses", *Chem. Sci.*, **6** (2015) 871–884.

[18]   V.W.-W. Yam and K.K.-W. Lo, "Recent advances in utilization of transition metal complexes and lanthanides as diagnostic tools", *Coord. Chem. Rev.*, **184** (1999) 157–240.

[19]   S.H. van Rijt and P.J. Sadler, "Current applications and future potential for bioinorganic chemistry in the development of anticancer drugs", *Drug Discov. Today*, **14** (2009) 1089–1097.

[20]   K.L. Haas and K.J. Franz, "Application of metal coordination chemistry to explore and manipulate cell biology", *Chem. Rev.*, **109** (2009) 4921–4960.

[21]   S.C. Srivastava, "Criteria for the selection of radionuclides for targeting nuclear antigens for cancer radioimmunotherapy", *Cancer Biother. Radiopharm.*, **11** (1996) 43–50.

[22]   R.D. Teo, J. Termini and H.B. Gray, "Lanthanides: Applications in cancer diagnosis and therapy", *J. Med. Chem.*, **59** (2016) 6012–6024.

[23]   I. Kostova, "Lanthanides as anticancer agents", *Curr. Med. Chem. – Anti-Cancer Agents*, **5** (2005) 591–602.

[24]   I. Kostova, N. Trendafilova and G. Momekov, "Theoretical, spectral characterization and antineoplastic activity of new lanthanide complexes", *J. Trace Elem. Med. Biol.*, **22** (2008) 100–111.

[25]   K. Liu, H. Li, X. Zhang, W. Shi and P. Cheng, "Constraining and tuning the coordination geometry of a lanthanide ion in metal−organic frameworks: Approach toward a single-molecule magnet", *Inorg. Chem.*, **54** (2015) 10224–10231.

[26]   C. Huang (2010) – *Rare-Earth Coordination Chemistry – Fundamentals and Applications*. John Wiley & Sons, Asia. pp 1–500.

[27]   S. Hirano and K.T. Suzuki, "Exposure, metabolism, and toxicity of rare earths and related compounds", *Environ. Health Perspect.,* **104** (1996) 85–95.

[28]   L. Armelao, S. Quici, F. Barigelleti, G. Accorsi, G. Bottaro, M. Cavazzini and E. Tondello, "Design of luminescent lanthanide complexes: From molecules to highly efficient photo-emitting materials", *Coord. Chem. Rev.,* **254** (2010) 487–505.

[29]   D.A. Atwood (2012) – *The Rare Earth Elements – Fundamentals and Applications*. John Wiley & Sons Ltd. pp 2–5.

[30]   P. Di Bernardo, A. Melchior, M. Tolazzi and P.L. Zanonato, "Thermodynamics of lanthanide(III) complexation in non-aqueous solvents", *Coord. Chem. Rev.,* **256** (2012) 328–351.

[31]   D. Xue, S. Zuo and H. Ratajczak, "Electronegativity and structural characteristics of lanthanides", *Physica B,* **352** (2004) 99–104.

[32]   Y. Yao, M. Ma, X. Xu, Y. Zhang, Q. Shen and W.-T. Wong, "Synthesis, reactivity, and characterization of amine bis(phenolate) lanthanide complexes and their application in the polymerization of ϵ-caprolactone", *Organometallics,* **24** (2005) 4014–4020.

[33]   H. Wada, S. Ooka, T. Yamamura and T. Kajiwara, "Light lanthanide complexes with crown ether and its aza derivative which show slow magnetic relaxation behaviors", *Inorg. Chem.,* **56** (2017) 147–155.

[34]   H.C. Aspinall, "Chiral lanthanide complexes: Coordination chemistry and applications", *Chem. Rev.,* **102** (2002) 1807–1850.

[35]   S. Cotton (2006) – *Lanthanide and Actinide Chemistry,* John Wiley & Sons: West Sussex, pp 2–56.

[36]   J. Cirera, E. Ruiz and S. Alvarez, "Continuous Shape Measures as a stereochemical tool in organometallic chemistry", *Organometallics,* **24** (2005) 1556–1562.

[37]   D. Casanova, J. Cirera, M. Llunell, P. Alemany, D. Avnir and S. Alvarez, "Minimal distortion pathways in polyhedral rearrangements", *J. Am. Chem. Soc.*, **126** (2004) 1755–1760.

[38]   T. Zhu, P. Chen, H. Li, W. Sun, T. Gao and P. Yan, "Structural effects on the photophysical properties of mono-β-diketonate and bis-β-diketonate Eu^{III} complexes", *Phys. Chem. Chem. Phys.*, **17** (2015) 16136–16144.

[39]   M. Llunell, D. Casanova, J. Cirera, P. Alemany and S. Alvarez, *SHAPE: Program for the Stereochemical Analysis of Molecular Fragments by Means of Continuous Shape Measures and Associated Tools, User's Manual Version 2.1*, 2013.

[40]   J. Goura, J.P.S. Walsh, F. Tuna and V. Chandrasekhar, "Tetranuclear lanthanide(III) complexes in a seesaw geometry: Synthesis, structure, and magnetism", *Inorg. Chem.,* **53** (2014) 3385–3391.

[41]   B. Yao, L. Zhu, Q. Jiang and H.A. Xia, "Safety monitoring in clinical trials", *Pharmaceutics*, **5** (2013) 94–106.

[42]   E.L. Andrade, A.F. Bento, J. Cavalli, S.K. Oliveira, R.C. Schwanke, J.M. Siqueira, C.S. Freitas, R. Marcon and J.B. Calixto, "Non-clinical studies in the process of new drug development – Part II: Good laboratory practice, metabolism, pharmacokinetics, safety and dose translation to clinical studies", *Braz. J. Med. Biol. Res.*, **49** (2016) 1–19.

[43]   H. Ersoy and F.J. Rybicki, "Biochemical safety profiles of gadolinium-based extracellular contrast agents and nephrogenic systemic fibrosis", *J. Magn. Reson. Imaging,* **26** (2007) 1190–1197.

[44]   K. Wang, R. Li, Yi Cheng and Bing Zhu, "Lanthanides – the future drugs?", *Coord. Chem. Rev.,* **190–192** (1999) 297–308.

[45]   S.P. Fricker, "The therapeutic application of lanthanides", *Chem. Soc. Rev.,* **35** (2006) 524–533.

[46]   K.S. Egorova and V.P. Ananikov, "Toxicity of metal compounds: Knowledge and myths", *Organometallics,* **36** (2017) 4071–4090.

[47]   M. Ceulemans, K. Nuyts, W.M. De Borggraeve and T.N. Parac-Vogt, "Gadolinium(III)-DOTA complex functionalized with BODIPY as a potential bimodal contrast agent for MRI and optical imaging", *Inorganics,* **3** (2015) 516–533.

[48]   Nibha, B.P. Baranwal, G. Singh and C.G. Daniliuc, "Synthesis, characterization and thermolysis of lanthanide metal nitrate complexes with 1,10-phenanthroline, Part-95", *J. Rare Earth.*, **32** (2014) 545–552.

[49]   Material Safety Data Sheet – ScienceLab: https://www.sciencelab.com/msds/ (accessed 24 October 2018, using the compound name)

[50]   C.A. Destefani, L.C. Motta, R.A. Costa, C.J. Macrino, J.F.P. Bassane, J.F.A. Filho, E.M. Silva, S.J. Greco, M-T.W.D. Carneiro, D.C. Endringer and W. Ramão, "Evaluation of acute toxicity of europium–organic complex applied as a luminescent marker for the visual identification of gunshot residue", *Microchem. J.,* **124** (2016) 195–200.

[51]   A. Cârâc, "Biological and biomedical applications of the lanthanides compounds: A mini review", *Proc. Rom. Acad.*, **19** (2017) 69–74.

[52]   A. Hussain and A.R. Chakravarty, "Photocytotoxic lanthanide complexes", *J. Chem. Sci*., **124** (2012) 1327–1342.

[53]   C.M. da Silva, D.L. da Silva, L.V. Modolo, R.B. Alves, M.A. de Resende, C.V.B. Martins and Â. de Fátima, "Schiff bases: A short review of their antimicrobial activities", *J. Adv. Res.*, **2** (2011) 1–8.

[54]   R.A. Abu Talip, M.G. Tay and H.F. Hashim, "Synthesis, characterization and antibacterial activities of hydrazone Schiff base compounds and its derivatives", *Malaysian Journal of Analytical Sciences,* **21** (2017) 1168–1175.

[55]   K.B. Gudasi, V.C. Havanur, S.A. Patil and B.R. Patil, "Antimicrobial study of newly synthesized lanthanide(III) complexes of 2-[2-hydroxy-3-methoxyphenyl]-3-[2-hydroxy-3-methoxybenzylamino]-1,2-dihydroquinazolin-4(3H)-one", *Metal-Based Drugs, Hindawi Publishing Corporation,* **2007** (2007) 1–7.

[56]   S. Zhang, W. Shi, L. Li, E. Duan and P. Cheng, "Lanthanide coordination polymers with "fsy-type" topology based on 4,4′-azobenzoic acid: Syntheses, crystal structures, and magnetic properties", *Inorg. Chem.,* **53** (2014) 10340–10346.

[57]   J.-C. G. Bünzli, "Rising stars in science and technology: Luminescent lanthanide materials", *Eur. J. Inorg. Chem.,* **44** (2017) 5058–5063.

[58]   S.H. Hewitt and S.J. Butler, "Application of lanthanide luminescence in probing enzyme activity", *Chem. Commun.,* **54** (2018) 6635–6647.

[59] A. Vogler and H. Kunkely, "Excited state properties of lanthanide complexes: Beyond *ff* states", *Inorg. Chim. Acta.,* **359** (2006) 4130–4138.

[60] X.-Z. Song, S.-Y. Song and H.-J. Zhang, "Luminescent lanthanide metal-organic frameworks", *Struct. Bond.,* **163** (2015) 109–144.

[61] J.-C. G. Bünzli and C. Piguet, "Taking advantage of luminescent lanthanide ions", *Chem. Soc. Rev.,* **34** (2005) 1048–1077.

[62] Y. Hasegawa, Y. Kitagawa and T. Nakanishi, "Effective photosensitized, electrosensitized, and mechanosensitized luminescence of lanthanide complexes", *NPG Asia Mater.,* **10** (2018) 52–55.

[63] D.V. Kolechko, F.A. Kolokolov, A.I. Oflidi, A.A. Pikula, V.T. Panyushkin, I.E. Mikhailov and G.A. Dushenko, "Novel luminescent lanthanides complexes with 1,10-phenanthroline-2,9-dicarboxylic acid", *Doklady Chemistry*, **441** (2011) 374–378.

[64] P. Kulkarni, S. Chellam and M.P. Fraser, "Tracking petroleum refinery emission events using lanthanum and lanthanides as elemental markers for $PM_{2.5}$", *Environ. Sci. Technol.,* **41** (2007) 6748–6754.

[65] I.V. Basalov, S.C. Rosca, D.M. Lyubov, A.N. Selikhov, G.K. Fukin, Y. Sarazin, J-F. Carpentier and A.A. Trifonov, "Divalent heteroleptic ytterbium complexes − Effective catalysts for intermolecular styrene hydrophosphination and hydroamination", *Inorg. Chem.*, **53** (2014) 1654–1661.

[66] A. Bencini, V. Lippolis, "1,10-Phenanthroline: A versatile building block for the construction of ligands for various purposes", *Coord. Chem. Rev.*, **254** (2010) 2096–2180.

[67] S. Seo and T.J. Marks, "Mild amidation of aldehydes with amines mediated by lanthanide catalysts", *Org. Lett.,* **10** (2008) 317–319.

[68] X. Pang, D. Li and A. Peng, "Application of rare-earth elements in the agriculture of China and its environmental behaviour in soil", *J. Soil. Sediment.*, **1** (2001) 124–129.

[69] K.B. Gudasi, R.V. Shenoy, R.S. Vadavi, M.S. Patil, S.A. Patil, R.R. Hanchinal, S.A. Desai and H. Lohithaswa, "Lanthanide(III) and yttrium(III) complexes of benzimidazole-2-acetic acid: Synthesis, characterisation and effect of La(III) complex on germination of wheat", *Bioinorg. Chem. and Applic.*, **2006** (2006) 1–8.

[70] H. Fashui, W. Ling and L. Chao, "Study of lanthanum on seed germination and growth of rice", *Biol. Trace Elem. Res.*, **94** (2003) 273–284.

[71] A.M. Khan, N.K. Abu Bakar, A.F. Abu Bakar, "Chemical speciation and bioavailability of rare earth elements (REEs) in the ecosystem", *Environ. Sci. Pollut. Res.*, **24** (2017) 22764–22789.

[72] G.N. Naik, R.P. Bakale, A.H. Pathan, S.G. Ligade, S.A. Desai and K.B. Gudasi, "2,4-Dichlorophenoxyacetic acid derived Schiff base and its lanthanide(III) complexes: Synthesis, characterization, spectroscopic studies, and plant growth activity", *J. Chem.*, **2013** (2013) 1–13.

[73] A.M. Abu-Dief and I.M.A. Mohamed, "A review on versatile applications of transition metal complexes incorporating Schiff bases", *BJBAS*, **4** (2015) 119–133.

[74] D.V. Saraf, P.A. Kulkarni, V.G. Deshpande and S.I. Habib, "Heterocyclic Schiff base Cu(II) metal complexes and their X-ray diffraction study", *Eur. J. Pharm. Med. Res.*, **4** (2017) 680.

[75] A. Kajal, S. Bala, S. Kamboj, N. Sharma and V. Saini, "Schiff bases: A versatile pharmacophore", *Journal of Catalysts*, **2013** (2013) 1–8.

[76] A. Hameed, M. al-Rashida, M. Uroos, S.A. Ali and K.M. Khan, "Schiff bases in medicinal chemistry: A patent review (2010–2015)", *Expert Opinion on Therapeutic Patents*, **27** (2017) 63–79.

[77] K. Andiappan, A. Sanmugam, E. Deivanayagam, K. Karuppasamy, H.-S. Kim and D. Vikraman, "*In vitro* cytotoxicity activity of novel Schiff base ligand–lanthanide complexes", *Sci. Rep.*, **8** (2018) 1–8.

[78] I. Rama and R. Selvameena, "Synthesis, structure analysis, anti-bacterial and *in vitro* anti-cancer activity of new Schiff base and its copper complex derived from sulfamethoxazole", *J. Chem. Sci.*, **127** (2015) 671–678.

[79] K. Brodowska and E. Łodyga-Chruścińska, "Schiff bases – interesting range of applications in various fields of science", *CHEMIK*, **68** (2014) 129–134.

[80] W.M. Al Momani, Z.A. Taha, A.M. Ajlouni, Q.M. Abu Shaqra and M. Al Zouby, "A study of *in vitro* antibacterial activity of lanthanides complexes with a tetradentate Schiff base ligand", *Asian Pac J. Trop. Biomed.*, **3** (2013) 367–370.

[81] K.S. Kumar, S. Ganguly, R. Veerasamy and E. De Clercq, "Synthesis, antiviral activity and cytotoxicity evaluation of Schiff bases of some 2-phenyl quinazoline-4(3)H-ones", *Eur. J. Med. Chem.*, **45** (2010) 5474–5479.

[82] N.P. Belskaya, W. Dehaen and V.A. Bakulev, "Synthesis and properties of hydrazones bearing amide, thioamide and amidine functions", *Special Issue Reviews and Accounts, ARKIVOC*, **2010** (2010) 275–332.

[83]   H.H. Monfared, O. Pouralimardan and C. Janiak, "Synthesis and spectral characterization of hydrazone Schiff bases derived from 2,4-dinitrophenylhydrazine. Crystal structure of salicylaldehyde-2,4-dinitrophenylhydrazone", *Z. Naturforsch.,* **62b** (2007) 717–720.

[84]   M.C. Foti, "Use and abuse of the DPPH• radical", *J. Agric. Food Chem.,* **63** (2015) 8765–8776.

[85]   S. Sarkar, A.A. Siddiqui, S.J. Saha, R. De, S. Mazumder, C. Banerjee, M.S. Iqbal, S. Nag, S. Adhikari and U. Bandyopadhyay, "Antimalarial activity of small-molecule benzothiazole hydrazones", *Antimicrob. Agents Chemother., American Society for Microbiology,* **60** (2016) 4217–4228.

[86]   B. Atchade, S.D.S. Kpoviessi, R.H. Fatondji, L.A. Ahoussi, J. Gbenou, G.C. Accrombessi, J.H. Poupaert and M. Moudachirou, "Synthesis, purity verification and comparison of antiplasmodial and antitrypanosomal activities of hydrazone derivatives and corresponding thiosemicarbazones", *J. Pharm. Chem. Biol. Sci.,* **3** (2015) 279–294.

[87]   Â. de Fátima, C. de Paula Pereira, C.R.S. Dau Gonçalves Olímpio, B.G. de Freitas Oliveira, L.L. Franco, P.H.C. da Silva, "Schiff bases and their metal complexes as urease inhibitors – A brief review", *J. Adv. Res.,* **13** (2018) 113–126.

[88]   X.-X. Qi, N. Ren, S.-L. Xu, J.-J. Zhang, G.-C. Zong, J. Gao, L.-N. Geng, S.-P. Wang and S.-K. Shi, "Lanthanide complexes with 3,4,5-triethoxybenzoic acid and 1,10-phenanthroline: synthesis, crystal structures, thermal decomposition mechanism and phase transformation kinetics", *RSC Adv.,* **5** (2015) 9261–9271.

[89]   M. Hu, L-Y. Yue, E.C. Sañudo, and S-M. Fang, "Three lanthanide complexes with mixed salicylate and 1,10-phenanthroline: syntheses, crystal structures, and luminescent/magnetic properties", *J. Coord. Chem.,* **69** (2016) 2164–2173.

[90]   C.A. Chang, B.H. Wu and B.Y. Kuan, "Macrocyclic lanthanide complexes as artificial nucleases and ribonucleases: Effects of pH, metal ionic radii, number of coordinated water molecules, charge, and concentrations of the metal complexes", *Inorg. Chem.,* **44** (2005) 6646–6654.

[91]   D. Tolan, V. Gandin, L. Morrison, A. El-Nahas, C. Marzano, D. Montagner and A. Erxleben, "Oxidative stress induced by Pt(IV) pro-drugs based on the cisplatin scaffold and indole carboxylic acids in axial position", *Sci. Rep.,* **6** (2016) 1–9.

[92]   F. Fares, N. Azzam, B. Fares, S. Larsen and S. Lindkaer-Jensen, "Benzene-poly-carboxylic acid complex, a novel anti-cancer agent induces apoptosis in human breast cancer cells", *PLoS ONE,* **9** (2014) 1–8.

[93]   A.Y. Mitrofanov, Y. Rousselin, R. Guilard, S. Brandés, A.G. Bessmertnykh-Lemeune, M.A. Uvarova and S.E. Nefedov, "Copper(II) complexes with phosphorylated 1,10-phenanthrolines: from molecules to infinite supramolecular arrays", *New J. Chem.*, **40** (2016) 5896–5905.

[94]   C.M. Al Matarneh, I.I. Mangalagiu, S. Shova and R. Danac, "Synthesis, structure, antimycobacterial and anticancer evaluation of new pyrrolo-phenanthroline derivatives", *J. Enzyme Inhib. Med. Chem.*, **31** (2016) 470–480.

[95]   K. De, J. Legros, B. Crousse, S. Chandrasekaran and D. Bonnet-Delpon, "Synthesis of substituted 8-aminoquinolines and phenanthrolines through a Povarov approach", *Org. Biomol. Chem.*, **9** (2011) 347–350.

[96]   P. Heffeter, M.A. Jakupec, W. Korner, S. Wild, N.G.V. Keyserlingk, L. Elbling, H. Zorbas, A. Korynevska, S. Knasmuller, H. Sutterluty, M. Micksche, B.K. Keppler and W. Berger, "Anticancer activity of the lanthanum compound [tris(1,10-phenanthroline)lanthanum(III)]trithiocyanate (KP772; FFC24)", *Bio. Chem. Pharm.*, **71** (2006) 426–440.

[97]   K. Kumar, P. Meera, M. Amutha Selvi and A. Dayalan, "Tris-(1,10-phenanthroline) cobalt(III) bromide chloride hexahydrate: Synthesis, characterization, antimicrobial screening and xrd studies", *Int. J. Chem. Sci.*, **9** (2011) 1421–1428.

[98]   F.W. Lewis, L.M. Harwood, M.J. Hudson, M.G.B. Drew, J.F. Desreux, G. Vidick, N. Bouslimani, G. Modolo, A. Wilden, M. Sypula, T.-H. Vu and J.-P. Simonin, "Highly efficient separation of actinides from lanthanides by a phenanthroline-derived bis-triazine ligand", *J. Am. Chem. Soc.*, **133** (2011) 13093–13102.

[99]   M. Correa-Ascencio, E.K. Galván-Miranda, F. Rascón-Cruz, O. Jiménez-Sandoval, S.J. Jiménez-Sandoval, R. Cea-Olivares, V. Jancik, R. Alfredo Toscano and V. García-Montalvo, "Lanthanide(III) complexes with 4,5-bis(diphenylphosphinoyl)-1,2,3-triazolate and the use of 1,10-phenanthroline as auxiliary ligand", *Inorg. Chem.*, **49** (2010) 4109–4116.

[100]   C. Xu, "Photophysical properties of lanthanide complexes with 5-nitro-1,10-phenanthroline", *Monatsh. Chem.*, **141** (2010) 631–635.

[101]   G.-C. Zong, J.-X. Huo, N. Ren, J.-J. Zhang, X.-X. Qi, J. Gao, L.-N. Geng, S.-P. Wang and S.-K. Shi, "Preparation, characterization and properties of four new trivalent lanthanide complexes constructed using 2-bromine-5-methoxybenzoic acid and 1,10-phenanthroline", *Dalton Trans.*, **44** (2015) 14877–14885.

CHAPTER 2

Materials and Methods

2.1   Materials

2.1.1   Chemicals

Distilled water was used for experiments done in aqueous solutions. The solvents, dimethyl sulfoxide ($\geq$99.0 %), ethanol (99.5 %), methanol (99.0 %) and tetrahydrofuran ($\geq$99.5 %) were purchased from Merck; diethyl ether (99.8 %) from Sigma-Aldrich; and dimethylformamide (99.5 %) from Ibhayi Lab Supplies. Analytical grade solvents were dried over 3 Å molecular sieves before use. The bases, sodium hydroxide (NaOH, $\geq$98.0 %) and triethyl amine ($\geq$99.0 %), were purchased from Merck, as was the deuterated DMSO used for ^{1}H and ^{13}C NMR spectroscopy.

The lanthanide acetates [Ln(OAc$_3$)$_3$·xH$_2$O] (Ln = La, Ce, Nd, Er and Yb; x = 4 for Yb) with 99.9 % purity were sourced from Sigma-Aldrich, and used without further purification. The nitrates of Ce(III), Pr(III), Nd(III), Sm(III), Gd(III) and Er(III) (99.9 %) were obtained from Sigma-Aldrich. [SmCl$_3$·6H$_2$O] was also purchased from Sigma-Aldrich and used as received.

The organic compounds benzhydrazide (98.0 %), nicotinohydrazide (97.0 %), salicylaldehyde (98.0 %), 2,6-dimethylphenylaniline (99.0 %), ethyl chlorooxoacetate (98.0 %), 1,10-phenanthroline ($\geq$99.0 %) and benzilic acid ($\geq$99.0 %) were all purchased from Sigma-Aldrich and used as supplied.

2.1.2   Laboratory consumables for anticancer tests

Dulbecco's Minimal Essential Medium (DMEM) growth medium, Roswell Park Memorial Institute (RPMI) 1640 medium and Dulbecco's Phosphate Buffered Saline (DPBS) were obtained from Hyclone Ltd. (USA). Trypsin and Trypan Blue Staining

Solution, and the heat-inactivated foetal bovine serum (HI-FBS) were sourced from Gibco (USA). Thiazolyl Blue Tetrazolium Blue (MTT) was obtained from Melford (UK). The 25 cm^2 and 75 cm^2 culture flasks, and 96-well tissue culture plates were purchased from Nest Biotechnologies (China). Dimethyl sulfoxide was obtained from Sigma-Aldrich (Germany).

2.1.3   Cell lines

The breast cancer (MCF-7) and endometrial carcinoma (HEC-1A) cell lines were purchased from the National Institute of Biomedical Innovation (Osaka, Japan). The leukemic monocytic (THP-1) cell line was kindly donated by M. Fortuin-Seedat (Nelson Mandela University, South Africa).

2.2   Procedures for *in vitro* anticancer analyses

2.2.1   Cell culture and maintenance

The MCF-7 and HEC-1A cancer cells were regularly maintained as monolayer cell cultures in 25 or 75 cm^2 cell culture flasks, in a growth medium consisting of DMEM supplemented with 10 % HI-FBS. The THP-1 cells were routinely maintained in RPMI-1640 medium supplemented with 10 % FBS, and the cells were fed by replacing the growth medium every four to five days. The cell lines were maintained in the range 1×10^5 – 1×10^7 cells/mL, with growth in a humidified atmosphere with 5 % CO_2 and 95 % air, at 37 °C. The MCF-7 cells were sub-cultured using a 1:10 split ratio, while the HEC-1A and THP-1 cell lines were sub-cultured using a 1:5 split ratio.

2.2.2   Preparation of compounds and controls

Stock solutions of the test agents (100 mM) were prepared in DMSO (100 %), which, on dilution, resulted in a final well concentration of less than 0.1 % DMSO, which did not adversely affect cell growth. The 0.1 % DMSO was used as a vehicle control.

Dilutions were performed on the day of the experiment, from stock solutions with complete growth medium to get a final well concentration of 100 μM. The compounds were tested at this concentration on each cell line.

Curcumin (diferuloylmethane, Figure 2.1), a biologically active component of the Indian *Curcuma longa* plant (turmeric), was used as a positive control [1,2]. The compound is a plant phenol, with notable pharmacological safety. It has a wide range of biological activities, such as anticancer, antibacterial, antidiabetic, antioxidant, antifungal and antiseptic activity [1-4]. The anticancer properties of the compound against multiple human carcinomas, including breast, ovarian, prostate, colon, pancreatic, and head and neck cancers, are ascribed to its ability to target multiple pathways that effect cellular death [1-4]. The mechanisms of action of the compound include its effect in biological pathways or on various growth factor receptors associated with cell cycle regulation, apoptosis, mutagenesis, metastasis, oncogene expression, angiogenesis and tumorigenesis [1,2]. For example, curcumin inhibits the production of nitric oxide and can scavenge DNA-damaging superoxide radicals [4]. In addition to its superoxide radical scavenging ability, curcumin inhibits Phase I enzymes (such as cytochrome p450 isoforms and p450 reductase) that generate a host of carcinogenic metabolites [1]. On the other hand, the compound induces Phase II enzymes (including glutathione *S*-transferase and glutathione reductase), which play a key role in detoxification of toxic metabolites [1].
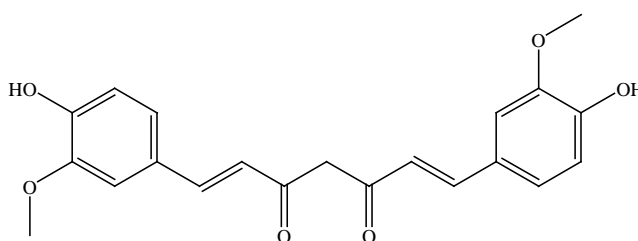
Figure 2.1: The chemical structure of curcumin (keto form) [1].

2.2.3   Cell counting using Trypan Blue

The trypan blue exclusion assay is a vital tool in determining cell viability [5,6]. This dye exclusion test is based on the principle that plasma membrane integrity is lost in

non-viable cells, allowing the dead cells to incorporate trypan blue, whilst intact plasma membranes of viable cells exclude the stain. Non-viable cells appear dark blue, while viable cells appear colourless under light microscopy [5,6].

Cell counting was done using a Neubauer counting chamber (Superior). Cells were diluted with Trypan blue stain (4 %) in the ratio 1:1. The total number of cells was calculated using the equation:

$$\text{Cells/mL} = \text{average cell count per square} \times \text{dilution factor} \times 10^4$$

2.2.4   Cell viability determination using the MTT assay

The 3-(4,5-dimethylthiazol-2-yl)-2,5-diphenyltetrazolium bromide (MTT) assay is one of the frequently used colorimetric methods for assessing cell cytotoxicity, proliferation or viability, based on cellular metabolic activity of NAD(P)H-dependent oxidoreductase enzymes [7-9]. This colorimetric assay depends on the reduction of the pale yellow tetrazolium salt (MTT) to purple formazan crystals in metabolically active cells [7,8]. The MTT salt enters the mitochondria of viable cells, where mitochondrial succinate dehydrogenase cleaves the tetrazolium rings of MTT, thus converting it to purple formazan crystals. The formazan crystals are easily dissolved in an organic solvent, such as DMSO or isopropanol, which can then be quantified spectrophotometrically at 540 nm [8-10]. The intense purple colour signifies higher cell viability, whereas a decrease in colour denotes a reduction in cell number due to cytotoxicity of a certain agent. Since reduction of MTT only occurs in metabolically active cells, the method is used to quantify the number of viable cells *versus* non-viable cells. For this research, the effect of the free ligands, metal salts, lanthanide complexes and controls on cell viability was determined using the MTT assay [8,10].

After reaching 80 % confluence, the cells were harvested and seeded at a density of 10000 cells/well in complete growth medium in 96-well tissue culture plates. Following an overnight incubation at 37 °C, treatment of the cells with the test compounds or the relevant controls was performed, at a final well concentration of

100 μM. One row of cells was left untreated, whilst another row received 0.1 % DMSO vehicle alone. The cells were incubated at 37 °C for 24 hours, followed by removal of the conditioned media from adherent (MCF-7 and HEC-1A) cells, after which MTT (0.5 mg/mL, 100 µL) was added to each well. For the suspension (THP-1) cell line, MTT (2.5 mg/mL) was added to the cells at 20 % v/v. The plates were then incubated for 3 hours at 37 °C, and the purple formazan crystals formed were solubilised in 100 µL DMSO (100 %). Absorbance was read at 540 nm using a ThermoMultiSkan Go microplate reader (Thermo Scientific, U.S.A.) against a DMSO blank. To correct for background interference in THP-1 cell suspensions, sample background controls were set up using equal volumes of MTT reagent and cell culture media.

The number of viable cells was extrapolated from a MTT standard curve (Figures S2.1a-c in Supplementary information) and the percentage cell viability was calculated as a percentage of the 0.1 % DMSO vehicle control. Each experiment was done in triplicate.

2.2.5   Statistical analysis

All data are reported as mean ± S.D. for triplicate experiments (n = 3). Non-parametric grouping of data was analysed by ANOVA and secondary data analysis for significance with Student's t-test. Values of $p < 0.05$ were considered significant.

2.3   Instrumentation

The melting points of organic compounds and coordination compounds were determined out using a Stuart® Melting Point Apparatus SMP30 [Benzoic acid (m.p. = 122.4 ^{o}C) used as a melting point standard]. Determination of temperatures were done on solid samples held within capillary tubes.

The elemental analysis for carbon, hydrogen and nitrogen was performed using an Elementar Vario EL Cube Elemental Analyzer.

HANNA instruments (HI) 2300 EC/TDS/NaCl Meter was used to perform conductivity measurements at 25 ^{o}C.

The UV-Vis spectroscopy of the free ligands and metal complexes was carried out on a PerkinElmer Lambda 35 UV/Vis spectrophotometer (path length = 1 cm), and processing done using *UV WinLab* software (v1.0.0).

Nuclear Magnetic Resonance (NMR) spectra were obtained at room temperature using a Bruker AvanceIII 400 NMR Spectrometer and *TopSpin 3.0* software was used in the acquisition of data. Analysis of spectra was performed using *ACD/Labs* software (version 12.0, 1997–2008).

The infrared spectra were obtained from a Bruker Tensor 27 FT-IR spectrophotometer, equipped with the Platinum attenuated total reflection (ATR) attachment. The samples were run neat on ATR and the recorded data was analysed using the *OPUS 6.5* software.

A Bruker Kappa Apex II X-ray Crystallography System was used for single-crystal diffractometry at 200 K, using graphite monochromated Mo Kα radiation (λ = 0.71073 Å). APEX2 (ver. 2014.11-0) was used for data collection and SAINT software (ver. 8.34A) for data reduction and cell refinement [11]. The structures were solved by direct methods using SHELXT-2018/2 and refined by least-squares procedures using SHELXL-2018/3 with ShelXle as a graphical interface [12-14]. Data were corrected for absorption effects using the numerical method implemented in SADABS (ver. 2014/5) [11]. All non-hydrogen atoms were refined anisotropically. Carbon-bound H atoms were placed in calculated positions and were included in the refinement in the riding model approximation, with Uiso(H) set to 1.2Ueq(C). The methyl group H atoms were allowed to rotate with a fixed angle around the C—C bond to best fit the experimental electron density (HFIX 137 in the SHELX program

suite), with Uiso(H) set to 1.5Ueq(C) [13]. The H atoms of the hydroxyl groups were allowed to rotate with a fixed angle around the C—O bond to best fit the experimental electron density (HFIX 147 in the SHELX program suite), with Uiso(H) set to 1.5Ueq(O) [13]. The nitrogen-bound H atoms were located on a difference Fourier map and refined freely. Molecular graphics were obtained using *ORTEPIII* for Windows v2014.1 and *Mercury 3.6* softwares [15,16].

Lanthanide geometry analyses were enabled by the *SHAPE 2.1* software. This program is based on the algorithm defined by Pinsky and Avnir (1998) for the calculation of continuous shape measures (CShM values) [17]. The polyhedral representations were created using *VESTA* software (version 3, 2006–2014) [18].

2.4   Molecular modelling

2.4.1   Geometry optimisation

In order to obtain information about the structure in solution (DMSO) and the gaseous phase of the neutral and monoanionic ligands, Density Functional Theory (DFT) calculations were performed using the *Gaussian 16* program package (Rev. B01), based on the Becke3-Lee-Yang-Parr (B3LYP) model and aug-cc-pVTZ basis set [19,20]. The molecular geometry (atomic coordinates) of the ligands was taken directly from the X-ray crystallography experimental results. Hydrogen positions were determined using the Riding Model [13].

The gas phase (in vacuo) was used for calculation of chemical properties of molecules. To compute molecular properties in solution, the implicit solvation model was also used in the calculation. Solvent effects were determined through single-point energy calculations utilising the self-consistent reaction field (SCRF) theory with the conductor-like polarisable continuum model (CPCM). The SCRF-CPCM calculations were carried out in DMSO at 298.15 K with the solvent dielectric constant of 46.826. Determination of single-point energies involved integration of orbitals or wavefunction using an "UltraFine Grid".

The optimisation algorithm included in *Gaussian* is the Berny algorithm – this constructed an approximate Hessian, utilising "very tight" convergence criteria for improved results. This algorithm used a maximum force of 9×10^{-6} and maximum displacement of 36×10^{-6}, while the root mean square (RMS) force and RMS displacement were 6×10^{-6} and 24×10^{-6}, respectively. The completion of each geometry optimisation was confirmed by the absence of imaginary frequency through frequency or vibrational analysis, as well as through inspection of the force- and displacement values relative to the Berny optimisation criteria.

Single-point energy calculations were performed after optimisation, upon which natural bond orbital (NBO) analysis was performed using *NBO 6.0* program [NBO 6.0.19 (05-Aug-2018)] [21-23]. The atomic charges were determined using Natural Population Analysis (NPA) of the ligands in solution and gaseous phase [24]. For better representation, the results were illustrated in graph form.

2.4.2   Molecular electrostatic potential surface

Electron density distribution, molecular shape and size in three dimensional representation was illustrated using molecular electrostatic potential (MEP) surface, generated using *MoleCoolQt64* software (2003–2012) [25]. The MEP is related to the electron density and is an important tool in the elucidation of nucleophilic or electrophilic sites, as well as understanding hydrogen bond interactions [26]. The colour-mapped isosurfaces were created using an isovalue of 0.05 atomic units (a.u.), interpolated from $200 \times 200 \times 200$ points per Gaussian cube; that is, for total SCF density and electrostatic potential. The surface and molecule are drawn using perspective projection, at a view angle of 27°. The contour belts are projected as black or grey curves onto the electron density isosurface. The electrostatic potential values (a.u.) associated with each set of contour belts are indicated by the black lines on the electrostatic potential (ESP) colour scale bar (the 'Rainbow' colour pallet was used). The electrostatic potential increases in the order red<orange<yellow<green<blue/violet, with blue/violet representing regions that are electron-poor or electrophilic (positive ESP sites), whereas red regions represent

negative ESP sites that are electron-rich or nucleophilic [19,26]. The electrostatic potential, $V(\vec{r})$ at a point $\vec{r}$ around a molecule is expressed as [27]:

$$V(\vec{r}) = \sum_A \frac{Z_A}{|\vec{R_A} - \vec{r}|} - \int \frac{\rho(\vec{r}')d\vec{r}'}{|\vec{r}' - \vec{r}|}$$

Where Z_A is the charge on nucleus A, located at R_A, and $\rho(r)$ is the electronic density function of the molecule acquired from its computed wave function [27].

2.4.3   Frontier molecular orbital analysis, and global and chemical reactivity descriptors

The highest occupied and lowest unoccupied molecular orbitals were visualised using *Avogadro* software (version 2, 1991). The highest occupied molecular orbital (*HOMO*) depicts the ability to donate an electron, whereas the lowest unoccupied molecular orbital (*LUMO*) acts as electron acceptors [26,28]. The *HOMO-LUMO* energy gaps (*ΔE*) of the ligands are dependent on the *HOMO* and *LUMO* energies (E_{HOMO} and E_{LUMO}) of the molecule and were determined with the formulae [19,26]:

First energy gap: $\Delta E = E_{LUMO} - E_{HOMO}$
Second energy gap: $\Delta E = E_{LUMO+1} - E_{HOMO-1}$
Third energy gap: $\Delta E = E_{LUMO+2} - E_{HOMO-2}$

The ionisation energies (*I*) and the electron affinities (*A*) of the organic compounds are related to the *HOMO* and *LUMO* energies, and are calculated based on the Koopman's theorem [26]. Electron affinity is the ability of a ligand to acquire one electron from a donor. As proposed by Robert Mulliken, an atom (which is part of a compound) with high electron affinity and high ionisation energy has a high tendency to accept an electron than to lose an electron [26,29]. It is thus highly electronegative. On the contrary, low electron affinity and ionisation energy means that the atom is

likely to lose an electron than accept electrons, making the atom electropositive. The equations for ionisation energy and electron affinity are as follows [26]:

$$I = -E_{HOMO}$$
$$A = -E_{LUMO}$$

Electronic structure descriptors or identifiers; hardness (η), softness (σ), electronegativity (χ_m), chemical potential (μ) and electrophilicity index (ω) for the ligands were derived from ionisation energy and electron affinity [26]. These identifiers control chemical activity and are important in drug design [26]. The global and chemical descriptors are defined by the following relationships [26,28]:

$$\eta = \frac{(I-A)}{2}$$

$$\mu = \frac{-(I+A)}{2}$$

$$\sigma = \frac{1}{\eta}$$

$$\omega = \frac{\mu^2}{2\eta}$$

$$\chi_m = \frac{I+A}{2}$$

The chemical potential gives the dipole moment or the average molecular polarisability [29]. Polar molecules are known for having a non-zero dipole moment, while apolar ones are identified by a zero dipole moment. The chemical potential is an important reactivity index which allows elucidation of biological properties associated with the interaction with the active sites of the molecule. The hardness measures the resistance of a molecule to the charge transfer [28]. The harder the molecule, the less reactive it is (the inverse being softness) [28]. Electronegativity is a measure of how strong a chemical species attracts electrons, while the electrophilicity index indicates the stabilisation energy of a molecule saturated by electronic charge from its surrounding environment [26].

2.5   Supplementary information
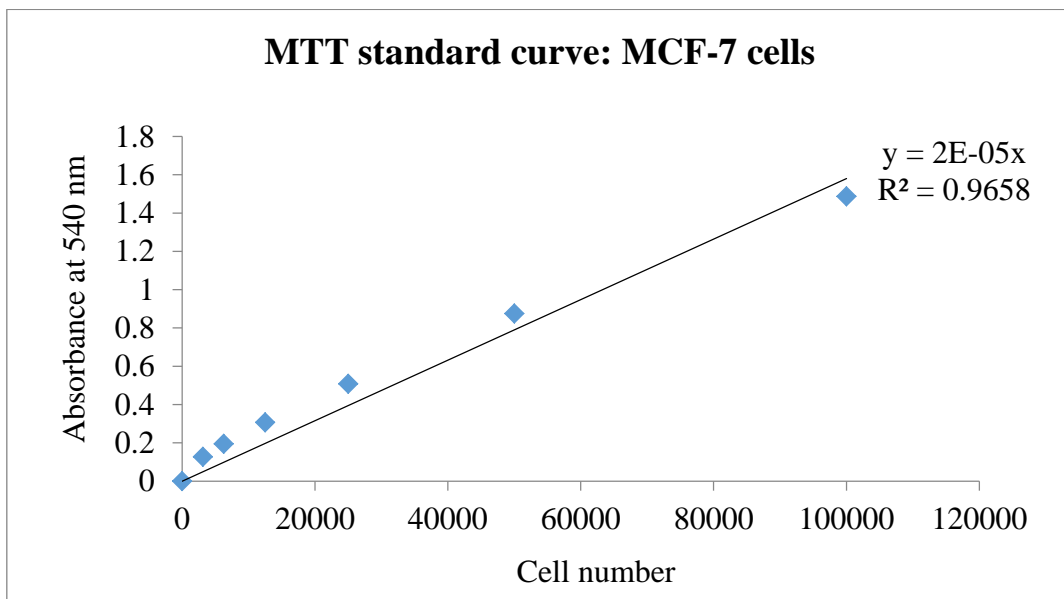
Figure S2.1a: The standard curve used in the quantification of MCF-7 cell number *via* the MTT assay. The equation obtained from a linear regression curve is indicated on the graph, as well as the correlation coefficient.
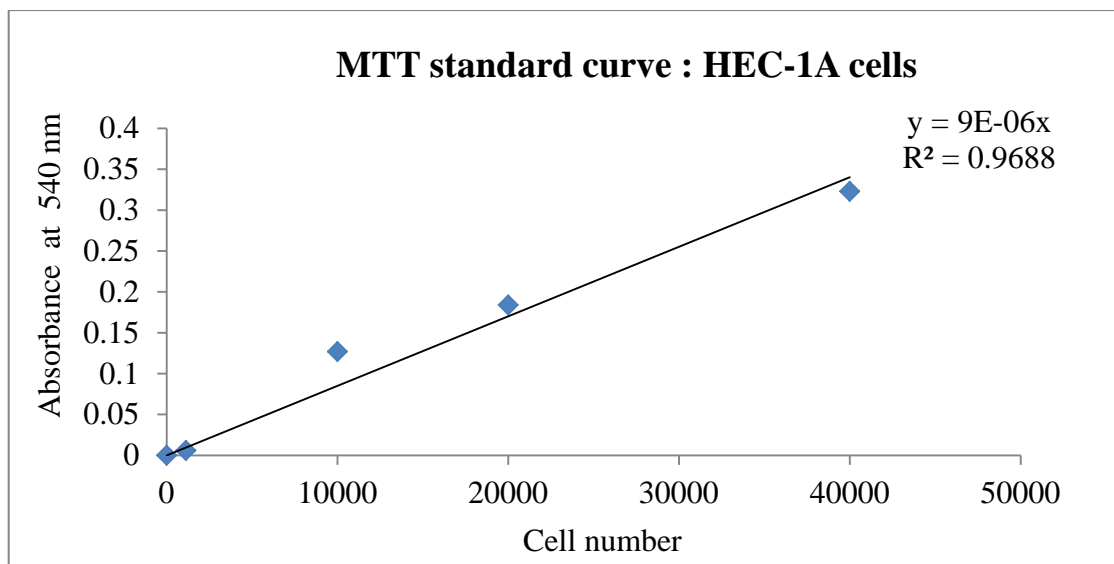
Figure S2.1b: The HEC-1A cell number standard curve ($R^2 = 0.9688$).
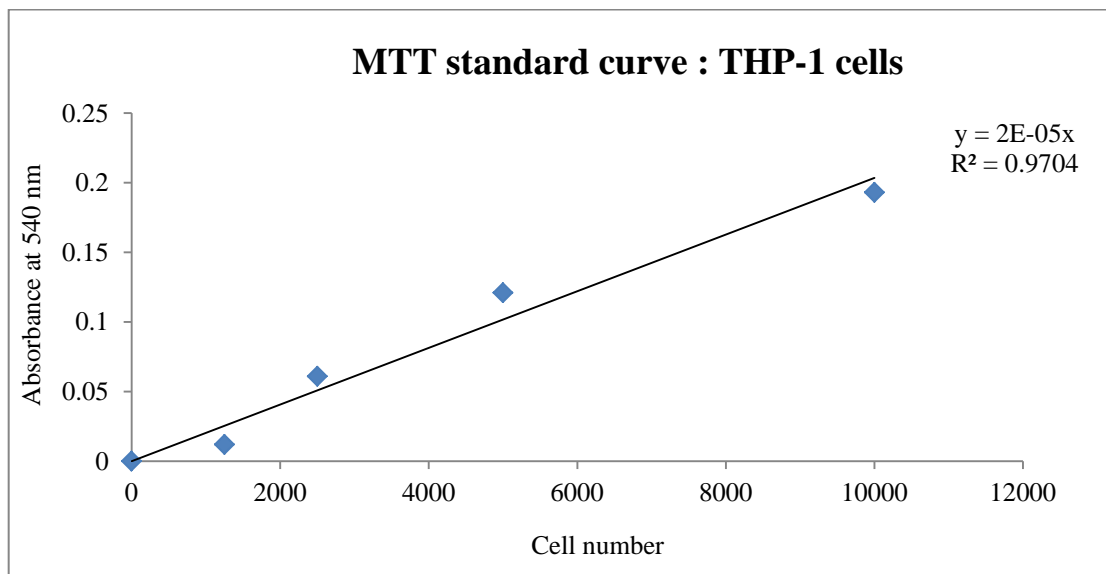
Figure S2.1c: The standard curve used to quantify THP-1 cell number using the MTT assay ($R^2 = 0.9704$).

2.6   References

[1]   R. Wilken, M.S. Veena, M.B. Wang and E.S. Srivatsan, "Curcumin: A review of anti-cancer properties and therapeutic activity in head and neck squamous cell carcinoma", *Molecular Cancer*, **10** (2011) 2–19.

[2]   J. Ravindran, S. Prasad and B.B. Aggarwal, "Curcumin and cancer cells: How many ways can curry kill tumor cells selectively?", *The AAPS Journal*, **11** (2009) 495–510.

[3]   S. Vellampatti, G. Chandrasekaran, S.B. Mitta, V.-K. Lakshmanan and S.H. Park, "Metallo-curcumin-conjugated DNA complexes induces preferential prostate cancer cells cytotoxicity and pause growth of bacterial cells", *Scientific Reports*, **8:14929** (2018) 1–11.

[4]   U. Banik, S. Parasuraman, A.K. Adhikary and N.H. Othman, "Curcumin: the spicy modulator of breast carcinogenesis", *Journal of Experimental & Clinical Cancer Research*, **36** (2017) 1–16.

[5]   B.A. Avelar-Freitas, V.G. Almeida , M.C.X. Pinto , F.A.G. Mourão, A.R. Massensini, O.A. Martins-Filho, E. Rocha-Vieira and G.E.A. Brito-Melo, "Trypan blue exclusion assay by flow cytometry", *Braz. J. Med. Biol. Res.*, **47** (2014) 307–315.

[6]   C.W. Wright, S.I. Melwani, J.D. Phillipson and D.C. Warhurst, "Determination of anti-giardial activity *in vitro* by means of soluble formazan production", *Trans. R. Soc. Trop. Med. Hyg.*, **86** (1992) 517–519.

[7]   M.V. Berridge and A.S. Tan, "Characterization of the cellular reduction of 3-(4,5-dimethylthiazol-2yl)-2,5-diphenyltetrazolium bromide (MTT): subcellular localization, substrate dependence, and involvement of mitochondrial electron transport in MTT reduction", *Arch. Biochem. Biophys.*, **303** (1993) 474–482.

[8]   A. Bahuguna, I. Khan, V.K. Bajpai and S.-C. Kang, "MTT assay to evaluate the cytotoxic potential of a drug", *Bangladesh J Pharmacol.*, **12** (2017) 115–118.

[9]   Z.-Q. Xu, X.-J. Mao, L. Jia, J. Xu, T.-F. Zhu, H.-X. Cai, H.-Y. Bie, R.-H. Chen and T.-L. Ma, "Synthesis, characterization and anticancer activities of two lanthanide(III) complexes with a nicotinohydrazone ligand", *J. Mol. Struct.*, **1102** (2015) 86–90.

[10]   T. Mosmann, "Rapid colorimetric assay for cellular growth and survival: application to proliferation and cytotoxicity assays", *J. Immunol. Methods*, **65** (1983) 55–63.

[11]   Bruker. APEX2, SAINT and SADABS. Bruker AXS Inc., Madison, WI, USA (2004).

[12]   G.M. Sheldrick, "SHELXT – Integrated space-group and crystal structure determination", *Acta Cryst.*, **A71** (2015) 3–8.

[13]   G.M. Sheldrick, "Crystal structure refinement with SHELXL", *Acta Cryst.*, **C71** (2015) 3–8.

[14]   C.B. Hübschle, G.M. Sheldrick and B. Dittrich, "ShelXle: a Qt graphical user interface for SHELXL", *J. Appl. Cryst.*, **44** (2011) 1281–1284.

[15]   L.J. Farrugia, "*WinGX* and *ORTEP for Windows*: an update", *J. Appl. Crystallogr.*, **45** (2012) 849–854.

[16]   C.F. Macrae, I.J. Bruno, J.A. Chisholm, P.R. Edgington, P. McCabe, E. Pidcock, L. Rodriguez-Monge, R. Taylor, J. van de Streek and P.A. Wood, "*Mercury CSD 2.0* – new features for the visualization and investigation of crystal structures", *J. Appl. Crystallogr.*, **41** (2008) 466–470.

[17]   M. Pinsky and D. Avnir, "Continuous Symmetry Measures. 5.   The Classical Polyhedra", *Inorg. Chem.*, **37** (1998) 5575–5582.

[18]   K. Momma and F. Izumi, "VESTA 3 for three-dimensional visualization of crystal, volumetric and morphology data", *J. Appl. Crystallogr.*, **44** (2011) 1272–1276.

[19]   M.S. Alam and D.-U. Lee, "Syntheses, crystal structure, Hirshfeld surfaces, fluorescence properties, and DFT analysis of benzoic acid hydrazone Schiff bases", *Spectrochim. Acta Part A: Molecular and Biomolecular Spectroscopy*, **145** (2015) 563–574.

[20]   R.A. Kendall, T.H. Dunning and R.J. Harrison, "Electron affinities of the first-row atoms revisited. Systematic basis sets and wave functions", *J. Chem. Phys.*, **96** (1992) 6796–6806.

[21]   E.D. Glendening, J.K. Badenhoop, A.E. Reed, J.E. Carpenter, J.A. Bohmann, C.M. Morales, C.R. Landis and F. Weinhold, Theoretical Chemistry Institute, University of Wisconsin, Madison, WI, (2013); http://nbo6.chem.wisc.edu/

[22]   E.D. Glendening, C.R. Landis and F. Weinhold, "NBO 6.0: Natural Bond Orbital Analysis Program", *J. Comput. Chem.*, **34** (2013) 1429–1437.

[23]   N.K. Nobel, K. Bamba, O.W. Patrice and N. Ziao, "NBO population analysis and electronic calculation of four azopyridine ruthenium complexes by DFT method", *Computational Chemistry*, **5** (2017) 51–64.

[24]   C. Theivarasu and R. Murugesan, "Natural Bond Orbital (NBO) population analysis of an energetic molecule 1-phenyl-2-nitroguanidine", *Int. J. Chem. Sci.*, **14** (2016) 2029–2050.

[25]   C.B. Hübschle and B. Dittrich, "MoleCoolQt - a molecule viewer for charge-density research", *J. Appl. Cryst.*, **44** (2011) 238–240.

[26]   A. Kanaani, D. Ajloo, H. Kiyani, H. Ghasemian, M. Vakili and M. Feizabadi, "Molecular structure, spectroscopic investigations and computational study on the potential molecular switch of (*E*)-1-(4-(2-hydroxybenzylideneamino)phenyl)ethanone", *Mol. Phys.*, **114** (2016) 2081–2097.

[27]   A. Zülfikaroğlu, H. Batı and N. Dege, "A theoretical and experimental study on isonitrosoacetophenone nicotinoyl hydrazone: Crystal structure, spectroscopic properties, NBO, NPA and NLMO analyses and the investigation of interaction with some transition metals", *J. Mol. Struct.*, **1162** (2018) 125–139.

[28]   N.A.Wazzan, I.B. Obot and S. Kaya, "Theoretical modeling and molecular level insights into the corrosion inhibition activity of 2-amino-1,3,4-thiadiazole and its 5-alkyl derivatives", *J. Mol. Liq.*, **221** (2016) 579–602.

[29]   S.E. Kariper, K. Sayin and D. Karakas, "Theoretical study on the antitumor properties of Ru(II) complexes containing 2-pyridyl, 2-pyridine-4-carboxylic acid ligands", *J. Mol. Struct.*, **1149** (2017) 473–486.

CHAPTER 3

Lanthanide(III) acetate complexes with benzohydrazone and nicotinohydrazone ligands

3.1   Introduction

Some tumour cells develop multidrug resistance (MDR) to other classes of anticancer drugs, such as Vinca alkaloids, anthracyclins and epipodophyllotoxins [1]. This poses a huge clinical challenge in successfully treating cancer. Multidrug resistant cell lines undergo cytogenetic and biochemical changes that include alteration in expression of protein kinase C, reduction in expression levels of mono-oxygenases, and overexpression of glutathione-related enzymes and *p*-glycoprotein. Multidrug resistant-positive breast cancer (MCF-7) cells exhibit enhanced expression levels of the protein cross-linking enzyme, tissue transglutaminase (tTGase) [1]. Hydrazones and their metal complexes exert cytotoxicities towards various cancer cell lines, some of which display drug resistance [1]. Coordination of these ligands with metals contribute to synergism on the antiproliferative action of the parent organic compounds [1,2]. Complexation allows for the introduction of numerous biologically active groups into a drug, thereby improving the spectrum of activity against the cancer cells, or enabling modification of the pharmacokinetic profile of the drugs [3]. The resulting cytotoxic effect of the metal-drug is more pronounced as a result of metal-drug synergism compared to the free ligand and the metal salt [3].
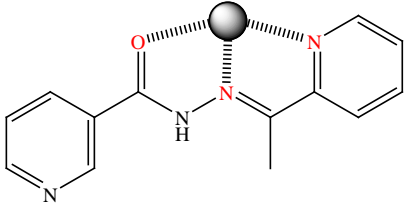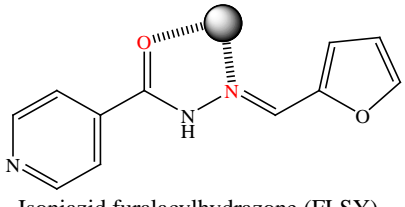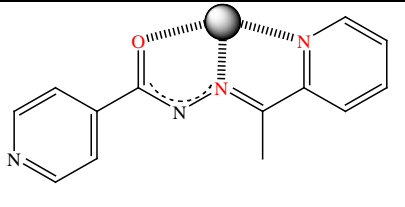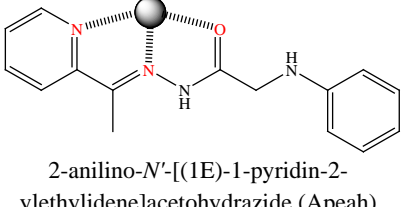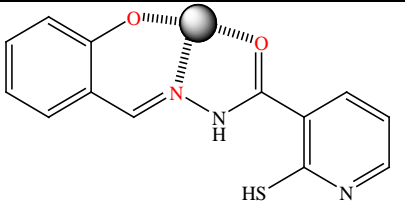
Lanthanide coordination compounds derived from hydrazones have also been investigated as potential antioxidants, antibacterial (as tuberculostats), antimalarial, antiviral, antifungal, anticonvulsant and anti-inflammatory agents [4-9]. Additionally, some of the lanthanide complexes have potential use as plant growth regulators, rodenticides, herbicides, nematocides and insecticides [7,10]. The significance of

hydrazones in the biomedical field is due to their ability to have different substituents attached to their structure, the reversible photochemically induced (*E*)-(*Z*) isomerisation of the double bond of the azomethine unit, as well as the ability to coordinate to metal ions under different chemical environments, depending on the attached substituent groups. A wide range of coordination modes is also achieved through the multiple functional groups on the hydrazones [7,8].

The reactions of 2-acetylpyridine nicotinohydrazone (penh) with [Ln(NO$_3$)$_3$·6H$_2$O] (Ln = Ce or Sm) yielded ten-coordinate, distorted bicapped square antiprism complexes, [Ce(penh)$_2$(H$_2$O)$_4$](NO$_3$)$_3$·4H$_2$O and [Sm(penh)$_2$(NO$_3$)$_2$](NO$_3$)·C$_2$H$_5$OH (Table 3.1) [11]. The Ln(III) ions of each complex are surrounded by two neutral tridentate hydrazone ligands containing the N$_2$O donor-atom set. In the Ce(III) complex, the coordination environment is completed by four oxygen atoms from four water molecules, while that of the Sm(III) compound has two bidentate nitrate anions [11]. These acylhydrazone-based complexes show significant antitumour activity against human colorectal cancer (lovo), human pancreatic cancer (PATU8988) and human gastric cancer (SGC7901) cell lines as determined by the MTT assay [11].

Metal complexes consisting of isonicotinoyl hydrazones were reported to show low resistivity to tuberculosis bacteria and high activity as antitubercular agents [7]. Hao *et al.* (2010) reported the preparation and characterisation of Pr(III) and Nd(III) complexes with (*E*)-*N*′-[1-(pyridin-2-yl)ethylidene]isonicotinohydrazide (**HL**) (Table 3.1) [12]. The DNA-binding studies of the complexes were investigated using viscosity measurements, electronic absorption, fluorescence and circular dichroic spectroscopy. The results indicated that the two complexes bind to calf thymus DNA *via* a groove binding mode, with the Pr(III) complex exhibiting higher binding affinity than the Nd(III) complex [12]. Moreover, the scavenging effects of the ligand and its Ln(III) complexes on superoxide (O$_2^-$·) and hydroxyl (OH·) radicals were determined *in vitro* by spectrophotometry. The complexes show enhanced antioxidant properties than the standard antioxidant, mannitol [12].

Table 3.1: Examples of hydrazone metal complexes used in biological and magnetic studies.

Structure and bonding mode of the ligand	Formula of the complex	Studies	Ref
2-acetylpyridine nicotinohydrazone (penh)	[Ce(penh)$_2$(H$_2$O)$_4$](NO$_3$)$_3$·4H$_2$O and [Sm(penh)$_2$(NO$_3$)$_2$](NO$_3$)·C$_2$H$_5$OH	Antitumour	[11]
Isoniazid furalacylhydrazone (FLSY)	[Ln(FLSY)(Lin)(NO$_3$)$_2$]NO$_3$·H$_2$O (Ln = La, Ce, Nd and Er; Lin = sodium salicylate)	Antitumour, DNA-binding and antibacterial	[13]
(*E*)-*N'*-[1-(2-pyridinyl)ethylidene]-isonicotinohydrazide (HL)	[Nd(L)$_2$(NO$_3$)(CH$_3$OH)$_2$]·C$_2$H$_5$OH and [Pr(L)$_2$(NO$_3$)(CH$_3$OH)$_2$]·C$_2$H$_5$OH	DNA binding and anti-oxidant	[12]
2-anilino-*N'*-[(1E)-1-pyridin-2-ylethylidene]acetohydrazide (Apeah)	[Ln(Apeah)$_2$(NO$_3$)(H$_2$O)]·2NO$_3$ (Ln = La, Pr, Nd, Sm, Eu, Gd, Tb, Dy and Y)	Antibacterial	[5]
(*E*)-*N'*-(2-hydroxybenzylidene)-2-mercaptonicotinohydrazide (HL)	[Ln$_2$L$_2$(OAc)$_4$(MeOH)$_2$]·2MeOH (Ln = Sm, Gd and Dy) [Tm$_2$L$_2$(OAc)$_4$(H$_2$O)$_2$]·4MeOH·2H$_2$O [Yb$_2$L$_2$(OAc)$_4$(MeOH)$_2$]·[Yb$_2$L$_2$(OAc)$_4$(H$_2$O)$_2$]·4H$_2$O	Magnetic	[14]

In addition to a diverse range of biological properties, Ln-hydrazone complexes are used as analytical reagents, and in producing dinuclear, trinuclear or polynuclear complexes exhibiting single-molecular magnetic (SMM) behaviour [7,14,15]. The magnetic properties of these lanthanide coordination compounds are important in cancer diagnosis [16]. The crystal structures and magnetic properties of five dinuclear acetato-bridged Ln(III) complexes have been reported (Table 3.1) [14]. Through magnetic susceptibility studies in the temperature range 1.9–300 K, it was shown that the Dy(III) complex exhibits SMM behaviour, with an energy barrier of 39.1 K, as a result of less distortion of the coordination geometry around the dysprosium ion. It was inferred that the coordination mode of the ligands, structural parameters and coordination geometry play a pivotal role in controlling the relaxation dynamics of SMMs [14].

Lanthanide acetate complexes of the hydrazone ligands, (*E*)-*N'*-(2-hydroxybenzylidene)benzohydrazide (**H₂phen**) and (*E*)-*N'*-(2-hydroxybenzylidene)nicotinohydrazide (**H₂Nic**) (Figure 3.1) were synthesised and characterised. The lanthanide acetates were chosen as they can enrich the coordination modes of the coordination compounds through multidentate acetate groups. Apart from coordinating monodentately (η^1) or bidentately (η^2), the acetate groups can bridge complexes by attaining the η^1:η^2:μ_2 mode [14]. The antitumour activity was screened for the free ligands, metal salts and their Ln(III) complexes against breast cancer (MCF-7), the endometrial carcinoma (HEC-1A) and the human monocytic (THP-1) cell lines. The results obtained show that the hydrazone ligands and complexes **1**–**4** are partially cytotoxic against MCF-7 cells, while the Schiff bases and **3**–**5** significantly inhibit cell growth in HEC-1A cells. The *in vitro* cytotoxicity also revealed no activity of all the compounds against THP-1 cells. This is vital in the development of new antitumour agents to substantially increase the success rate of cancer treatments. The study of three types of cancer cell lines was motivated by the existence of genetic and epigenetic variations amongst the various types of tumours, leading to different clinical outcomes. Since the cancer cell lines do not have equal value as tumour models, therapeutic agents are expected to possess different mechanisms of action and therapeutic efficacies [17,18].
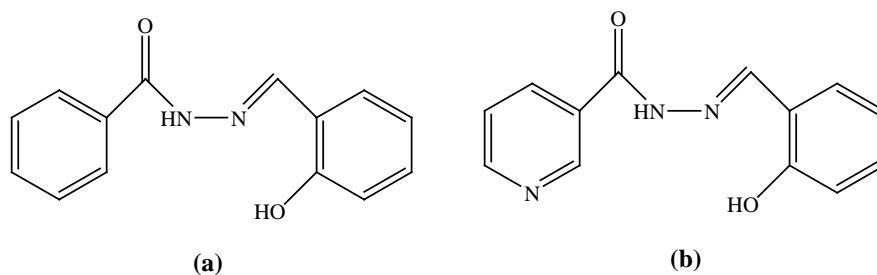
Figure 3.1: The structures of: **(a) H₂phen** and **(b) H₂Nic**.

3.2 Procedure for the preparation of hydrazone ligands

3.2.1 Synthesis of (*E*)-*N′*-(2-hydroxybenzylidene)benzohydrazide (H₂phen)

The hydrazone ligand, **H₂phen**, was prepared using the literature method of related compounds (Scheme 3.1) [5,13,14]. Benzohydrazide (2.815 g, 20.676 mmol) was added to the salicylaldehyde (2.525 g, 20.676 mmol) in absolute methanol (20 mL). After refluxing for 3 hours, the resulting yellow solution was concentrated using a rotary evaporator. The white precipitate was filtered, dried and recystallised from ethanol. Yield = 75.3 %, m.p. = 168.2 °C. Anal. *Calcd*. for $C_{14}H_{12}N_2O_2$ (%): C, 69.99; H, 5.03; N, 11.66. Found: C, 68.99; H, 4.76; N, 11.42. UV-Vis (DMF, λ_{max} nm (ε, L.mol^{-1}cm^{-1})): 290 (25416), 300 (26304), 331 (21255). IR (v_{max}/cm^{-1}): v(OH)$_{phenol}$ 3265(m), v(N-H) 3057(w), v(C=O) 1669(s), v(C=N) 1622;1594(s), v(N-N) 1012(m). ^{1}H NMR (400 MHz, DMSO-d_6, δ ppm): 6.87-7.00 (m, 2H), 7.31 (t, *J*=7.34 Hz, 1H), 7.55 (br. s., 3 H) 7.60 (d, *J*=6.60 Hz, 1H), 7.94 (d, *J*=7.09 Hz, 2H), 8.65 (s, 1H), 11.33 (br. s., 1H), 12.13 (br. s., 1H).

3.2.2 Synthesis of (*E*)-*N′*-(2-hydroxybenzylidene)nicotinohydrazide (H₂Nic)

The organic compound, **H₂Nic**, was synthesised as outlined in Scheme 3.1 [5,13,14]. Salicylaldehyde (2.485 g, 20.349 mmol) in absolute methanol (20 mL) was added to a methanolic solution of nicotinohydrazide (2.791 g, 20.349 mmol). The reaction mixture was refluxed for 3 hours. The white crystalline solid formed on cooling was filtered, dried and recrystallised from ethanol. **H₂Nic** was obtained as a white solid.

Yield: 73.4 %, m.p. = 245.4 ^{o}C. Anal. *Calcd*. for $C_{13}H_{11}N_3O_2$ (%): C, 64.72; H, 4.60; N, 17.42. Found: C, 64.12; H, 4.42; N, 17.23. UV-Vis (DMF, λ_{max} nm (ε, L.mol^{-1}cm^{-1})): 290 (33256), 300 (31326), 331 (24750). IR (v_{max}/cm^{-1}): v(C=O) 1633(s), v(C=N) 1603(s), v(pyridyl) 1567(m), v(N-N) 1029(m). ^{1}H NMR (400 MHz, DMSO- d_6, δ ppm): 6.90-6.99 (m, 2H), 7.33 (t, *J*=7.34 Hz, 1H), 7.61 (d, *J*=7.58 Hz, 1H), 7.82-7.88 (m, 2H), 8.68 (s, 1H), 8.80 (br. s., 2H), 11.10 (br. s., 1H), 12.29 (br. s., 1H).
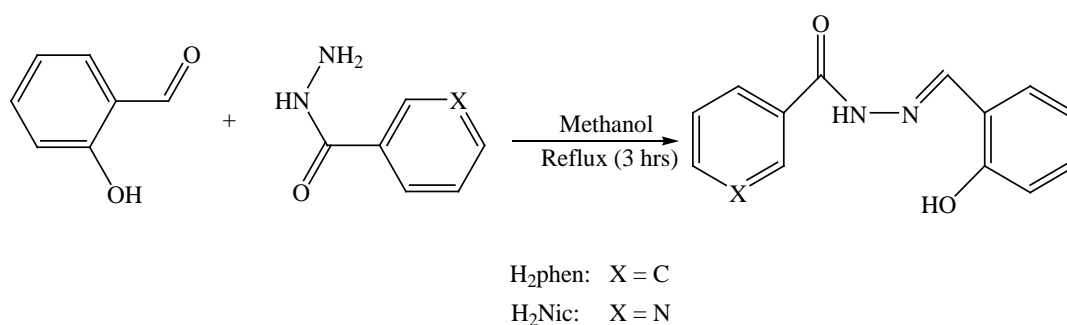
H$_2$phen: X = C
H$_2$Nic: X = N

Scheme 3.1: Synthesis of the hydrazone ligands, **H$_2$phen** and **H$_2$Nic**.

3.3   Synthesis of the complexes

3.3.1   Synthesis of [La$_2$(Hphen)$_2$(OAc)$_4$(H$_2$O)$_2$]·DMF·H$_2$O   (1)

La(OAc)$_3$·xH$_2$O (0.223 g, 0.668 mmol) was added to a solution of **H$_2$phen** (0.160 g, 0.668 mmol) in 5 mL DMF. After refluxing the reaction mixture for 2 hours at 70 ^{o}C, the solution was filtered off and diethyl ether (10 mL) was allowed to diffuse slowly into the yellow solution at room temperature. Yellow X-ray quality crystals were obtained after 3 weeks. Yield = 0.178 g (22.0 % based on the La(III) salt), m.p. >300 ^{o}C. Anal. *Calcd*. for $C_{36}H_{38}La_2N_4O_{14}$, 2($C_3H_7NO$), 2($H_2O$) (%): C, 41.67; H, 4.66; N, 6.94. Found: C, 41.34; H, 4.84; N, 6.82. Conductivity (25 ^{o}C, 10^{-3} M, DMF): 4.58 ohm^{-1}cm^{2}mol^{-1}. UV-Vis (DMF, λ_{max} nm (ε, L.mol^{-1}cm^{-1})): 277 (33136), 301 (34680), 318 (36261), 329 (34673), 398 (42203). IR (v_{max}/cm^{-1}): v(O-H)$_{water}$ 3498-3092(b), v(C=O) 1659(s), v(C=N) 1610(s), v_{as}(COO$^-$) 1436(s), v_s(COO$^-$) 1392(s), v(N-N) 1009(m), v(La-O) 585(m), v(La-N) 402(m).

3.3.2   Synthesis of complexes 2–5

Compounds **2–5** were synthesised using the following general procedure. [Ln(OAc)$_3$·xH$_2$O] (Ln = La, Nd, Er and Yb; for Yb, x = 4) dissolved in 5 mL DMF was added to a 2 mL methanolic solution of **H$_2$Nic**. The resulting mixture was refluxed continuously for 2 hours, followed by filtration of the yellow solution to dispose of undissolved material. Yellow single crystals suitable for X-ray crystallography were grown within 1–3 weeks under vapour diffusion using diethyl ether (10 mL).

[La$_2$(HNic)$_2$(OAc)$_4$(H$_2$O)$_2$]·DMF·H$_2$O   (2)

H$_2$Nic (0.206 g, 0.854 mmol), La(OAc)$_3$·xH$_2$O (0.285 g, 0.854 mmol). Yield = 0.198 g (19.1 % based on the La(III) salt), m.p. >300 °C. Anal. *Calcd*. for C$_{34}$H$_{36}$La$_2$N$_6$O$_{14}$, 2(C$_3$H$_7$NO), 2(H$_2$O) (%): C, 39.62; H, 4.49; N, 9.24. Found: C, 39.73; H, 4.46; N, 9.27. Conductivity (25 °C, 10^{-3} M, DMF): 7.18 ohm^{-1}cm^{2}mol^{-1}. UV-Vis (DMF, λ_{max} nm (ε, L.mol^{-1}cm^{-1})): 275 (22295), 290 (21571), 299 (24304), 317 (25152), 401 (24931). IR (ν_{max}/cm^{-1}): ν(O-H)$_{water}$ 3558-2995(b), ν(C=O) 1673(s), ν(C=N) 1616(s), ν(pyridyl) 1544(m), ν_{as}(COO$^-$) 1438(s), ν_s(COO$^-$) 1395(s), ν(N-N) 1012(m), ν(La-O) 574(m), ν(La-N) 422(m).

[Nd$_2$(HNic)$_2$(OAc)$_4$(H$_2$O)$_2$]·DMF·H$_2$O   (3)
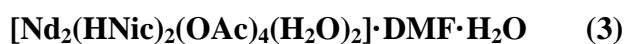
H$_2$Nic (0.215 g, 0.891 mmol), Nd(OAc)$_3$·xH$_2$O (0.606 g, 1.786 mmol). Yield = 0.314 g (28.7 % based on the Nd(III) salt), m.p. >300 °C. Anal. *Calcd*. for C$_{34}$H$_{36}$Nd$_2$N$_6$O$_{14}$, 2(C$_3$H$_7$NO), 2(H$_2$O) (%): C, 39.27; H, 4.45; N, 9.16. Found: C, 39.73; H, 4.32; N, 8.97. Conductivity (25 °C, 10^{-3} M, DMF): 6.31 ohm^{-1}cm^{2}mol^{-1}. UV-Vis (DMF, λ_{max} nm (ε, L.mol^{-1}cm^{-1})): 320 (23523), 327 (20500), 401 (38205). IR (ν_{max}/cm^{-1}): ν(O-H)$_{water}$ 3558-2995(b), ν(C=O) 1655(s), ν(C=N) 1614(s), ν(pyridyl) 1544(m), ν_{as}(COO$^-$) 1434(s), ν_s(COO$^-$) 1393(s), ν(N-N) 1013(m), ν(La-O) 587(m), ν(La-N) 424(m).

[Er$_2$(HNic)$_2$(OAc)$_4$(H$_2$O)$_2$]·DMF   (4)

H$_2$Nic (0.149 g, 0.618 mmol), Er(OAc)$_3$·xH$_2$O (0.213 g, 0.618 mmol). Yield = 0.175 g (22.9 % based on the Er(III) salt), m.p. >300 °C. Anal. *Calcd*. for C$_{34}$H$_{36}$Er$_2$N$_6$O$_{14}$,

2(C$_3$H$_7$NO) (%): C, 38.95; H, 4.09; N, 9.09. Found: C, 38.84; H, 4.06; N, 8.97. Conductivity (25 ^{o}C, 10^{-3} M, DMF): 6.37 ohm^{-1}cm^{2}mol^{-1}. UV-Vis (DMF, λ_{max} nm (ε, L.mol^{-1}cm^{-1})): 309 (18492), 327 (15117), 397 (31810). IR (v_{max}/cm^{-1}): v(O-H)$_{water}$ 3558-3095(b), v(C=O) 1621(s), v(pyridyl) 1545(m), v_{as}(COO$^-$) 1457(s), v_s(COO$^-$) 1393(s), v(N-N) 1012(m), v(La-O) 569(m), v(La-N) 430(m).

[Yb$_2$(HNic)$_2$(OAc)$_4$(H$_2$O)$_2$]·DMF   (5)

H$_2$Nic (0.0703 g, 0.292 mmol), Yb(OAc)$_3$·4H$_2$O (0.246 g, 0.583 mmol). Yield = 0.115 g (31.7 % based on the Yb(III) salt), m.p. >300 ^{o}C. Anal. *Calcd.* for C$_{36}$H$_{38}$Yb$_2$N$_4$O$_{14}$, 2(C$_3$H$_7$NO) (%): C, 38.59; H, 4.05; N, 9.00. Found: C, 38.48; H, 4.12; N, 9.03. Conductivity (25 ^{o}C, 10^{-3} M, DMF): 7.00 ohm^{-1}cm^{2}mol^{-1}. UV-Vis (DMF, λ_{max} nm (ε, L.mol^{-1}cm^{-1})): 315 (21335), 327 (18106), 397 (24989). IR (v_{max}/cm^{-1}): v(O-H)$_{water}$ 3558-3095(b), v(C=O) 1656(s), v(C=N) 1609(s), v(pyridyl) 1544(m), v_{as}(COO$^-$) 1446(s), v_s(COO$^-$) 1398(s), v(N-N) 1019(m), v(La-O) 567(m), v(La-N) 430(m).

3.4   Results and Discussion

The yields for the metal complexes are low (19.1–31.7 %). High reaction yields can be attempted by changing solvents, molar ratios of reactants and reaction conditions (temperature and pH). Complexes **1–5** (1×10^{-3} M in DMF at 25 ^{o}C) gave molar conductivity values in the range 4.58–7.18 ohm^{-1}cm^{2}mol^{-1}, suggesting the non-electrolytic nature of the complexes [19]. All the coordination compounds are crystalline solids and were found to be non-hygroscopic and thus air-stable. The complexes are soluble in DMSO, DMF and water, and slightly soluble in methanol, ethanol and acetonitrile, but insoluble in dichloromethane, chloroform and diethyl ether.

Deprotonation of the hydrazone phenol group occurred, yielding mono-anionic ligands, **Hphen$^-$** and **HNic$^-$**, which coordinated tridentately to produce metal complexes with a 1:1 Ln:ligand ratio (Scheme 3.2).

$[La(OAc)_3 \cdot xH_2O]$ + H_2phen $\xrightarrow[\text{Et}_2\text{O}]{\text{DMF}}$ $[La_2(Hphen)_2(OAc)_4(H_2O)_2] \cdot DMF \cdot H_2O$

(1)

$[Ln(OAc)_3 \cdot xH_2O]$ + yH_2Nic

$[Ln_2(HNic)_2(OAc)_4(H_2O)_2] \cdot DMF \cdot H_2O$

Ln = La **(2)** or Nd **(3)**
(9-coordinate)

y = 1 for La and Er
y = 2 for Nd and Yb

$[Ln_2(HNic)_2(OAc)_4(H_2O)_2] \cdot DMF$

Ln = Er **(4)** or Yb **(5)**
(8-coordinate)
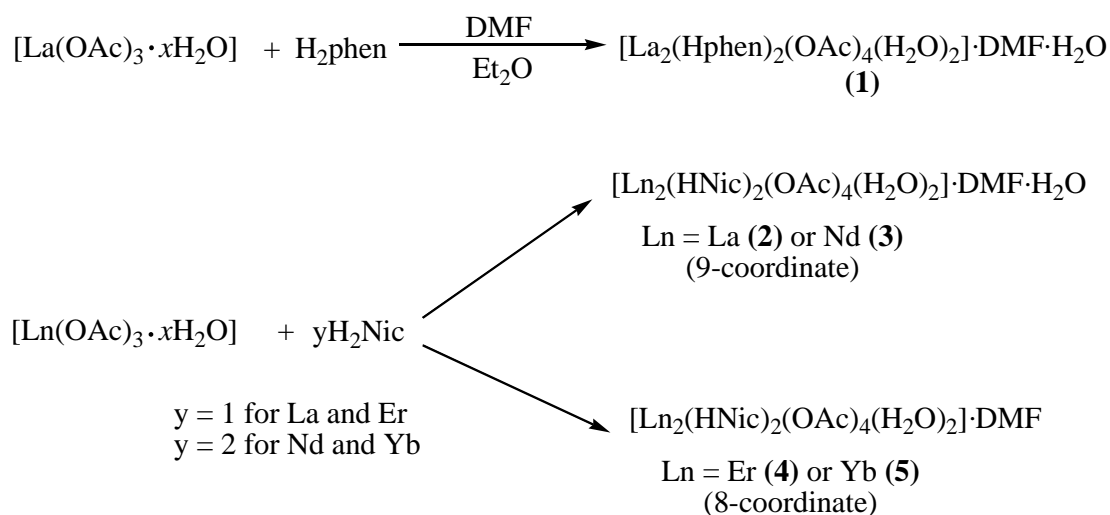
Scheme 3.2: Synthetic route of Ln(III) complexes derived from **H₂phen** and **H₂Nic**.

3.4.1   FT-IR spectroscopy

Comparison of the infrared spectra of the free hydrazone ligands and the complexes confirmed the formation of the metal chelates. In the IR spectrum of **H₂phen**, a sharp band at approximately 1669 cm^{-1} is characteristic of the C=O vibration (Figure 3.2a) [5,13,20]. The peaks due to the v(C=N) vibration appear at 1622 and 1594 cm^{-1} as strong absorption bands, while the weak band at 3057 cm^{-1} is ascribed to the N-H stretching vibrations [5,11,20,21]. The v(N-N) appears at 1012 cm^{-1}. Upon complexation to La(III), the phenolic O-H band of **H₂phen** disappears, indicating deprotonation of the hydrazone ligand (Figure 3.2a). In the free ligand, this v(OH) occurs at 3265 cm^{-1}, but is replaced by a broad band due to the coordinated water molecules (3493–3091 cm^{-1}), which also obscures the N-H stretch [5]. The bands attributed to the v(C=N) and the v(C=O) are shifted to lower frequencies (1610 and 1659 cm^{-1}, respectively) in the spectrum of complex **1**. This suggests the involvement of the nitrogen atom of the azomethine moiety and the carbonyl oxygen in the coordination of the ligand to the metal ion [5]. The new bands appearing in the spectrum of **1** at 1436, 1392, 585 and 402 cm^{-1} are assigned to contributions from the asymmetric v(COO⁻), and the symmetric v(COO⁻), v(La-O) and v(La-N), respectively [4,13,20,22].

The band observed at 1633 cm^{-1} in the IR spectrum of **H₂Nic** is due to the C=O bond frequency, which is shifted to lower energies in **2**, **3** and **5** (1673, 1655, 1656 cm^{-1}, respectively), and to higher energy in **4** (1621 cm^{-1}) (Figure 3.2b and 3.2c) [11,13,21,23]. The spectra of **2**–**5** exhibit broad bands within the range 3558–2995 cm^{-1}, which is assignable to v(O-H) of the coordinated water molecules. Bands in the far infrared region (587–422 cm^{-1}) can be assigned to Ln-O and Ln-N vibrations in **2**–**5** [20,22,24]. Further evidence of coordination of the hydrazone ligand, **H₂Nic**, was provided by the appearance of acetate vibrational bands [4,13]. The peaks appearing at 1029 and 1567 cm^{-1} of the free **H₂Nic** are assigned to contributions from the stretching vibrations of the N-N and pyridyl groups, respectively [4,5,20]. There is a considerable lowering of the v(N-N) and v(pyridyl) frequencies in the spectra of the complexes, with the vibrational bands found in the ranges 1019–1012 and 1545–1544 cm^{-1}, respectively, in **2**–**5**. The shifts of bands to lower frequencies are due to decreases in the stretching force of the bonds as a result of the coordination of the ligand to the metal ions [21]. The key IR frequencies of the ligands and **1**–**5** are summarised in Table 3.2.
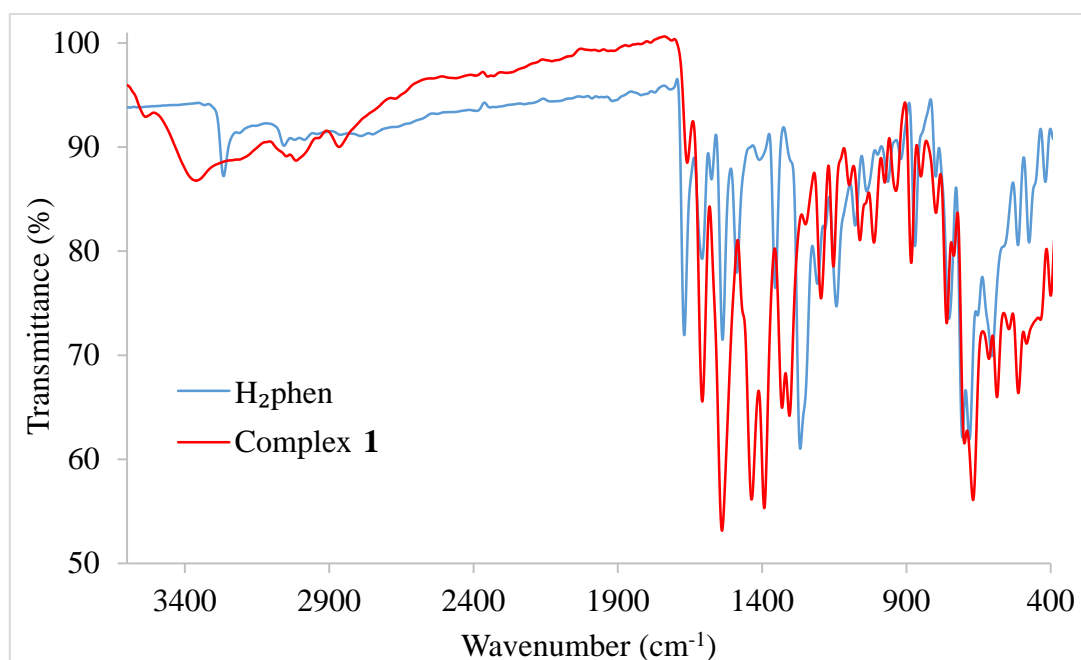
Figure 3.2a: Overlay IR spectra of **H₂phen** and complex **1**.
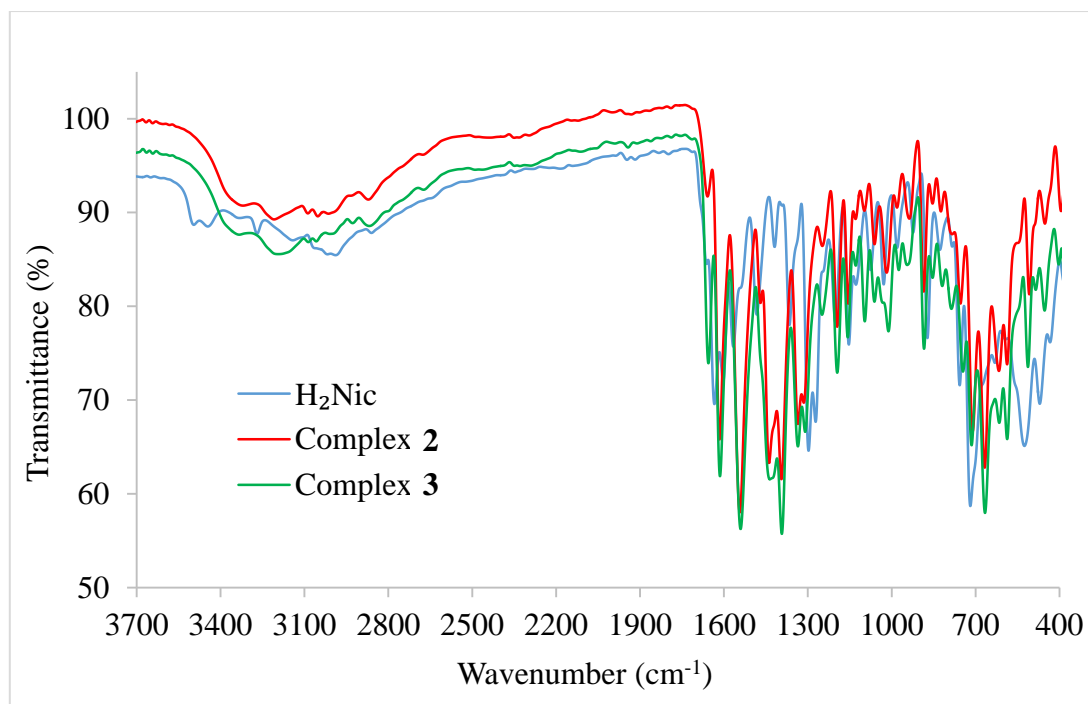
Figure 3.2b: IR spectra of **H₂Nic** and complexes **2** and **3**.
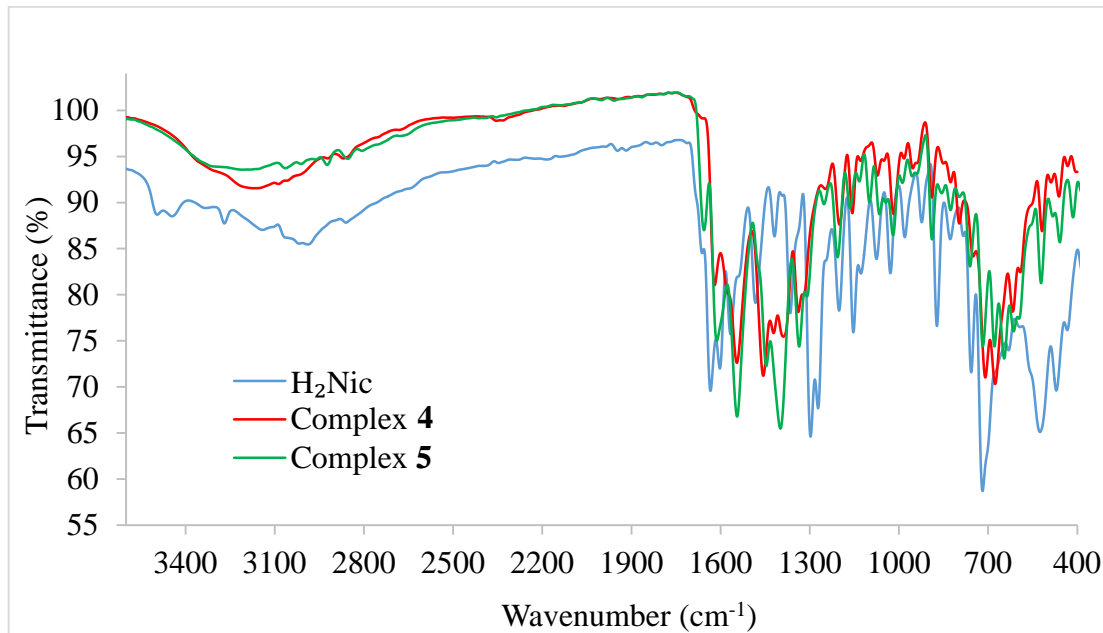
Figure 3.2c: IR spectra of **H₂Nic** and complexes **4** and **5**.

Table 3.2: Spectral IR band frequencies (cm^{-1}) of the hydrazone ligands and complexes **1**–**5**.

Compound	ν(C=N)	ν(C=O)	ν(N-H)	ν(N-N)	$\nu_{pyridyl}$	ν_{as}(COO$^-$)	ν_s(COO$^-$)	ν(Ln-O)	ν(Ln-N)
H$_2$phen	1622, 1594	1669	3057	1012	-	-	-	-	-
H$_2$Nic	1603	1633	3266	1029	1567	-	-	-	-
1	1610	1659	-	1009	-	1436	1392	585	402
2	1616	1673	-	1012	1544	1438	1395	574	422
3	1614	1655	-	1013	1544	1434	1393	587	424
4	-	1621	-	1012	1545	1457	1393	569	430
5	1609	1656	-	1019	1544	1446	1398	567	430

3.4.2   NMR analysis

The ^{1}H NMR spectra of the free hydrazone ligands in DMSO-d_6 and the atom-numbering scheme of the organic compounds are shown in Figures 3.3a and 3.3b. The ^{13}C NMR spectra of the hydrazones are shown in Figures 3.3c and 3.3d, with peak assignment details given in Table 3.3 (see the molecular structure inserts for carbon atom-labelling of the compounds).
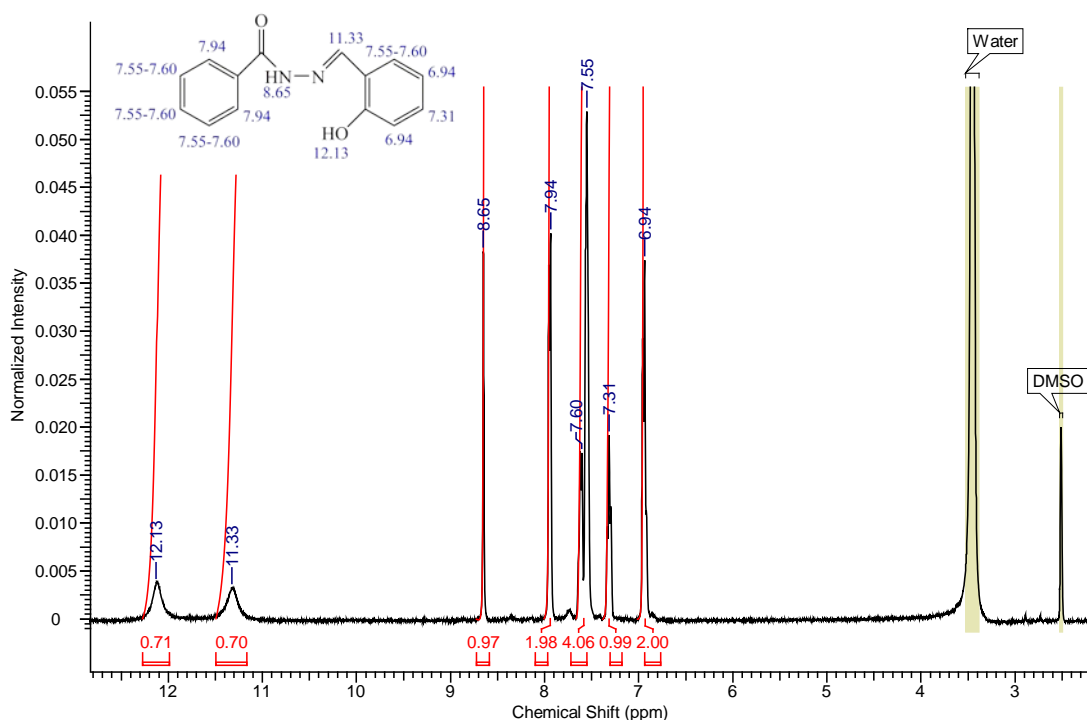
Figure 3.3a: The proton NMR spectrum of **H$_2$phen**.
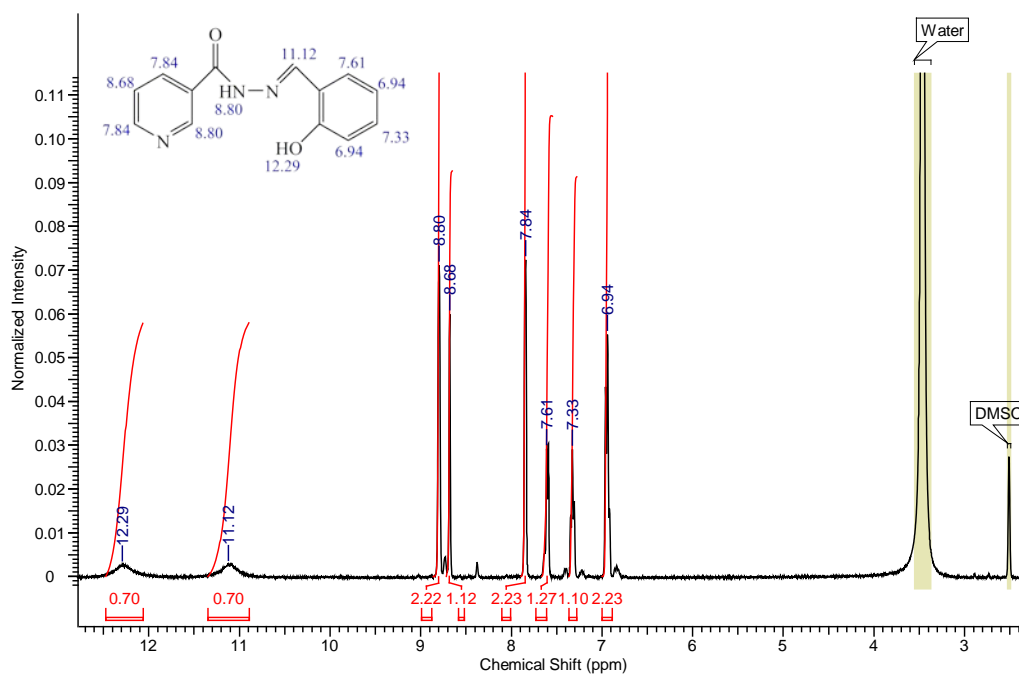
Figure 3.3b: The proton NMR spectrum of **H₂Nic** in DMSO-*d₆*.
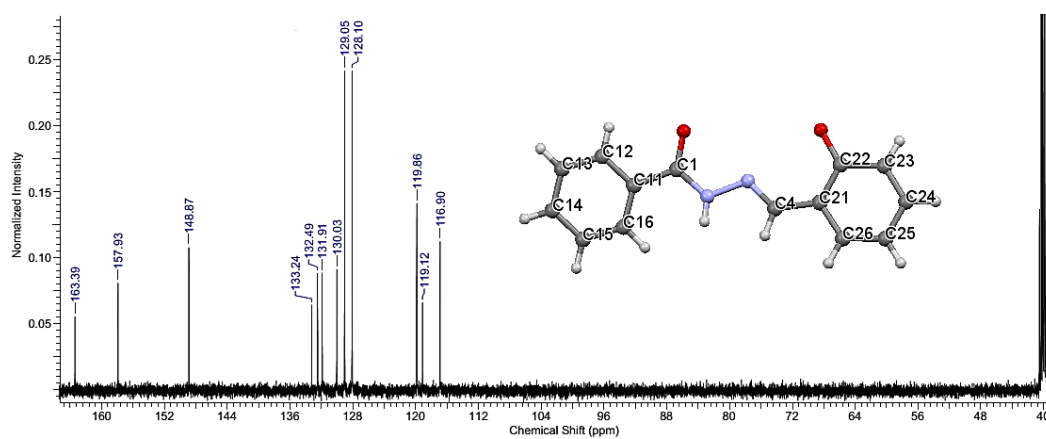
Figure 3.3c: ^{13}C NMR spectrum of **H₂phen**.
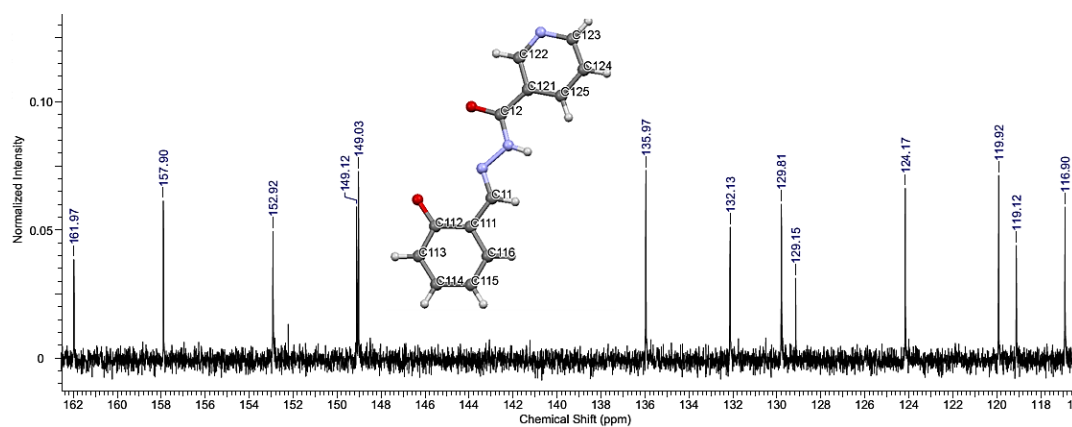
Figure 3.3d: ^{13}C NMR spectrum of **H₂Nic**.

Table 3.3: Signal assignment in the ^{13}C NMR spectra of the hydrazone ligands.

H₂phen		H₂Nic	
Chemical shift (ppm)	**Assignment**	**Chemical shift (ppm)**	**Assignment**
116.90	C23	116.90	C113
119.12	C21	119.12	C111
119.86	C25	119.92	C115
128.10	C12 and C16	124.17	C124
129.05	C13 and C15	129.15	C116
130.03	C26	129.81	C121
131.91	C14	132.13	C114
132.49	C24	135.97	C125
133.24	C11	149.03	C11
148.87	C4	149.12	C123
157.93	C22	152.92	C122
163.39	C1	157.90	C112
		161.97	C12

Complexes **1**–**3** yielded the ^{1}H NMR spectra that are different to those of the free ligands (Figure 3.3e). The spectra of the La(III) and Nd(III) complexes exhibit more peaks than expected for the Schiff base ligands. The additional signals in the range -0.07 to 2.89 ppm (except for the DMSO-d_6 signal at 2.5 ppm) can be attributed to the methyl group protons of the crystallographic DMF and the chelating or bridging acetates. The proton resonances of the diamagnetic La(III) complexes are shifted upfield relative to those of the free ligand which is possibly due to shielding effects [25].
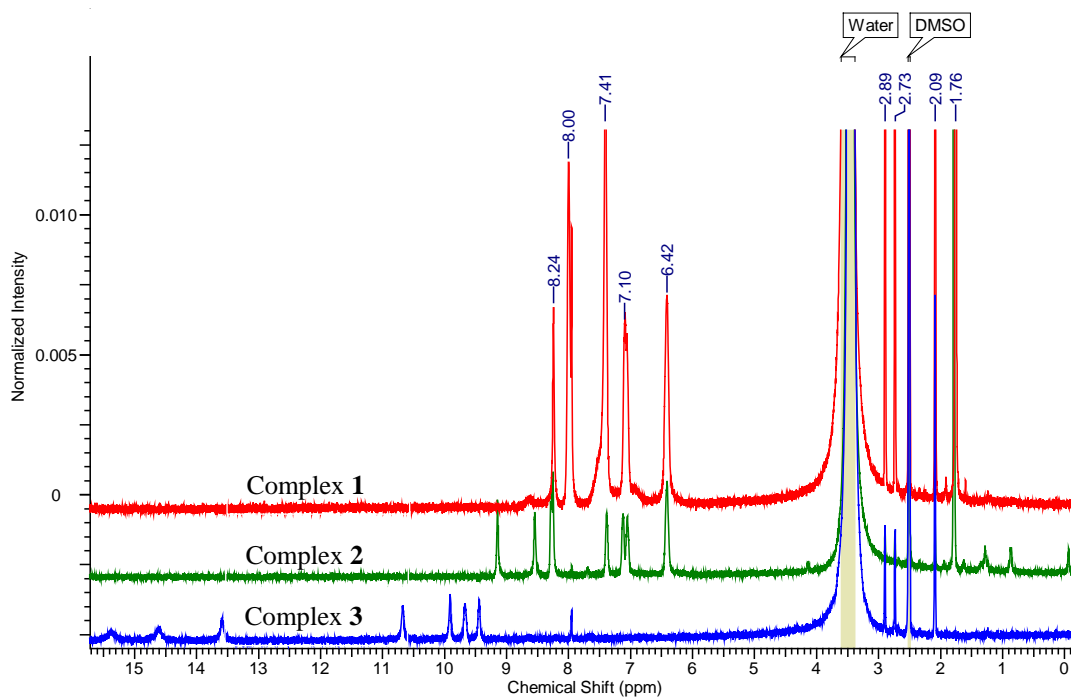
Figure 3.3e: The proton NMR spectra of **1**–**3**.

In **1** and **2**, the broad signal of the phenolic –OH disappeared, depicting coordination of the phenolic oxygen to the La(III) ions after deprotonation. In the free ligand this signal appears as a singlet at 12.13 ppm. Induced downfield shifts of **H₂Nic** protons are observed for the Nd(III) complex. Formation of the metal-ligand bonds in **3** led to a decrease in electron density around the ligand protons, causing these protons to resonate at a lower field. The paramagnetic shifts are produced by an interaction between the unpaired *f*-electrons of the lanthanide ions with the resonating nucleus *via* delocalisation of the *f*-electron density towards the resonating nucleus, or predominantly in a through-space dipole manner [25,26]. No useful information was obtained for **4** and **5** due to the paramagnetic nature of Er(III) and Yb(III), although the paramagnetic Nd(III) ion in **3** resulted in no significant line broadening in its ^{1}H NMR spectrum [26].

3.4.3   UV-Vis spectroscopy

The UV-Vis absorption spectra of the two hydrazone ligands and complexes **1**–**5** were performed at room temperature in DMF (Figures 3.4a-b). The three absorption peaks at 290, 300 and 331 nm in the free ligands are ascribed to the π→π* transition of the aromatic rings, n→π* transition of the carbonyl (C=O) and the n→π* transition of the azomethine (C=N) groups, respectively [20]. All the presented complexes exhibit a new broad absorption peak at 397 nm which is not found in the free ligands. This new absorption band is attributed to the significant hyperchromic shifted n→π* transition of the C=N group due to the ligand to metal charge transfer [27]. An additional two bands are observed in **1** and **2**. Further proof that coordination occurred is indicated by shifts in absorption bands, as well as changes in peak intensities and patterns upon complexation [20]. The shifts of spectral bands to lower energy are ascribed to the effect of the crystal field, as a result of inter-electronic repulsion between 4*f* electrons [5].
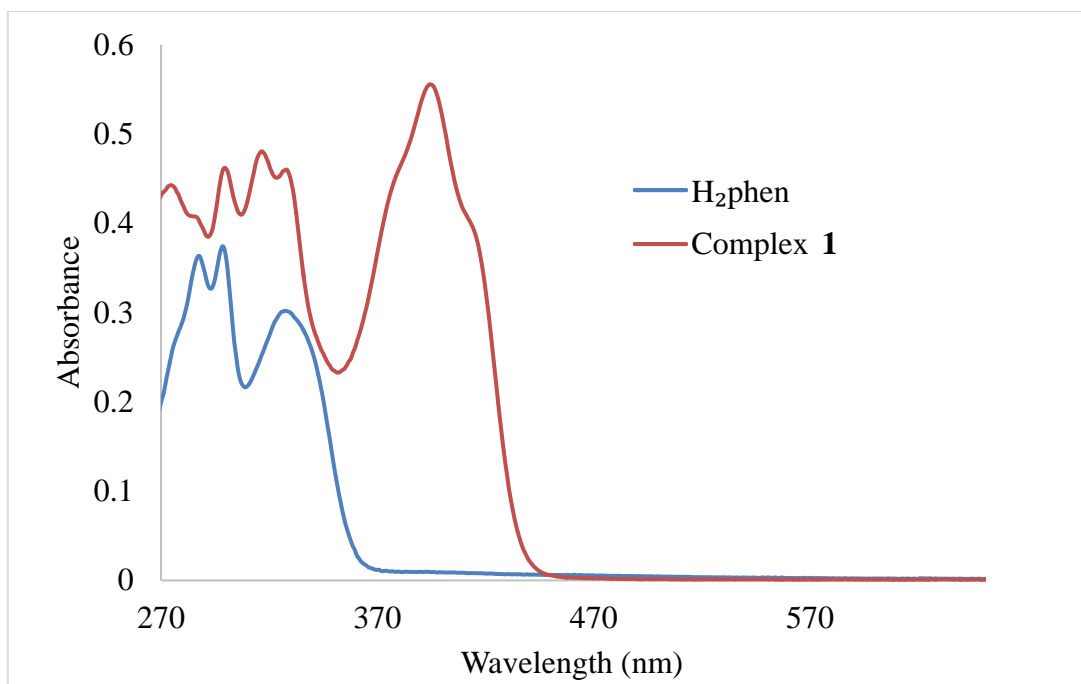
Figure 3.4a: UV-Vis spectra of the free **H₂phen** and **1** in DMF.
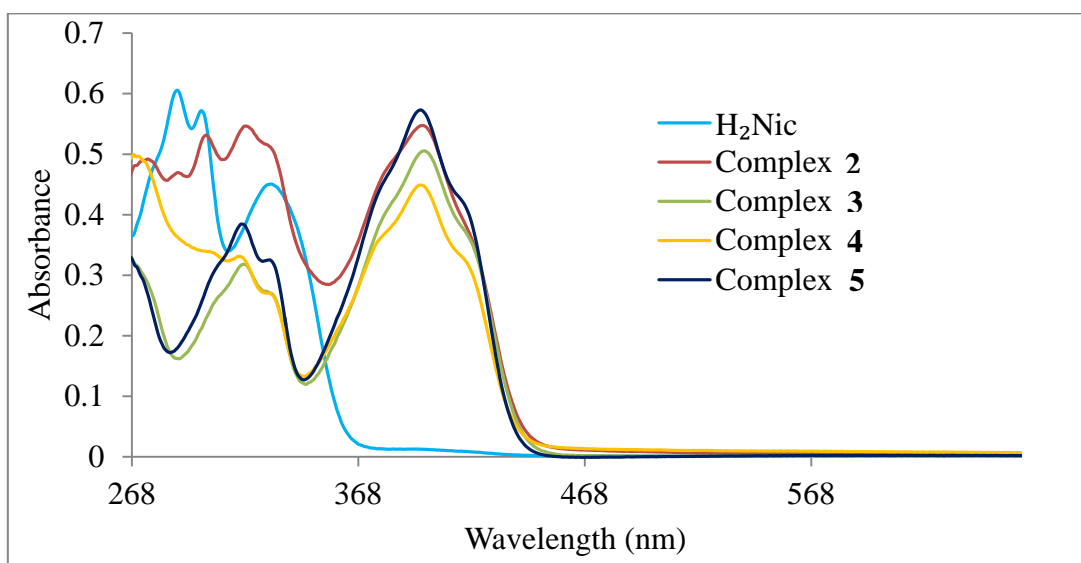
Figure 3.4b: UV-Vis spectra of DMF solutions of **H₂Nic** and **2–5**.

3.4.4   Coordination polyhedra determination

The coordination geometries of the Ln(III) ions were determined through continuous shape measure (CShM) calculations using *SHAPE 2.1* software; the results are listed

in Table 3.4. For the nona-coordinate complexes **1**–**3**, the coordinated geometry is classified as a distorted spherical capped square antiprism (CSAPR-9, C_{4v}) with CShM values of 2.55876, 2.51433 and 2.39721, respectively (Figure 3.5a) [28]. The obtained geometries however show a small difference in deviation parameters compared to the muffin (MFF-9) structure (symmetry C_s), having corresponding distortion parameters equal to 2.60624, 2.62707 and 2.48010 [28]. It is therefore possible for the coordination spheres of lanthanum and neodymium to exist as the intermediate between the CSAPR-9 and MFF-9 geometry [28,29]. Both **4** and **5** display eight-coordinate triangular dodecahedron (TDD-8) geometries (D_{2d}), with the Yb(III) complex (CShM = 1.58330) exhibiting a lower deviation from the ideal geometry than the Er(III) complex (CShM = 1.63522) (Figure 3.5b). The representative coordination polyhedra of **1** and **4** are shown in Figures 3.5a and 3.5b, respectively.

Table 3.4: The molecular geometries of complexes **1**–**5** as predicted by CShM analysis [28,29].

Complex	C.N.	Shape	Symmetry	CShM	Polyhedral volume (Å^3)	Average bond length (Å)
1	9	CSAPR-9	C_{4v}	2.55876	32.8844	2.5629
2	9	CSAPR-9	C_{4v}	2.51433	32.8359	2.5605
3	9	CSAPR-9	C_{4v}	2.39721	30.8384	2.5040
4	8	TDD-8	D_{2d}	1.63522	22.9162	2.3530
5	8	TDD-8	D_{2d}	1.58330	22.3926	2.3343

C.N. = Coordination number

All the CShM values obtained lie between 0.1 and 3, which is considered significant but still correspond to a small distortion from an ideal geometry [30,31]. It is noticed that the nine-coordinate complexes gave higher deviation parameters compared to eight-coordinate complexes, and the deviation parameters tend to decrease across the period. These distortions from the reference shape are ascribed to the metal ionic radii, flexibility of the coordinating ligands, and the coordination numbers of the lanthanide ions [30,32]. The Er(III) and Yb(III) complexes gave the smallest deviations from the ideal shape due to their smaller size, and thus stronger ligand binding that results in less flexibility, as well as less steric repulsion due to lower

coordination numbers, as opposed to the La(III) and Nd(III) complexes that possess bigger metal ions, longer bonds and higher coordination numbers [32]. The polyhedral volume is seen to decrease with the decrease in the metal ionic size, with a significant difference between the nine-coordinate and eight-coordinate chelates. The size of the metal ion, average bond lengths, coordination numbers, polyhedral volume and CShM values are therefore correlated.
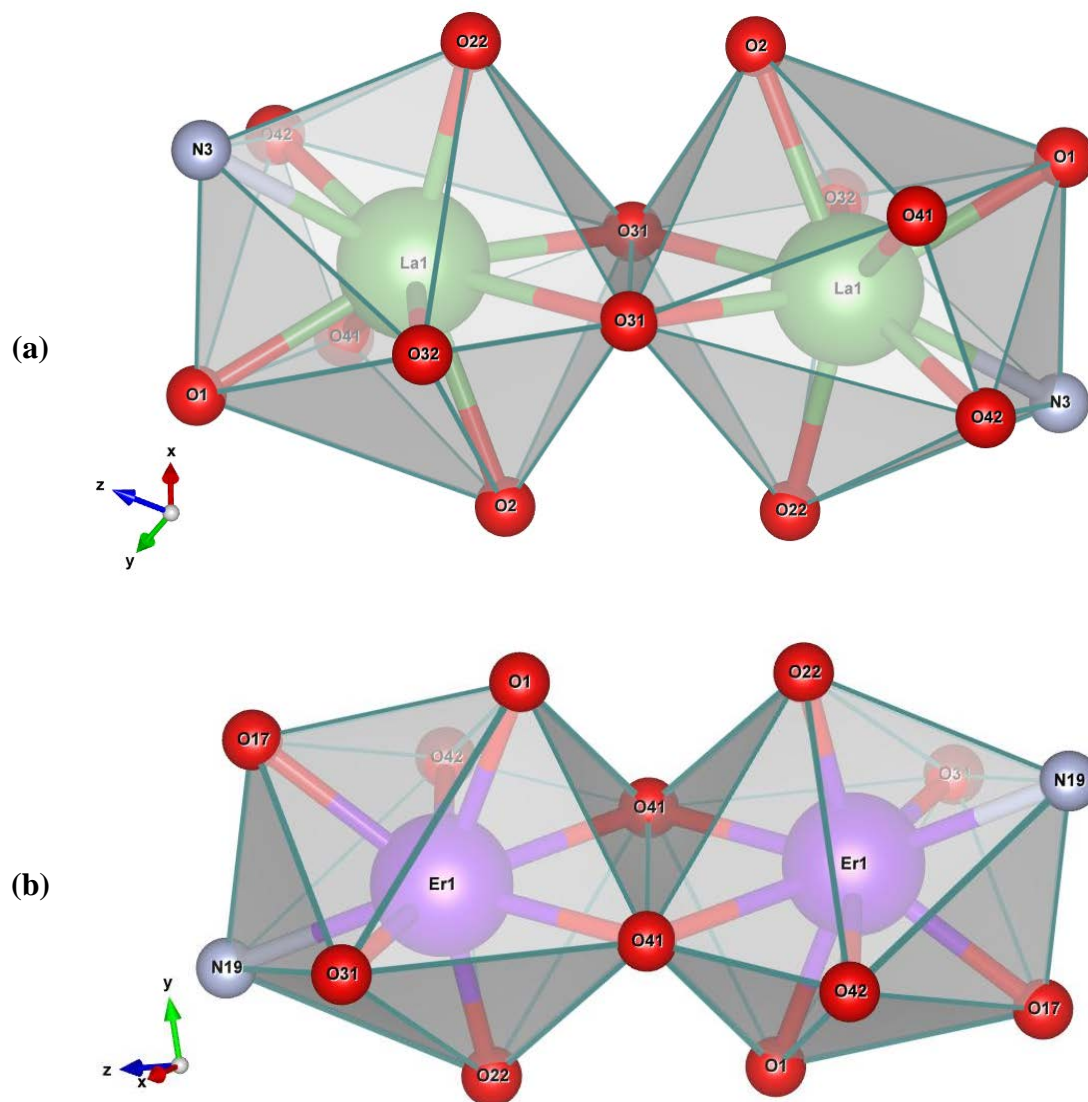
Figure 3.5: The distorted polyhedral representations of: **(a)** spherical capped square antiprismatic $(LaO_8N)_2$; **(b)** triangular dodecahedron $(ErO_7N)_2$.

3.4.5 X-ray crystallography

Complexes **1–5** are centrosymmetric and feature double acetate-bridged Ln(III) dimers with the general formulae $[La_2(Hphen)_2(OAc)_4(H_2O)_2]\cdot DMF\cdot H_2O$, $[Ln_2(HNic)_2(OAc)_4(H_2O)_2]\cdot DMF\cdot H_2O$ (Ln = La and Nd) and $[Ln_2(HNic)_2(OAc)_4(H_2O)_2]\cdot DMF$ (Ln = Er and Yb) (Figures 3.6a-e). Coordination compounds **1–3** crystallise in the triclinic space group *P-1* (Z = 1), while **4** and **5** were found to crystallise in the monoclinic space group $P2_1/c$ (Z = 2). Crystal data and structure refinement parameters are provided in Table S3.1a and S3.1b of supplementary information.
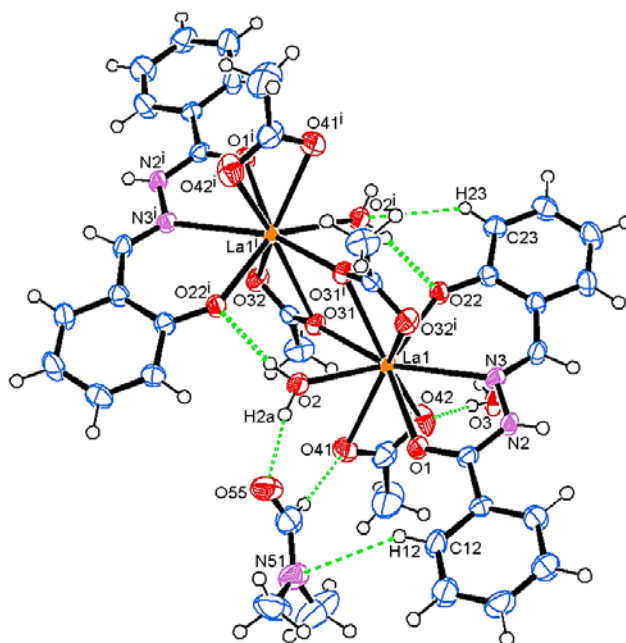
Figure 3.6a: A perspective view of **1** with partial atom-numbering scheme (50 % probability level; hydrogen bond network is shown by green dashed lines).

Crystallographic studies showed that in **1–3** the metal ion is nine-coordinate, and bonded to eight oxygen atoms (with two oxygen atoms originating from the phenoxide and carbonyl groups of the tridentate *O,N,O*-donor ligands **H₂phen** and **H₂Nic**, one oxygen from a water molecule, two from the η^2–acetate group and three provided by the bridging $\eta^1{:}\eta^2{:}\mu_2$–acetate groups) and one hydrazone nitrogen atom (Figure 3.6f) [14,32]. The *H*-atom of the phenol group of the hydrazones was

deprotonated to give a more reactive mono-anionic ligand. The hydrazone ligands, the η^1:η^2:μ_2–acetate groups and the water molecules, exhibited the same bonding mode in complexes **4** and **5**. In contrast, the coordination numbers in **4** and **5** were found to be equal to eight. The lower coordination numbers were afforded by the replacement of the bidentate acetate groups in **1**–**3** with the acetate groups in the form η^1 in **4** and **5** (Figure 3.6f) [14,32].
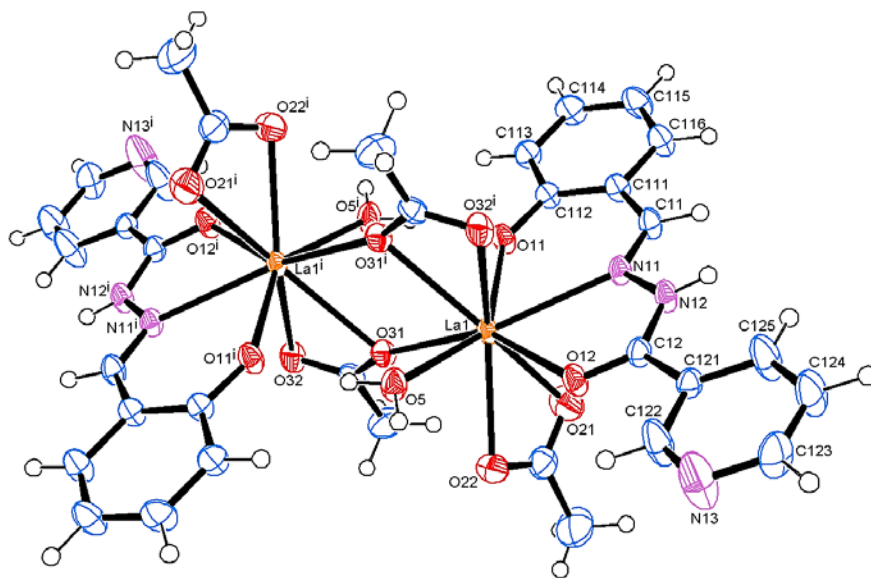
Figure 3.6b: The ORTEP plot of **2**, along with partial atom-numbering scheme, with 50 % thermal ellipsoids (lattice H_2O and DMF molecules are omitted for clarity).
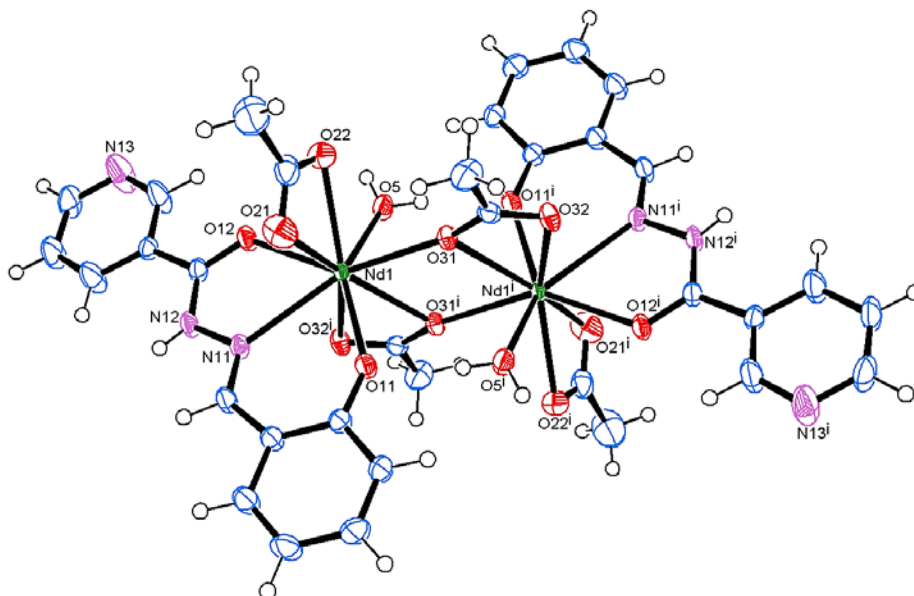
Figure 3.6c: The ORTEP drawing of **3** with partial atom-labelling (crystallographic H_2O and DMF molecules are omitted for clarity).
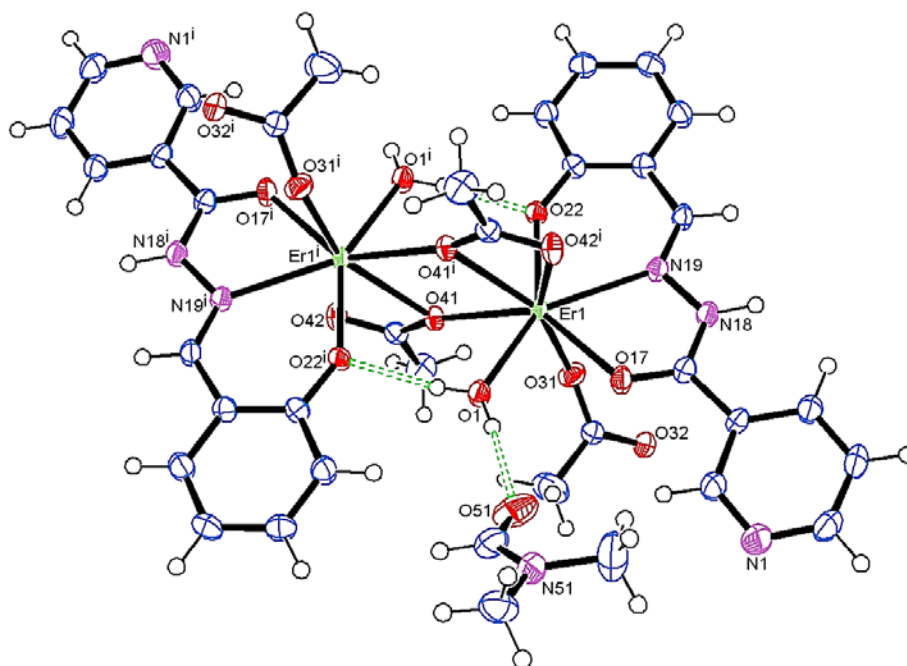
Figure 3.6d: The molecular structure and partial atom-labelling of **4** (50 % probability ellipsoids). The green dashed lines indicate hydrogen bonding (weak C-H⋯O contacts not shown).
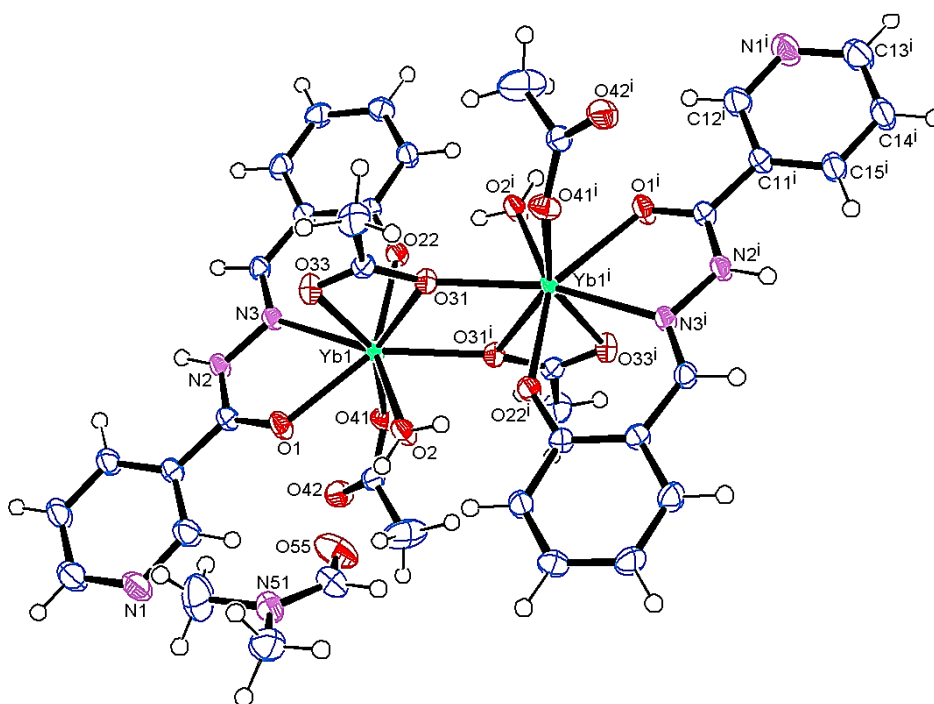
Figure 3.6e: The molecular structure of the Yb(III) complex displaying 50 % probability displacement ellipsoids and partial atom-labelling.

η^2 (bidentate) η^1:η^2:μ_2 (chelating/bridging) η^1 (monodentate)
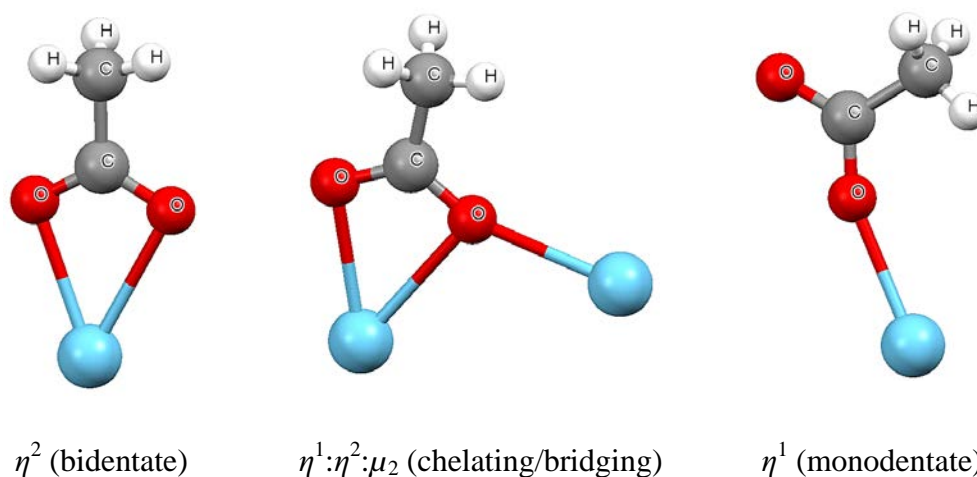
Figure 3.6f: The different binding modes of acetate groups (blue spheres = metal ions) [14,32].

Selected bond parameters of the compounds are listed in Table 3.5a. The Ln-O bond lengths in the hydrazone complexes are in the range 2.2037(16) to 2.7213(16) Å. The shortest Ln-O bonds are formed by the phenolato oxygen atoms [2.2037(16) to 2.3970(17) Å], suggesting their stronger binding, while the longest Ln-O bonds (weaker binding) are contributed by the bridging acetato oxygen atoms. The Ln-$O_{carbonyl}$ links lie in the range 2.3285(18) to 2.4982(12) Å and the Ln-N bonds vary from 2.4672(19) to 2.6927(17) Å. Coordination of water molecules result in average Ln-O bond lengths of approximately 2.4408 Å. The Ln···Ln distances have a linear decrease as the atomic number increases (ranging from 4.266 to 4.000 Å); the bridging angles (Ln1–$O_{bridging}$–Ln1A) are between 109.86(6)^o and 112.75(8)^o. The chelation of each hydrazone ligand produces one six membered (LnNCCCO) and a five membered (LnNNCO) chelate ring, with bite angles in the ranges 61.04(5) – 65.86(6)^o and 68.32(5) – 73.16(6)^o, respectively. Ligand bite angles increase with a decrease in the ionic radii, with a similar decrease in the Ln-O and Ln-N bond lengths being observed from La(III) to Yb(III), as expected due to the lanthanide contraction. It is noticed that changing the phenyl group of **H₂phen** (in **1**) to a pyridyl group in **H₂Nic** (in **2**) has no significant effect on bonding parameters and modes, although most of the corresponding bond distances in **2** are slightly shorter than in **1**.

Table 3.5a: Selected bond lengths and angles for compounds **1**–**5**.

1		2 (La)	3 (Nd)	4		5	
Bond lengths (Å)							
La1-O1	2.4865(16)	Ln1-O5	2.5462(14)	2.4781(14)	Er1-O1	2.330(2)	Yb1-O1	2.3285(18)
La1-O2	2.5441(17)	Ln1-O11	2.3956(12)	2.3451(13)	Er1-O17	2.339(2)	Yb1-O2	2.3055(17)
La1-O22	2.3970(17)	Ln1-O12	2.4982(12)	2.4477(13)	Er1-O22	2.218(2)	Yb1-O22	2.2037(16)
La1-O31	2.4886(15)	Ln1-O21	2.5455(16)	2.4851(17)	Er1-O31	2.231(3)	Yb1-O31	2.4865(18)
La1-O41	2.6188(18)	Ln1-O22	2.5925(14)	2.5458(14)	Er1-O41	2.328(2)	Yb1-O33	2.3712(19)
La1-O42	2.5404(19)	Ln1-O31	2.4910(11)	2.4393(13)	Er1-N19	2.479(2)	Yb1-O41	2.206(2)
La1-N3	2.6927(17)	Ln1-N11	2.6878(13)	2.6275(15)	Er1-O41a	2.501(2)	Yb1-N3	2.4672(19)
La1-O31a	2.7213(16)	Ln1-O31a	2.7122(12)	2.6504(13)	Er1-O42a	2.398(3)	Yb1-O31a	2.3179(16)
La1-O32a	2.5770(18)	Ln1-O32a	2.5753(13)	2.5171(13)	Er···Er	4.022 Å	Yb···Yb	4.000 Å
La···La	4.266 Å	Ln···Ln	4.257 Å	4.191 Å				
Bond angles (°)							
O1-La1-O22	129.47(5)	O11-Ln1-O12	129.70(4)	132.21(4)	O17-Er1-O22	137.96(7)	O1-Yb1-O22	138.86(6)
O1-La1-N3	61.17(5)	O11-Ln1-N11	68.66(4)	69.87(4)	O17-Er1-N19	65.49(7)	O1-Yb1-N3	65.86(6)
O22-La1-N3	68.32(5)	O12-Ln1-N11	61.04(4)	62.34(4)	O22-Er1-N19	72.64(7)	O22-Yb1-N3	73.16(6)
O31-La1-O31a	70.14(5)	O21-Ln1-O22	50.35(5)	51.49(5)	O41-Er1-O41a	67.25(7)	O31-Yb1-O33	53.21(6)
O41-La1-O42	50.18(6)	O31-Ln1-O31a	70.28(4)	69.19(4)	O41a-Er1-O42a	52.77(6)	O31-Yb1-O31a	67.31(6)
O31a-La1-O32a	48.74(5)	Ln1-O31-Ln1a	109.73(4)	110.81(5)	Er1-O41-Er1a	112.75(8)	Yb1-O31-Yb1a	112.69(7)
La1-O31-La1a	109.86(6)							

All bond parameters are normal and fall within similar ranges to those reported by Zhang *et al.* (2014) on dinuclear lanthanide complexes of Sm, Gd, Dy, Tm and Yb with the hydrazone ligand (*E*)-*N′*-(2-hydroxybenzylidene)-2-mercaptonicotinohydrazide) [14]. The Ln-O and Ln-N bond distances with this hydrazone were found to lie in the ranges 2.211(4) – 2.624(5) Å and 2.476(4) – 2.622(7) Å, respectively, whereas the Ln···Ln distances were observed between 4.0128(12) and 4.1802(10) Å [14]. Bond distances and angles are also comparable to lanthanide complexes derived from related hydrazone ligands, such as *N′*-(pyridin-2-ylmethylidene)benzohydrazide, 2-acetylpyridine nicotinohydrazone and (*E*)-*N′*-[1-(pyridin-2-yl)ethylidene]isonicotinohydrazide [11,12,33].

A lower coordination number was expected for the heavier lanthanides relative to their lighter counter-parts due to the smaller size of the Er(III) and Yb(III) ions compared to La(III) and Nd(III) ions. The +6 charge of the two Ln(III) ions in the

dinuclear complexes is therefore neutralised by two mono-deprotonated hydrazone molecules and four acetate groups. A comparison of the secondary coordination spheres of the complexes reveals crystallographic water and DMF molecules in **1**–**3**, and only one DMF molecule in the outer spheres of **4** and **5**. These lattice solvent molecules play a key role in stabilising the metal complexes through intermolecular hydrogen bonds [11].

Meticulous analysis of the X-ray diffraction data of the dinuclear complexes **1**–**5** show the existence of hydrogen bonding interactions of the type O-H⋯O and N-H⋯O (Figures 3.6a and 3.6d; Table 3.5b). The complexes are further stabilised by networks of weak non-covalent C-H⋯O interactions. In **1**–**3**, the O-H groups of the coordinated water molecules are hydrogen bonded to the phenolate *O*-atoms [-H⋯O; 1.965(18)–1.984(16) Å], as well as the *O*-atoms of the crystallographic DMF [-H⋯O; 1.887(16)–1.894(15) Å]. The other kinds of O-H⋯O hydrogen bonds are apparent between the –OH group of lattice water molecules, and the oxygen atoms of the chelating- and bridging-acetate groups as acceptors. In the La(III) and Nd(III) complexes, the N-H of the Schiff base ligands interacts with the *O*-atoms of the crystallographic water molecules [average -H⋯O = 1.98 Å].

The crystal structures of the Er(III) and Yb(III) complexes are also stabilised by classical hydrogen bonds (Figure 3.6d; Table 3.5b). The two types of hydrogen bonds existing in these complexes involve the –OH group of the coordinated water molecules as donors, and the oxygen atoms of the phenolate groups and the lattice DMF as acceptors. Hydrogen bonds of the N-H⋯O type in **4** and **5** are facilitated by the N-H of **H₂Nic** and the free oxygen of the monodentately coordinated acetate groups. Hydrogen bond geometries in **4** and **5** indicate *D*-H⋯*A* angles of 159(4) and 164(3)^{o}, respectively.

Table 3.5b: Hydrogen bond geometry (Å, °) in complexes **1–5**.

D-H⋯*A*	*D*-H	H⋯*A*	*D*⋯*A*	*D*-H⋯*A*
Complex 1				
N2-H2⋯O3	0.81(2)	2.01(2)	2.804(3)	169(3)
O2-H2A⋯O55	0.84(2)	1.892(19)	2.720(3)	171(3)
O2-H2B⋯O22	0.840(16)	1.965(18)	2.794(2)	169(3)
O3-H3A⋯O32	0.83(2)	1.94(2)	2.769(2)	175(2)
O3-H3B⋯O42	0.83(3)	1.88(3)	2.706(3)	176(3)
C4-H4⋯O3	0.95	2.48	3.277(3)	141
C12-H12⋯O1	0.95	2.42	2.746(3)	100
C16-H16⋯O3	0.95	2.36	3.292(3)	166
C52-H52C⋯O55	0.98	2.37	2.785(4)	104
C54-H54⋯O41	0.95	2.40	3.340(4)	168
Complex 2				
D-H⋯*A*	*D*-H	H⋯*A*	*D*⋯*A*	*D*-H⋯*A*
O5-H5A⋯O11	0.834(15)	1.984(16)	2.8078(16)	169(2)
O5-H5B⋯O4	0.833(16)	1.887(16)	2.713(2)	171(2)
O6-H6A⋯O21	0.840(2)	1.860(2)	2.699(2)	177(3)
O6-H6B⋯O32	0.840(2)	1.920(2)	2.7558(19)	173.4(19)
N12-H12⋯O6	0.840(2)	1.950(2)	2.7776(19)	169(2)
Complex 3				
D-H⋯*A*	*D*-H	H⋯*A*	*D*⋯*A*	*D*-H⋯*A*
O5-H5A⋯O11	0.833(14)	1.970(15)	2.7944(18)	170(2)
O5-H5B⋯O4	0.832(15)	1.894(15)	2.721(2)	173(3)
O6-H6A⋯O21	0.83(3)	1.86(3)	2.697(2)	176(2)
O6-H6B⋯O32	0.83(2)	1.94(2)	2.763(2)	173(2)
N12-H12⋯O6	0.81(2)	1.98(2)	2.777(2)	173(2)
Complex 4				
D-H⋯*A*	*D*-H	H⋯*A*	*D*⋯*A*	*D*-H⋯*A*
O1-H1A⋯O51	0.83(2)	1.92(2)	2.748(4)	175(3)
O1-H1B⋯O22	0.83(3)	1.95(3)	2.770(3)	169(3)
N18-H18⋯O32	0.98(4)	1.80(4)	2.735(3)	159(4)
Complex 5				
D-H⋯*A*	*D*-H	H⋯*A*	*D*⋯*A*	*D*-H⋯*A*
N2-H2⋯O42	0.90(3)	1.87(3)	2.743(3)	164(3)
O2-H2A⋯O55	0.838(15)	1.925(15)	2.761(3)	175(2)
O2-H2B⋯O22	0.831(17)	1.940(18)	2.762(2)	170(2)

D = donor, *A* = acceptor

3.4.6   Atomic charge analysis of the ligands

The electron distribution in the various sub-shells of the atomic orbitals of the hydrazone ligands was portrayed through the natural population analysis (NPA) method with B3LYP functional and aug-cc-pVTZ basis set (Figures 3.7a-d) [34-37]. The accumulation of charges on selected atoms and the accrual of electrons in the core, valence and Rydberg sub-shells are depicted in Table 3.6 [34]. The phenolate oxygen, the carbonyl oxygen and the azomethine nitrogen atoms were found to

accumulate the most electronegative charge of -0.79149, -0.67878 and -0.41671 in DMSO, respectively. A similar trend in the gas implies an order of bond lengths: Ln-$O_{phenolate}$ < Ln-$O_{carbonyl}$ < Ln-$N_{azomethine}$, as the most electronegative atoms are more inclined to donate electrons, based on the electrostatic characteristic of the compound [35]. All the hydrogen atoms are positively charged (in the range 0.10735–0.38076), as well as the carbon atoms (C5, C15 and C17) attached to electronegative atoms (O1, O2 and N3). The oxygen and nitrogen atoms withdraw electrons and hence, the electron population at C5, C15 and C17 is less and show a positive charge, with the highest positive charge accumulated on the carbon atom bonded to the phenolate oxygen. Natural population analysis also showed that the nitrogen and the aromatic carbon atoms (with the exception of C5) bear negative charges. The negative charges on the aromatic carbons are due to the aromatic π-electron system [38].
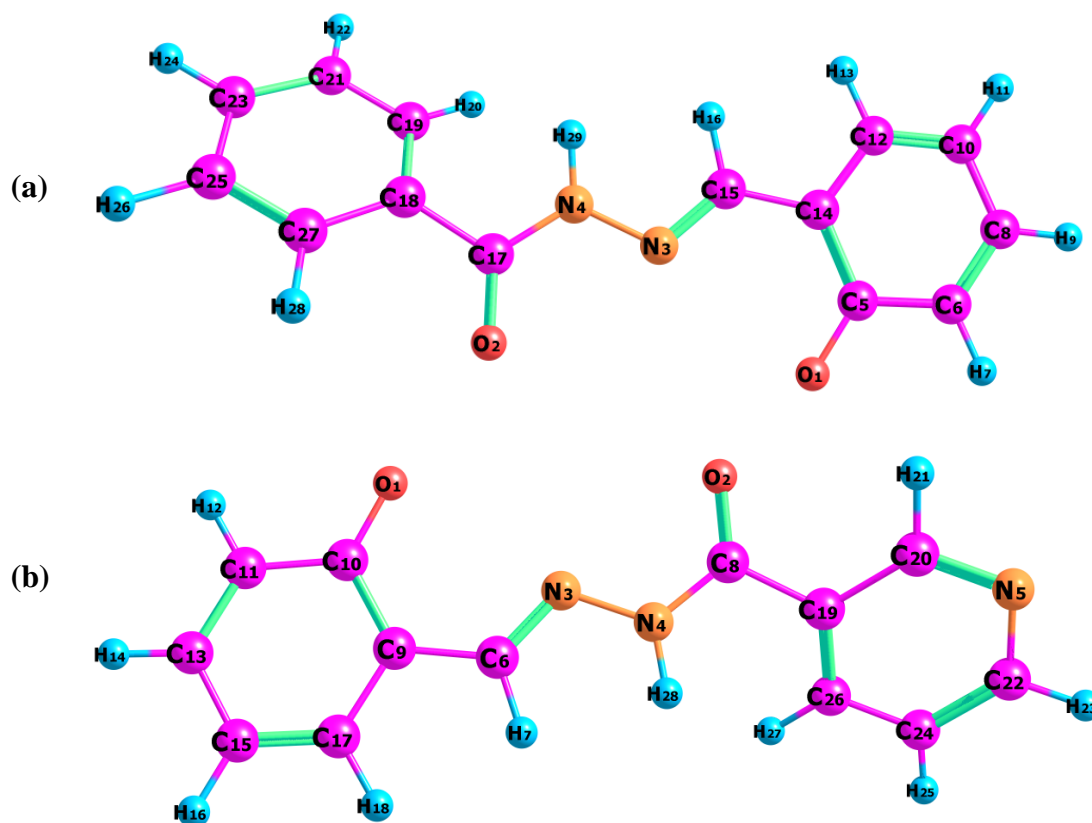
Figure 3.7a and 3.7b: Optimised molecular structures with atom-numbering scheme of: **(a) Hphen⁻** and **(b) HNic⁻**.
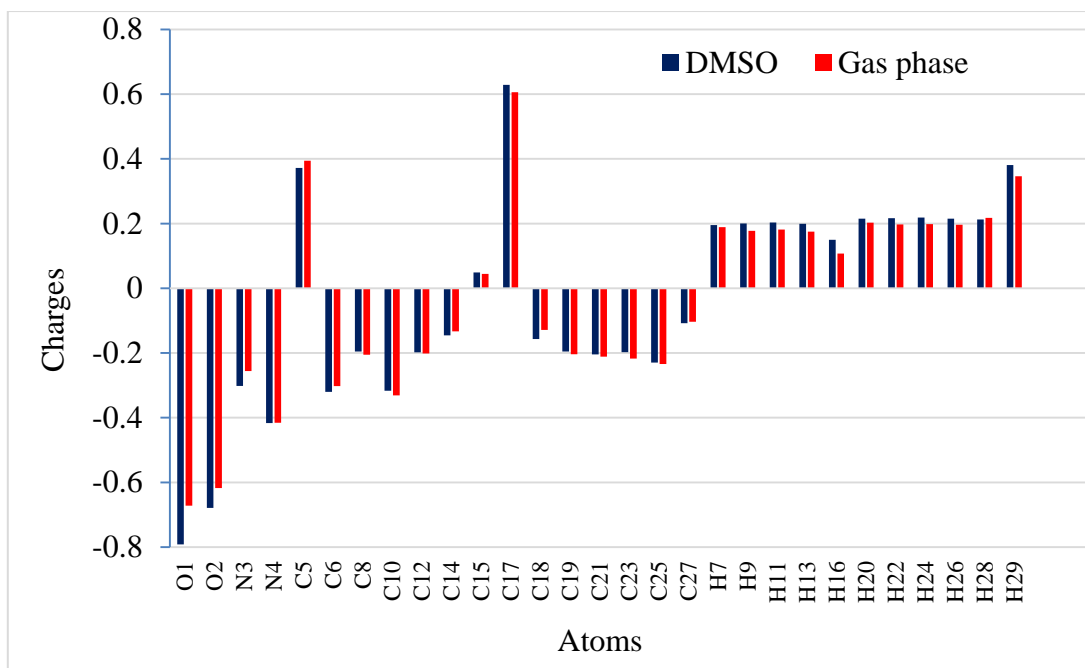
Figure 3.7c: The NPA atomic charge distribution of **Hphen⁻** in the gas phase and DMSO.
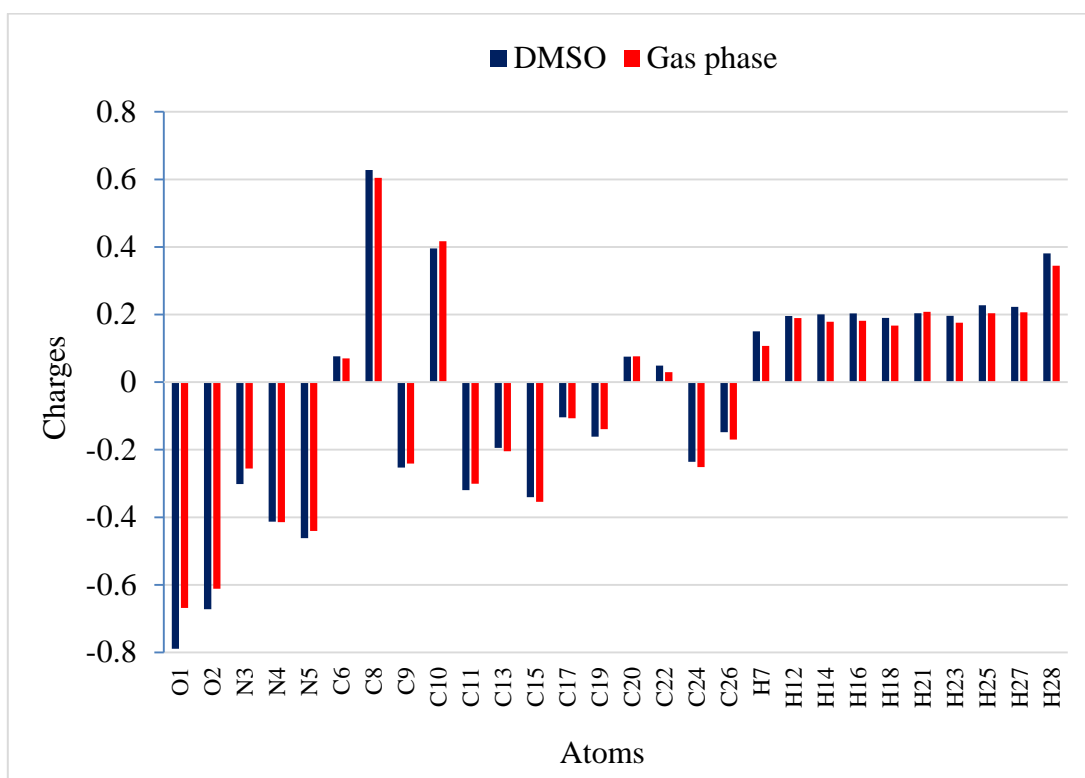
Figure 3.7d: The NPA plot for **HNic⁻** to indicate atomic charge distribution.

Table 3.6: Natural population analysis showing allotment of electrons between core, valence and Rydberg orbitals for selected atoms in hydrazone ligands in DMSO.

Atom	Charge	Core	Valence	Rydberg	Total
		H_2phen			
O1	-0.79149	2.00000	6.76831	0.02319	8.79149
O2	-0.67878	2.00000	6.65425	0.02454	8.67878
N3	-0.30206	1.99999	5.26364	0.03843	7.30206
N4	-0.41671	1.99999	5.39130	0.02542	7.41671
C6	-0.32031	1.99999	4.29838	0.02195	6.32031
C17	0.62867	1.99999	3.33424	0.03710	5.37133
H16	0.14966	0.00000	0.84644	0.00389	0.85034
H29	0.38076	0.00000	0.61524	0.00400	0.61924
Core	35.99980 (99.9995 % of 36)				
Valence	89.49428 (99.4381 % of 90)				
Rydberg	0.50592 (0.4015 % of 126)				
		H_2Nic			
Atom	**Charge**	**Core**	**Valence**	**Rydberg**	**Total**
O1	-0.78912	2.00000	6.76603	0.02309	8.78912
O2	-0.67210	2.00000	6.64768	0.02442	8.67210
N3	-0.30186	1.99999	5.26461	0.03726	7.30186
N4	-0.41296	1.99999	5.38761	0.02535	7.41296
N5	-0.46203	1.99999	5.42557	0.03646	7.46203
C8	0.62786	1.99999	3.33656	0.03559	5.37214
C15	-0.34043	-0.34043	1.99999	4.30906	0.03138
H7	0.15024	0.00000	0.84581	0.00395	0.84976
H28	0.38095	0.00000	0.61501	0.00404	0.61905
Core	35.99981 (99.9995 % of 36)				
Valence	89.48535 (99.4282 % of 90)				
Rydberg	0.51484 (0.4086 % of 126)				

All the hydrogen and carbon atoms (bonded to electronegative *O-* and *N*-atoms), namely C6, C8, C10, C20 and C22 in H_2Nic were predicted through NPA to have a net positive charge [36,37]. The electron deficiency (positive charge) on these carbon atoms is a result of the withdrawal of electrons by nitrogen and oxygen atoms, and hence the electron population is less. It is noted that the most negative load (-0.78912) is located on the phenolate oxygen atom. Single-crystal X-ray diffraction studies of the complexes confirmed participation of the phenolate *O*-atoms (as acceptors) of both **H_2phen** and **H_2Nic** in hydrogen bond formation with water and crystallographic DMF molecules, thus further stabilising the coordination compounds (Table 3.5b) [36]. These phenolate oxygens give the shortest bond lengths with the metal ions due to the highest charge density, compared to the carbonyl oxygen and azomethine nitrogen atoms that also possess negative charges [39]. All the nitrogen atoms (N3,

N4 and N5) bear negative atomic charge, with the pyridyl nitrogen (N5) having the largest negative charge in comparison to the other *N*-atoms. The pyridyl nitrogen atom, however, does not coordinate due to its unfavourable configuration that does not promote selectivity, brought about by formation of stable 5- or 6-membered rings [40]. The remaining atoms C9, C11, C13, C15, C17, C19, C24 and C26 show negative partial charges over them. The sum of the natural charges for both hydrazone ligands was found to be -1.00000, thus confirming deprotonation to give phenolate groups.

Figures 3.7e and 3.7f illustrate the molecular electrostatic potential (MEP) isosurfaces for the deprotonated hydrazone ligands, **Hphen⁻** and **HNic⁻**, which are useful in reactivity studies and in depicting molecular shape and size [41]. The MEP maps of both hydrazones indicate negative charge regions (red and yellow) that show electrophilic reactivity; these regions covered the phenolate and carbonyl oxygens, and the azomethine nitrogen atoms [39,42]. The phenolate oxygen atom is the most electronegative, and is therefore anticipated to be the most reactive part in these Schiff bases. The hydrazone MEP thus supports the *O,N,O*-donor behaviour of the Schiff bases, and takes into consideration the unfavourable orientation of the pyridyl *N*-atom of **HNic⁻** for coordination [40]. From the MEP maps, it is observed that the positive (blue) regions are distributed over the hydrogen atoms, with these expected to exhibit nucleophilic reactivity [42].

It is important to note that the phenolate rings of both ligands are more electron-rich compared to the phenyl ring of **Hphen⁻** or the pyridyl ring of **HNic⁻**. This can be ascribed to the negative charge on the anionic phenolate ring being delocalised throughout the ring through resonance to ensure stabilisation [38]. For **HNic⁻**, the electron density is not evenly distributed over the pyridyl ring due to the negative inductive effect of the electronegative sp^2-hybridised nitrogen atom [38,43]. Furthermore, the nitrogen lone electron pair is not part of the aromatic π-system, resulting in less resonance stabilisation, or a π-deficient system [38,43].
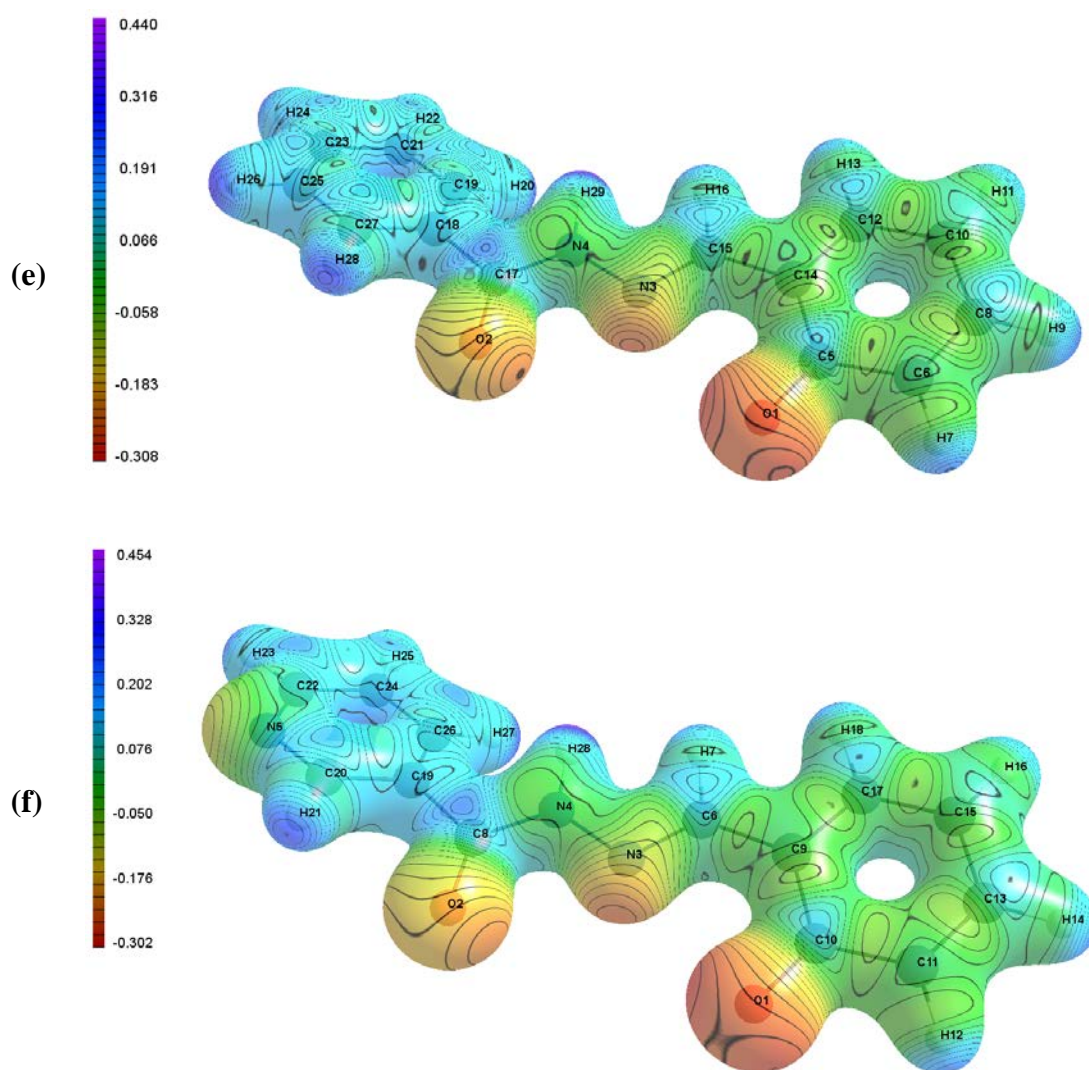
Figures 3.7e and 3.7f: Calculated MEP map of: **(e) Hphen⁻** and **(f) HNic⁻**. The MEP partial charges are coloured, based on the gradient indicated to the left of each ligand. The maps were drawn using an isovalue of 0.05.

An investigation into the electrophilic and nucleophilic regions of potential anticancer drugs is vital in elucidating hydrogen bond interactions, nucleophilic and electrophilic reactions involving the anticancer agent, DNA (or enzymes) and the solvent medium [44].

3.4.7 Frontier molecular orbital analysis and global and chemical reactivity descriptors

Frontier molecular orbital (FMO) analysis helps in explaining stability, energy transfer and chemical reactivity in the molecule [45-48]. According to the Koopmans theorem, the energies of the highest occupied molecular orbitals (*HOMO*) and lowest unoccupied molecular orbitals (*LUMO*) are directly related to the ionisation potential and electron affinity, respectively [45-47]. The *HOMO–LUMO* energy gap is responsible for the strength and stability of the compounds, as well as elucidating coordination properties. A large intermolecular charge transfer in the molecule or chemical reactivity is indicated by small energy gaps [45,47].

The *HOMO* and *LUMO* of **HNic⁻** is better stabilised compared to **Hphen⁻**. The *HOMO–LUMO* energy gap of **Hphen⁻** (3.347 eV) is higher than that of **HNic⁻** (3.180 eV) (Figures 3.8a and 3.8b). The energy gaps of the *HOMO-LUMO* vicinal molecular orbitals (*HOMO*-1 and *LUMO*+1) are calculated to be 5.057 and 4.629 eV for **Hphen⁻** and **HNic⁻**, respectively. These results therefore depict better stabilisation of both the *HOMO* and *LUMO* of **HNic⁻** compared to **Hphen⁻** [46,47].

The stability, optical polarisability and reactivity of the hydrazone ligands were defined using chemical and global reactivity descriptors, based on the energies of the transition levels of the FMOs (Table 3.7). The slightly lower ionisation potential value of **Hphen⁻** (4.871 eV) compared to **HNic⁻** (4.898 eV) shows that **Hphen⁻** is a better electron donor [45,49]. To gain insight into the behaviour of the hydrazone chemical systems, hardness and softness calculations revealed that **Hphen⁻** has a higher hardness value (η = 1.674 eV) whilst **HNic⁻** possesses a larger softness value of 0.629 eV^{-1}. As a softer molecule, **HNic⁻** is thus expected to be more polarisable than **Hphen⁻** [45,46,49].
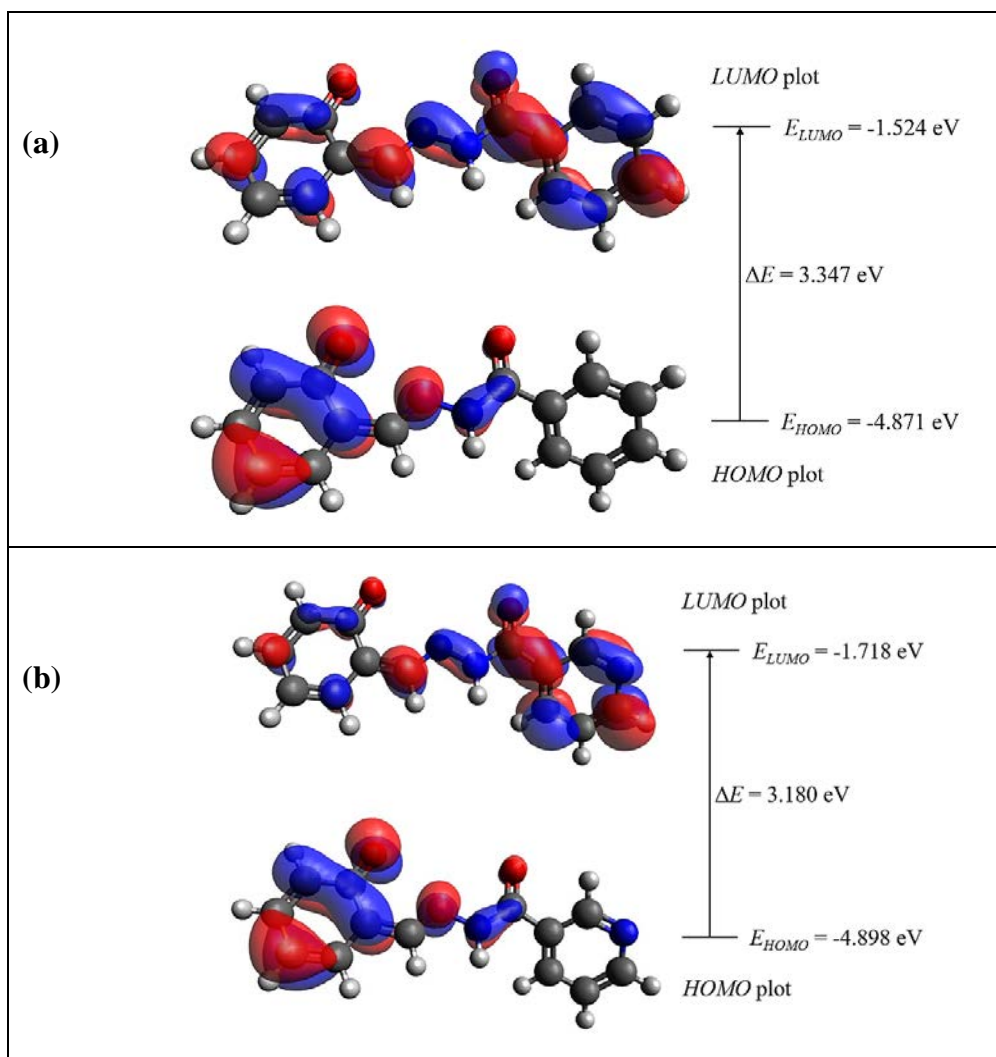
Figures 3.8a and 3.8b: The frontier molecular orbitals plot of: **(a) Hphen⁻** and **(b) HNic⁻** calculated at B3LYP/aug-cc-pVTZ in the solvent (DMSO), indicating *HOMO-LUMO* energy gaps. The orbital surfaces were generated using an isovalue of 0.03.

The chemical potentials of the Schiff bases are negative (**Hphen⁻** = -3.198 eV; **HNic⁻** = -3.308 eV), showing that the compounds are stable and do not decompose spontaneously into constituent elements [45,46,49]. When the system is saturated by electrons from the external environment, **Hphen⁻** has a tendency to act as a better and more reactive nucleophile (lower electrophilicity (ω) of 3.055 eV), while **HNic⁻** is a better electrophile due to its higher ω-value [45,46,50]. Through analysis of the electrophilicity index values, the toxicities of the compounds in biological activity can be predicted or estimated since toxicity is reasonably correlated with electrophilicity

[49-51]. A compound with a low electrophilicity index is anticipated to have less toxicity [49-51].

Table 3.7: Global and chemical parameters of **Hphen**⁻ and **HNic**⁻.

		Hphen⁻	HNic⁻
Global and chemical reactivity descriptor	**Symbols**	**Values (eV)**	**Values (eV)**
Energy of *HOMO*	E_{HOMO}	−4.871	−4.898
Energy of *LUMO*	E_{LUMO}	−1.524	−1.718
Energy of *HOMO*-1	$E_{HOMO\text{-}1}$	−5.822	−5.848
Energy of *LUMO*+1	E_{LUMO+1}	−0.765	−1.219
Energy of *HOMO*-2	$E_{HOMO\text{-}2}$	−6.154	−6.196
Energy of *LUMO*+2	E_{LUMO+2}	−0.680	−0.832
First energy gap	$\Delta E = LUMO - HOMO$	3.347	3.180
Second energy gap	$\Delta E = LUMO+1 - HOMO\text{-}1$	5.057	4.629
Third energy gap	$\Delta E = LUMO+2 - HOMO\text{-}2$	5.474	5.364
Ionisation energy (I)	$-E_{HOMO}$	4.871	4.898
Electron affinity (A)	$-E_{LUMO}$	1.524	1.718
Hardness (η)	$\dfrac{(I-A)}{2}$	1.674	1.590
Chemical potential (μ)	$\dfrac{-(I+A)}{2}$	−3.198	−3.308
Softness (σ)	$\dfrac{1}{\eta}$	0.597	0.629
Electrophilicity index (ω)	$\dfrac{\mu^2}{2\eta}$	3.055	3.441
Electronegativity (χ_m)	$\dfrac{I+A}{2}$	3.198	3.308

Softness (σ) values are in eV^{-1}.

3.4.8   Anticancer screen

The free hydrazone ligands, lanthanide acetate salts and Ln(III)-hydrazone complexes were screened for cytotoxicity using the MTT assay, against MCF-7, HEC-1A and THP-1 cells (Figure 3.9). Cytotoxicity analysis of the compounds was accomplished by exposing the cells to 100 μM of the organic and coordination compounds for 24

hours, followed by evaluation of mitochondrial enzymatic reduction of MTT to formazan [52]. A compound is considered cytotoxic if a standard concentration of 100 μM reduces the viability of cells or growth of cells to 50 % or less [52].

The viability (set at 100 %) of all three cancer cell lines were not affected and were considered as having 100 % cell viability after exposure to 0.1 % DMSO vehicle control. The cells were treated with 100 μM $[La(OAc_3)_3 \cdot xH_2O]$, $[Nd(OAc_3)_3 \cdot xH_2O]$, $[Er(OAc_3)_3 \cdot xH_2O]$ and $[Yb(OAc_3)_3 \cdot 4H_2O]$ for 24 hours. None of the tested metal salts exhibited statistically significant increases in cytotoxicity, with the $[La(OAc_3)_3 \cdot xH_2O]$ treatment significantly resulting in increase in THP-1 cell proliferation (122.0 ± 12.76 %, $p < 0.05$). No cytotoxic effects were observed in THP-1 cells ($p > 0.05$) for all the tested compounds (free ligands, metal salts and complexes) (Figure 3.9).
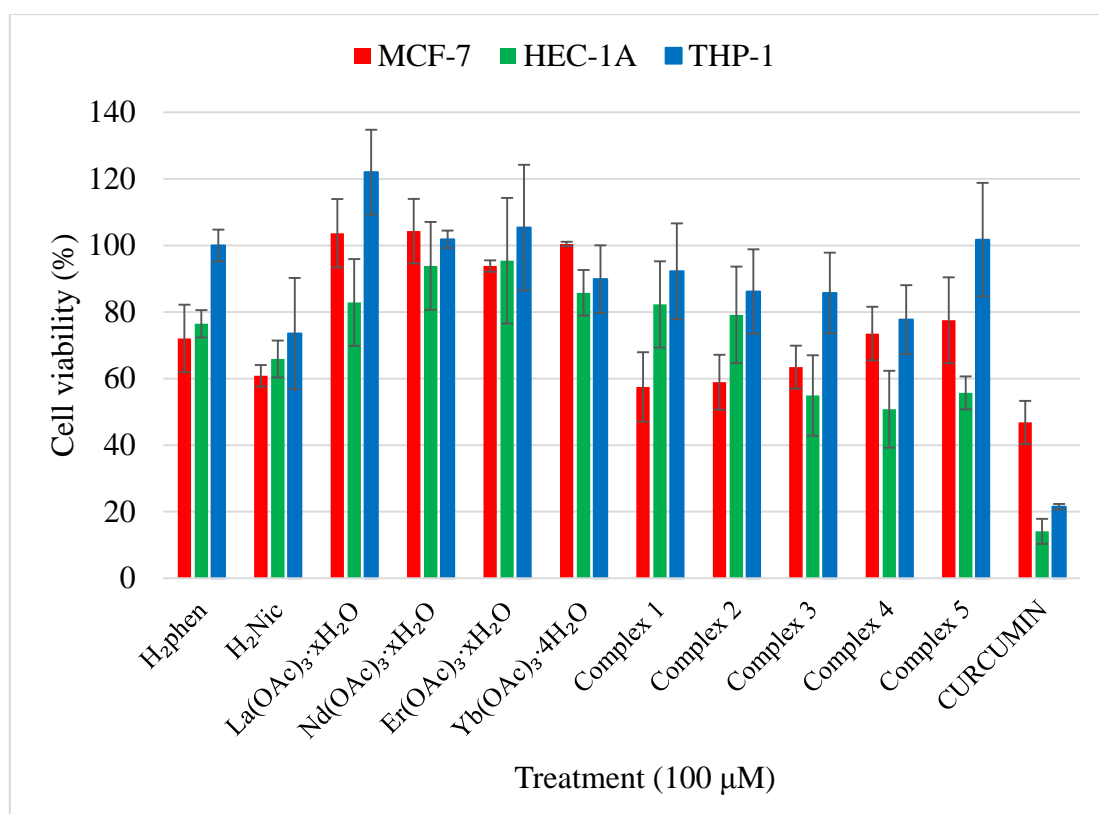
Figure 3.9: Cytotoxic effects of the compounds on MCF-7, HEC-1A and THP-1 cells using the MTT assay. Mean values of three independent experiments ± SD are shown.

In the MCF-7 cell line, cell viability was significantly reduced ($p<0.05$) after 24 hours of exposure to 100 μM of **H₂phen**, **H₂Nic** and complexes **1**–**4**. The results also indicated that the cytotoxicity of **1**–**3** is similar to that of the positive control (curcumin) in MCF-7 cells ($p>0.05$), with approximately 50 % inhibition achieved. The inhibitory effects of the compounds are in the order: curcumin ≈ **1** ≈ **2** > **H₂Nic** > **3** > **4** ≈ **H₂phen**. The ligand **H₂Nic** exhibits greater toxicity compared to **H₂phen** in all three cell lines. One of the factors that might be responsible for such activity is the presence of the pyridyl moiety in **H₂Nic** [53,54]. Higher biological activity for **H₂Nic** relative to **H₂phen** can also be related to the higher electrophilicity of **HNic⁻** (ω = 3.441 eV) than **Hphen⁻** (ω = 3.055 eV). Electrophilicity is an important electronic parameter in the stabilisation of drugs in the active sites, as well as in the reactions with nucleophilic sites in macromolecules (such as DNA or proteins) and eventually leading to cytotoxicity [55,56].

Compounds **3**, **4**, **5**, **H₂phen** and **H₂Nic** exerted cytotoxic effects in HEC-1A cells ($p<0.05$), while **3**–**5** have similar cytotoxicity against this cancer cell line ($p<0.05$) (~50 % inhibition at 100 μM). The inhibitory effects exerted by the free hydrazone ligands and the coordination complexes **3** and **4** occur in both MCF-7 and HEC-1A cell lines, but not in THP-1 cells. This infers that hormone-responsive (estrogen-dependent) breast and endometrial cancer cell lines could be sensitive to these compounds [57-59]. Further testing is thus needed to confirm the sensitivity of the hormone-dependent cells to the compounds. The lanthanum(III) complexes **1** and **2** were, however, selectively toxic towards MCF-7 cells and not HEC-1A or THP-1 cells. In the HEC-1A and THP-1 cell lines, curcumin significantly reduced cell viability over 24 hours ($p<0.05$), with cell viability reduced to 14.1±3.76 % and 21.5±0.83 %, respectively.

3.5   Conclusion

Metal complexes of **H₂phen** and **H₂Nic** were successfully isolated, in which the monodeprotonated hydrazones acted as *O,N,O*–donor ligands, and three coordination modes η^2, η^1:η^2:μ_2 and η^1 were revealed for the acetate groups. The formation of the

compounds was further ascertained by melting points, elemental analysis, IR, NMR and UV-Vis spectroscopy studies.

The ligands and lattice solvents of the metal complexes contain distinct oxygen and nitrogen atoms that were found to play an important role in stabilisation of the crystal structure through hydrogen bond formation. It is therefore worthwhile investigating which of the atoms significantly affect the functioning of the anticancer agents.

Natural population analysis was performed on ligands in DMSO and gas. This is important in understanding chemical reactivity, and predicting the formation of hydrogen bonding that plays a role in the stabilisation of the crystal structure [36]. Regarding the atomic charges on hydrazone ligands, the lowest charges were found on $O_{phenolate}$, $O_{carbonyl}$ and $N_{azomethine}$ atoms. This gave rise to tridentate *O,N,O*-donor chelates, comprising of five- and six-ring stable complexes. Molecular electrostatic potential analysis was used in characterisation of electron-deficient and electron-rich regions of hydrazone systems, to decipher molecular reactivity.

The results obtained show that the lanthanide metal salts are not cytotoxic in the three cancer cell lines studied. It is therefore concluded that complexation of the metals with the hydrazones can be a way of reducing cancer cell viability as shown by improved cytotoxicity of complex **1** compared to **H₂phen** against MCF-7 cells. The biological studies clearly show that the hydrazone ligands and complexes **1**–**4** are partially cytotoxic against MCF-7 cells, while the free ligands and **3**–**5** inhibit cell growth in HEC-1A cells. The *in vitro* cytotoxicity also revealed no activity of all the compounds against THP-1 cells – no adverse effect on the monocytic cells of the immune system. None of the compounds tested were as effective as curcumin in reducing viability of the three cancer cell lines.

Redesigning and developing other hydrazone-derived lanthanide complexes with mechanisms of action that are distinct from the known and synthesised compounds will lead to novel compounds with an enhanced cytotoxic profile. This can be

achieved through substitution of some substituents on the ligands, or by constructing an entirely new hydrazone compound.

3.6 Supplementary information

3.6.1 Crystallographic data

Table S3.1a: Crystal and structure refinement data for complexes **1**–**3**.

	1	**2**	**3**
Formula	$C_{36}H_{38}La_2N_4O_{14}$, $2(C_3H_7NO)$, $2(H_2O)$	$C_{34}H_{36}La_2N_6O_{14}$, $2(C_3H_7NO)$, $2(H_2O)$	$C_{34}H_{36}N_6Nd_2O_{14}$, $2(C_3H_7NO)$, $2(H_2O)$
M_r (g.mol^{-1})	1210.75	1212.73	1223.39
Crystal system	Triclinic	Triclinic	Triclinic
Space group	*P-1* (No. 2)	*P-1* (No. 2)	*P-1* (No. 2)
a, b, c [Å]	8.3667(4), 12.4857(6), 12.5934(5)	8.3393(5), 12.3411(6), 12.4739(6)	8.2828(3), 12.3706(4), 12.3775(4)
α, β, γ (°)	80.688(2), 73.428(2), 89.374(2)	78.960(5), 74.105(2), 89.365(2)	79.081(2), 89.320(2), 74.046(2)
V (Å^3)	1243.43(10)	1210.67(11)	1196.23(7)
Z	1	1	1
ρ (g.cm^{-3})	1.617	1.663	1.698
μ (mm^{-1})	1.771	1.820	2.227
$F(000)$	608	608	614
Crystal size (mm)	$0.07 \times 0.10 \times 0.29$	$0.13 \times 0.16 \times 0.38$	$0.11 \times 0.13 \times 0.32$
Temperature (K)	200	200	200
Mo *Kα* radiation, λ (Å)	0.71073	0.71073	0.71073
θ (min-max) (°)	2.2, 28.3	1.7, 28.3	1.7, 28.3
Data set	-11≤*h*≤11; -16≤*k*≤16; -16≤*l*≤16	-11≤*h*≤11; -16≤*k*≤16; -16≤*l*≤16	-11≤*h*≤11; -16≤*k*≤16; -16≤*l*≤16
Tot., Unique data, R_{int}	32850, 6110, 0.026	53560, 6013, 0.018	54258, 5936, 0.026
Observed [I>2σ(I)] reflections	5476	5697	5539
$N_{reflections}$, $N_{parameters}$	6110, 331	6013, 331	5936, 331
$R[F^2>2\sigma(F^2)]$, $wR(F^2)$, S	0.0250, 0.0548, 1.04	0.0166, 0.0415, 1.06	0.0169, 0.0413, 1.05
$\Delta\rho_{min}$, $\Delta\rho_{max}$ (e.Å^{-3})	-0.49, 2.10	-0.32, 1.32	-0.37, 1.10

Table S3.1b: Crystal data and structure refinement parameters of **4** and **5**.

	4	5
Formula	**$C_{34}H_{36}Er_2N_6O_{14}$, 2($C_3H_7NO$)**	**$C_{34}H_{36} N_6O_{14}Yb_2$, 2($C_3H_7NO$)**
M_r (g.mol^{-1})	1233.40	1244.96
Crystal system	Monoclinic	Monoclinic
Space group	$P2_1/c$ (No. 14)	$P2_1/c$ (No. 14)
a, b, c [Å]	11.427(5), 19.168(8), 11.077(5)	11.3880(4), 19.2010(7), 11.1177(4)
α, β, γ (°)	90, 113.066(16), 90	90, 113.438(2), 90
V (Å^3)	2232.3(17)	2230.43(14)
Z	2	2
ρ (g.cm^{-3})	1.835	1.854
μ (mm^{-1})	3.814	4.247
F(000)	1220	1228
Crystal size (mm)	$0.19 \times 0.25 \times 0.33$	$0.18 \times 0.44 \times 0.44$
Temperature (K)	200	200
Mo $K\alpha$ radiation, λ (Å)	0.71073	0.71073
θ (min-max) (°)	2.1, 28.4	1.9, 28.3
Data set	$-14 \leq h \leq 15$; $-25 \leq k \leq 25$; $-14 \leq l \leq 14$	$-15 \leq h \leq 15$; $-25 \leq k \leq 25$; $-14 \leq l \leq 14$
Tot., Unique data, R_{int}	40750, 5559, 0.035	31541, 5559, 0.020
Observed [I>2σ(I)] reflections	4688	5205
$N_{reflections}$, $N_{parameters}$	5559, 314	5559, 302
$R[F^2>2\sigma(F^2)]$, $wR(F^2)$, S	0.0222, 0.0490, 1.06	0.0187, 0.0430, 1.11
$\Delta\rho_{min}$, $\Delta\rho_{max}$ (e.Å^{-3})	-0.63, 0.79	-1.33, 1.43

3.6.2 Molecular modelling data

Table S3.2a: Natural population analysis of **Hphen⁻** at the DFT/B3LYP level using the aug-cc-pVTZ basis set in the gas phase and DMSO.

Atoms	Natural charge (DMSO)	Population	Natural charge (gas)	Population
O1	-0.79149	8.79149	-0.67173	8.67173
O2	-0.67878	8.67878	-0.61767	8.61767
N3	-0.30206	7.30206	-0.25572	7.25572
N4	-0.41671	7.41671	-0.41573	7.41573
C5	0.37205	5.62795	0.39423	5.60577
C6	-0.32031	6.32031	-0.30227	6.30227
C8	-0.19554	6.19554	-0.20531	6.20531
C10	-0.31690	6.31690	-0.33125	6.33125
C12	-0.19802	6.19802	-0.20159	6.20159
C14	-0.14536	6.14536	-0.13297	6.13297
C15	0.04893	5.95107	0.04441	5.95559
C17	0.62867	5.37133	0.60581	5.39419
C18	-0.15696	6.15696	-0.12877	6.12877
C19	-0.19570	6.19570	-0.20415	6.20415
C21	-0.20441	6.20441	-0.21130	6.21130
C23	-0.19746	6.19746	-0.21751	6.21751
C25	-0.22968	6.22968	-0.23404	6.23404
C27	-0.10773	6.10773	-0.10346	6.10346
H7	0.19554	0.80446	0.18900	0.81100
H9	0.20030	0.79970	0.17770	0.82230
H11	0.20344	0.79656	0.18162	0.81838
H13	0.19910	0.80090	0.17514	0.82486
H16	0.14966	0.85034	0.10735	0.89265
H20	0.21535	0.78465	0.20254	0.79746
H22	0.21665	0.78335	0.19721	0.80279
H24	0.21871	0.78129	0.19809	0.80191
H26	0.21532	0.78468	0.19655	0.80345
H28	0.21264	0.78736	0.21774	0.78226
H29	0.38076	0.61924	0.34606	0.65394
Total	**-1.00000**	**126.00000**	**-1.00000**	**126.00000**

Table S3.2b: Natural population analysis of **HNic⁻** at the DFT/B3LYP level using the aug-cc-pVTZ basis set in the gas phase and DMSO.

Atoms	Natural charge (DMSO)	Population	Natural charge (gas)	Population
O1	-0.78912	8.78912	-0.66858	8.66858
O2	-0.67210	8.67210	-0.61141	8.61141
N3	-0.30186	7.30186	-0.25597	7.25597
N4	-0.41296	7.41296	-0.41435	7.41435
N5	-0.46203	7.46203	-0.44067	7.44067
C6	0.07621	5.92379	0.07010	5.92990
C8	0.62786	5.37214	0.60434	5.39566
C9	-0.25310	6.25310	-0.24109	-6.24109
C10	0.39577	5.60423	0.41700	5.58300

………**Table S3.2b continued**

Atoms	Natural charge (DMSO)	Population	Natural charge (gas)	Population
C11	-0.31952	6.31952	-0.30080	6.30080
C13	-0.19460	6.19460	-0.20452	6.20452
C15	-0.34043	6.34043	-0.35421	6.35421
C17	-0.10430	6.10430	-0.10688	6.10688
C19	-0.16145	6.16145	-0.13923	6.13923
C20	0.07546	5.92454	0.07627	5.92373
C22	0.04905	5.95095	0.02933	5.97067
C24	-0.23563	6.23563	-0.25145	6.25145
C26	-0.14799	6.14799	-0.17024	6.17024
H7	0.15024	0.84976	0.10730	0.89270
H12	0.19558	0.80442	0.18937	0.81063
H14	0.20067	0.79933	0.17850	0.82150
H16	0.20306	0.79694	0.18164	0.81836
H18	0.19011	0.80989	0.16706	0.83294
H21	0.20370	0.79630	0.20784	0.79216
H23	0.19623	0.80377	0.17592	0.82408
H25	0.22736	0.77264	0.20363	0.79637
H27	0.22283	0.77717	0.20667	0.79333
H28	0.38095	0.61905	0.34440	0.65560
Total	-1.00000	126.00000	-1.00000	126.00000

3.6.3   Anticancer activity tests

Table S3.3: Summary of cytotoxicity of the hydrazone ligands and five metal complexes.

Compound (100 μM)	Cells		
	MCF-7	**HEC-1A**	**THP-1**
	Cell viability (%)		
La(OAc$_3$)$_3$·xH$_2$O	103.7±10.28	82.87±13.03	122.0±12.76
Nd(OAc$_3$)$_3$·xH$_2$O	104.3±9.69	93.87±13.18	101.9±2.62
Er(OAc$_3$)$_3$·xH$_2$O	93.8±1.70	95.4±18.87	105.4±18.88
Yb(OAc$_3$)$_3$·4H$_2$O	100.5±0.65	85.8±6.85	89.9±10.16
H$_2$phen	72.1±10.17	76.5±4.11	100.0±4.75
H$_2$Nic	60.8±3.24	65.9±5.55	73.5±16.71
Complex **1**	57.5±10.44	82.3±12.96	92.3±14.38
Complex **2**	58.9±8.26	79.1±14.51	86.1±12.70
Complex **3**	63.4±6.44	54.9±12.07	85.7±12.13
Complex **4**	73.5±8.04	50.8±11.54	77.8±10.34
Complex **5**	77.5±12.90	55.7±4.95	101.8±17.06
CURCUMIN	46.8±6.46	14.1±3.76	21.5±0.83

3.7   References

[1]   S. Padhye, Z. Afrasiabi, E. Sinn, J. Fok, K. Mehta and N. Rath, "Antitumor metallothiosemicarbazonates: Structure and antitumor activity of palladium complex of phenanthrenequinone thiosemicarbazone", *Inorg. Chem.*, **44** (2005) 1154–1156.

[2]   K.B. Gudasi, R.V. Shenoy, R.S. Vadavi, M.S. Patil, S.A. Patil, R.R. Hanchinal, S.A. Desai and H. Lohithaswa, "Lanthanide(III) and yttrium(III) complexes of benzimidazole-2-acetic acid: Synthesis, characterisation and effect of La(III) complex on germination of wheat", *Bioinorg. Chem. Applic.*, **2006** (2006) 1–8.

[3]   U. Ndangi, N. Mhlongo and M.E. Soliman, "Metal complexes in cancer therapy – an update from drug design perspective", *Drug Des. Dev. Ther.*, **11** (2017) 599–616.

[4]   M.N. Gueye, M. Dieng, I.E. Thiam, D. Lo, A.H. Barry, M. Gaye and P. Retailleau, "Lanthanide(III) complexes with tridentate Schiff base ligand, antioxidant activity and X-ray crystal structures of the Nd(III) and Sm(III) complexes", *S. African. J. Chem.,* **70** (2017) 8–15.

[5]   V.C. Havanur, D.S. Badiger, S.G. Ligade and K.B. Gudasi, "Synthesis, characterization and antimicrobial study of lanthanide(III) complexes of 2-anilino-*N'*-[pyridine-2-ylethylidene]acetohydrazide", *Der Pharma Chemica*, **3** (2011) 292–304.

[6]   F.-Y. Chen and S.-Y. He, "Studies on lanthanide(III) ternary mixed ligand complexes with *N*-(2-propionic acid)-salicyloyl hydrazone and isonicotinic acid: Synthesis, characterization, and antibacterial activities", *Synthesis and Reactivity in Inorganic, Metal-Organic, and Nano-Metal Chemistry*, **38** (2008) 642–646.

[7]   B. Moksharagni and K. Hussain Reddy, "A review on pharmaceutical applications of lanthanide complexes with nicotinoyl and isonicotinoyl hydrazones", *EJBPS*, **5** (2018) 810–817.

[8]   M.A. Fernández, J.C. Barona, D. Polo-Cerón and Manuel N. Chaur, "Photochemical and electrochemical studies on lanthanide complexes of 6-(hydroxymethyl)pyridine-2-carboxaldehyde[2-methyl-pyrimidine-4,6-diyl]bis-hydrazone", *Rev. Colomb. Quim*, **43** (2014) 5–11.

[9]   F.R. Pavan, P.I. da S. Maia, S.R.A. Leite, V.M. Deflon, A.A. Batista, D.N. Sato, S.G. Franzblau and C.Q.F. Leite, "Thiosemicarbazones, semicarbazones, dithiocarbazates and hydrazide/hydrazones: Anti–mycobacterium tuberculosis activity and cytotoxicity", *Eur. J. Med. Chem.*, **45** (2010) 1898–1905.

[10]   H. Qu, X. Yu, X. Zhi, M. Lv and H. Xu, "Natural-product-based insecticidal agents 14. Semisynthesis and insecticidal activity of new piperine-based hydrazone derivatives against *Mythimna separata* Walker *in vivo*", *Bioorganic Med. Chem. Lett.*, **23** (2013) 5552–5557.

[11]   Z.-Q. Xu, X.-J. Mao, L. Jia, J. Xu, T.-F. Zhu, H.-X. Cai, H.-Y. Bie, R.-H. Chen and T.-L. Ma, "Synthesis, characterization and anticancer activities of two lanthanide(III) complexes with a nicotinohydrazone ligand", *J. Mol. Struct.*, **1102** (2015) 86–90.

[12]   Z.-Y. Hao, Q.-W. Liu, J. Xu, L. Jia and S.-B. Li, "Synthesis, characterization, antioxidant activities, and DNA-binding studies of (*E*)-*N′*-[1-(pyridin-2-l)ethylidene]isonicotinohydrazide and its Pr(III) and Nd(III) complexes", *Chem. Pharm. Bull.*, **58** (2010) 1306–1312.

[13]   L.-F. Chu, Y. Shi, D.-F. Xu, H. Yu, J.-R. Lin and Q.-Z. He, "Synthesis and biological studies of some lanthanide complexes of Schiff base", *Synthesis and Reactivity in Inorganic, Metal-Organic, and Nano-Metal Chemistry*, **45** (2015) 1617–1626.

[14]   H. Zhang, S-Y. Lin, S. Xue, C. Wang and J. Tang, "Acetato-bridged dinuclear lanthanide complexes with single molecule magnet behaviour for the Dy_2 species", *Dalton Trans.*, **43** (2014) 6264−6268.

[15]   M.U. Anwar, S.S. Tandon, L.N. Dawe, F. Habib, M. Murugesu and L.K. Thompson, "Lanthanide complexes of tritopic bis(hydrazone) ligands: Single-molecule magnet behaviour in a linear Dy^{III}_3 complex", *Inorg. Chem.*, **51** (2012) 1028−1034.

[16]   R.D. Teo, J. Termini and H.B. Gray, "Lanthanides: Applications in cancer diagnosis and therapy", *J. Med. Chem.*, **59** (2016) 6012–6024.

[17]   D. Ferreira, F. Adega and R. Chaves, "The importance of cancer cell lines as in vitro models in cancer Methylome Analysis and Anticancer Drugs Testing", *Oncogenomics and Cancer Proteomics – Novel Approaches in Biomarkers Discovery and Therapeutic Targets in Cancer*, **Chapter 6** (2013) 139–159.

[18]   J.-P. Gillet, S. Varma and M.M. Gottesman, "The clinical relevance of cancer cell lines", *J. Natl. Cancer Inst.*, **105** (2013) 452–458.

[19]   X.-X. Qi, N. Ren, S.-L. Xu, J.-J. Zhang, G.-C. Zong, J. Gao, L.-N. Geng, S.-P. Wang and S.-K. Shi, "Lanthanide complexes with 3,4,5-triethoxybenzoic acid and 1,10-phenanthroline: synthesis, crystal structures, thermal decomposition mechanism and phase transformation kinetics", *RSC Adv.*, **5** (2015) 9261–9271.

[20]   A.M. Ajlouni, Q. Abu-Salem, Z.A. Taha, A.K. Hijazi and W. Al Momani, "Synthesis, characterization, biological activities and luminescent properties of lanthanide complexes with [2-thiophenecarboxylic acid, 2-(2-pyridinylmethylene)hydrazide] Schiff bases ligand", *J. Rare Earth.*, **34** (2016) 986–993.

[21]   M. Gaye, F.B. Tamboura and A.S. Sall, "Spectroscopic Studies of some lanthanide(III) nitrate complexes synthesized from a new ligand 2,6-bis-(salicylaldehyde hydrazone)-4-chlorophenol", *Bull. Chem. Soc. Ethiop.*, **17** (2003) 27–34.

[22]   S.K. Patil, N.B. Mallur and V.M. Naik, "Synthesis, spectroscopic and antimicrobial studies of 3*D*–bivalent metal complexes derived from 2-imidazoyl mercaptoaceto hydrazone", *IJPRD*, **4** (2012) 143–152.

[23]   K.B. Gudasi, V.C. Havanur, S.A. Patil and B.R. Patil, "Antimicrobial study of newly synthesized lanthanide(III) complexes of 2-[2-hydroxy-3-methoxyphenyl]-3-[2-hydroxy-3-methoxybenzylamino]-1,2-dihydroquinazolin-4(3H)-one", *Metal-Based Drugs,* **2007** (2007) 1–7.

[24]   Z.A. Taha, A.M. Ajlouni, T.S. Ababneh, W. Al-Momani, A.K. Hijazi, M. Al Masri and H. Hammad, "DFT computational studies, biological and antioxidant activities, and kinetics of thermal decomposition of 1,10-phenanthroline lanthanide complexes", *Struct. Chem.*, **28** (2017) 1907–1918.

[25]   A.A. Ansari, "Paramagnetic NMR shift, spectroscopic and molecular modeling studies of lanthanide(III)-morin complexes", *J. Coord. Chem.*, **61** (2008) 3869–3878.

[26]   M.D. Regulacio, N. Tomson and S.L. Stoll, "Dithiocarbamate precursors for rare-earth sulfides", *Chem. Mater.*, **17** (2005) 3114–3121.

[27]   L. Pavelek, V. Ladányi, M. Nečas, Z. Moravec, K. Wichterle, "Synthesis and characterization of lanthanide complexes with a pentadentate triazine-based ligand", *Polyhedron*, **119** (2016) 134–141.

[28]   M. Llunell, D. Casanova, J. Cirera, P. Alemany and S. Alvarez, *SHAPE: Program for the Stereochemical Analysis of Molecular Fragments by Means of Continuous Shape Measures and Associated Tools, User's Manual Version 2.1*, 2013.

[29]   X. Wang, M. Zhu, J. Wang and L. Li, "Unusual Gd–nitronyl nitroxide antiferromagnetic coupling and slow magnetic relaxation in the corresponding Tb analogue", *Dalton Trans.*, **44** (2015) 13890–13896.

[30]   J. Cirera, E. Ruiz and S. Alvarez, "Continuous Shape Measures as a stereochemical tool in organometallic chemistry", *Organometallics,* **24** (2005) 1556–1562.

[31]   T. Zhu, P. Chen, H. Li, W. Sun, T. Gao and P. Yan, "Structural effects on the photophysical properties of mono-*β*-diketonate and bis-*β*-diketonate Eu[III] complexes", *Phys. Chem. Chem. Phys.*, **17** (2015) 16136–16144.

[32]   K. Liu, H. Li, X. Zhang, W. Shi and P. Cheng, "Constraining and tuning the coordination geometry of a lanthanide ion in metal−organic frameworks: Approach toward a single-molecule magnet", *Inorg. Chem.*, **54** (2015) 10224–10231.

[33]   D.G. Paschalidis and W.T.A. Harrison, "Two mixed-ligand lanthanide–hydrazone complexes: $[Pr(NCS)_3(pbh)_2]·H_2O$ and $[Nd(NCS)(NO_3)(pbh)_2(H_2O)]NO_3·2.33H_2O$ [pbh is *N'*-(pyridin-2-ylmethylidene)benzohydrazide, $C_{13}H_{11}N_3O$]", *Acta Cryst.*, **E72** (2016) 191–195.

[34]   C. Theivarasu and R. Murugesan, "Natural Bond Orbital (NBO) population analysis of an energetic molecule 1-phenyl-2-nitroguanidine", *Int. J. Chem. Sci.*, **14** (2016) 2029–2050.

[35]   N.K. Nobel, K. Bamba, O.W. Patrice and N. Ziao, "NBO population analysis and electronic calculation of four azopyridine ruthenium complexes by DFT method", *Computational Chemistry*, **5** (2017) 51–64.

[36]   S. Gatfaoui, N. Issaoui, A. Mezni, F. Bardak, T. Roisnel, A. Atac and H. Marouani, "Synthesis, structural and spectroscopic features, and investigation of bioactive nature of a novel organic-inorganic hybrid material 1*H*-1,2,4-triazole-4-ium trioxonitrate", *J. Mol. Struct.*, **1150** (2017) 242–257.

[37]   J.M. Mir, R.C. Maurya, P.K. Vishwakarma, D.K. Rajak, B.A. Malik, P.S. Jaget and P. Bohre, "Synthesis and conjoint experimental-DFT characterization of some pyrazolone functionalized dioxovanadium(V) Schiff base complexes", *J. Theor. Comput. Sci.*, **4** (2017) 152.

[38]   J.A. Joule and K. Mills (2010) – *Heterocyclic Chemistry*, 5th ed., John Wiley & Sons, Ltd., pp 6–7.

[39]   F.S. Tiago, P.H.O. Santiago, M.M.P. Amaral, J.B.L. Martins and C.C. Gatto, "New Cu(II) complex with acetylpyridine benzoyl hydrazone: experimental and theoretical analysis", *J. Coord. Chem.*, **69** (2016) 330–342.

[40]   A. Roca-Sabio, M. Mato-Iglesias, D. Esteban-Gómez, A. de Blas, T. Rodríguez-Blas and C. Platas-Iglesias, "The effect of ring size variation on the structure and stability of lanthanide(III) complexes with crown ethers containing picolinate pendants", *Dalton Trans.*, **40** (2011) 384–392.

[41]   Z. Demircioğlu, Ç.A. Kaştaş and O. Büyükgüngör, "Theoretical analysis (NBO, NPA, Mulliken Population Method) and molecular orbital studies (hardness, chemical potential, electrophilicity and Fukui function analysis) of

(*E*)-2-((4-hydroxy-2-methylphenylimino)methyl)-3-methoxyphenol", *J. Mol. Struct.*, **1091** (2015) 183–195.

[42] A.O. Sarioğlu, T.T. Tok, M. Akkurt, M.N. Tahir and M. Sönmez, "Synthesis and structural properties of *N*-3,4-(dichlorophenyl)-3-oxo-3-phenyl-2-(phenylcarbonyl)propanamide and its Cu(II) complex", *Turk. J. Chem.*, **40** (2016) 76–92.

[43] J. McMurry (2010) – *Organic Chemistry with Biological Applications,* 2nd ed., Brooks/Cole, Cengage Learning, pp 319–320.

[44] P.S. Kushwaha and P.C. Mishra, "Molecular electrostatic potential maps of the anti-cancer drugs daunomycin and adriamycin: an *ab initio* theoretical study", *J. Mol. Struct. (Theochem)*, **636** (2003) 149–156.

[45] N.S. Babu and D. Jayaprakash, "Global and reactivity descriptor studies of cyanuric acid tautomers in different solvents by using of Density Functional Theory (DFT)", *IJSR*, **4** (2015) 615–620.

[46] A. Bendjeddou, T. Abbaz, A. Gouasmia and D. Villemin, "Quantum chemical studies on molecular structure and reactivity descriptors of some *p*-nitrophenyl tetrathiafulvalenes by Density Functional Theory (DFT)", *Acta Chim. Pharm. Indica*, **6** (2016) 32–44.

[47] M. Asad, Z.N. Siddiqui, A.M. Asiri and A. Mahmood, "Synthesis, DFT and biological studies of novel 3,6-dimethyl-1,8-diphenyl-diazocino[3,4-c:7,8-c']bispyrazole", *J. Mol. Struct.*, **1176** (2019) 66–72.

[48] A. Gil, M. Melle-Franco, V. Branchadell and M.J. Calhorda, "How the intercalation of phenanthroline affects the structure, energetics, and bond properties of DNA base pairs: Theoretical study applied to adenine−thymine and guanine−cytosine tetramers", *J. Chem. Theory Comput.*, **11** (2015) 2714−2728.

[49] R.N. Devi, S. Israel and C. Ancline, "An analysis of structural, electronic and reactivity properties of MetforminChloride using XRD and DFT approach", *Mechanics, Materials Science Engineering Journal, Magnolithe*, **9** (2017).

[50] P.K. Chattaraj and S. Giri, "Electrophilicity index within a conceptual DFT framework", *Annu. Rep. Prog. Chem., Sect. C*, **105** (2009) 13–39.

[51] K. Bellifa and S.M. Mekelleche, "QSAR study of the toxicity of nitrobenzenes to *Tetrahymena pyriformis* using quantum chemical descriptors", *Arab. J. Chem.*, **9** (2016) S1683–S1689.

[52] N. Dahan-Farkas, C. Langley, A.L. Rousseau, D.B. Yadav, H. Davids and C.B. de Koning, "6-Substituted imidazo[1,2-a]pyridines: Synthesis and

biological activity against colon cancer cell lines HT-29 and Caco-2", *Eur. J. Med. Chem.,* **46** (2011) 4573–4583.

[53]   A. Chaubey and S.N. Pandeya, "Pyridine" a versatile nucleuse in pharmaceutical field", *Asian J. Pharm. Clin. Res.*, **4** (2011) 5–8.

[54]   P.M. Lukasik, S. Elabar, F. Lam, H. Shao, X. Liu, A.Y. Abbas and S. Wang, "Synthesis and biological evaluation of imidazo[4,5-*b*]pyridine and 4-heteroarylpyrimidine derivatives as anti-cancer agents', *Eur. J. Med. Chem.*, **57** (2012) 311–322.

[55]   J.Y. Chen, H. Jiang, S.J. Chen, C. Cullen, C.M. Sabbir Ahmed and Y.-H. Lin, "Characterization of electrophilicity and oxidative potential of atmospheric carbonyls", *Environ. Sci.: Processes Impacts*, **21** (2019) 856–866.

[56]   A. Morales-Bayuelo, "Molecular quantum similarity, Chemical reactivity and database screening of 3D pharmacophores of the protein kinases A, B and G from *Mycobacterium tuberculosis*", *Molecules*, **22** (2017) 1027.

[57]   A.S. Levenson and V.C. Jordan, "MCF-7: The first hormone-responsive breast cancer cell line", *Perspectives in Cancer Research,* **57** (1997) 3071–3078.

[58]   S. Ali and R.C. Coombes, "Endocrine-responsive breast cancer and strategies for combating resistance", *Nat. Rev. Cancer,* **2** (2002) 101–112.

[59]   E. Castro-Rivera and S. Safe, "Estrogen- and antiestrogen-responsiveness of HEC1A endometrial adenocarcinoma cells in culture", *J. Steroid Biochem. Mol. Biol.,* **64** (1998) 287–295.

CHAPTER 4

Synthesis, characterisation and cytotoxic activity of Ln(III) complexes with *N*-(2,6-dimethylphenyl)oxamate in cancer cell lines

4.1   Introduction

The prevalence of cancer is rising each year, resulting in cancer becoming the leading cause of death worldwide [1]. Among the most commonly diagnosed types of cancers are breast (in women), endometrial, prostate, colorectal, and lung cancer [1-4]. The metallodrug cisplatin has been extensively used in cancer chemotherapy since the 1960s, although its clinical applications are limited due to adverse effects, such as nausea, ototoxicity, low hydrolytic stability and resistance in some cancer cells [5,6]. This has encouraged researchers to investigate alternative metal complexes as potential anticancer agents, with improved effectiveness towards cancer.

Previous studies have demonstrated that complexes of the 4*f* elements have a relevant role in chemotherapy, since the Ln(III) compounds actively inhibit tumour growth due to the ability of lanthanide to suppress iron uptake, alter signal transduction and inhibit reactive oxygen species production through binding to hydro-peroxides [7,8]. In addition, the lanthanides can mask free radicals by means of magnetic interactions [7]. Problems associated with platinum-based anticancer agents can thus potentially be overcome by resorting to lanthanide-based drugs.

The *d*- and *f*-block metal complexes containing carboxylic acids have been widely studied due to their potential use as anticancer agents [9]. Oxamic acid is among the simplest carboxylic acid ligands examined (Figure 4.1) which has tumour growth inhibition properties [9-11]. Oxamate (a structural analogue of pyruvate), or its

derivatives, act by targeting aerobic glycolysis (an abnormal process related to tumour progression and metastasis) through competitive inhibition of pyruvate conversion to lactate by the enzyme lactate dehydrogenase A (LDHA) [9-11]. For example, oxamate significantly inhibits the proliferation of non-small cell lung cancer (NSCLC) cells, with the investigation revealing lower toxicity in normal cells [12].

oxamic acid

N-(2,6-dimethylphenyl)oxamic acid
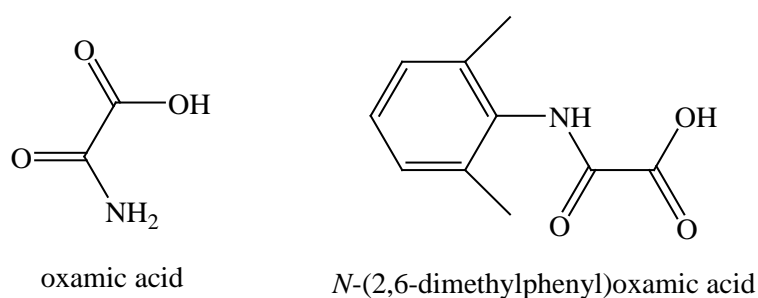
Figure 4.1: Structures of oxamic acid and *N*-(2,6-dimethylphenyl)oxamic acid [9-11].

Complexation studies of oxamic acid and its derivatives with *d*- and *f*-block metals indicated that these ligands have interesting ligating properties, as they can chelate in a bidentate mode to the metal ions either *via* both oxygen atoms, or through one nitrogen atom and one oxygen atom [9,13]. For example, X-ray analysis of the Co(III) complex, $[Co(C_2O_3NH_2)_2(OH_2)_2]\cdot2H_2O$ revealed coordination of oxamic acid as a bidentate *O,O*-donor ligand. Other reports showed that oxamic acid can act mono-, bi-, tri- or tetradentately (bridging) in its mono- or dianionic form [9,13]. Monodentate coordination is possible for the monoanionic ligand using an *O*-atom of the carboxylic group, while tridentate binding occurs through all the oxygen atoms. The carboxylic and amide protons are ionisable to yield a dianionic ligand, which can act as a bridging ligand in dinuclear or polynuclear complexes [13].

Lanthanide complexes are vital, not only in therapy, but also in cancer diagnosis, due to the versatile magnetic characteristics of the metal ion 4*f* electronic configuration [14]. Lanthanide-based single-ion magnets are also of potential use in quantum computing devices or high-density magnetic memories [15]. An example of a complex showing slow magnetic relaxation behaviour is the mononuclear Dy(III)-oxamate complex derived from *N*-(2,6-dimethylphenyl)oxamic acid (**H₂L**, Figure 4.1)

in a controlled basic media [15]. The isolated mononuclear Dy(III) coordination compound, which is stabilised by metal-ligand bonds and hydrogen bonding, has the formula $Me_4N[Dy(HL)_4] \cdot 2CH_3CN$. The oxamate ligands assume the O,O'-chelating mode, forming an eight-coordinate environment with distorted D_{2d} dodecahedron geometry [15].

This chapter reports the preparation of the solid-state Ce(III), Nd(III), Gd(III) and Er(III) complexes with N-(2,6-dimethylphenyl)oxamate (**Hpma⁻**) (Scheme 4.1), and their characterisation by means of micro-analyses, infrared (IR), UV-Vis-NIR and nuclear magnetic resonance (NMR) spectroscopy, as well as single-crystal X-ray crystallography. We herein present Ln(III)–oxamate coordination polymers of the formula: $\{[Ln(Hpma)_3(MeOH)(H_2O)] \cdot 2MeOH\}_n$ (Ln = Ce (**1**) and Nd (**2**)), $\{[Gd_2(Hpma)_6(MeOH)_4] \cdot 6MeOH\}_n$ (**3**), $\{[Er_2(Hpma)_6(MeOH)(H_2O)_3] \cdot 2MeOH\}_n$ (**4**) and $[Ln_2Na_2(Hpma)_8(EtOH)(H_2O)_6]_n$ (Ln = Nd (**5**) and Gd (**6**)). Density Functional Theory (DFT) calculations were performed to compare theoretical calculations and experimental findings, and to confirm experimental results. This work also aims at investigating the anticancer properties of the oxamate compounds by determining their *in vitro* cytotoxicities against breast cancer (MCF-7), the endometrial carcinoma (HEC-1A) and the human monocytic (THP-1) cell lines using the 3-(4,5-dimethylthiazol-2-yl)-2,5-diphenyltetrazolium bromide (MTT) assay [16,17]. Anticancer screen serve to identify compounds that may act as lead compounds in the design of novel chemotherapeutic agents.
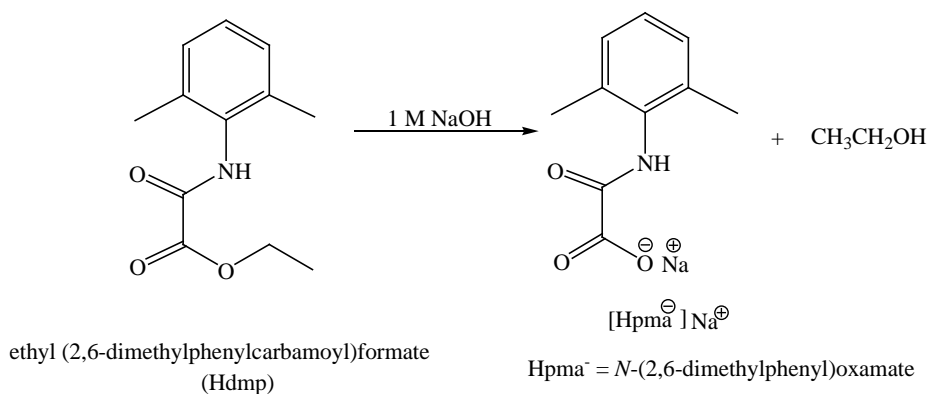
Scheme 4.1: Hydrolysis of the proligand **Hdmp** to the anionic oxamate ligand **Hpma⁻** [18].

4.2   Synthesis of the ligand and complexes

4.2.1   Synthesis of ethyl (2,6-dimethylphenylcarbamoyl)formate (Hdmp)

The proligand **Hdmp** was synthesised according to the literature procedure [18]. 2,6-Dimethylphenylaniline (10.22 mL, 83 mmol) in 250 mL THF was treated with 9.3 mL ethyl chlorooxoacetate (9.273 mL, 83 mmol) in the presence of 12 mL triethyl amine (11.569 mL, 83.002 mmol). The mixture was continuously stirred for 30 minutes at room temperature, under a nitrogen atmosphere. The resulting solution was filtered and the solvent was removed under vacuum to yield an oily colourless crude product, which quickly solidified. The white solid was suspended into water and filtered off, washed with diethyl ether, and then dried under vacuum. Yield = 93.0 %, m.p. = 177.1 ^{o}C. Anal. *Calcd* for $C_{12}H_{15}NO_3$ (%): C, 65.14; H, 6.83; N, 6.33. Found: C, 65.12; H, 6.78; N, 6.27. IR (cm^{-1}): v(N-H) 3252(s), v(C-H) 3060, 2980, 2936(w), v(C=O) 1763, 1688(s), v(C=C) 1525(s), v(C-O-C) 1298–1176(m). ^{1}H NMR (400 MHz, DMSO-d_6, δ ppm): 1.33 (t, *J*=6.97 Hz, 3H), 2.14 (s, 6H), 4.31 (q, *J*=7.17 Hz, 2H), 7.11 (m, 3H), 10.29 (br. s., 1H). ^{13}C NMR (400 MHz, DMSO-d_6, δ ppm): 14.34, 18.36, 62.73, 127.64, 128.27, 134.09, 135.59, 156.25, 161.32.

4.2.2   Synthesis of complexes 1–4

A mixture of 3 mL 1M NaOH and **Hdmp** (≈3 mmol) was heated until the ligand dissolved. An aqueous solution of 1 mmol [Ln(NO$_3$)$_3$·xH$_2$O] (Ln = Ce, Nd, Gd and Er) was mixed with the ligand solution. The resulting white precipitate was filtered, washed with distilled water and diethyl ether and dried. Dissolution in methanol, followed by slow diffusion into the solution resulted in X-ray quality crystals within 5 days (Scheme 4.2).

{[Ce(Hpma)$_3$(MeOH)(H$_2$O)]·2MeOH}$_n$ (1)

Hdmp (0.664 g, 3 mmol), 1 M NaOH (3 mL), [Ce(NO$_3$)$_3$·6H$_2$O] (0.434 g, 1 mmol), Yield = 0.536 g (64.5 % based on the Ce(III) salt); white crystals, m.p. >300.0 ^{o}C. Anal. *Calcd*. for $C_{31}H_{36}CeN_3O_{11}$, 2(CH$_4$O) (%): C, 47.71; H, 5.34; N, 5.06. Found: C, 47.63; H, 5.19; N, 5.26. Conductivity (10^{-3} M, DMF): 3.55 ohm^{-1}cm^{2}mol^{-1}. IR (cm^{-1}): v(O-H) 3613–3125(b), v(C-H) 3052–2931(w), v(C=O) 1635(s), v(Ln-O) 447(w).

$$3\ \text{Hdmp} + 3\ \text{NaOH} + [\text{Ln(NO}_3)_3 \cdot x\text{H}_2\text{O}]$$

x = 6 for Ce, Nd and Gd

x = 5 for Er

H₂O/Reflux — Recryst. using methanol → {[Ln(Hpma)₃(MeOH)(H₂O)]· 2MeOH}ₙ

Ln = Ce (**1**) and Nd (**2**)

H₂O/Reflux — Recryst. using methanol → {[Gd₂(Hpma)₆(MeOH)₄]·6MeOH}ₙ (**3**)

H₂O/Reflux — Recryst. using methanol → {[Er₂(Hpma)₆(MeOH)(H₂O)₃]·2MeOH}ₙ (**4**)

H₂O/Methanol — Reflux → [Ln₂Na₂(Hpma)₈(EtOH)(H₂O)₆]ₙ

Ln = Nd (**5**) and Gd (**6**)

Hpma⁻ =
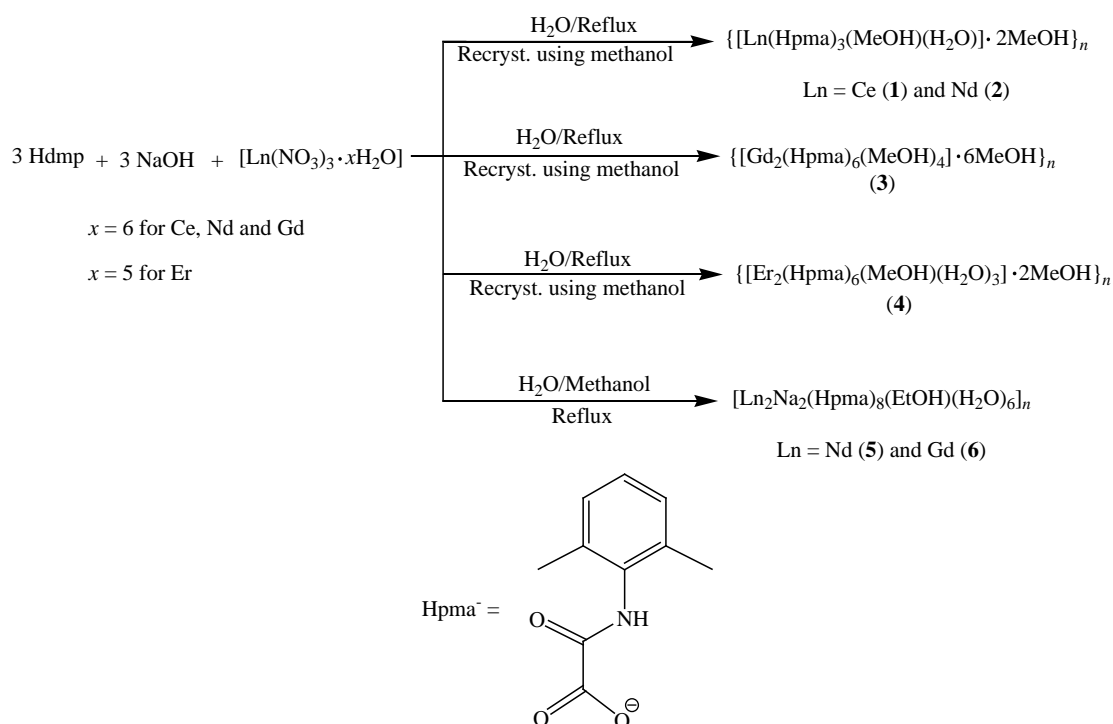
Scheme 4.2: Schematic diagram for the preparation of the six metal complexes derived from **Hdmp**.

{[Nd(Hpma)$_3$(MeOH)(H$_2$O)]·2MeOH}$_n$ (2)

Hdmp (0.662 g, 2.992 mmol), 1 M NaOH (3 mL), [Nd(NO$_3$)$_3$·6H$_2$O] (0.437 g, 0.997 mmol), Yield = 0.531 g (63.7 % based on the Nd(III) salt); purple crystals, m.p. >300.0 °C. Anal. *Calcd.* for C$_{31}$H$_{35}$NdN$_3$O$_{11}$, 2(CH$_4$O) (%): C, 47.53; H, 5.20; N, 5.04. Found: C, 47.45; H, 5.18; N, 5.07. Conductivity (10^{-3} M, DMF): 3.58 ohm^{-1}cm^{2}mol^{-1}. IR (cm^{-1}): v(O-H) 3613–3125(b), v(C-H) 3052–2931(w), v(C=O) 1635(s), v(Ln-O) 450(w).

{[Gd$_2$(Hpma)$_6$(MeOH)$_4$]·6MeOH}$_n$ (3)
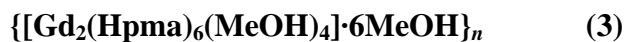
Hdmp (0.663 g, 2.996 mmol), 1 M NaOH (3 mL), [Gd(NO$_3$)$_3$·6H$_2$O] (0.452 g, 1.001 mmol), Yield = 0.497 g (55.6 % based on the Gd(III) salt); white crystals, m.p. >300.0 °C. Anal. *Calcd.* for C$_{64}$H$_{76}$Gd$_2$N$_6$O$_{22}$, 6(CH$_4$O) (%): C, 47.02; H, 5.64; N, 4.70. Found: C, 47.12; H, 5.48; N, 4.82. Conductivity (10^{-3} M, DMF): 14.45 ohm^{-1}cm^{2}mol^{-1}. IR (cm^{-1}): v(O-H) 3613–3125(b), v(C-H) 3052–2929(w), v(C=O) 1635(s), v(Ln-O) 447(w).

{[Er$_2$(Hpma)$_6$(MeOH)(H$_2$O)$_3$]·2MeOH}$_n$ **(4)**

Hdmp (0.664 g, 3 mmol), 1 M NaOH (3 mL), [Er(NO$_3$)$_3$·5H$_2$O] (0.443 g, 0.999 mmol), Yield = 0.578 g (70.6 % based on the Ce(III) salt); pink crystals, m.p. = 278.3 °C. Anal. *Calcd.* for C$_{61}$H$_{70}$Er$_2$N$_6$O$_{22}$, 2(CH$_4$O) (%): C, 46.20; H, 4.80; N, 5.13. Found: C, 46.48; H, 4.74; N, 5.33. Conductivity (10^{-3} M, DMF): 51.90 ohm^{-1}cm^{2}mol^{-1}. IR (cm^{-1}): v(O-H) 3613–3125(b), v(C-H) 3052–2929(w), v(C=O) 1637(s), v(Ln-O) 447(w).

4.2.3   Synthesis of complexes 5 and 6

A mixture of 3 mmol **Hdmp** dispersed in water and 3 mL 1M NaOH was heated until the ligand dissolved. A 1 mmol [Ln(NO$_3$)$_3$·6H$_2$O] (Ln = Nd and Gd) aqueous solution was added to the ligand solution and a white precipitate formed. The mixture was refluxed, and then methanol was added until the precipitate dissolved. The solution was cooled and was kept at room temperature until single crystals formed after 7 days.

[Nd$_2$Na$_2$(Hpma)$_8$(EtOH)(H$_2$O)$_6$]$_n$ **(5)**

Hdmp (0.666 g, 3.010 mmol), 1 M NaOH (3 mL), [Nd(NO$_3$)$_3$·6H$_2$O] (0.438 g, 1 mmol), Yield = 0.489 g (48.3 % based on the Nd(III) salt); purple crystals, m.p. = 276.8 °C. Anal. *Calcd.* for C$_{82}$H$_{95}$N$_8$Na$_2$Nd$_2$O$_{30}$, O (%): C, 48.50; H, 4.72; N, 5.52. Found: C, 48.51; H, 4.68; N, 5.79. Conductivity (10^{-3} M, DMF): 46.90 ohm^{-1}cm^{2}mol^{-1}. IR (cm^{-1}): v(O-H) 3613–3125(b), v(C-H) 3052–2929(w), v(C=O) 1635(s), v(Ln-O) 452(w).

[Gd$_2$Na$_2$(Hpma)$_8$(EtOH)(H$_2$O)$_6$]$_n$ **(6)**

Hdmp (0.660 g, 2.978 mmol), 1 M NaOH (3 mL), [Gd(NO$_3$)$_3$·6H$_2$O] (0.453 g, 1 mmol), Yield = 0.493 g (48.2 % based on the Ce(III) salt); white crystals, m.p. = 277.5 °C. Anal. *Calcd.* for C$_{81.69}$H$_{94.23}$Gd$_2$N$_8$Na$_2$O$_{30}$, O (%): C, 48.17; H, 4.63; N, 5.48. Found: C, 47.84; H, 4.67; N, 5.35. Conductivity (10^{-3} M, DMF): 53.40 ohm^{-1}cm^{2}mol^{-1}. IR (cm^{-1}): v(O-H) 3613–3125(b), v(C-H) 3052–2929(w), v(C=O) 1636(s), v(Ln-O) 447(w).

4.3   Results and discussion

4.3.1   FT-IR spectroscopy

The infrared spectra of the proligand **Hdmp** and its Ln(III) complexes (Figure 4.2) exhibit similar spectral features due to their related coordination environments [19]. The strong v(N-H) of **Hdmp** located at 3252 cm^{-1} is replaced by broad bands in **1**–**6** in the region 3613–3125 cm^{-1}, indicating the presence of O-H stretching vibrations of the water or methanol molecules in the metal complexes [18,20,21]. The high frequency spectral region of the proligand **Hdmp** also exhibits typical C-H vibrations (3060, 2980 and 2936 cm^{-1}), while the C-H vibrations of the phenyl rings of the oxamate ligands in the complexes show a slight red-shift (3052–2929 cm^{-1}) relative to Hdmp [18]. Two strong absorptions occurring at 1763 and 1688 cm^{-1} correspond to the characteristic C=O stretching vibrations in **Hdmp** [18,22]. These strong v(C=O) appear as single bands in all the title complexes, at approximately 1635 cm^{-1}, hence confirming the role of the oxamate oxygen atoms in coordination [18,22]. A series of four absorption peaks in the range 1298–1176 cm^{-1}, typical of the C-O-C bonds, are observed for the free ligand. The latter disappear upon coordination, thus confirming complete conversion of **Hdmp** to **Hpma**$^-$ [20]. After complexation, the weak Ln-O vibrations are assigned to the bands found at 452–447 cm^{-1}, which show the involvement of the oxygen atoms in the primary coordination sphere of the lanthanide(III) ions [20,23].

4.3.2   NMR analysis

Nuclear magnetic resonance experiments on **Hdmp** and the complexes were performed in DMSO-d_6 (Figures 4.3a and 4.3b). For complexes **3**, **4** and **6**, the paramagnetic nature of the Gd(III) and Er(III) ions gave rise to signal broadening and featureless ^{1}H NMR spectra, while **1**, **2** and **5** gave clearly defined spectra, though there appears discernible evidence of some broadening [24]. In concurrence with the IR spectral and X-ray crystallographic data, the ^{1}H-NMR spectra of the coordination compounds **1**, **2** and **5** clearly shows formation of the **Hpma**$^-$ anion from **Hdmp**, as indicated by the disappearance of the ethyl group signals after coordination [18]. The

N-H group peaks of the ligand gives a broad signal in **1** (δ = 12.29 ppm), but are not seen in the spectra of **2** and **5**, suggesting participation of the oxamate moieties in ligand coordination [18]. The spectra of the complexes also exhibit **Hpma⁻** methyl proton signals peaking at 1.55, 1.57 and 1.51 ppm, an indication that the methyl groups undergo a significant shift in the chemical environment relative to **Hdmp** (δ = 2.14 ppm) upon hydrolysis [25]. Downfield to the methyl proton peaks of **1**, **2** and **5**, are resonances attributable to the aromatic proton signals of the oxamate ligands (6.37–6.57 ppm), which are also more shielded than the proligand aromatic protons (7.11 ppm).
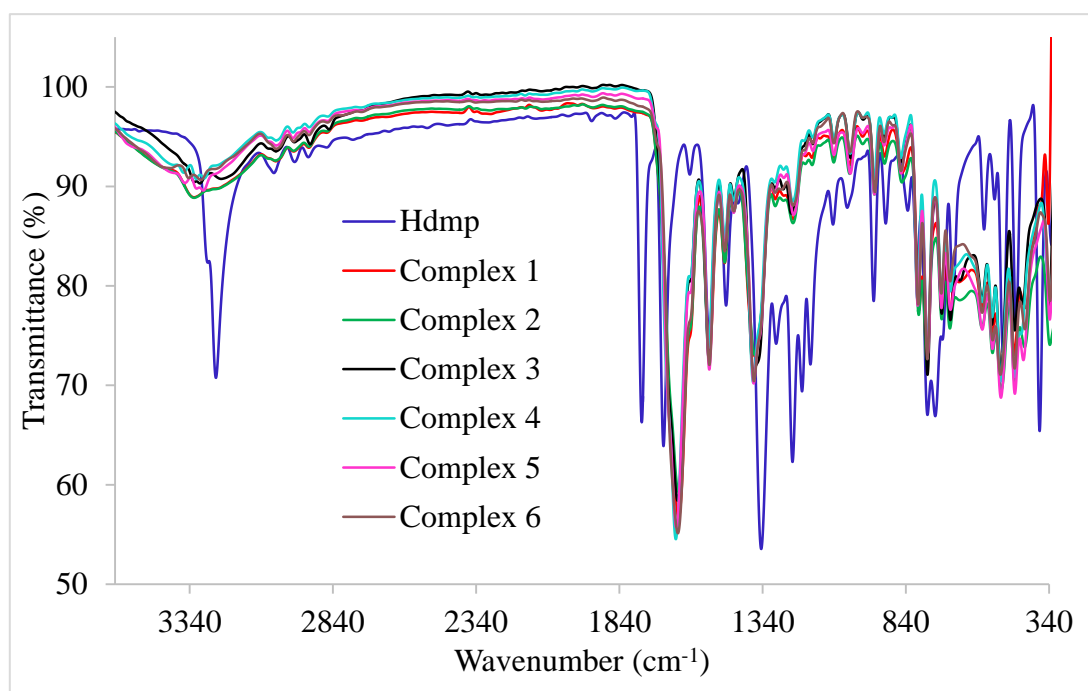
Figure 4.2: Overlay IR spectra of **Hdmp** and **1**–**6**.
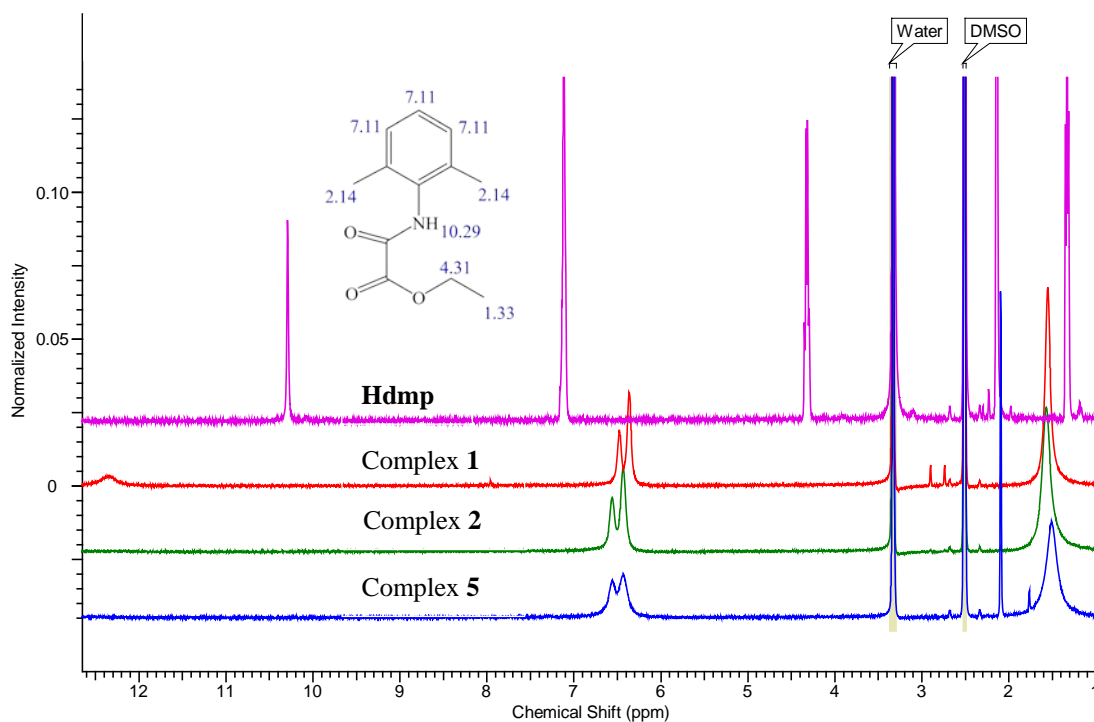
Figure 4.3a: Overlay ^{1}H NMR spectra of **Hdmp**, and the Ln(III) complexes **1**, **2** and **5** in DMSO-d_6.
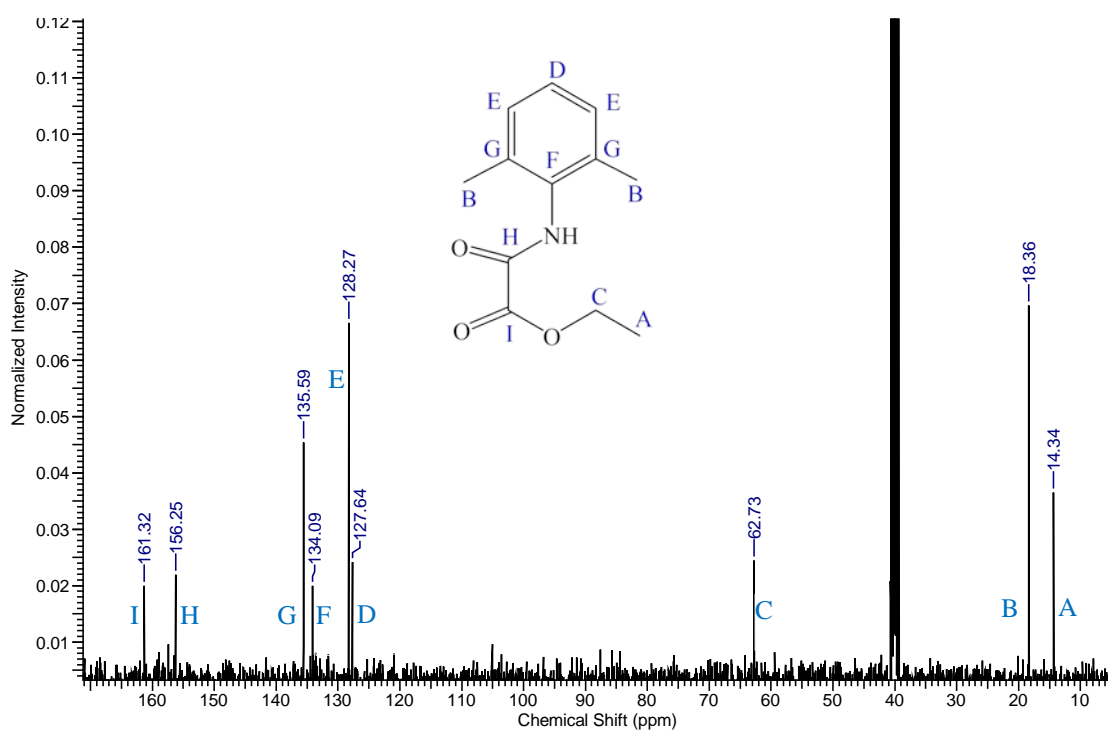
Figure 4.3b: ^{13}C NMR spectrum of **Hdmp**.

4.3.3   UV-Vis-NIR spectroscopy

The ligand **Hdmp** and the trivalent complexes of Ce(III) and Gd(III)complex **3** have no significant absorption in the ultraviolet, visible and near-infrared regions. The UV-Vis-NIR spectra of **2**, **4**, **5** and **6** are displayed in Figure 4.4, and the assignment of absorption bands is shown in Table 4.1. Absorption peaks of the Nd(III), Er(III) and Gd(III) complexes arise from the Laporte-forbidden *f-f* transitions from the ground level of $^4I_{9/2}$, $^4I_{15/2}$ and $^8S_{7/2}$, respectively, to the excited *J*-levels of the 4*f*-configuration [26-30]. The spectra of **2** and **5** are similar, with absorption maxima at 511, 522, 582 and 745 nm in the visible region, corresponding to transitions from the $^4I_{9/2}$ ground level to the excited *J*-levels $^4G_{9/2}$, $^4G_{7/2}$, $^4G_{5/2} + {}^2G_{7/2}$ and $^4F_{7/2} + {}^4S_{3/2}$, respectively [26-28,31]. The peak observed in the NIR region at 800 nm is assigned to the *f-f* transition from the ground level to the 4*f*-configurations $^4F_{5/2} + {}^2H_{9/2}$, while those appearing at 869 and 876 nm are attributed to a transition from $^4I_{9/2}$ to $^4F_{3/2}$. The Er(III) complex **4** shows the most intense bands positioned at 379 and 522 nm that are due to the transitions $^4I_{15/2} \rightarrow {}^4G_{11/2}$ and $^4I_{15/2} \rightarrow {}^2H_{11/2}$ [29,32-34].
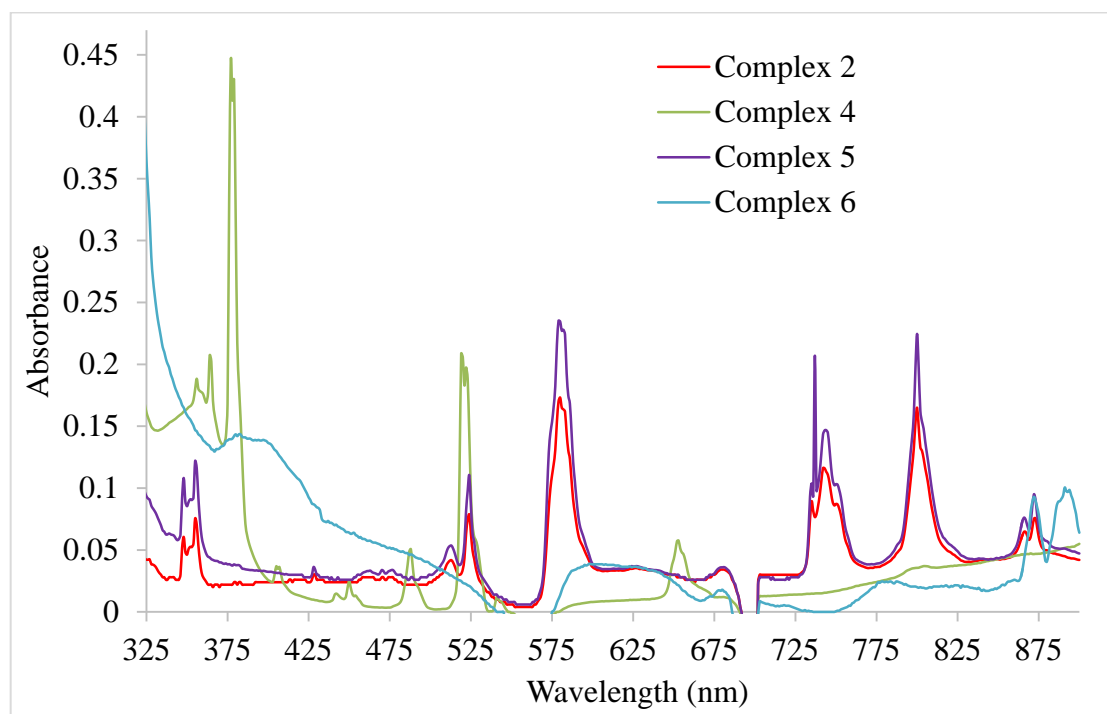
Figure 4.4: The UV-Vis-NIR spectra of **2**, **4**, **5** and **6** in DMF.

Table 4.1: Absorption bands for complexes **2** and **4–6** [26-29,31-35].

Complex 2 and 5		Complex 4	
λ_{max} (nm)	*J*-levels	λ_{max} (nm)	*J*-levels
348, 356	$^4I_{9/2} \rightarrow {}^4D_{3/2} + {}^4D_{5/2}$	360	$^4I_{15/2} \rightarrow {}^2G_{7/2}$
	$+ {}^4D_{1/2} + {}^2I_{11/2}$		
432	$\rightarrow {}^2P_{1/2}$	365	$\rightarrow ({}^4G_{9/2}, {}^2K_{15/2})$
511	$\rightarrow {}^4G_{9/2}$	379	$\rightarrow {}^4G_{11/2}$
522	$\rightarrow {}^4G_{7/2}$	409	$\rightarrow {}^2H_{9/2}$
582	$\rightarrow {}^4G_{5/2} + {}^2G_{7/2}$	446	$\rightarrow {}^4F_{5/2}$
745	$\rightarrow {}^4F_{7/2} + {}^4S_{3/2}$	452	$\rightarrow {}^4F_{3/2}$
800	$\rightarrow {}^4F_{5/2} + {}^2H_{9/2}$	491	$\rightarrow {}^4F_{7/2}$
869, 876	$\rightarrow {}^4F_{3/2}$	522	$\rightarrow {}^2H_{11/2}$
		544	$\rightarrow {}^4S_{3/2}$
Complex 6		654	$\rightarrow {}^4F_{9/2}$
$\square$381	$^8S_{7/2} \rightarrow {}^6P_{7/2}$		

4.3.4   Coordination polyhedra determination

The geometries of the NaO_5, NaO_6, LnO_9 and LnO_8 coordination polyhedra of the lanthanide complexes with **Hpma**⁻ were evaluated by continuous shape measures using *SHAPE 2.1* software, for quantification of the degree of distortion of the Ln(III) coordination geometry (Table 4.2). The polyhedral data generated using *VESTA* is presented in Figure 4.5. The shape analysis of the nine-coordinate complexes **1** and **2** highlight the coordination geometry of the distorted spherical tricapped trigonal prism (TCTPR-9), with D_{3h} symmetry [36,37]. The Nd(III) complex **2** is closer to the TCTPR-9 geometry than complex **1** with the larger metal Ce(III) ion. The continuous shape measures obtained for the spherical capped square antiprism (CSAPR-9) shape in **1** (CShM = 0.92568) and **2** (CShM = 0.82770), however, exhibit a small difference from TCTPR-9 geometry [38]. Hence, the coordination spheres of **1** and **2** can be considered as the intermediate between CSAPR-9 and TCTPR-9 geometries [38,39]. The coordination polyhedron of the octa-coordinated Er1 atom of **4** can be viewed as

square antiprism (SAPR-8), with a deviation parameter from ideal SAPR-8 of 0.43454 [40].

Table 4.2: Summary of *SHAPE* analysis for complexes **1**–**6**.

Complex	Coordination number	Shape (and symmetry)	CShM	Polyhedral volume ($Å^3$)	Average bond length (Å)
1	9	TCTPR-9 (D_{3h})	0.85318	32.4845	2.5247
2	9	TCTPR-9 (D_{3h})	0.77701	31.3620	2.4944
3	9 (Gd1)	CSAPR-9 (C_{4v})	0.46072	29.0919	2.4407
	9 (Gd2)	CSAPR-9 (C_{4v})	0.42825	29.1601	2.4417
4	8 (Er1)	SAPR-8 (D_{4d})	0.43454	22.5763	2.3547
	9 (Er2)	CSAPR-9 (C_{4v})	0.28116	27.2691	2.3890
5	9 (Nd1)	CSAPR-9 (C_{4v})	0.87740	30.5853	2.4865
	9 (Nd2)	CSAPR-9 (C_{4v})	0.94332	30.5194	2.4904
	6 (Na1)	OC-6 (O_h)	1.90099	18.0288	2.4206
	5 (Na2)	vOC-5 (C_{4v})	3.09930	10.9901	2.4329
6	9 (Gd1)	CSAPR-9 (C_{4v})	0.68425	29.0390	2.4405
	9 (Gd2)	CSAPR-9 (C_{4v})	0.76846	28.9252	2.4428
	6 (Na1)	OC-6 (O_h)	2.08861	17.7130	2.4086
	5 (Na2)	vOC-5 (C_{4v})	3.00016	10.8749	2.4208

The least CShM parameters for the nine-coordinate Ln(III) ions of **3**–**6** indicate the distorted CSAPR-9 geometry (C_{4v}). Despite having a similar coordination environment, the Gd(III) coordination polyhedra in **3** display a small difference in CShM values. Distortion parameters are in the order Nd(III) > Gd(III) > Er(III). The other closest geometries for Nd1 (complex **5**) and Gd1 (complex **6**) is TCTPR-9, with deviation values of 0.98091 and 0.86226, respectively; while that of Gd2 (complex **6**) is muffin geometry (MFF-9) (CShM = 0.93876) [36,38,39]. In addition, the oxygen atoms around the hexa-coordinate Na cations in **5** and **6** form two square-based pyramids, adopting an octahedron (OC-6) shape (CShM values of 1.90099 and 2.08861, respectively), whereas the geometry of the five-coordinate Na ions can be described as vacant octahedron (vOC-5), possessing C_{4v} symmetry [41,42].

(a)

(b)   **(c)**

(d)   **(e)**
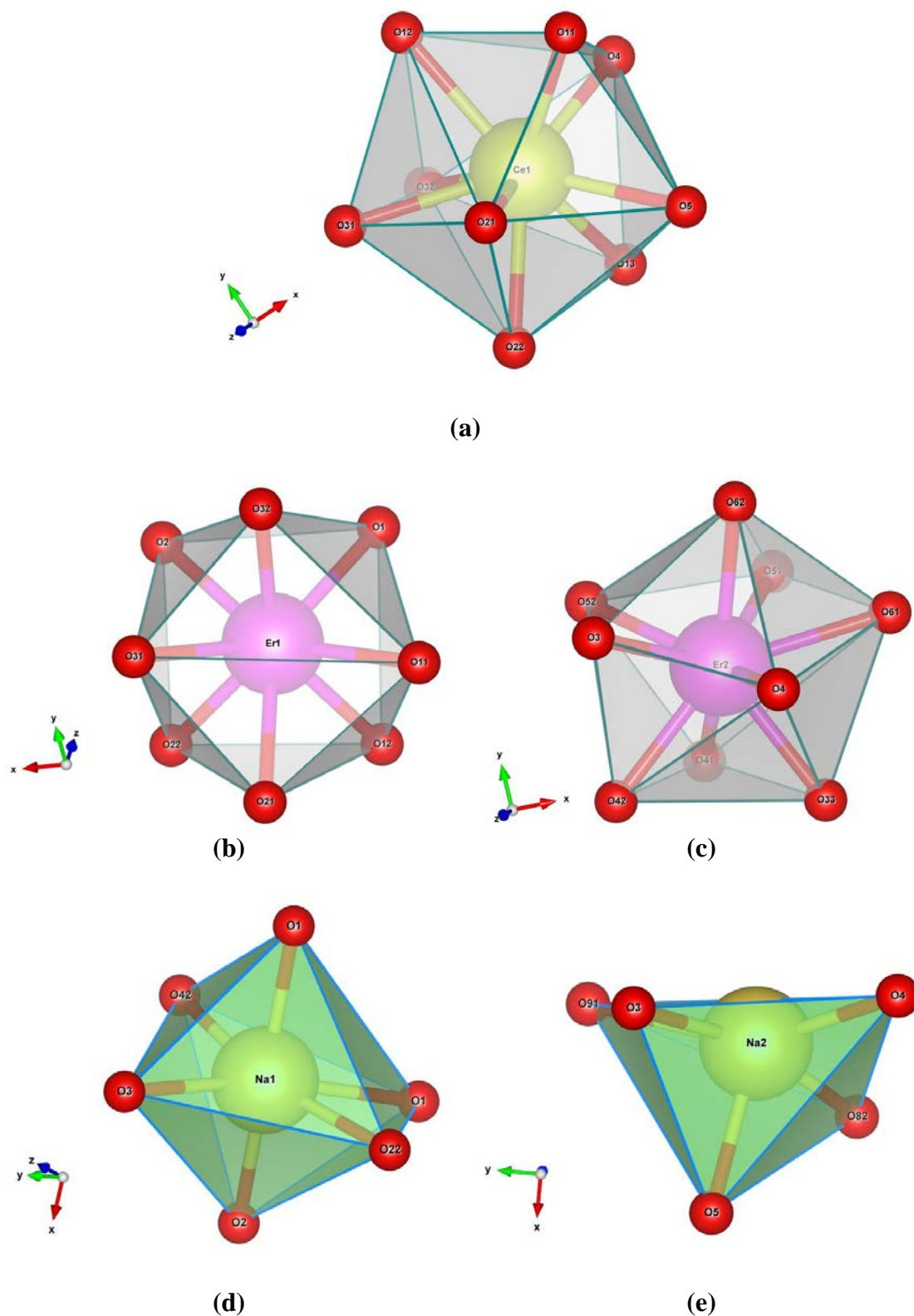
Figure 4.5: The polyhedral views showing the geometries of the coordination environments of: **(a)** Ce(III) in **1**; (**b** and **c**) the eight- and nine-coordinate Er(III) ions in **4**; (**d** and **e**) six- and five-coordinate Na(I) ions in **5**.

For all the coordination compounds, there is no significant distortions from the ideal polyhedra (CShM values ≤ 3) [40,43,44]. There is a better fit to the ideal polyhedra as the atomic number of the 4*f* elements increase, as evidenced by the smaller shape measure values. This is due to the shorter and stronger bonds, as well as decreased room for angular distortions as the metal ions get smaller [43]. The volume of the coordination polyhedra is controlled by the size of the metal ions, as well as the coordination numbers. Smaller metal ions and lower coordination numbers result in smaller polyhedral volume. A comparison between the Ln(III) coordination environments of all the complexes reflect the highest polyhedral volume for the nine-coordinate Ce(III) compound (32.4845 Å^3), and the smallest polyhedron size for the eight-coordinate Er1 in **4** (22.5763 Å^3).

4.3.5   X-ray crystallography

The reactions in aqueous mixtures between the lanthanide nitrate salts and **Hdmp** (Figure 4.6a), in the presence of NaOH, yield interesting Ln(III)–organic coordination polymers, formulated as; $\{[Ln(Hpma)_3(MeOH)(H_2O)]\cdot 2MeOH\}_n$ (Ln = Ce and Nd), $\{[Gd_2(Hpma)_6(MeOH)_4]\cdot 6MeOH\}_n$, $\{[Er_2(Hpma)_6(MeOH)(H_2O)_3]\cdot 2MeOH\}_n$ and $[Ln_2Na_2(Hpma)_8(EtOH)(H_2O)_6]_n$ (Ln = Nd and Gd) (Figures 4.6b-g; see Tables 4.3a and 4.3b for bond parameters). X-ray diffraction studies of the single crystals revealed that the isostructural complexes **1** and **2** crystallise in the monoclinic space groups *I2/a*, whereas **3**–**6** give the triclinic crystal structures, belonging to the *P-1* space group. Complexes **5** and **6** are also structurally analogous to each other. The polymeric complexes feature Ln-Hpma moieties bridged by **Hpma**⁻, giving one-dimensional (1D) zig-zag chains of the –Ln–O–C–O–Ln– type, with the Ln⋯Ln separation varying from 6.271 Å (complex **2**) to 6.843 Å (complex **5**), thus showing well isolated mononuclear units (Figure 4.6h) [45-47]. The chelating and bridging modes of **Hpma**⁻ *via* only the oxygen atoms are indicated in Figure 4.6i [48-50].

Three bidentate **Hpma**⁻ ligands, one methanol and one water molecule form mononuclear units of **1** and **2**, which are connected to each another through the fourth bridging oxamate ligand (Figures 4.6b and 4.6c). The Ce(III) and Nd(III) ions are

nine-coordinate with the oxygen atoms bonded to form a distorted spherical tricapped trigonal prism geometry. Furthermore, there are two non-coordinating methanol molecules present in the lattices.
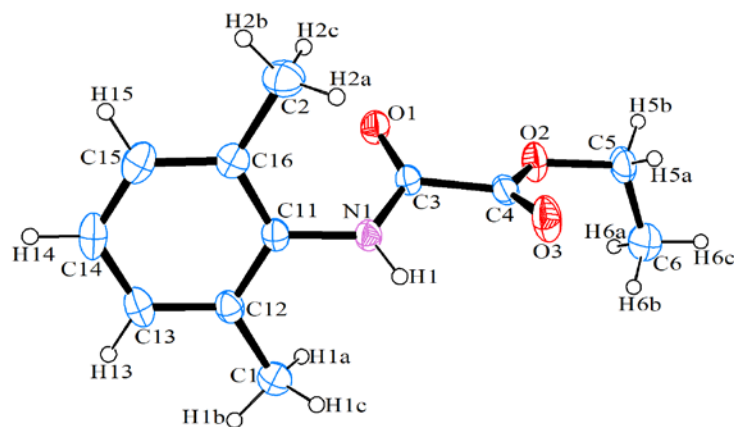
Figure 4.6a: *ORTEP* view of the proligand **Hdmp** showing 50 % probability displacement ellipsoids and atom-labelling.
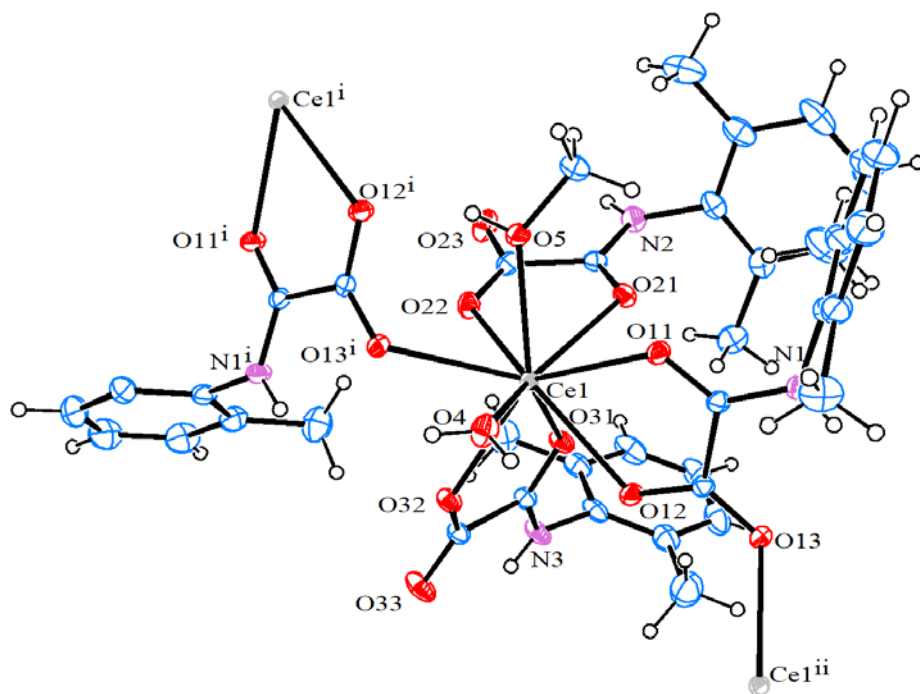
Figure 4.6b: The structure of the molecule present in complex **1** (30 % probability ellipsoids).
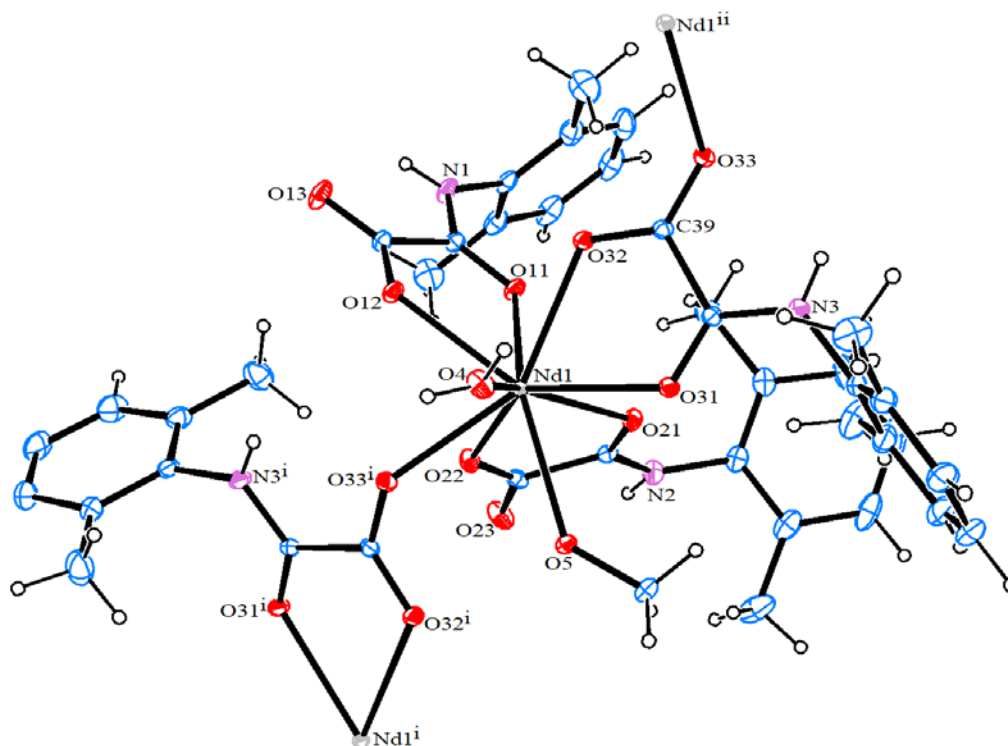
Figure 4.6c: *ORTEP* view of complex **2** (30 % probability ellipsoids).
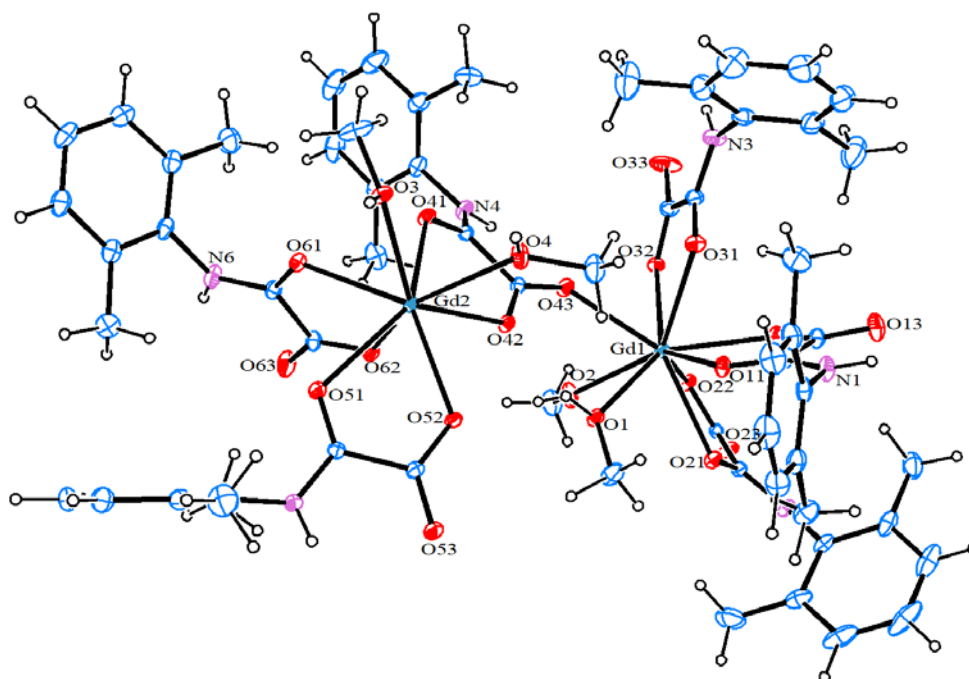
Figure 4.6d: Molecular structure of the dinuclear unit of **3** with displacement ellipsoids drawn at the 30 % probability level.
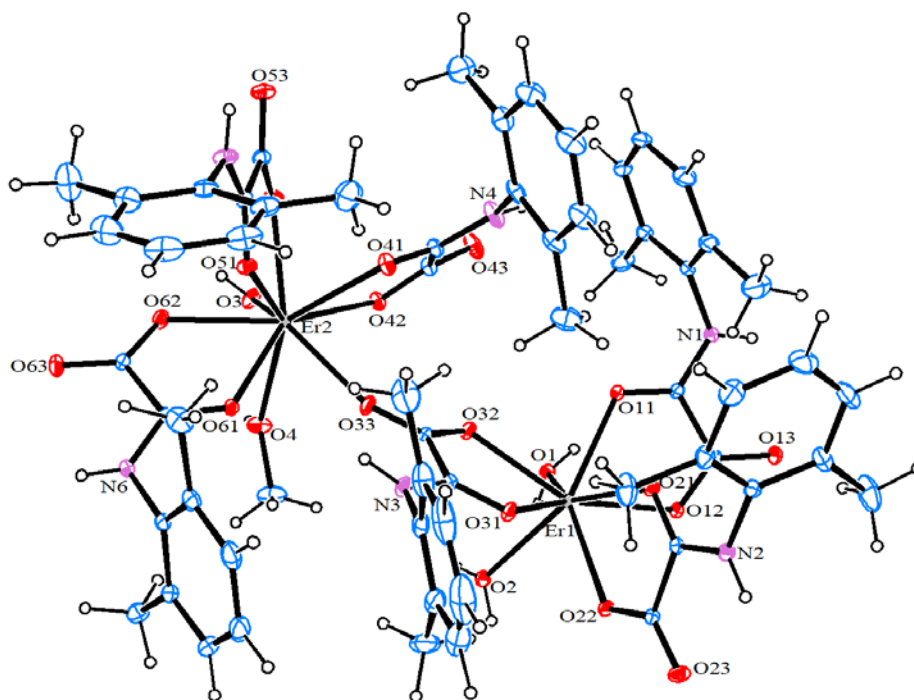
Figure 4.6e: *ORTEP* view of the dinuclear unit of **4** showing 30 % probability displacement ellipsoids and partial atom-labelling scheme.
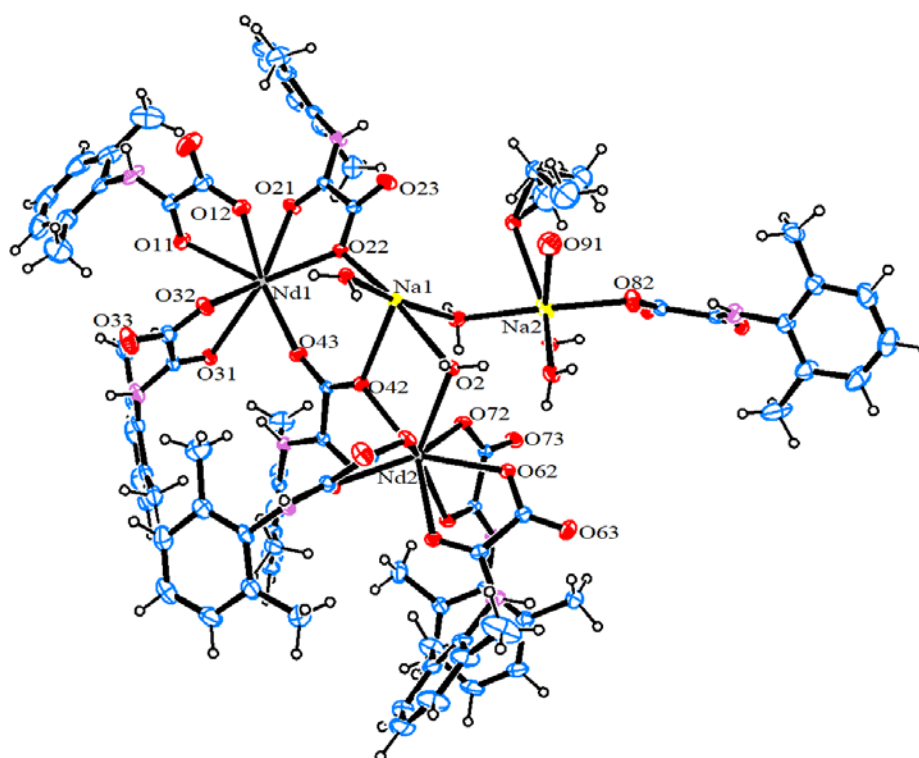
Figure 4.6f: *ORTEP* diagram (thermal ellipsoids at 30 % probability) with a partial atom-numbering scheme for the heterometallic complex found in **5**.
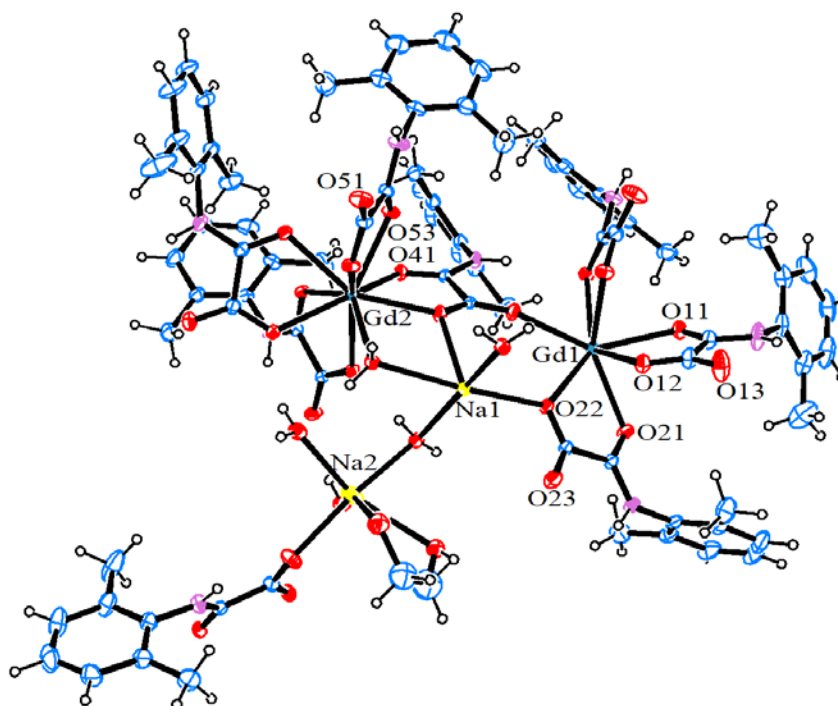
Figure 4.6g: *ORTEP* view of the heterometallic unit of complex **6** showing 30 % probability displacement ellipsoids and the atom-labelling.
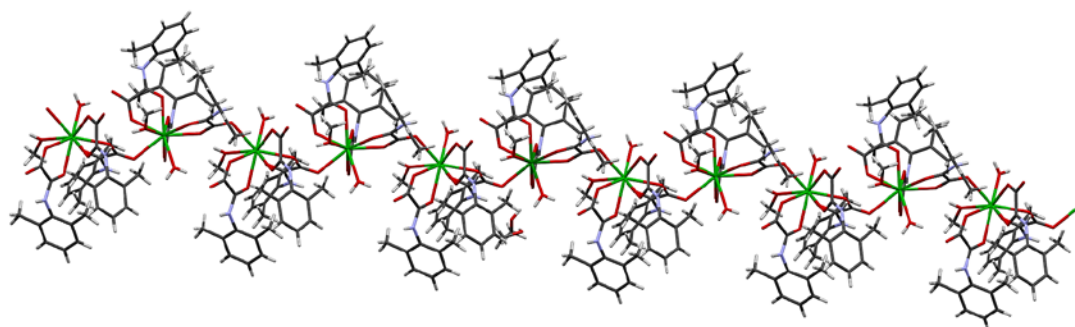
Figure 4.6h: One-dimensional zig-zag network in **1** constructed by μ_2-**Hpma**⁻ (<u>Key</u>: Ln = green, C = gray, N = blue, O = red).

Complex **3** is characterised by dinuclear units containing similar spherical capped square antiprism GdO_9 cores, with each nona-coordinate environment constructed from three chelating **Hpma**⁻ ligands, two methanol molecules and one oxygen atom from the bridging (tridentate) **Hpma**⁻ (Figure 4.6d). Complex **4** gives metal centres comprising distinct $Er(1)O_8$ (SAPR-8) and $Er(2)O_9$ (CSAPR-9) cores linked by chelating/bridging **Hpma**⁻ (Figure 4.6e). The Er1 coordination sphere is made up of

three bidentately coordinated **Hpma**⁻ ligands and two water molecules, whilst the nine-coordinate Er2 ion is surrounded by three η^2-bonded oxamates, one methanol, one water molecule and an *O*-atom from the tridentate **Hpma**⁻. In addition, the metal complexes **3** and **4** feature lattice methanol solvates (six for complex **3** and two for complex **4**).
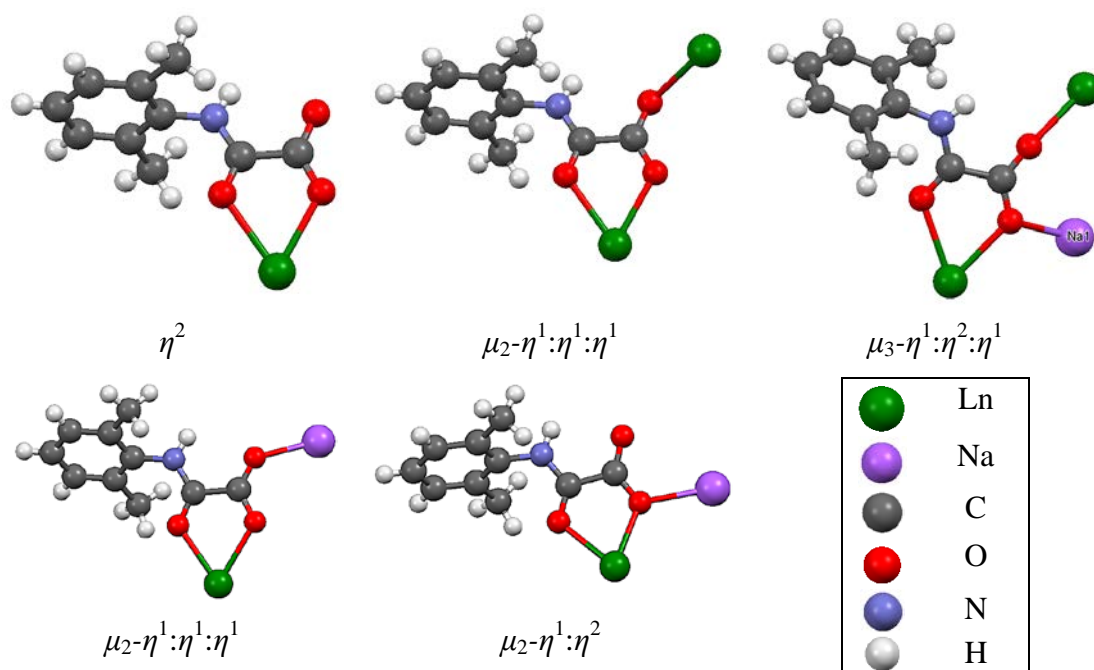
Figure 4.6i: The coordination modes of **Hpma**⁻ in the metal complexes (binding modes containing Na(I) ions belong to **5** and **6** only) [48-50].

Coordination compounds **5** and **6** yielded lanthanide(III)-sodium(I) complexes, with Ln₂Na₂ (Ln = Nd and Gd) cores bridged by the μ_2-η^1:η^1:η^1, μ_3-η^1:η^2:η^1 and μ_2-η^1:η^2 oxamate ligands, as well as by the μ_2-H₂O oxygen atoms (Figures 4.6f, 4.6g and 4.6j) [48-50]. The asymmetric unit contains two nine-coordinate Ln(III) ions with CSAPR-9 geometry. The Ln1 atom is surrounded by three η^2 **Hpma**⁻, two *O*-atoms from the bidentately coordinated μ_2-η^1:η^2 **Hpma**⁻ and one oxygen provided by μ_3-η^1:η^2:η^1 bonded **Hpma**⁻, whereas the O₉ donor-set of Ln2 is fulfilled with six oxygen atoms from *O,O*-donor oxamate ligands (O52, O53, O61, O62, O71, O72), two oxygen atoms from a bridging **Hpma**⁻ and a μ_2-O bridging water molecule. Each Na1 is in a

hexa-coordinate environment, linked to four μ_2-O atoms of water, and two oxygen atoms from the μ_2-η^1:η^2 and the μ_3-η^1:η^2:η^1 **Hpma⁻**, while the vacant octahedron geometry of Na2 is constructed from five *O*-atoms (two H_2O molecules, one μ_2-O_{water}, one disordered ethanol and one bridging oxygen of **Hpma⁻**). The crystal structures of the heterometallic complexes feature rhomboidal Ln-O-Na-O cores, where bridging occurs through the *O*-atoms of **Hpma⁻** and water molecules, having bridging oxygen atoms lying almost equidistant between the metal ions [M-O_{Hpma-} and M-O_{water} (M = Nd, Gd and Na) bonds vary from 2.3776–2.469(2) and 2.5150(16)–2.566(2) Å, respectively] [51]. The O-M-O, Ln-O_{water}-Na and Ln-O_{Hpma-}-Na bond angles in these rhomboids are in the ranges 65.83(6)–67.0397), 107.63(8)–108.04(7) and 117.15(8)–117.17(7)^o, respectively. The Ln-O_{water}-Na bond angles do not display any anomalies and compare well with the 108.66(9)^o Gd–O–Gd angle in [$Gd_2(bfa)_4L_2$]CH_2Cl_2 (bfa = benzoyltrifluoroacetone and **HL** = 2-[[(4-methylphenyl)imino]methyl]-8-hydroxyquinoline) [52]. The Na(I) ions are connected to each other *via* the water oxygen atoms, with Na1–O_{water}–Na2 angles of 120.32^o (complex **5**) and 121.19(8)^o (complex **6**).
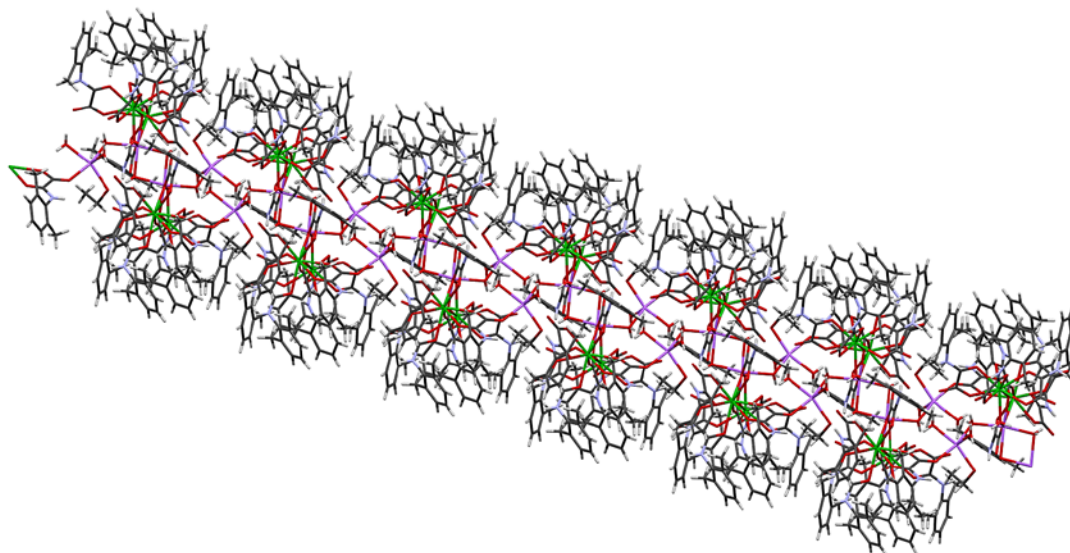
Figure 4.6j: A 1D network in **5** and **6** linked *via* μ_2-**Hpma⁻**, μ_3-**Hpma⁻**, as well as μ_2-H_2O (<u>Key</u>: Ln = green, Na = purple, C = gray, N = blue, O = red).

All metal complexes are comprised of bidentately (η^2) coordinated **Hpma⁻** ligands, leading to five-membered chelate rings with O-Ln-O angles of 63.51(4)–69.80(6)^o

and Ln-O$_{Hpma^-}$ distances of 2.2722(18)–2.4752(12) Å, which are comparable to those in the previously reported dysprosium(III) complex containing *N*-(2,6-dimethylphenyl) oxamic acid [Dy-O bond lengths = 2.340(2)−2.407(2) Å; O-Dy-O bite angles = 67.36(8) to 68.04(7)°] (Tables 4.3a and 4.3b) [15]. The shortening of the C4-O2 bond [1.3138(17) Å] of **Hdmp** in complexes [e.g. O12-C19 = 1.2564(19) Å in **1**] suggest a double bond character in **Hpma**$^-$ as a result of delocalisation across the oxamate moiety [53]. The Ln-O$_{water}$ and Ln-O$_{MeOH}$ distances spanning the ranges 2.3369(19)–2.5049(13) Å and 2.391(2)–2.5404(12) Å, respectively, are similar to those in the triaqua[2,6-diacetylpyridine bis(benzoylhydrazone)]methanollanthanide(III) complexes reported by Kachi-Terajima *et al.* (2018) [Ln-O$_{water}$ = 2.313(2)–2.428(2) Å and Ln-O$_{MeOH}$ = 2.472(2)–2.4867(18) Å, Ln = Tb and Dy] [54]. The Na-O$_{oxamate}$ bond lengths of **5** and **6** [spanning the range 2.336(3)–2.476(2) Å], compare well with the bond parameters in the alkaline salts of bis(oxamato)palladate(II) complexes reported by Fortea-Pérez *et al.* (2014) [Na-O$_{oxamate}$ = 2.273(5)–2.909(5) Å] [55]. The decrease in the Ln-O distances with increasing atomic number is observed, as can be expected as a result of the lanthanide contraction [46,50,56].

The crystal structures of **1**–**6** are further stabilised by networks of medium strength hydrogen bonds of the N-H⋯O and O-H⋯O type, as presented in Figure 4.6k and Table 4.3c [36,57-59]. Only intermolecular N-H⋯O bonds [H⋯O = 2.232(17)–2.408(17) Å] are found in the proligand, which are satisfied by the amide N-H groups of one molecule and the oxygens of the oxamate group from a neighbouring molecule. It is important to note that these hydrogen bond interactions in the metal complexes involve the crystallographic methanol solvents, and have *DA* (Donor⋯Acceptor) distances in the range 2.644(3)–3.182(3) Å. The N-H⋯O bonds are apparent between the amide N-H (donor) and the solvent molecules, and the *O*-atoms of **Hpma**$^-$ as acceptors. As observed in **1** and **2**, the two lattice methanol solvents along with the coordinated water and the bonded oxygen atoms of **Hpma**$^-$ play a key role in establishing O-H⋯O interactions. In **3**, the methanol molecules in the primary and secondary coordination spheres act as donors, assuring connectivity with the oxygen atoms of the oxamate ligands. As shown in Figure 4.6k, the coordinated water

molecules of **4** form hydrogen bonds with the lattice methanol molecules, for example O2-H2A···O5 with *DA* distance of 2.663(3) Å. The crystal structures of the heterometallic complexes **5** and **6** are also stabilised by a variety of hydrogen bonds, some of which involve monodentate and bridging water molecules as hydrogen donors and oxamate oxygens as acceptors. The crystal packing of the metal complexes is supplemented by weak contacts: C-H$_{Hpma–}$···O$_{Hpma–}$ (**1**–**6**), C-H$_{MeOH}$···O$_{Hpma–}$ (**2**–**4**), C-H$_{Hpma–}$···O$_{MeOH}$ (**3**), C-H$_{MeOH}$···O$_{MeOH}$ (**4**), C-H$_{Hpma–}$···O$_{H2O}$ (**5**), as well as C-H$_{Hpma–}$···N$_{Hpma–}$ (**5** and **6**) [60].

4.3.6   Atomic charge analysis of the ligands

The total atomic charges of the anionic oxamate were determined by the Natural Population Analysis (NPA) method, and are presented in graphical form shown in Figure 4.7b (see Figure 4.7a for atom-numbering) [61]. According to the NPA method, the obtained atomic charges indicate that C22, C23 and H24 have larger positive atomic charges compared to the other hydrogen atoms. Atoms O1, O2 and O3 exhibit the most negative atomic charges (-0.6720, -0.76420 and -0.79536 in DMSO). Natural population analysis predicted the same tendencies on the net atomic charges of the aforementioned atoms in the gas phase, with the charges on O1, O2 and O3 being -0.63226, -0.70104 and -0.78570, respectively. This explains the ability of the atoms to network with the positively-charged component, with O3 having a stronger coordination ability to form stronger (shorter) Ln-O bonds [62]. The calculated results thus concur with most of the experimental Ln-O$_{oxamate}$ results obtained through X-ray diffraction studies. The nitrogen atom N4 displays electronegativity (-0.63544 in DMSO and -0.67626 in the gas phase) lower than that of the oxygens. The electronegative *O*-atoms therefore have the tendency to donate electrons, while the electropositive carbon and hydrogen atoms have a tendency to accept electrons [61,63,64]. The presence of large negative charges on the oxygen and nitrogen atoms, and positive charges on the hydrogen atoms suggest the possibility of intermolecular interactions in the crystal structure [65].

Table 4.3a: Selected geometric parameters (Å, °) for **Hdmp** and lanthanide complexes **1**–**3**.

Hdmp		{[Ln(Hpma)$_3$(MeOH)(H$_2$O)]·2MeOH}$_n$				{[Gd$_2$(Hpma)$_6$(MeOH)$_4$]· 6MeOH}$_n$	
		1 (Ln = Ce)		**2** (Ln = Nd)		3	
Bond lengths (Å)							
O1-C3	1.2140(17)	Ce1-O4	2.5049(13)	Nd1-O4	2.4723(18)	Gd1-O1	2.459(2)
O2-C4	1.3138(17)	Ce1-O5	2.5404(12)	Nd1-O5	2.5091(15)	Gd1-O2	2.478(2)
O2-C5	1.4651(19)	Ce1-O11	2.5296(12)	Nd1-O11	2.5333(15)	Gd1-O11	2.3901(19)
O3-C4	1.1914(19)	Ce1-O12	2.5190(10)	Nd1-O12	2.4599(15)	Gd1-O12	2.4376(19)
N1-C3	1.3384(17)	Ce1-O21	2.5457(12)	Nd1-O21	2.5162(15)	Gd1-O21	2.5087(19)
N1-C11	1.4286(17)	Ce1-O22	2.4752(12)	Nd1-O22	2.4421(15)	Gd1-O22	2.3782(18)
C1-C12	1.502(2)	Ce1-O31	2.5684(12)	Nd1-O31	2.4967(15)	Gd1-O31	2.4824(19)
N1-H1	0.846(16)	Ce1-O32	2.4926(12)	Nd1-O32	2.4950(14)	Gd1-O32	2.4010(18)
		Ce1-O13a	2.5469(11)	Nd1-O33b	2.5251(15)	Gd1-O43	2.4320(19)
		Ce···Ce	6.289	Nd···Nd	6.271	Gd···Gd	6.294
Bond angles (°)							
C4-O2-C5	116.99(12)	O11-Ce1-O12	63.51(4)	O11-Nd1-O12	64.37(5)	O11-Gd1-O12	67.24(6)
C3-N1-C11	122.93(12)	O21-Ce1-O22	65.11(4)	O21-Nd1-O22	65.92(5)	O21-Gd1-O22	66.10(6)
C3-N1-H1	115.8(11)	O31-Ce1-O32	63.52(4)	O31-Nd1-O32	63.99(5)	O31-Gd1-O32	66.13(6)
O1-C3-N1	125.49(13)					O41-Gd2-O42	66.52(6)
N1-C3-C4	112.58(12)					O51-Gd2-O52	66.68(6)
O2-C4-O3	126.63(14)					O61-Gd2-O62	66.49(6)

The accrual of charges on selected atoms and the distribution of electrons in the core, valence and Rydberg sub-shells of **Hpma$^-$**, are shown in Table 4.4. Furthermore, NPA in the solvent shows that 102 electrons in the ligand have the sub-shell distributions as follows:

            Core: 27.99986 (99.9995 % of 28)

            Valence: 73.60526 (99.4666 % of 74)

            Rydberg: 0.39488 (0.3871 % of 102)

Molecular electrostatic potential (MEP) mapping was applied in the interpretation and prediction of the reactive behaviour of **Hpma$^-$** in nucleophilic and electrophilic reactions, as well as in depicting the shape of the oxamate ligand (Figure 4.7c) [61,66]. This is important in predicting chemical reactivities in hydrogen bond interactions and biological systems [67]. The oxygen atoms of **Hpma$^-$** are associated

with a strong negative molecular electrostatic potential region. The concentration of maximum electron density on the oxygen atoms enables interaction with trivalent metal ions to form *O,O*-donor chelates, as well as the participation of the remaining *O*-atom in bridging. In addition to bonding with Ln(III) ions, the MEP region around the oxygen atoms suggest that these oxygen atoms can also act as hydrogen bond acceptors, which is consistent with X-ray analysis, which stabilises the complex. The nitrogen atom comparatively possesses a smaller negative MEP region.

Table 4.3b: Selected bond lengths (Å) and angles (°) for metal complexes **4–6**.

{[Er$_2$(Hpma)$_6$(MeOH)(H$_2$O)$_3$]·2 MeOH}$_n$		[Ln$_2$Na$_2$(Hpma)$_8$(EtOH)(H$_2$O)$_6$]$_n$	
4		**5** (Ln = Nd)	**6** (Ln = Gd)
Bond lengths (Å)		**Bond lengths (Å)**	
Er1-O1	2.3537(17)	Ln1-O11	2.496(2)	2.449(2)
Er1-O2	2.3369(19)	Ln1-O12	2.496(2)	2.4538(19)
Er1-O11	2.3240(18)	Ln1-O21	2.475(2)	2.4296(17)
Er1-O12	2.3547(18)	Ln1-O22	2.4628(19)	2.4142(17)
Er1-O21	2.4051(15)	Ln1-O31	2.5476(18)	2.5015(16)
Er1-O22	2.2722(18)	Ln1-O32	2.500(2)	2.4460(18)
Er1-O31	2.4227(18)	Ln1-O43	2.429(2)	2.3930(18)
Er1-O32	2.3681(18)	Ln1-O81b	2.477(2)	2.4365(18)
Er2-O33	2.3333(18)	Ln1-O83b	2.494(2)	2.4406(18)
Er···Er	6.497	Na1-O1	2.326(2)	2.310(2)
		Na1-O2	2.566(2)	2.544(2)
Bond angles (°)		Na1-O3	2.388(2)	2.385(2)
O11-Er1-O12	69.75(6)	Na1-O22	2.476(2)	2.460(2)
O21-Er1-O22	69.80(6)	Na1-O42	2.386(2)	2.3776(18)
O31-Er1-O32	67.12(6)	Na1-O1a	2.382(2)	2.375(2)
O41-Er2-O42	66.97(5)	Ln···Ln	6.843	6.768
O51-Er2-O52	67.58(6)	Na···Na	4.171	4.169
O61-Er2-O62	67.72(6)			
		Bond angles (°)	
		O11-Ln1-O12	64.90(7)	65.92(6)
		O21-Ln1-O22	66.26(7)	67.51(6)
		O22-Ln1-O43	76.07(7)	75.19(6)
		O31-Ln1-O32	64.05(6)	65.29(6)
		O41-Ln2-O42	64.35(6)	65.49(6)
		O52-Ln2-O53	65.41(6)	66.59(6)
		O61-Ln2-O62	66.04(6)	67.26(6)
		O71-Ln2-O72	65.56(6)	66.68(5)

Complex **1**   Complex **3**

Complex **4**   Complexes **5** and **6**
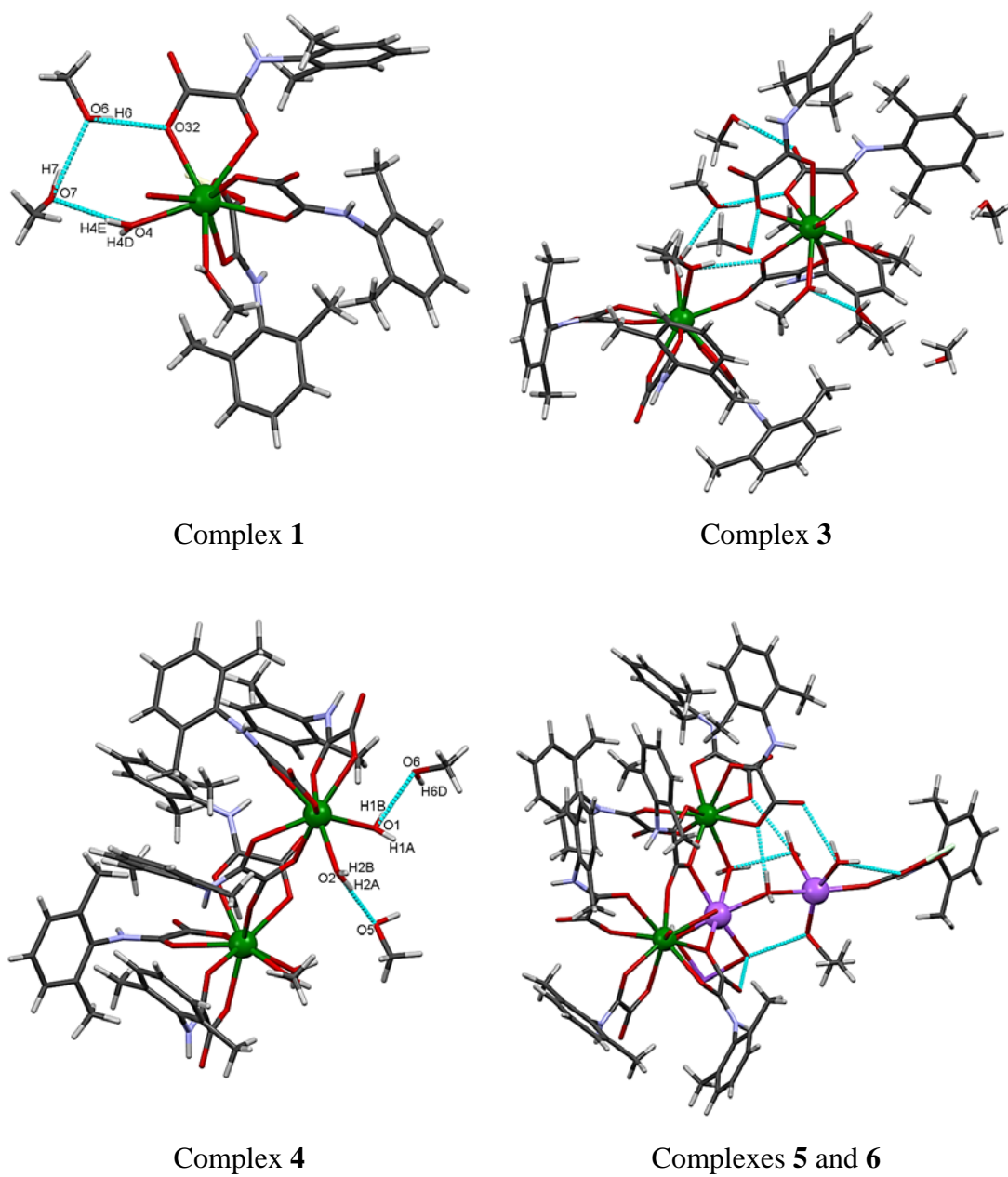
Figure 4.6k: Hydrogen bonding interactions in metal complexes **1** and **3**–**6**.

Table 4.3c: Selected hydrogen bonding geometries (Å, °) for **Hdmp** and **1–4**.

		Hdmp		
D-H⋯*A*	*D*-H	H⋯*A*	*D*⋯*A*	*D*-H⋯*A*
N1-H1⋯O3	0.846(16)	2.408(17)	2.7389(17)	104.0(13)
N1-H1⋯O1	0.846(16)	2.232(17)	3.0519(16)	163.3(16)
C1-H1C⋯O1	0.9600	2.5900	3.448(2)	149.00
C2-H2C⋯O1	0.9600	2.5000	3.083(2)	119.00

		Complex 1		
D-H⋯*A*	*D*-H	H⋯*A*	*D*⋯*A*	*D*-H⋯*A*
N1-H1⋯O13	0.84(2)	2.35(2)	2.7156(17)	106.7(16)
N1-H1⋯O6	0.84(2)	2.13(2)	2.9335(18)	160.6(18)
N2-H2⋯O23	0.80(2)	2.23(2)	2.6601(19)	114.4(17)
N3-H3⋯O33	0.81(2)	2.387(19)	2.7194(18)	105.5(16)
O4-H4D⋯O23	0.831(16)	1.936(16)	2.7506(17)	166(2)
O4-H4E⋯O7	0.839(16)	2.000(17)	2.825(2)	168(2)
O5-H5⋯O12	0.832(14)	1.934(18)	2.7157(16)	156.2(19)
O6-H6⋯O32	0.8400	1.8700	2.6916(16)	164.00
O7-H7⋯O6	0.8400	1.9200	2.744(2)	167.00

		Complex 2		
D-H⋯*A*	*D*-H	H⋯*A*	*D*⋯*A*	*D*-H⋯*A*
N1-H1⋯O13	0.82(3)	2.40(3)	2.726(3)	105(2)
N2-H2⋯O23	0.83(3)	2.22(3)	2.659(3)	114(3)
N3-H3⋯O33	0.82(3)	2.35(3)	2.719(2)	108(2)
N3-H3⋯O6	0.82(3)	2.16(3)	2.935(3)	158(3)
O4-H4A⋯O7	0.870(17)	1.984(18)	2.844(3)	170(3)
O4-H4B⋯O23	0.84(2)	1.94(2)	2.757(2)	162(3)
O6-H6⋯O12	0.8400	1.8700	2.692(2)	164.00
O7-H7⋯O6	0.8400	1.9200	2.741(3)	167.00

		Complex 3		
D-H⋯*A*	*D*-H	H⋯*A*	*D*⋯*A*	*D*-H⋯*A*
N1-H1⋯O9	0.89(3)	2.10(3)	2.845(4)	141(3)
N1-H1⋯O13	0.89(3)	2.33(4)	2.692(3)	104(3)
O1-H1D⋯O42	0.83(3)	1.90(3)	2.694(3)	159(3)
N2-H2⋯O23	0.88(2)	2.34(3)	2.725(3)	107(2)
O2-H2D⋯O6	0.81(4)	1.88(4)	2.681(3)	169(3)
O3-H3D⋯O22	0.84(3)	1.88(3)	2.685(3)	161(3)
N4-H4⋯O43	0.88(2)	2.39(3)	2.731(3)	103(2)
N4-H4⋯O70	0.88(2)	1.94(2)	2.802(3)	164(3)
O5-H5D⋯O63	0.8400	2.0000	2.796(3)	158.00

		Complex 4		
D-H⋯*A*	*D*-H	H⋯*A*	*D*⋯*A*	*D*-H⋯*A*
N1-H1⋯O13	0.89(3)	2.37(3)	2.720(3)	104(2)
N1-H1⋯O63	0.89(3)	1.99(3)	2.825(3)	155(3)
O1-H1A⋯O23	0.84(2)	1.81(2)	2.649(2)	175(4)
O2-H2A⋯O5	0.83(2)	1.83(2)	2.663(3)	175(2)
O2-H2B⋯O12	0.84(4)	2.12(4)	2.954(3)	175(4)
O3-H3A⋯O1	0.80(4)	1.96(4)	2.755(3)	172(4)
O3-H3B⋯O42	0.78(4)	2.24(4)	2.929(2)	149(5)
O6-H6D⋯O62	0.8400	2.2400	2.993(3)	149.00
O6-H6D⋯O63	0.8400	2.2600	3.012(3)	150.00

D = donor, *A* = acceptor
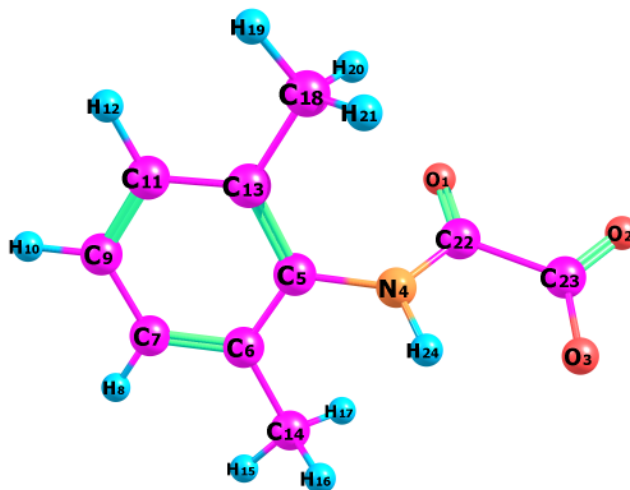
Figure 4.7a: Optimised B3LYP/aug-cc-pVTZ molecular structure of **Hpma⁻** in DMSO.
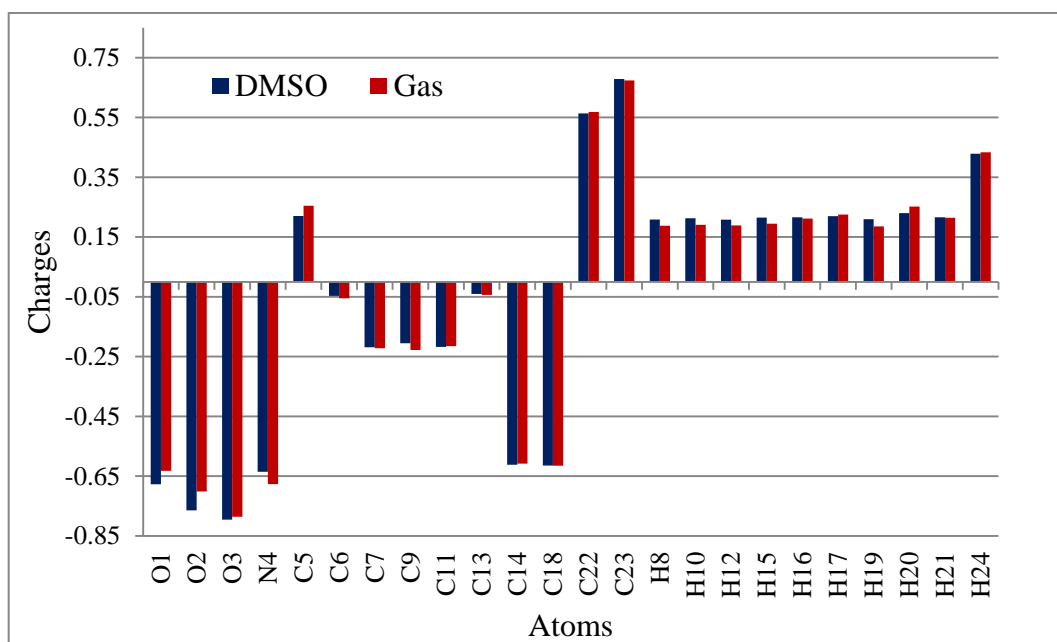
Figure 4.7b: The natural charge distribution of **Hpma⁻** at DFT/B3LYP/aug-cc-pVTZ in the gas phase and DMSO.

Table 4.4: Accrual of natural charges in the core, valence and Rydberg orbitals for selected atoms of **Hpma**$^-$ in DMSO.

Atom	Charge	Core	Valence	Rydberg	Total
O1	-0.67720	2.00000	6.65040	0.02680	8.67720
O2	-0.76420	2.00000	6.73769	0.02651	8.76420
O3	-0.79536	2.00000	6.76949	0.02588	8.79536
N4	-0.63544	1.99999	5.60139	0.03406	7.63544
C23	0.67881	1.99999	3.26991	0.05129	5.32119
C18	-0.61449	1.99999	4.60310	0.01140	6.61449
H12	0.20813	0.00000	0.78975	0.00213	0.79187
H24	0.42881	0.00000	0.56567	0.00553	0.57119
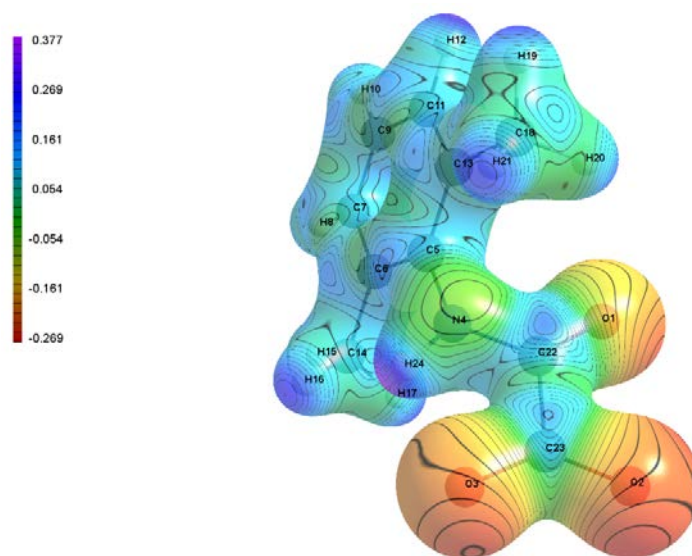
Figure 4.7c: The molecular electrostatic potential map of **Hpma**$^-$ evaluated using the B3LYP/aug-cc-pVTZ method in DMSO.

4.3.7 Frontier molecular orbital analysis and global and chemical reactivity descriptors

Some of the most imperative parameters for biological chemistry, chemical reactivity and drug design, like the *HOMO* (highest unoccupied molecular orbital), *LUMO* (lowest unoccupied molecular orbital) and the *HOMO-LUMO* gaps of **Hpma**$^-$ were calculated using the basis set B3LYP/aug-cc-pVTZ and visualised from computed data using *Avogadro* software (Figure 4.8 and Table 4.5) [68]. The *HOMO*, *HOMO*-1 (second highest) and *HOMO*-2 (third highest) energies in order are -6.233, -6.554 and -6.654 eV, whereas the *LUMO*, *LUMO*+1 (second lowest) and *LUMO*+2 (third

lowest) was calculated to be -0.784, -0.339 and -0.245 eV. The observed energy gaps pertaining to the energy needed to achieve the electronic transitions between the *HOMO–LUMO*, *HOMO*-1–*LUMO*+1 and *HOMO*-2–*LUMO*+2 are 5.449, 6.215 and 6.409 eV, respectively. These energy gaps play an important role in the elucidation of the chemical stability of the molecule, with a highly stable molecule depicted by a high gap, and a low energy gap being typical of high reactivity [68,69]. The ionisation potential (I = $-E_{HOMO}$ = 6.233 eV) and electron affinity (A = $-E_{LUMO}$ = 0.784 eV) were predictable from the *HOMO* and *LUMO* energy values [68].
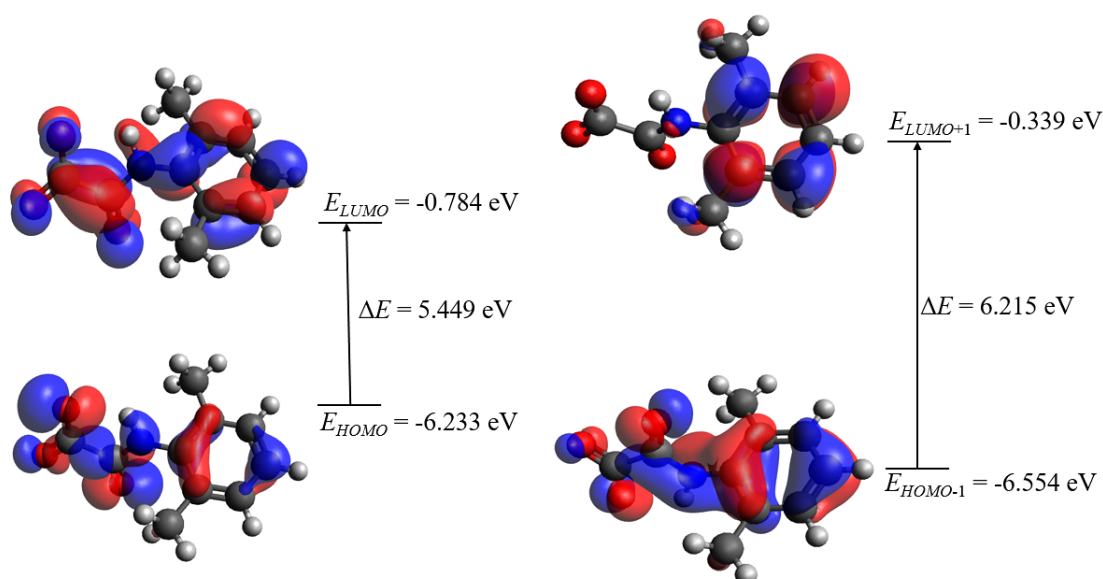
Figure 4.8: The frontier molecular orbitals plot of **Hpma⁻** showing *HOMO-LUMO* energy gaps for vicinal orbitals. An isovalue of 0.03 was used in creating orbital surfaces.

The global reactivity descriptors, such as chemical potential (μ), hardness (η), softness (σ), electrophilicity index (ω) and electronegativity (χ_{m}), were determined by resorting to ionisation potential and electron affinity obtained from the *HOMO* and *LUMO* energies, with results being μ = -3.509 eV, η = 2.725 eV, σ = 0.367 eV^{-1}, ω = 2.259 eV and χ_{m} = 3.509 eV [68,69]. These parameters are an efficient tool in providing theoretical insights into the biological activity and behaviour of the whole chemical species when the compound enters the body as an anticancer drug [70,71]. Calculations for the local reactivity parameters: electrodonating (ω^{-}) power,

electroaccepting (ω^+) power and the net electrophilicity ($\Delta\omega^\pm$), are also included (Table 4.5) to give information regarding the behaviour of specific sites in the molecule, which is crucial in reactivity elucidation and selectivity trends [72-74]. The electrodonating power ($\omega^- = 4.354$ eV) shows the propensity to donate charge, whereas the electroaccepting capacity ($\omega^+ = 0.845$ eV) indicates the tendency of a system to accept charge; with the ω^- value of the molecule being more important than its electroaccepting ability [73-75]. The net electrophilicity (electron-accepting ability relative to its electron-donating capacity) is equal to 5.199 eV [76].

Table 4.5: Global and chemical parameters of **Hpma$^-$** calculated with the B3LYP density functional with the aug-cc-pVTZ basis set and the SCRF-CPCM solvation model using DMSO as the solvent (Softness in eV^{-1} and other descriptors are in eV).

Global and chemical reactivity descriptor	Symbols	Values (eV)
Energy of *HOMO*	E_{HOMO}	-6.233
Energy of *LUMO*	E_{LUMO}	-0.784
Energy of *HOMO*-1	$E_{HOMO\text{-}1}$	-6.554
Energy of *LUMO*+1	E_{LUMO+1}	-0.339
Energy of *HOMO*-2	$E_{HOMO\text{-}2}$	-6.654
Energy of *LUMO*+2	E_{LUMO+2}	-0.245
First energy gap	$\Delta E = LUMO - HOMO$	5.449
Second energy gap	$\Delta E = LUMO+1 - HOMO\text{-}1$	6.215
Third energy gap	$\Delta E = LUMO+2 - HOMO\text{-}2$	6.409
Ionisation energy (I)	$-E_{HOMO}$	6.233
Electron affinity (A)	$-E_{LUMO}$	0.784
Hardness (η)	$\dfrac{(I-A)}{2}$	2.725
Chemical potential (μ)	$\dfrac{-(I+A)}{2}$	-3.509
Softness (σ)	$\dfrac{1}{\eta}$	**0.367 eV^{-1}**
Electrophilicity index (ω)	$\dfrac{\mu^2}{2\eta}$	2.259
Electronegativity (χ_m)	$\dfrac{I+A}{2}$	3.509
Electrodonating power (ω^-)	$\dfrac{(3I+A)^2}{16(I-A)}$	4.354
Electroaccepting power (ω^+)	$\dfrac{(I+3A)^2}{16(I-A)}$	0.845
Net electrophilicity ($\Delta\omega^\pm$)	$\omega^+ - (-\omega^-) = \omega^+ + \omega^-$	5.199

4.3.8   Anticancer screen

The MCF-7, HEC-1A and THP-1 cell viability was determined after exposure to 100 μM of the proligand **Hdmp**, Ln(III) nitrate salts, Ln(III) oxamate complexes and curcumin, for 24 hours. As shown in Figure 4.9, the results indicate that when exposed to $[Ce(NO_3)_3 \cdot 6H_2O]$, the cell viability of the MCF-7 cells decreased ($p < 0.05$). Likewise, $[Nd(NO_3)_3 \cdot 6H_2O]$ exerted cytotoxic effects in HEC-1A cells ($p < 0.05$). The cytotoxicities of **Hdmp**, $[Ln(NO_3)_3 \cdot xH_2O]$ (Ln = Gd and Er) and metal complexes **1–6** were also tested against the three cell lines for comparison, but no significant cytotoxicity was found ($p > 0.05$).
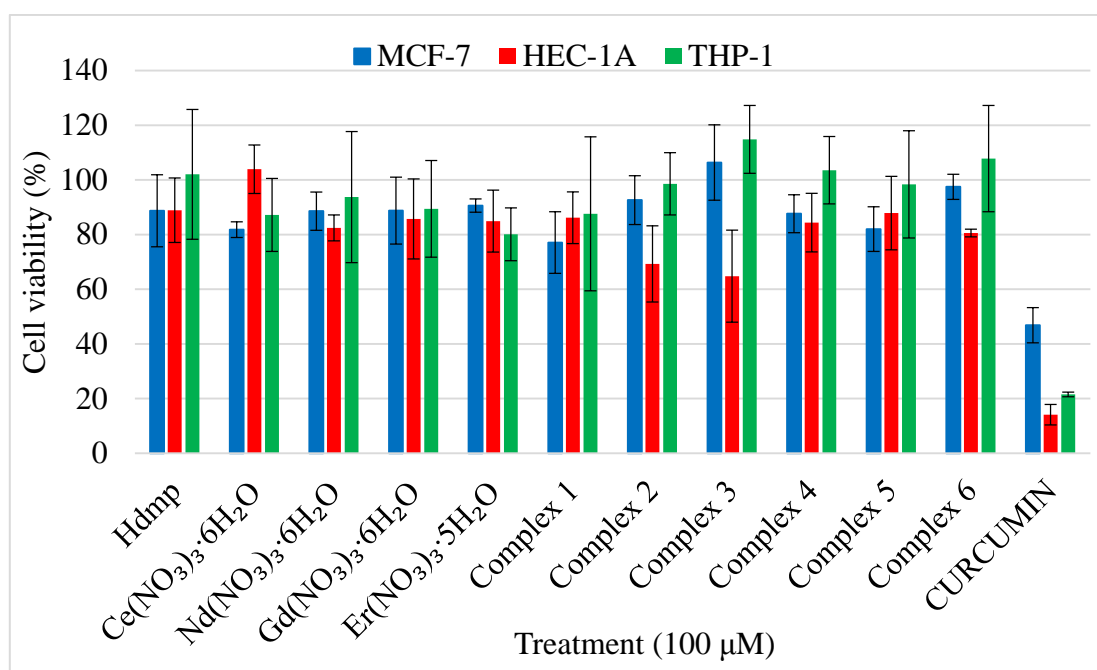
Figure 4.9: Cytotoxic effects of the compounds on MCF-7, HEC-1A and THP-1 cells using the MTT assay. Mean values of three independent experiments ± SD are shown.

The greatest cytotoxicity was exhibited by curcumin, which decreased cell viabilities to 46.8±6.46, 14.1±3.76 and 21.5±0.83 % for MCF-7, HEC-1A and THP-1 cells, respectively. The cytotoxicity of curcumin is explicated by its ability to regulate multiple cell signalling pathways, such as cell proliferation, senescence, apoptosis and protein kinase pathway [77,78].

For each assay, the viability of the THP-1 cells treated with the proligand, lanthanide salts and the coordination compounds were not significantly affected, suggesting no adverse effects on THP-1 cell line counterparts, *i.e.* primary monocytes or human peripheral blood monocytes (Figure 4.9) [79-81]. This, however, has to be validated by further *in vitro* and *in vivo* studies.

4.4   Conclusion

Syntheses of six novel oxamates of trivalent rare-earth metals (Ce, Nd, Gd and Er) in basic media have been successfully reported. The compositions and structures of these polymeric complexes have been characterised by elemental analyses, conductivity measurements, IR, UV-Vis-NIR, NMR and X-ray diffraction studies. The X-ray crystallography results indicate that **Hpma⁻** possesses a variety of chelating and bridging modes displayed by the three oxygen atoms. The units of **1**–**4** contain lattice methanol molecules, which afford with oxygen atoms needed in the formation of some O-H···O links. The oxamate ligands adopt μ_2- and μ_3-bridging modes, generating one-dimensional coordination polymers. In the heterometallic polymers **5** and **6**, interconnection of Ln(III) and Na(I) ion centres is also supplemented by the μ_2-bridging water molecules. The experimental bond parameters were in excellent agreement with related compounds in literature.

Using B3LYP/aug-cc-pVTZ level, NPA of *N*-(2,6-dimethylphenyl)oxamate has been performed to evaluate partial atomic charges. The *HOMO* and *LUMO* energies, as well as the MEP surfaces, assisted in determining chemical reactivity of the title anionic ligand. Partial atomic charges and MEP surfaces of the oxamate are corroborated by crystal data.

The MTT assay was employed to quantify MCF-7, HEC-1A and THP-1 cell populations after exposure to 100 µM of the compounds, followed by determining the reduction of mitochondrial MTT to formazan. Although no sign of anticancer activities can be observed for the title complexes, the rare-earth metal salts [Ce(NO$_3$)$_3$·6H$_2$O] and [Nd(NO$_3$)$_3$·6H$_2$O] showed modest cytotoxicity against MCF-7

and HEC-1A cells, respectively. These results indicate that these two metal salts could be potential starting materials in the development of anticancer agents. Further attempts will be concentrated on the preparation of other complexes from **Hdmp** or **Hpma**$^-$ derivatives. Since the oxamate complexes were found to be non-toxic towards cancer cells, other potential uses of the coordination compounds, such as catalysis, can also be investigated.

4.5 Supplementary information

4.5.1 Crystal data and refinements

Table S4.1a: Crystal and structure refinement data for **1** and **2**.

	1	2
Formula	$C_{31}H_{36}CeN_3O_{11}$, $2(CH_4O)$	$C_{31}H_{35}NdN_3O_{11}$, $2(CH_4O)$
M_r (g.mol^{-1})	830.83	833.94
Crystal system	Monoclinic	Monoclinic
Space group	*I2/a* (No. 15)	*I2/a* (No. 15)
a, b, c [Å]	22.8156(9), 12.5043(5), 27.7448(11)	22.7183(18), 12.4573(11), 27.8520(2)
α, β, γ (°)	90, 93.288(3), 90	90, 92.929(6), 90
V (Å^3)	7902.4(5)	7872.1(11)
Z	8	8
ρ (g.cm^{-3})	1.397	1.407
μ (mm^{-1})	1.214	1.381
F(000)	3400	3408
Crystal size (mm)	$0.09 \times 0.16 \times 0.37$	$0.18 \times 0.39 \times 0.69$
Temperature (K)	200	200
Mo *Kα* radiation, λ (Å)	0.71073	0.71073
θ (min-max) (°)	1.8, 28.3	2.4, 28.4
Data set	$-30{\leq}h{\leq}26$; $-16{\leq}k{\leq}16$; $-36{\leq}l{\leq}37$	$-29{\leq}h{\leq}30$; $-16{\leq}k{\leq}16$; $-37{\leq}l{\leq}37$
Tot., Unique data, R_{int}	90084, 9810, 0.025	55177, 9811, 0.018
Observed [I>2σ(I)] reflections	8693	8835
$N_{reflections}$, $N_{parameters}$	9810, 486	9811, 483
$R[F^2>2\sigma(F^2)]$, $wR(F^2)$, S	0.0186, 0.0456, 1.06	0.0224, 0.0606, 1.14
$\Delta\rho_{min}$, $\Delta\rho_{max}$ (e.Å^{-3})	-0.47, 0.83	-0.90, 1.36

Table S4.1b: Crystal and structure refinement data for **3**–**6**.

	3	**4**
Formula	$C_{64}H_{76}Gd_2N_6O_{22}$, $6(CH_4O)$	$C_{61}H_{70}Er_2N_6O_{22}$, $2(CH_4O)$
M_r (g.mol^{-1})	1788.06	1637.84
Crystal system	Triclinic	Triclinic
Space group	*P-1* (No. 2)	*P-1* (No. 2)
a, b, c [Å]	11.7874(5), 17.7660(8), 21.0024(10)	14.5404(7), 14.9104(7), 19.1140(9)
α, β, γ (°)	73.394(2), 78.014(2), 80.235(2)	106.487(2), 95.985(2), 116.654(2)
V (Å^3)	4094.3(3)	3419.2(3)
Z	2	2
ρ (g.cm^{-3})	1.450	1.591
μ (mm^{-1})	1.685	2.519
$F(000)$	1828	1652
Crystal size (mm)	$0.06 \times 0.30 \times 0.50$	$0.11 \times 0.41 \times 0.70$
Temperature (K)	200	200
Mo *Kα* radiation, λ (Å)	0.71073	0.71073
θ (min-max) (°)	1.2, 28.4	1.6, 28.4
Data set	$-15 \le h \le 15$; $-23 \le k \le 23$; $-27 \le l \le 28$	$-19 \le h \le 18$; $-13 \le k \le 19$; $-25 \le l \le 25$
Tot., Unique data, R_{int}	92833, 20449, 0.030	61425, 17016, 0.018
Observed [I>2σ(I)] reflections	16558	15123
$N_{reflections}$, $N_{parameters}$	20449, 1023	17016, 924
$R[F^2>2\sigma(F^2)]$, $wR(F^2)$, S	0.0282, 0.0650, 1.08	0.0204, 0.0472, 1.15
$\Delta\rho_{min}$, $\Delta\rho_{max}$ (e.Å^{-3})	-0.93, 2.10	-0.94, 1.58

	5	**6**
Formula	$C_{82}H_{95.55}N_8Na_2Nd_2O_{30.45}$, O	$C_{81.69}H_{94.23}Gd_2N_8Na_2O_{30}$, O
M_r (g.mol^{-1})	2030.93	2044.64
Crystal system	Triclinic	Triclinic
Space group	*P-1* (No. 2)	*P-1* (No. 2)
a, b, c [Å]	11.4098(6), 20.9380(11), 21.5456(11)	11.3308(5), 20.7995(10), 21.5254(10)
α, β, γ (°)	111.678(2), 93.897(3), 99.470(3)	111.771(2), 93.982(2), 98.973(2)
V (Å^3)	4671.2(4)	4608.5(4)
Z	2	2
ρ (g.cm^{-3})	1.444	1.474
μ (mm^{-1})	1.191	1.519
$F(000)$	2074	2077
Crystal size (mm)	$0.11 \times 0.25 \times 0.32$	$0.26 \times 0.36 \times 0.64$
Temperature (K)	200	200
Mo *Kα* radiation, λ (Å)	0.71073	0.71073
θ (min-max) (°)	1.7, 28.3	1.8, 28.4
Data set	$-15 \le h \le 15$; $-27 \le k \le 27$; $-28 \le l \le 28$	$-15 \le h \le 15$; $-27 \le k \le 27$; $-28 \le l \le 28$
Tot., Unique data, R_{int}	168695, 23316, 0.039	328001, 22932, 0.022
Observed [I>2σ(I)] reflections	18868	20371
$N_{reflections}$, $N_{parameters}$	23316, 1196	22932, 1172
$R[F^2>2\sigma(F^2)]$, $wR(F^2)$, S	0.0269, 0.0655, 1.01	0.0255, 0.0653, 1.11
$\Delta\rho_{min}$, $\Delta\rho_{max}$ (e.Å^{-3})	-0.94, 1.03	-0.84, 3.49

4.5.2 Molecular modelling data

Table S4.2: Natural population analysis of **Hpma⁻** at the DFT/B3LYP level using the aug-cc-pVTZ basis set in the gas phase and DMSO.

Atoms	Natural charge (dmso)	Population	Natural charge (gas)	Population
O1	-0.67720	8.67720	-0.63226	8.63226
O2	-0.76420	8.76420	-0.70104	8.70104
O3	-0.79536	8.79536	-0.78570	8.78570
N4	-0.63544	7.63544	-0.67626	7.67626
C5	0.22013	5.77987	0.25482	5.74518
C6	-0.04667	6.04667	-0.05499	6.05499
C7	-0.21885	6.21885	-0.22175	6.22175
C9	-0.20547	6.20547	-0.22800	6.22800
C11	-0.21779	6.21779	-0.21499	6.21499
C13	-0.04026	6.04026	-0.04373	6.04373
C14	-0.61191	6.61191	-0.60775	6.60775
C18	-0.61449	6.61449	-0.61520	6.61520
C22	0.56376	5.43624	0.56844	5.43156
C23	0.67881	5.32119	0.67376	5.32624
H8	0.20880	0.79120	0.18759	0.81241
H10	0.21293	0.78707	0.19075	0.80925
H12	0.20813	0.79187	0.18855	0.81145
H15	0.21509	0.78491	0.19493	0.80507
H16	0.21609	0.78391	0.21168	0.78832
H17	0.21961	0.78039	0.22544	0.77456
H19	0.20972	0.79028	0.18577	0.81423
H20	0.22991	0.77009	0.25196	0.74804
H21	0.21586	0.78414	0.21435	0.78565
H24	0.42881	0.57119	0.43364	0.56636
Total charge	**-1.00000**		**-1.00000**	

4.5.3   Anticancer activity tests

Table S4.3: Summary of cytotoxicity of **Hdmp**, metal salts and Ln(III)-oxamate complexes.

Compound (100 μM)	Cells		
	MCF-7	HEC-1A	THP-1
	Cell viability (%)		
Ce(NO$_3$)$_3$·6H$_2$O	81.8±2.88	103.9±8.89	87.2±13.36
Nd(NO$_3$)$_3$·6H$_2$O	88.6±6.99	82.4±4.77	93.7±23.98
Gd(NO$_3$)$_3$·6H$_2$O	88.8±12.26	85.7±14.64	89.4±17.70
Er(NO$_3$)$_3$·5H$_2$O	90.6±2.42	84.9±11.36	80.1±9.67
Hdmp	88.7±13.17	88.9±11.81	102.0±23.74
Complex **1**	77.1±11.27	86.2±9.44	87.6±28.16
Complex **2**	92.6±8.91	69.3±13.93	98.56±11.37
Complex **3**	106.4±13.82	64.8±16.84	114.8±12.41
Complex **4**	87.6±6.94	84.4±10.70	103.5±12.33
Complex **5**	82.0±8.18	87.9±13.43	98.4±19.61
Complex **6**	97.5±4.59	80.6±1.40	107.8±19.45
CURCUMIN	46.8±6.46	14.1±3.76	21.5±0.83

4.6   References

[1]   American Cancer Society. *Global Cancer Facts & Figures*, 3rd Edition, Atlanta: American Cancer Society; 2015, pp 1–10.

[2]   R. Shah, K. Rosso and S.D. Nathanson, "Pathogenesis, prevention, diagnosis and treatment of breast cancer", *World J. Clin. Oncol.*, **5** (2014) 283–284.

[3]   M.I. Nounou, F. ElAmrawy, N. Ahmed, K. Abdelraouf, S. Goda and H. Syed-Sha-Qhattal, "Breast Cancer: Conventional diagnosis and treatment modalities and recent patents and technologies", *Breast Cancer: Basic and Clinical Research*, **9** (2015) 17–34.

[4]   A. Talhouk and J.N. McAlpine, "New classification of endometrial cancers: The development and potential applications of genomic-based classification in research and clinical care", *Gynecologic Oncology Research and Practice,* **3** (2016) 1–12.

[5]   X. Wang, M. Yan, Q. Wang, H. Wang, Z. Wang, J. Zhao, J. Li and Z. Zhang, "*In vitro* DNA-binding, anti-oxidant and anticancer activity of indole-2-carboxylic acid dinuclear copper(II) complexes", *Molecules*, **22** (2017) 1–13.

[6]   Y. Ellahioui, S. Prashar and S. Gómez-Ruiz, "Anticancer applications and recent investigations of metallodrugs based on gallium, tin and titanium", *Inorganics*, **5** (2017) 1–23.

[7]   K. Wang, R. Li, Yi Cheng and B. Zhu, "Lanthanides – the future drugs?", *Coord. Chem. Rev.,* **190–192** (1999) 297–308.

[8]   I. Kostova, "Lanthanides as anticancer agents", *Curr. Med. Chem. – Anti-Cancer Agents*, **5** (2005) 591–602.

[9]   S.P. Perlepes, T.F. Zafiropoulos, J.K. Kouinis and A.G. Galinos, "Lanthanide(III) complexes of oxamic acid", *Z. Naturforsch.*, **36b** (1981) 697–703.

[10]   Z. Zhao, F. Han, S. Yang, J. Wu and W. Zhan, "Oxamate-mediated inhibition of lactate dehydrogenase induces protective autophagy in gastric cancer cells: Involvement of the Akt–mTOR signaling pathway", *Cancer Lett.*, **358** (2015) 17–26.

[11]   C.J. Valvona and H.L. Fillmore, "Oxamate, but not selective targeting of LDH-A, inhibits medulloblastoma cell glycolysis, growth and motility", *Brain Sci.*, **8** (2018) 1–12.

[12]   Y. Yang, D. Su, L. Zhao, D. Zhang, J. Xu, J. Wan, S. Fan and M. Chen, "Different effects of LDH-A inhibition by oxamate in non-small cell lung cancer cells", *Oncotarget*, **5** (2014) 11886–11895.

[13]   F.J. Caires, W.D.G. Nunes, C. Gaglieri, A.L.C.S. do Nascimento, J.A. Teixeira, G.A.C. Zangaro, O. Treu-Filho and M. Ionashiro, "Thermoanalytical, spectroscopic and DFT studies of heavy trivalent lanthanides and yttrium(III) with oxamate as ligand", *Mater. Res.*, **20** (2017) 937–944.

[14]   R.D. Teo, J. Termini and H.B. Gray, "Lanthanides: Applications in cancer diagnosis and therapy", *J. Med. Chem.*, **59** (2016) 6012–6024.

[15]   F.R. Fortea-Pérez, J. Vallejo, M. Julve, F. Lloret, G. De Munno, D. Armentano and E. Pardo**,** "Slow magnetic relaxation in a hydrogen-bonded 2D array of mononuclear dysprosium(III) oxamates"**,** *Inorg. Chem.*, **52** (2013) 4777−4779.

[16]   M.V. Berridge and A.S. Tan, "Characterization of the cellular reduction of 3-(4,5-dimethylthiazol-2yl)-2,5-diphenyltetrazolium bromide (MTT): subcellular localization, substrate dependence, and involvement of mitochondrial electron transport in MTT reduction", *Arch. Biochem. Biophys.*, **303** (1993) 474–482.

[17]   A. Bahuguna, I. Khan, V.K. Bajpai and S.-C. Kang, "MTT assay to evaluate the cytotoxic potential of a drug", *Bangladesh J. Pharmacol.*, **12** (2017) 115–118.

[18]   F.R. Fortea-Pérez, D. Armentano, M. Julve, G. De Munno and S.-E. Stiriba, "Bis(oxamato)palladate(II) complexes: synthesis, crystal structure and application to catalytic Suzuki reaction", *J. Coord. Chem.*, **67** (2014) 4003–4015.

[19]   Z.A. Taha, A.M. Ajlouni, T.S. Ababneh, W. Al-Momani, A.K. Hijazi, M. Al Masri and H. Hammad, "DFT computational studies, biological and antioxidant activities, and kinetics of thermal decomposition of 1,10-phenanthroline lanthanide complexes", *Struct. Chem.*, **28** (2017) 1907–1918.

[20]   L. Pavelek, V. Ladányi, M. Nečas, Z. Moravec and K. Wichterle, "Synthesis and characterization of lanthanide complexes with a pentadentate triazine-based ligand", *Polyhedron*, **119** (2016) 134–141.

[21]   X. Feng, L.-L. Zhou, L.-Y. Wang, J.-G. Zhou, Z.-Q. Shi and J.-J. Shang, "Two unique lanthanide–organic frameworks based on 1*H*-2-methyl-4,5-imidazole-dicarboxylate and oxalate: Crystal structure, luminescence and magnetic properties", *Inorg. Chim. Acta*, **394** (2013) 696–702.

[22]   G.-C. Zong, J.-X. Huo, N. Ren, J.-J. Zhang, X.-X. Qi, J. Gao, L.-N. Geng, S.-P. Wang and S.-K. Shi, "Preparation, characterization and properties of four

new trivalent lanthanide complexes constructed using 2-bromine-5-methoxybenzoic acid and 1,10-phenanthroline", *Dalton Trans.*, **44** (2015) 14877–14885.

[23] L.-N. Sun, H.-J. Zhang, Q.-G. Meng, F.-Y. Liu, L.-S. Fu, C.-Y. Peng, J.-B. Yu, G.-L. Zheng and S.-B. Wang, "Near-infrared luminescent hybrid materials doped with lanthanide (Ln) complexes (Ln = Nd, Yb) and their possible laser application", *J. Phys. Chem. B*, **109** (2005) 6174–6182.

[24] E.J. Shiells, L.S. Natrajan, D. Sykes, M. Tropiano, P. Cooper, A.M. Kenwright and S. Faulkner, "Lanthanide complexes of DOTA monoamide derivatives bearing an isophthalate pendent arm", *Dalton Trans.*, **40** (2011) 11451–11457.

[25] C.J. Athira, Y. Sindhu, M.S. Sujamol and K. Mohanan, "Synthesis and spectroscopic characterization of some lanthanide(III) nitrate complexes of ethyl 2-[2-(1-acetyl-2-oxopropyl)azo]-4,5-dimethyl-3-thiophenecarboxyate", *J. Serb. Chem. Soc.*, **76** (2011) 249–261.

[26] R.K. Agarwal, S. Prasad, R. Garg and S.K. Sidhu, "Synthesis and preliminary structural characterization of some lanthanide(III) semicarbazone complexes", *Bull. Chem. Soc. Ethiop.*, **20** (2006) 167–172.

[27] R.K. Agarwal and A. Kumar, "Synthesis, physico-chemical and biological properties of some mixed ligand complexes of trivalent lanthanides with 4[*N*-(4′-dimethylamino-benzalidene)amino] antipyrine thiosemicarbazone and pyridine", *J. Appl. Chem. Res.*, **16** (2011) 40–58.

[28] K. Raja, A. Suseelamma and K.H. Reddy, "Synthesis, spectral properties, DNA binding interactions and DNA cleavage studies of lanthanide(III) complexes of 2-acetylpyridine acetoylhydrazone: The X-ray crystal structure of 10-coordinate Ce(III) and Sm(III) complexes", *J. Iran Chem. Soc.*, **12** (2015) 1473–1486.

[29] N. Guskos, J. Majszczyk, J. Typek, G. Zolnierkiewicz, E. Tomaszewicz and K. Aidinis, "Relative intensities of *f-f* transitions of erbium(III) ion studied by photoacoustic spectroscopy", *Rev. Adv. Mater. Sci.*, **23** (2010) 97–101.

[30] R.K. Agarwal, R.K. Garg and S.K. Sindhu, "Synthesis and magneto-spectral investigations of some six and nine coordinated complexes of lanthanide(III) derived from 4[*N*-(2′-hydroxy-1′-naphthalidene)amino]antipyrinethiosemicarbazone", *J. Iran Chem. Soc.*, **2** (2005) 203–211.

[31] L.B. Su, Q.G. Wang, H.J. Li, G. Brasse, P. Camy, J.L. Doualan, A. Braud, R. Moncorgé, Y.Y. Zhan, L.H. Zheng, X.B. Qian and J. Xu, "Spectroscopic properties and CW laser operation of Nd,Y-codoped CaF_2 single crystals", *Laser Phys. Lett.*, **10** (2013) 1–4.

[32]   K.A. Thiakou, V. Nastopoulos, A. Terzis, C.P. Raptopoulou and S.P. Perlepes, "Di-2-pyridyl ketone in lanthanide(III) chemistry: Mononuclear and dinuclear erbium(III) complexes", *Polyhedron*, **25** (2006) 539–549.

[33]   W. Ma, L. Su, X. Xu, J. Wang, D. Jiang, L. Zheng, X. Fan, C. Li, J. Liu and J. Xu, "Effect of erbium concentration on spectroscopic properties and 2.79 μm laser performance of Er:CaF$_2$ crystals", *Opt. Mater. Express*, **6** (2016) 409–415.

[34]   P. Martin-Ramos, M. Ramos-Silva, F. Lahoz, I.R. Martin, P. Chamorro-Posada, M.E.S. Eusebio, V. Lavin and J. Martin-Gil, "Highly fluorinated erbium(III) complexes for emission in the C-band", *J. Photochem. Photobiol. A*: *Chem.*, **292** (2014) 16–25.

[35]   S. Mohan, K.S. Thind and G. Sharma, "Effect of Nd^{3+} concentration on the physical and absorption properties of sodium-lead-borate glasses", *Braz. J. Phys.*, **37** (2007) 1306–1313.

[36]   M.N. Gueye, M. Dieng, I.E. Thiam, D. Lo, A.H. Barry, M. Gaye and P. Retailleau, "Lanthanide(III) complexes with tridentate Schiff base ligand, antioxidant activity and X-ray crystal structures of the Nd(III) and Sm(III) complexes", *S. African. J. Chem.,* **70** (2017) 8–15.

[37]   H.R. Suh, H.S. Suh, S.S. Yun, E.K. Lee and S.K. Kang, "Triaquatris(2,6-dinitrophenolato)neodymium(III)", *Acta Cryst.*, **E58** (2002) m284–m286.

[38]   S.P. Petrosyants, A.B. Ilyukhin, A.V. Gavrikov, Y.A. Mikhlina, L.N. Puntus, E.A. Varaksina, N.N. Efimov and V.M. Novotortsev, "Luminescent and magnetic properties of mononuclear lanthanide thiocyanates with terpyridine as auxiliary ligand", *Inorg. Chim. Acta*, **486** (2019) 499–505.

[39]   X. Wang, M. Zhu, J. Wang and L. Li, "Unusual Gd–nitronyl nitroxide antiferromagnetic coupling and slow magnetic relaxation in the corresponding Tb analogue", *Dalton Trans.*, **44** (2015) 13890–13896.

[40]   K. Liu, H. Li, X. Zhang, W. Shi and P. Cheng, "Constraining and tuning the coordination geometry of a lanthanide ion in metal−organic frameworks: Approach toward a single-molecule magnet", *Inorg. Chem.*, **54** (2015) 10224–10231.

[41]   L. Kayser, R. Pattacini, G. Rogez and P. Braunstein, "Nuclearity of nickel and mixed sodium–nickel complexes: dependence on the spacer in chelating pyridine-alcoholate ligands", *Chem. Commun.*, **46** (2010) 6461–6463.

[42]   M.A. Palacios, J. Morlieras, J.M. Herrera, A.J. Mota, E.K. Brechin, S. Triki and E. Colacio, "Synthetic ability of dinuclear mesocates containing 1,3-bis(diazinecarboxamide)benzene bridging ligands to form complexes of

increased nuclearity. Crystal structures, magnetic properties and theoretical studies", *Dalton Trans.*, **46** (2017) 10469–10483.

[43]   J. Cirera, E. Ruiz and S. Alvarez, "Continuous Shape Measures as a stereochemical tool in organometallic chemistry", *Organometallics,* **24** (2005) 1556–1562.

[44]   T. Zhu, P. Chen, H. Li, W. Sun, T. Gao and P. Yan, "Structural effects on the photophysical properties of mono-β-diketonate and bis-β-diketonate Eu^{III} complexes", *Phys. Chem. Chem. Phys.*, **17** (2015) 16136–16144.

[45]   M. Stolárová, J. Černák, M. Tomás, I. Ara, M. Orendáč and L.R. Falvello, "Two novel coordination polymers in the family of lanthanide complexes with *o*-phenylenedioxydiacetato as ligand", *Polyhedron*, **88** (2015) 149–155.

[46]   D.N. Bazhin, Y.S. Kudyakova, A.S. Bogomyakov, P.A. Slepukhin, G.A. Kim, Y.V. Burgart and V.I. Saloutin, "Dinuclear lanthanide–lithium complexes based on fluorinated β-diketonate with acetal group: magnetism and effect of crystal packing on mechanoluminescence", *Inorg. Chem. Front.*, **6** (2019) 40–49.

[47]   M.-S. Liu, Q.-Y. Yu, Y.-P. Cai, C.-Y. Su, X.-M. Lin, X.-X. Zhou and J.-W. Cai, "One-, two-, and three-dimensional lanthanide complexes constructed from pyridine-2,6-dicarboxylic acid and oxalic acid ligands", *Cryst. Growth Des.*, **8** (2008) 4083–4091.

[48]   Z. Feng, X. Zhu, S. Wang, S. Wang, S. Zhou, Y. Wei, G. Zhang, B. Deng and X. Mu, "Synthesis, structure, and reactivity of lanthanide complexes incorporating indolyl ligands in novel hapticities", *Inorg. Chem.*, **52** (2013) 9549−9556.

[49]   Y.-H. Luo, F.-X. Yue, X.-Y. Yu, X. Chen and H. Zhang, "Coordination polymers of lanthanide complexes with benzene dicarboxylato ligands", *CrystEngComm.*, **15** (2013) 6340–6348.

[50]   C. Huang (2010) – *Rare-Earth Coordination Chemistry – Fundamentals and Applications*, John Wiley & Sons, Asia. pp 91–229.

[51]   K. Shen, Y. Diskin-Posner, L.J.W. Shimon, G. Leitus, R. Carmieli and R. Neumann, "Aerobic oxygenation catalyzed by first row transition metal complexes coordinated by tetradentate mono-carbon bridged bisphenanthroline ligands: intra- *versus* intermolecular carbon–hydrogen bond activation", *Dalton Trans.*, **48** (2019) 6396–6407.

[52]   W.-M. Wang, W.-W Duan, L.-C. Yue, Y.-L. Wang, W.-Y. Ji, C.-F. Zhang, M. Fang and Z.-L. Wu, "Magnetic refrigeration and single-molecule magnet behaviour of two lanthanide dinuclear complexes (Ln = Gd^{III},Tb^{III}) based on 8-hydroxyquinolin derivatives", *Inorg. Chim. Acta*, **466** (2017) 145–150.

[53] M.W. Drover, J.A. Love and L.L. Schafer, "1,3-*N,O*-complexes of late transition metals. Ligands with flexible bonding modes and reaction profiles", *Chem. Soc. Rev.*, **46** (2017) 2913–2940.

[54] C. Kachi-Terajima and N. Kimura, "Crystal structures of two isotypic lanthanide(III) complexes: triaqua[2,6-diacetylpyridine bis(benzoylhydrazone)]methanollanthanide(III) trichloride methanol disolvates (Ln^{III} = Tb and Dy)", *Acta Cryst.*, **E74** (2018) 535–538.

[55] F.R. Fortea-Pérez, N. Marino, D. Armentano, G. De Munno, M. Julve and S.-E. Stiriba, "Solid-state *cis–trans* isomerism in bis(oxamato)palladate(II) complexes: synthesis, structural studies and catalytic activity", *CrystEngComm.*, **16** (2014) 6971–6988.

[56] R. Ilmi and K. Iftikhar, "Structure elucidation by sparkle/RM1, effect of lanthanide contraction and photophysical properties of lanthanide(III) trifluoroacetylacetonate complexes with 1,10-phenanthroline", *J. Photochem. Photobiol. A: Chem.*, **325** (2016) 68–82.

[57] S. Ullmann, P. Hahn, L. Blömer, A. Mehnert, C. Laube, B. Abel and B. Kersting, "Dinuclear lanthanide complexes supported by a hybrid salicylaldiminato/calix[4]arene-ligand: synthesis, structure, and magnetic and luminescence properties of $(HNEt_3)[Ln_2(HL)(L)]$ (Ln = Sm^{III}, Eu^{III}, Gd^{III}, Tb^{III})", *Dalton Trans.*, **48** (2019) 3893–3905.

[58] J. Vančo, Z. Trávníček, O. Kozák and R. Boča, "Structural, magnetic and luminescent properties of lanthanide complexes with *N*-salicylideneglycine", *Int. J. Mol. Sci.*, **16** (2015) 9520–9539.

[59] L. Puntus, K. Zhuravlev, K. Lyssenko, M. Antipin and I. Pekareva, "Luminescence and structural properties of lanthanide complexes of Schiff bases derived from pyridoxal and amino acids", *Dalton Trans.*, **36** (2007) 4079–4088.

[60] Y. Gu, T. Kar and S. Scheiner, "Fundamental properties of the CH···O interaction: Is it a true hydrogen bond?", *J. Am. Chem. Soc.*, **121** (1999) 9411–9422.

[61] Z. Demircioğlu, Ç.A. Kaştaş and O. Büyükgüngör, "Theoretical analysis (NBO, NPA, Mulliken Population Method) and molecular orbital studies (hardness, chemical potential, electrophilicity and Fukui function analysis) of (*E*)-2-((4-hydroxy-2-methylphenylimino)methyl)-3-methoxyphenol", *J. Mol. Struct.*, **1091** (2015) 183–195.

[62] P. Lu, Y. Wu, H. Kang, H. Wei, H. Liu and M. Fang, "What can pK_a and NBO charges of the ligands tell us about the water and thermal stability of metal organic frameworks?", *J. Mater. Chem. A*, **2** (2014) 16250–16267.

[63]   A. Thirunavukkarasu, R. Karunathan, J. Mallika and V. Sathyanarayanamoorthi, "Vibrational and quantum chemical analysis of 3-methyl-2,6-diphenyl piperidin-4-one using HF and DFT methods", *Indian J. Pure Appl. Phys.*, **52** (2014) 653–670.

[64]   F.S. Tiago, P.H.O. Santiago, M.M.P. Amaral, J.B.L. Martins and C.C. Gatto, "New Cu(II) complex with acetylpyridine benzoyl hydrazone: experimental and theoretical analysis", *J. Coord. Chem.*, **69** (2016) 330–342.

[65]   N. Günay, Ö. Tamer, D. Kuzalic, D. Avc and Y. Atalay, "Theoretical investigation of *N*-methyl-*N'*-(4-nitrobenzylidene) pyrazine-2-carbohydrazide: Conformational study, NBO analysis, molecular structure and NMR spectra", *Acta Phys. Pol. A*, **127** (2015) 701–710.

[66]   P.S. Kushwaha and P.C. Mishra, "Molecular electrostatic potential maps of the anti-cancer drugs daunomycin and adriamycin: an *ab initio* theoretical study", *J. Mol. Struct. (Theochem)*, **636** (2003) 149–156.

[67]   M.S. Alam and D.-U. Lee, "Syntheses, crystal structure, Hirshfeld surfaces, fluorescence properties, and DFT analysis of benzoic acid hydrazone Schiff bases", *Spectrochim. Acta Part A*, **145** (2015) 563–574.

[68]   S. Gatfaoui, N. Issaoui, A. Mezni, F. Bardak, T. Roisnel, A. Atac and H. Marouani, "Synthesis, structural and spectroscopic features, and investigation of bioactive nature of a novel organic-inorganic hybrid material 1*H*-1,2,4-triazole-4-ium trioxonitrate", *J. Mol. Struct.*, **1150** (2017) 242–257.

[69]   N. Kalaiarasi and S. Manivarman, "Synthesis, spectroscopic characterization, computational exploration of 6-(2-(2,4-dinitrophenylhydrazano)-tetrahydro-2-thioxopyrimidin-4(1h)-one", *Orient. J. Chem.,* **33** (2017) 304–317.

[70]   S.E. Kariper, K. Sayin and D. Karakas, "Theoretical study on the antitumor properties of Ru(II) complexes containing 2-pyridyl, 2-pyridine-4-carboxylic acid ligands", *J. Mol. Struct.*, **1149** (2017) 473–486.

[71]   A. Kumer, N. Sarker and S. Paul, "The simulating study of *HOMO*, *LUMO*, thermo physical and quantitative structure of activity relationship (QSAR) of some anticancer active ionic liquids", *EJERE*, **3** (2019) 1–10.

[72]   J.L. Gázquez, A. Cedillo and A. Vela, "Electrodonating and electroaccepting powers", *J. Phys. Chem. A*, **111** (2007) 1966–1970.

[73]   J. Frau and D. Glossman-Mitnik, "Conceptual DFT descriptors of amino acids with potential corrosion inhibition properties calculated with the latest Minnesota Density Functionals", *Front. Chem.*, **5** (2017) 1–8.

[74]   J. Frau and D. Glossman-Mitnik, "Conceptual DFT study of the local chemical reactivity of the colored BISARG melanoidin and its protonated derivative", *Front. Chem.*, **6** (2018) 1–9.

[75]   N. Flores-Holguín, J. Frau and D. Glossman-Mitnik, "Conceptual DFT as a chemoinformatics tool for the study of the Taltobulin anticancer peptide", *BMC Res. Notes*, **12** (2019) 1–4.

[76]   P.K. Chattaraj, A. Chakraborty and S. Giri, "Net Electrophilicity", *J. Phys. Chem. A*, **113** (2009) 10068–10074.

[77]   J. Ravindran, S. Prasad and B.B. Aggarwal, "Curcumin and cancer cells: How many ways can curry kill tumor cells selectively?", *The AAPS Journal*, **11** (2009) 495–510.

[78]   U. Banik, S. Parasuraman, A.K. Adhikary and N.H. Othman, "Curcumin: the spicy modulator of breast carcinogenesis", *J. Exp. Clin. Cancer Res.*, **36** (2017) 1–16.

[79]   W. Chanput, J.J. Mes and H.J. Wichers, "THP-1 cell line: An *in vitro* cell model for immune modulation approach", *Int. Immunopharmacol.*, **23** (2014) 37–45.

[80]   H. Bosshart and M. Heinzelmann, "THP-1 cells as a model for human monocytes", *Ann. Transl. Med.*, **4** (2016) 438.

[81]   T.L. Heil, K.R. Volkmann, J.C. Wataha and P.E. Lockwood, "Human peripheral blood monocytes *versus* THP-1 monocytes for *in vitro* biocompatibility testing of dental material components", *J. Oral Rehabil.*, **29** (2002) 401–407.

CHAPTER 5

Lanthanide complexes with *N*-(2,6-dimethylphenyl)oxamate and 1,10-phenanthroline

5.1   Introduction

Cancer is one of the most fatal diseases worldwide, with chemotherapy being the most effective strategy for reducing the mortality rate [1,2]. Among the chemotherapeutic agents, the platinum-based drugs (cisplatin, carboplatin and oxaliplatin) and desferrioxamine (DFO) are widely used and play an important role because of their effectiveness [1,3,4]. However, the use of platinum-based chemotherapeutics is associated with adverse effects, such as ototoxicity, nephrotoxicity and peripheral neuropathy, as well as the relapsing of tumours into a platinum-resistant form [1,3]. The utilisation of the iron chelator, DFO, additionally has disadvantages, including short half-life in the plasma and poor membrane penetrability [4]. These limitations have provided an impetus for the exploration of the periodic table to identify alternative compounds to be developed as effective anticancer agents. As a result, the coordination compounds of lanthanides, titanium and ruthenium as potential anticancer agents are expanding fields of research [1,5,6].

The chemistry of 1,10-phenanthroline (**phen**) and carboxylic acid derivatives plays a crucial role in the coordination chemistry of transition metals and lanthanides [7,8]. Metallic coordination is regarded as an efficient strategy in the design of effective metal-based drugs that are used in the prevention, diagnosis and treatment of diseases [5,8,9]. Coordination of bioactive ligands to metals can improve the pharmacological properties, while inactive ligands, on the other hand, may acquire bioactivity [8,9].

Oxamates are of interest to bio-inorganic chemists due to their remarkable ability to form stable coordination compounds, their flexibility, and the availability of two or more coordination sites that enable them to form mono- and polynuclear complexes with diversified coordination modes (Figure 5.1a) [8,10-14]. The carboxylate groups not only play a key role in structural bonding, but are also vital in hydrogen bonding interactions with protic groups of proteins [10].
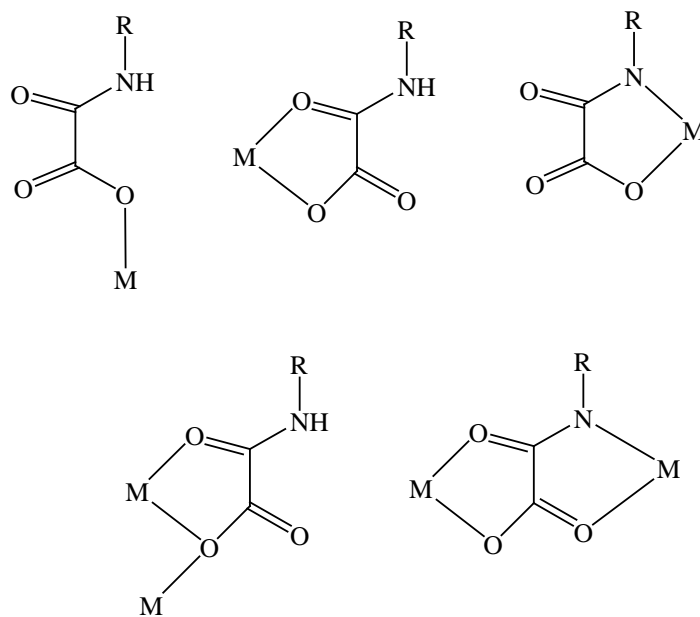
R = aliphatic or aromatic group

M = metal ion, e.g. Pd(II), Cu(II), Co(III), Y(III) and Dy(III)

Figure 5.1a: Some of the coordination modes of monoanionic and dianionic oxamate ligands with transition metal ions and lanthanide ions [10-14].

Oxamate (Figure 5.1b) and its derivatives, such as *N*-ethyl oxamate and *N-sec*-butyl oxamate, are promising anticancer agents, as they target lactate dehydrogenase (LDHA), a key enzyme in the aerobic glycolytic pathway (a metabolic pathway involved in metastasis), by competing with LDHA's substrate, pyruvate (Figure 5.1b) for the binding sites [15-17]. Antagonism of the LDHA substrate-binding sites by inhibitors such as oxamate leads to a reduction in enzymatic conversion of pyruvate to lactate, thereby promoting the participation of pyruvate in mitochondrial metabolism

and cytotoxicity [17]. The inhibitory effects of LDHA by oxamates, or their metal complexes, result in inhibition of breast, cervical, leukemia, medulloblastoma (malignant paediatric brain tumour), glioblastoma, non-small cell lung cancer (NSCLC) and liver cancer cell metabolism and proliferation [14,15,18-20]. An example of metal compounds that are cytotoxic towards leukemia cells are diamagnetic square-planar Pd(II)-oxamate complexes [14]. Moreover, oxamate has been found to enhance sensitivity to doxorubicin in doxorubicin-resistant chondrosarcoma cells, chemo-resistant human colon adenocarcinoma cells (HT29-dx), and in human malignant mesothelioma (HMM) cells [18,21].
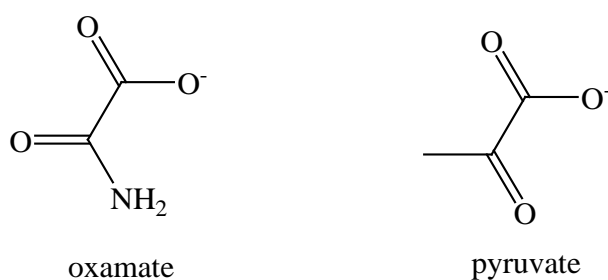
Figure 5.1b: Structures of oxamate and pyruvate [17].

On the other hand, 1,10-phenanthroline and its derivatives form a group of potential iron chelators and DNA cleaving agents, which can be developed specially for cancer chemotherapy [4,7]. Iron is essential for cell growth processes, especially DNA synthesis; without it, the cell cycle cannot be completed and the cell cannot progress from the G1 phase (first growth phase) to the S phase (DNA synthesis) [4]. The anticancer properties and the chelating ability of 1,10-phenanthroline that ensures stability of the metal complexes accounts for its use in this research as an auxiliary ligand [7,8,22].

The structural features and biological relevance (ability to inhibit glycolysis and other relevant metabolic processes) of mixed-ligand complexes, thus motivated the synthesis and characterisation of lanthanide complexes incorporating *N*-(2,6-dimethylphenyl)oxamate (**Hpma⁻**, Scheme 5.1) and **phen**, with a view to assess the anticancer activities of the compounds on breast cancer (MCF-7), the endometrial

carcinoma (HEC-1A) and the human monocytic (THP-1) cell lines. The anticancer screen of the mixed-ligand complexes containing oxamate and **phen**, indicated that the addition of **phen** as an auxiliary ligand could enhance the anticancer properties of the complexes [4]. To disentangle various aspects related to the metal complexation chemistry, some theoretical aspects of the ligands were studied. This opens numerous routes to expand the wide range of applications for mixed-ligand complexes of oxamates and phenanthrolines toward medicinal chemistry.
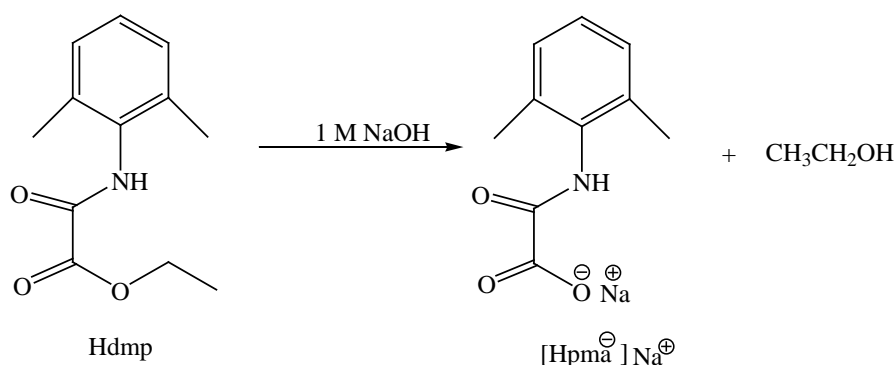
Scheme 5.1: Conversion of the proligand **Hdmp** to **Hpma⁻**, which in turn coordinates with metal ions [14].

5.2 Synthesis of the complexes

5.2.1 Synthesis of Ln(III) acetate complexes with Hdmp and phen

The following general procedure was adopted in the synthesis of Ln(III) acetate complexes with **Hdmp** and **phen**. $[Ln(OAc)_3 \cdot xH_2O]$ (Ln = La (**1**), Ce (**2**), Nd (**3**), Er (**4**) or Yb (**5**), x = 4 for Yb) was added to a 6 mL ethanolic solution of 1,10-phenanthroline monohydrate. A few drops of distilled water were added to completely dissolve the mixture, followed by reflux of the resultant solution under a dinitrogen atmosphere for 1 hour. An ethanolic solution of **Hdmp** mixed with 1 M NaOH (1:1 molar ratio) was then added, and reflux continued for a further 2 hours at 60 °C. The solutions afforded single X-ray quality crystals within 7 days, upon slow vapour diffusion using diethyl ether at room temperature.

[La(Hpma)$_2$(phen)$_2$(OAc)]·2H$_2$O   (1)

1,10-Phenanthroline monohydrate (0.370 g, 1.867 mmol), [La(OAc)$_3$·xH$_2$O] (0.312 g, 0.935 mmol), **Hdmp** (0.207 g, 0.936 mmol), 1 M NaOH (0.936 mL), Yield = 0.472 g (26.1 % based on the La(III) salt); white crystals, m.p. = 342.0 ^{o}C. Anal. *Calcd*. for 2(C$_{46}$H$_{39}$LaN$_6$O$_8$), 3(O) (%): C, 57.17; H, 4.07; N, 8.69. Found: C, 57.21; H, 3.94; N, 8.67. Conductivity (10^{-3} M, DMF): 11.88 ohm^{-1}cm^{2}mol^{-1}. IR (cm^{-1}): v(N-H) 3249(w), v(C=O) 1663, 1633(s), v(C=C) 1520(s), v(C-H) 851, 728(s), v(Ln-N) 418(m).

[Ce(Hpma)$_2$(phen)$_2$(OAc)]·2H$_2$O   (2)

1,10-Phenanthroline monohydrate (0.144 g, 0.726 mmol), [Ce(OAc)$_3$·xH$_2$O] (0.152 g, 0.363 mmol), **Hdmp** (0.0804 g, 0.363 mmol), 1 M NaOH (0.363 mL), Yield = 0.198 g (28.2 % based on the Ce(III) salt); yellow crystals, m.p. = 328.5 ^{o}C. Anal. *Calcd*. for 2(C$_{46}$H$_{39}$CeN$_6$O$_8$), 3(O) (%): C, 57.08; H, 4.06; N, 8.68. Found: C, 57.01; H, 4.01; N, 8.59. Conductivity (10^{-3} M, DMF): 14.58 ohm^{-1}cm^{2}mol^{-1}. IR (cm^{-1}): v(N-H) 3247(w), v(C=O) 1662, 1633(s), v(C=C) 1520(s), v(C-H) 852, 727(s), v(Ln-N) 418(m).

[Nd(Hpma)$_2$(phen)$_2$(OAc)]·2H$_2$O   (3)

1,10-Phenanthroline monohydrate (0.753 g, 3.798 mmol), [Nd(OAc)$_3$·xH$_2$O] (1.288 g, 3.797 mmol), **Hdmp** (0.420 g, 1.898 mmol), 1 M NaOH (1.898 mL), Yield = 0.916 g (24.6 % based on the Nd(III) acetate salt); purple crystals, m.p. = 293.4 ^{o}C. Anal. *Calcd*. for C$_{46}$H$_{39}$N$_6$NdO$_8$, H$_2$O, O (%): C, 56.26; H, 4.21; N, 8.56. Found: C, 56.19; H, 4.19; N, 8.52. Conductivity (10^{-3} M, DMF): 4.98 ohm^{-1}cm^{2}mol^{-1}. IR (cm^{-1}): v(N-H) 3225(w), v(C=O) 1666, 1597(s), v(C=C) 1520(s), v(C-H) 845, 724(s), v(Ln-N) 424(m).

[Er(Hpma)$_2$(phen)(OAc)(H$_2$O)]·EtOH·H$_2$O   (4)

1,10-Phenanthroline monohydrate (0.176 g, 0.888 mmol), [Er(OAc)$_3$·xH$_2$O] (0.152 g, 0.441 mmol), **Hdmp** (0.0980 g, 0.443 mmol), 1 M NaOH (0.443 mL), Yield = 0.121 g (31.4 % based on the Er(III) salt); pink crystals, m.p. = 291.3 ^{o}C. Anal. *Calcd*. for C$_{34}$H$_{33}$ErN$_4$O$_9$, C$_2$H$_6$O, H$_2$O (%): C, 49.53; H, 4.73; N, 6.42. Found: C, 49.46; H, 4.64; N, 6.41. Conductivity (10^{-3} M, DMF): 32.60 ohm^{-1}cm^{2}mol^{-1}. IR (cm^{-1}): v(N-H)

3214(w), v(C=O) 1678, 1616(s), v(C=C) 1520(s), v(C-H) 842, 722(s), v(Ln-N) 429(m).

[Yb(Hpma)$_3$(phen)]·2EtOH   (5)

1,10-Phenanthroline monohydrate (0.108 g, 0.545 mmol), [Yb(OAc)$_3$·4H$_2$O] (0.115 g, 0.272 mmol), **Hdmp** (0.060 g, 0.271 mmol), 1 M NaOH (0.271 mL), Yield = 0.098 g (35.3 % based on the Yb(III) salt); white crystals, m.p. = 283.6 ^{o}C. Anal. *Calcd*. for C$_{42}$H$_{38}$N$_5$O$_9$Yb, 2(C$_2$H$_6$O) (%): C, 54.06; H, 4.93; N, 6.85. Found: C, 53.98; H, 4.90; N, 6.79. Conductivity (10^{-3} M, DMF): 17.55 ohm^{-1}cm^{2}mol^{-1}. IR (cm^{-1}): v(N-H) 3214(w), v(C=O) 1678, 1616(s), v(C=C) 1520(s), v(C-H) 842, 722(s), v(Ln-N) 429(m).

5.2.2   Synthesis of Ln(III) nitrate complexes with Hdmp and 1,10-phenanthroline

The following general procedure was used in the synthesis of Ln(III) nitrate complexes with **Hdmp** and **phen**. A colourless homogeneous (2:1 mole ratio) mixture of **Hdmp** and 1,10-phenanthroline monohydrate in an 8 mL ethanolic solution (ethanol:water = 3:2 v/v) was prepared. To this, 1 M NaOH was added and the solution magnetically stirred for 1 hour at room temperature. [Ln(NO$_3$)$_3$·6H$_2$O] (Ln = Nd or Gd) was then added and the mixture refluxed for a further 1 hour. The solution was filtered off to remove undissolved material, and diethyl ether was allowed to diffuse into the solution. Single crystals suitable for X-ray crystallography were obtained within 5 days.

[Nd(Hpma)$_3$(phen)(H$_2$O)]·4H$_2$O   (6)

Hdmp (0.185 g, 0.836 mmol), 1,10-phenanthroline monohydrate (0.083 g, 0.419 mmol), 1 M NaOH (0.836 mL), [Nd(NO$_3$)$_3$·6H$_2$O] (0.367 g, 0.837 mmol), Yield = 0.328 g (39.9 % based on the Nd(III) nitrate salt); purple crystals, m.p. = 294.6 ^{o}C. Anal. *Calcd*. for C$_{42}$H$_{40}$N$_5$NdO$_{10}$, 4(O) (%): C, 51.32; H, 4.10; N, 7.12. Found: C, 51.39; H, 4.18; N, 7.07. Conductivity (10^{-3} M, DMF): 7.84 ohm^{-1}cm^{2}mol^{-1}. IR (cm^{-1}):

v(O-H) 3559–3081(w), v(C=O) 1638(s), v(C=C) 1521(s), v(C-H) 852, 721(s), v(Ln-N) 420(m).

[Gd(Hpma)₃(phen)(H₂O)]·4H₂O   (7)

Hdmp (0.189 g, 0.854 mmol), 1,10-phenanthroline monohydrate (0.085 g, 0.428 mmol), 1 M NaOH (0.854 mL), [Gd(NO₃)₃·6H₂O] (0.385 g, 0.853 mmol), Yield = 0.331 g (38.8 % based on the Gd(III) nitrate salt); white crystals, m.p. = 302.4 °C. Anal. *Calcd*. for C₄₂H₄₀GdN₅O₁₀, 2(O) (%): C, 50.44; H, 4.03; N, 7.00. Found: C, 50.38; H, 4.12; N, 6.86. Conductivity (10⁻³ M, DMF): 22.57 ohm⁻¹cm²mol⁻¹. IR (cm⁻¹): v(O-H) 3559–3081(w), v(C=O) 1638(s), v(C=C) 1521(s), v(C-H) 852, 721(s), v(Ln-N) 420(m).

5.3   Results and discussion

A one-pot synthesis procedure was applied in the preparation of the coordination compounds, which yielded air and moisture stable complexes. The use of NaOH as a base led to the hydrolysis of the proligand **Hdmp** to yield monoanionic **Hpma⁻**, which is more reactive with the metal acetates and nitrates (Scheme 5.2). The synthetic methodology reported by Fortea-Pérez *et al.* (2014) for the preparation of bis(oxamato)palladate(II) complexes using tetrabutylammonium hydroxide (*n*-Bu₄NOH) and potassium hydroxide (KOH) as bases instead of NaOH, affording *N*-2,6-dimethylphenyloxamate dianions from **Hdmp**, was utilised [14]. Elemental analyses data confirmed bonding of the Ln(III) ions with **Hpma⁻** and **phen** in the ratios 1:2:2 (complexes **1**–**3**), 1:2:1 (complex **4**) and 1:3:1 (complexes **5**–**7**).

The molar conductivity values (4.98–32.60 ohm⁻¹cm²mol⁻¹) of the coordination compounds in DMF indicate their non-electrolyte nature [23]. The complexes are thus regarded to be neutral with all the anionic **Hpma⁻** and/or acetate ligands found in the primary coordination sphere.
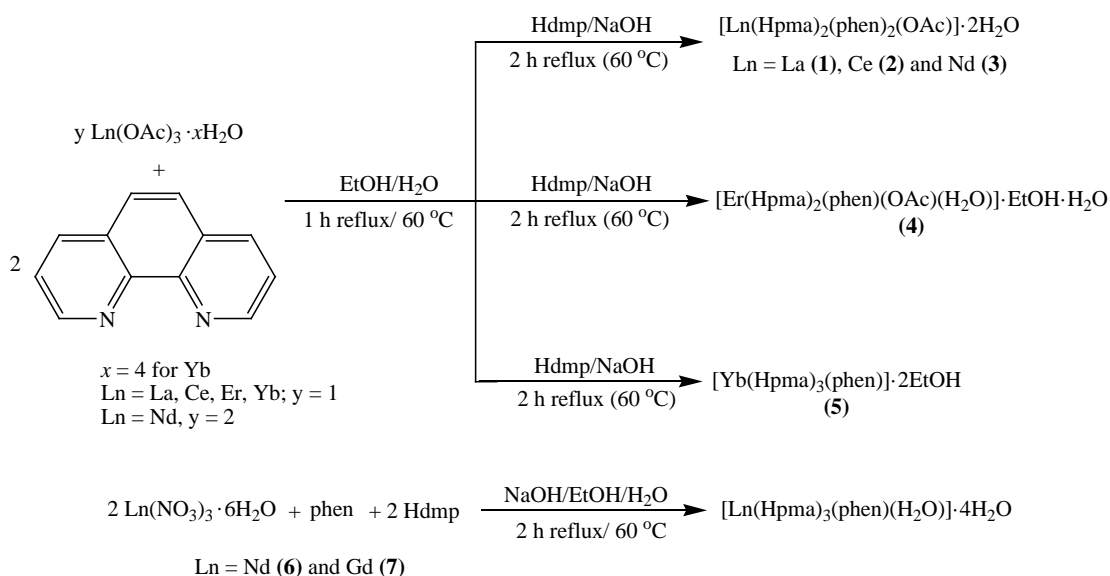
Scheme 5.2: Different lanthanide complexes prepared from **Hdmp** and **phen** in the presence of NaOH.

5.3.1 FT-IR spectroscopy

The IR spectra of the free ligands and the synthesised complexes are presented in Figures 5.2a-5.2c. It can be noted that the IR spectra of **1**–**3** are almost identical, while those of the isostructural complexes **6** and **7** also resemble each other, indicating similar coordination environments around the Ln(III) ions [23]. The shifts observed in the spectra of Ln(III) complexes are attributed to the weakening of the N-H and C=O bonds upon coordination [23,24]. The strong v(N-H) of **Hdmp** is found in the high-frequency region at 3252 cm^{-1} – this band is red-shifted to 3249–3214 cm^{-1} in complexes **1**–**5** [14]. In the free **Hdmp**, the C=O stretching vibrations occur at 1763 and 1688 cm^{-1}. These bands are observed at lower wavenumbers in the metal complexes (1678–1597 cm^{-1}), thus confirming participation of the oxamate oxygen atoms in direct bonding to the metal ions [14,22]. The v(C=C) in **Hdmp** (1525 cm^{-1}) is red-shifted in **1**–**7** ($\approx$1520 cm^{-1}).
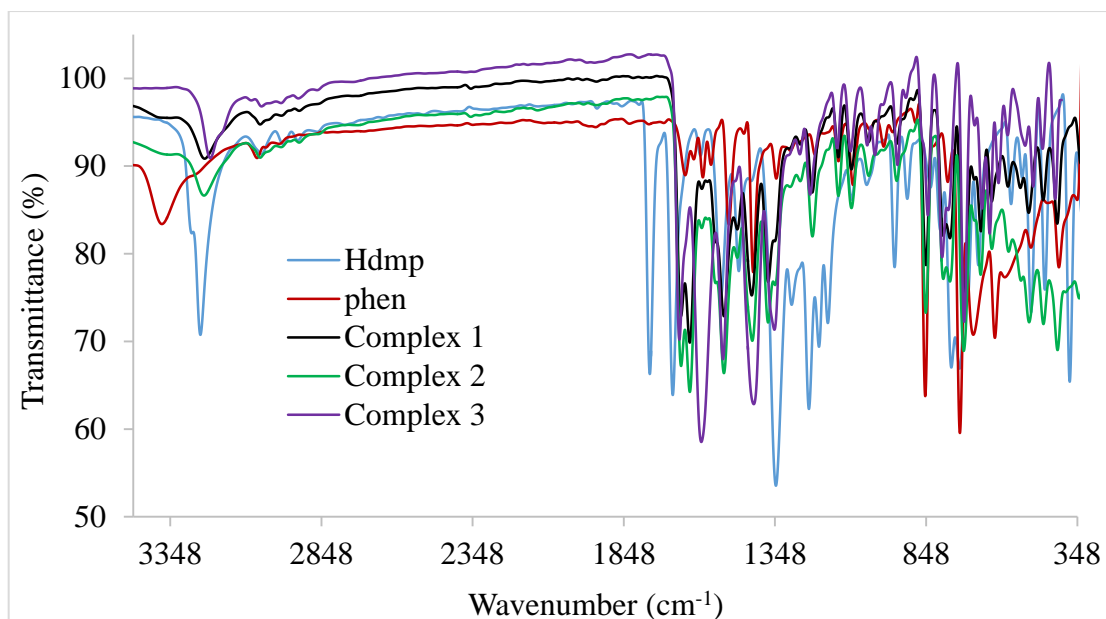
Figure 5.2a: Overlay IR spectra of the free ligands and complexes **1**–**3**.
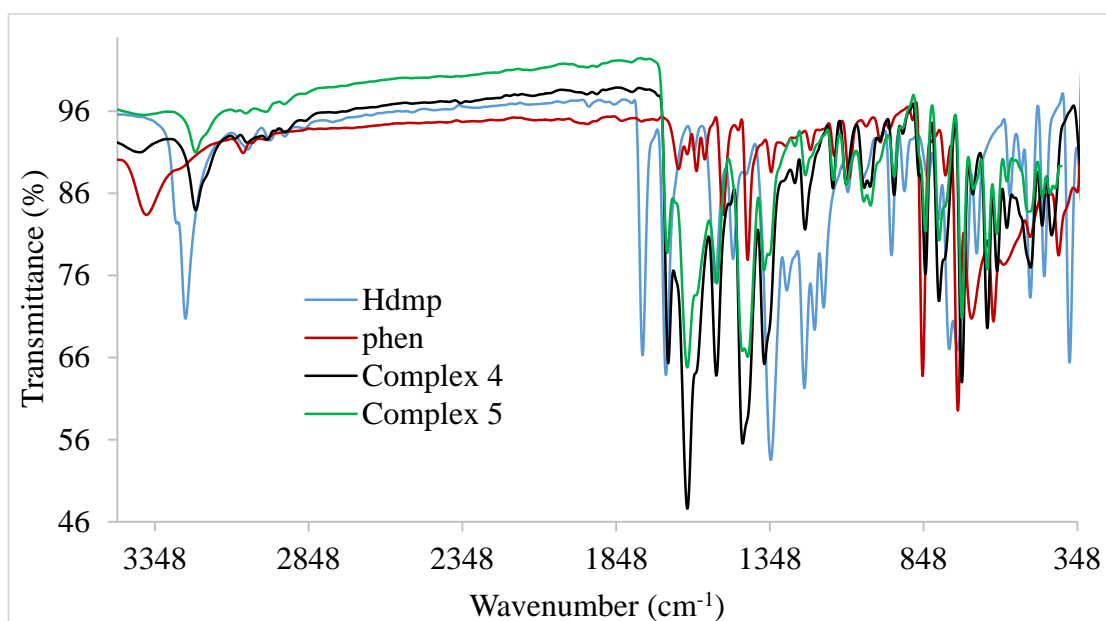
Figure 5.2b: Overlay infrared spectra of **Hdmp**, **phen** and complexes **4** and **5**.

The free ligand 1,10-phenanthroline monohydrate exhibits a broad vibration band with a maximum at 3371 cm^{-1}, indicating the presence of a water molecule [23]. This band completely disappears in the spectra of complexes **1**–**5**, but re-appears in **6** and **7** (3559–3081 cm^{-1}). The C-H bending vibrations are observed at 852 and 738 cm^{-1} in

phen, with the band at 852 cm^{-1} remaining unaffected after complexation with the metal ions in **2**, **6** and **7**; while being red-shifted (851–842 cm^{-1}) in **1** and **3–5** [22,24]. The absorption peak at 738 cm^{-1} also experiences red-shifts upon coordination with all metal ions, appearing in the range 728–721 cm^{-1}. Furthermore, the blue-shifts of the C=C vibration of **phen** (1505 cm^{-1} *versus* ≈1520 cm^{-1} in **1–7**), and the appearance of the non-ligand absorption peaks in the region 429–418 cm^{-1} that are typical of Ln-N vibrations, reveal that the nitrogen atoms of **phen** form coordinative bonds with the Ln(III) ions in **1–7** [22,25].
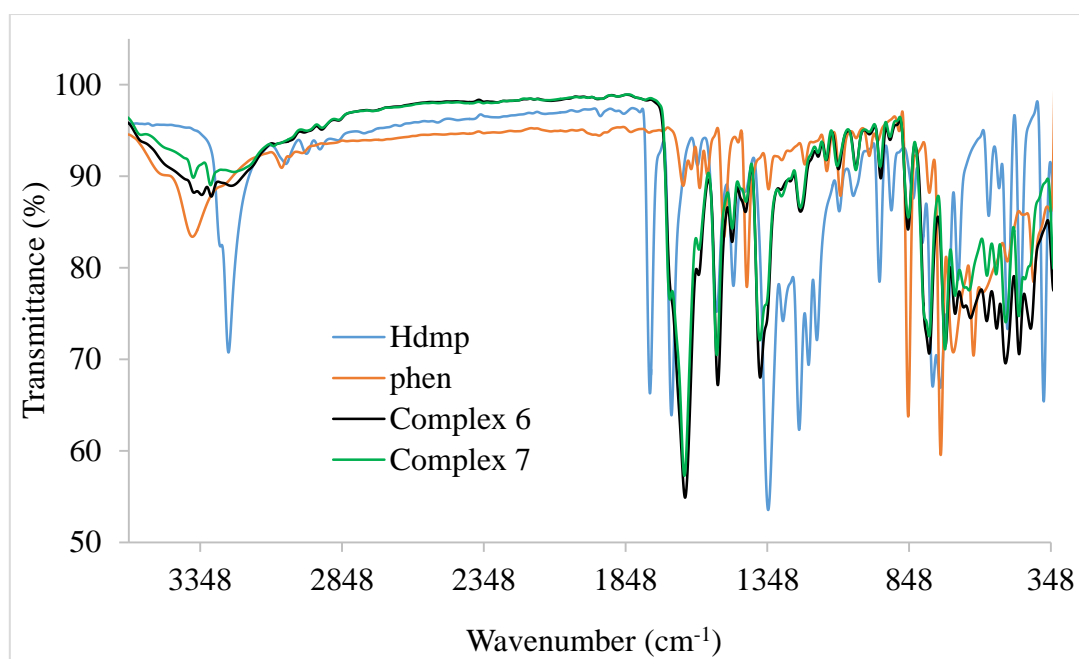
Figure 5.2c: Overlay IR spectra of the free **Hdmp** and **phen**, and coordination compounds **6** and **7**.

5.3.2 NMR analysis

The ^{1}H NMR spectra of the free ligands and complexes **1-7** in DMSO-d_6 are depicted in Figures 5.3a and 5.3b. The ^{1}H NMR spectra of the complexes indicate the disappearance of the ethyl groups of **Hdmp**, thus supporting formation of the **Hpma$^-$** monoanion [14]. The participation of the oxamate moiety in coordination to the metal ions is shown by the absence of the signal due to the –NH group in the spectra of all the complexes. These observations have been confirmed by X-ray diffraction studies

on single crystals. The ^{1}H NMR spectra of the complexes show distinct peaks at 7.05 ppm (complex **1**), 6.42–6.52 ppm (complex **2**), 6.45–6.57 ppm (complex **3**) and 6.39–6.52 ppm (complex **6**), which are characteristic of the aromatic rings of **Hpma⁻**, with substantial signal broadening [26,27]. Upfield signals at 1.65, 1.60, 1.57 and 1.49 ppm are typical of the oxamate methyl protons in **1**–**3** and **6**, respectively. Due to the paramagnetic nature of the Gd(III) ion in **7**, it is expectedly found that the proton chemical shifts are distributed through a range of -2.91 to 9.13 ppm, with the shielding effect occurring only on **Hpma⁻** protons [26-28]. The resonances due to **phen** protons at 9.11, 8.48, 7.99 and 7.76 ppm remain almost unaffected after coordination to all the different metal ions [23].
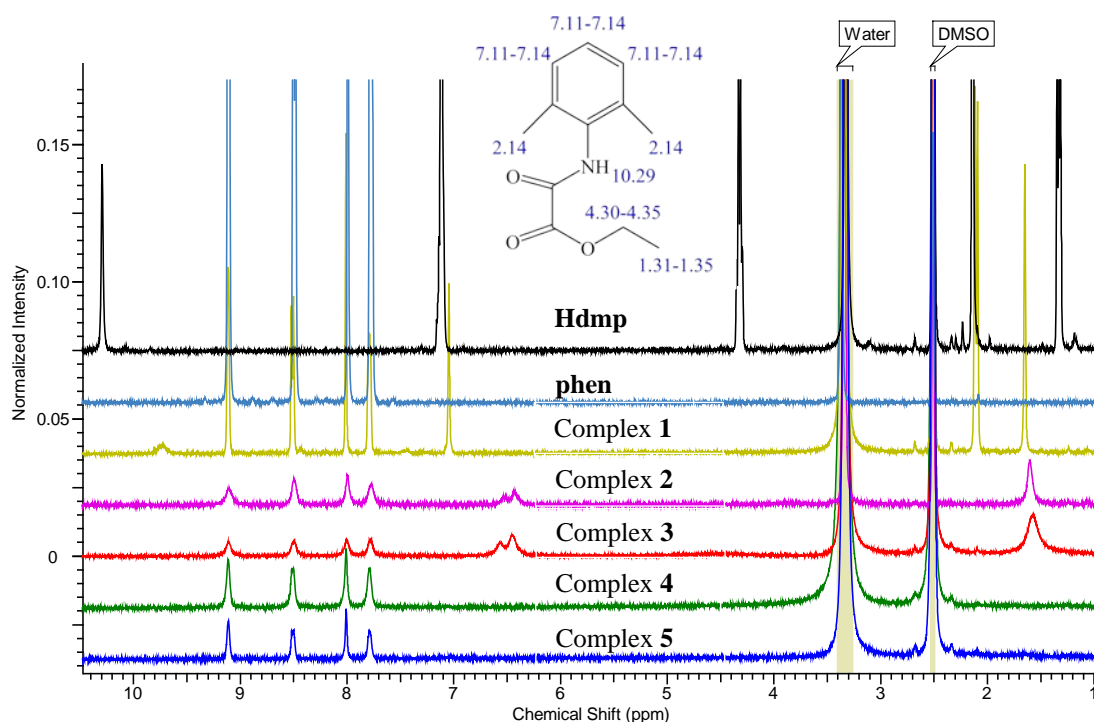
Figure 5.3a: ^{1}H NMR spectra of **Hdmp**, **phen** and complexes **1**–**5**.
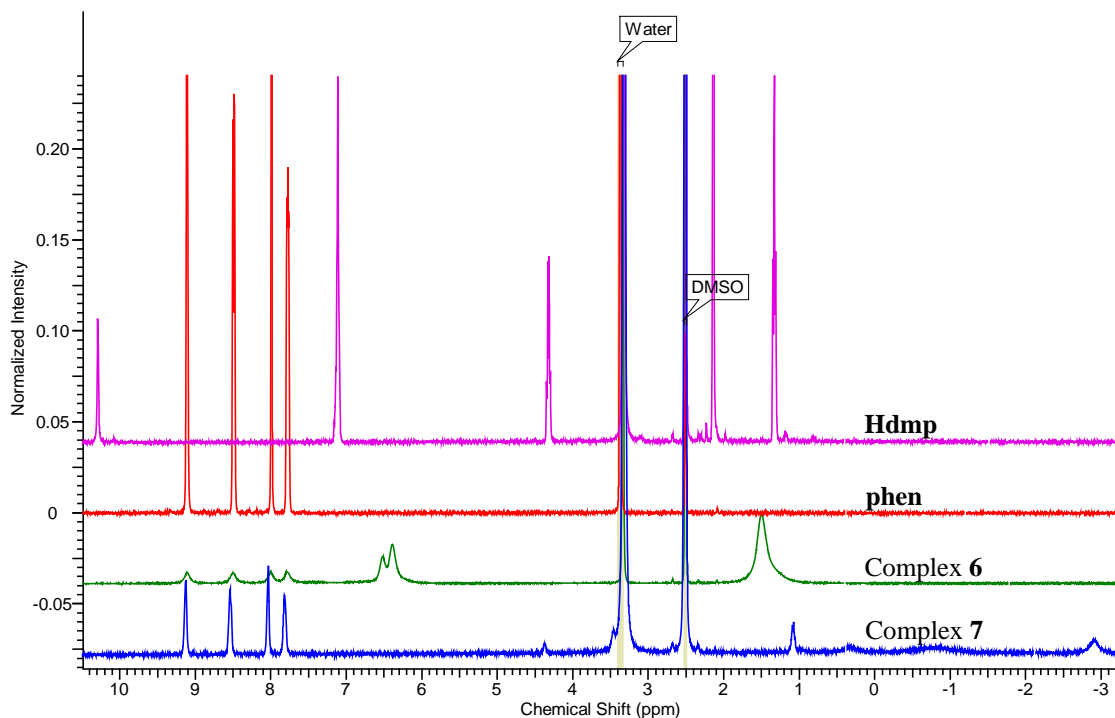
Figure 5.3b: ^{1}H NMR spectra of the free ligands **Hdmp** and **phen**, and metal complexes **6** and **7** in DMSO-d_6.

5.3.3 UV-Vis-NIR spectroscopy

The absorption spectra of **phen** and the metal complexes in the UV-Vis-NIR range (310-935 nm) are shown in Figures 5.4a and 5.4b. The maximum absorption bands positioned at 324 nm for **phen** and **1**–**7** are associated with the π→π* transitions of **phen** [29,30].

The insets show more resolved *f–f* transition bands of the complexes. The La(III) and Ce(III) complexes show no significant absorption in the investigated range. In the case of complex **3**, the maxima around 444, 515, 525, 585, 745, 801 and 873 nm are assigned to electronic transitions from $^4I_{9/2}$ to the excited states $^2P_{1/2}$, $^4G_{9/2}$, $^4G_{7/2}$, $^4G_{5/2}$ + $^2G_{7/2}$, $^4F_{7/2}$ + $^4S_{3/2}$, $^4F_{5/2}$ + $^2H_{9/2}$ and $^4F_{3/2}$, respectively [31-36]. The Nd(III) ion of **6** also gives discrete absorption bands in the visible and near infrared regions, located at 434, 453-485, 514, 524, 580, 684, 744 and 799. These transitions originate from the

$^4I_{9/2}$ ground state to the various excited states of Nd(III): $^2P_{1/2}$, $^4G_{11/2}$ + $^2D_{3/2}$, $^4G_{9/2}$, $^4G_{7/2}$, $^4G_{5/2}$ + $^2G_{7/2}$, $^4F_{9/2}$, $^4F_{7/2}$ + $^4S_{3/2}$ and $^4F_{5/2}$ + $^2H_{9/2}$, respectively [31-38].
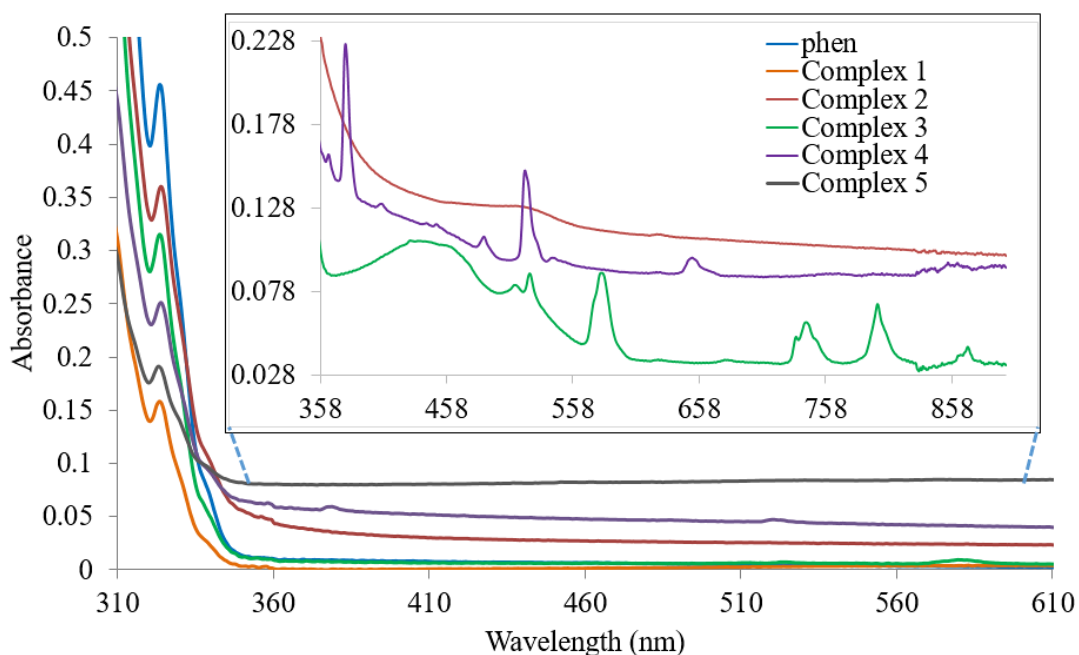
Figure 5.4a: Electronic absorption spectra of the free **phen** ligand and **1-5** in 1 cm path length cells. The weak peaks due to *f-f* transitions are indicated in the inset.
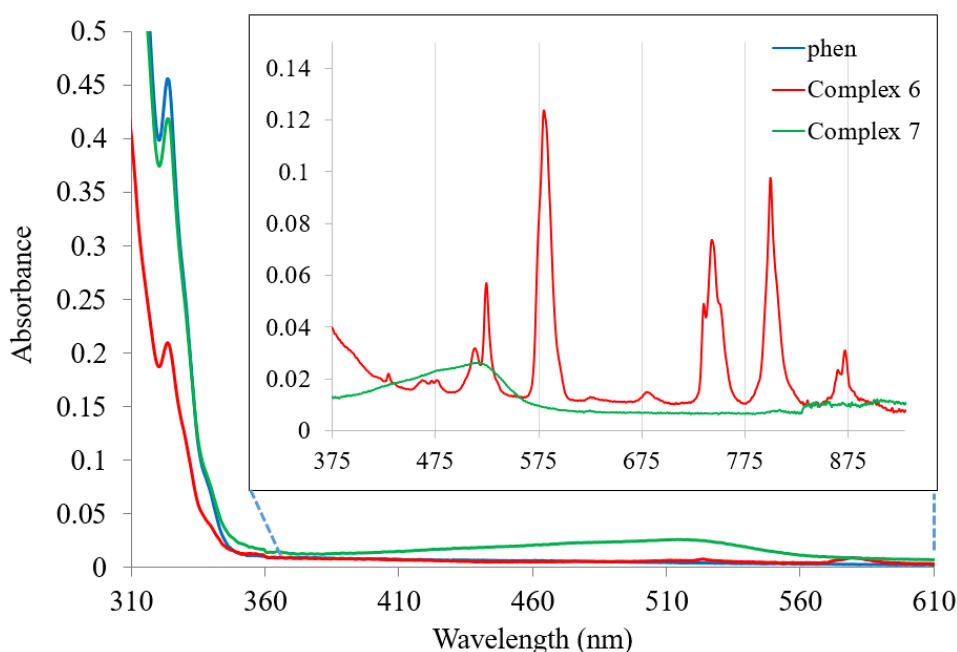
Figure 5.4b: The UV-Vis-NIR absorption spectra of **phen**, **6** and **7**. The weak Laporte-forbidden *f-f* transition peaks are shown in the inset.

Sharp bands due to intra-configurational $4f^{11}$–$4f^{11}$ electronic transitions from the $^4I_{15/2}$ ground state to the excited levels of the Er(III) ion of **4** can be discerned. The peaks correspond to the transitions from $^4I_{15/2}$ to ($^4G_{9/2}$+$^2K_{15/2}$) (365 nm), $^4G_{11/2}$ (378 nm), $^2H_{9/2}$ (409 nm), $^4F_{7/2}$ (488 nm), $^2H_{11/2}$ (522 nm) and $^4F_{9/2}$ (655 nm) [34,39-41]. The broad absorption band in the spectrum of the Gd(III) complex (**7**) is due to the transition from the ground level $^8S_{7/2}$ [42,43].

5.3.4   Coordination polyhedra determination

Utilising the program *SHAPE*, the coordination geometries of **1**–**7** were identified, and the CShM values suggest moderate deviations from ideal symmetry (Table 5.1) [44-46]. The coordination polyhedra around the ten-coordinate Ln(III) ions of the isostructural complexes **1**–**3** is sphenocorona J87 (JSPC-10), with continuous shape measures (CShMs) of 2.70209, 2.67702 and 2.59160, respectively, while the nine-coordinate complexes **4**, **6** and **7** exhibit the distorted spherical capped square antiprism (CSAPR-9) geometry. Representations of each geometry in terms of complexes **1**, **4** and **5** are depicted in Figure 5.5. Deca-coordinate compounds thus show C_{2v} symmetry and are composed of 22 edges and layers in the ratio 2:4:2:2, and 12_3+2_4 faces (twelve triangles and two squares) [47]. The irregular coordination polyhedron about the eight-fold coordinate Yb(III) ion of **5** can be viewed as a distorted square antiprism (SAPR-8) (D_{4d} symmetry), having a polyhedral volume of 23.1290 Å^3 and a CShM value equal to 0.89761 [48].

Table 5.1: Shape analysis of Ln(III) complexes with **Hpma**$^-$ and **phen** using *SHAPE 2.1* software.

Complex	Coordination number	Shape	Symmetry	CShM	Polyhedral volume (Å^3)	Average bond length (Å)
1	10	JSPC-10	C_{2v}	2.70209	40.4309	2.6462
2	10	JSPC-10	C_{2v}	2.67702	39.6386	2.6276
3	10	JSPC-10	C_{2v}	2.59160	38.2945	2.5960
4	9	CSAPR-9	C_{4v}	1.19572	28.7525	2.4353
5	8	SAPR-8	D_{4d}	0.89761	23.1290	2.3563
6	9	CSAPR-9	C_{4v}	0.42967	31.9855	2.5185
7	9	CSAPR-9	C_{4v}	0.38084	30.2801	2.4710
Other close geometries with low CShM values						
Complex **4**: Muffin (MFF-9); C_s symmetry; CShM = 1.28065						
Complex **6**: MFF-9; C_s symmetry; CShM = 0.77475						
Complex **7**: MFF-9; C_s symmetry; CShM = 0.75273						

Complex **1**   Complex **4**

Complex **5**
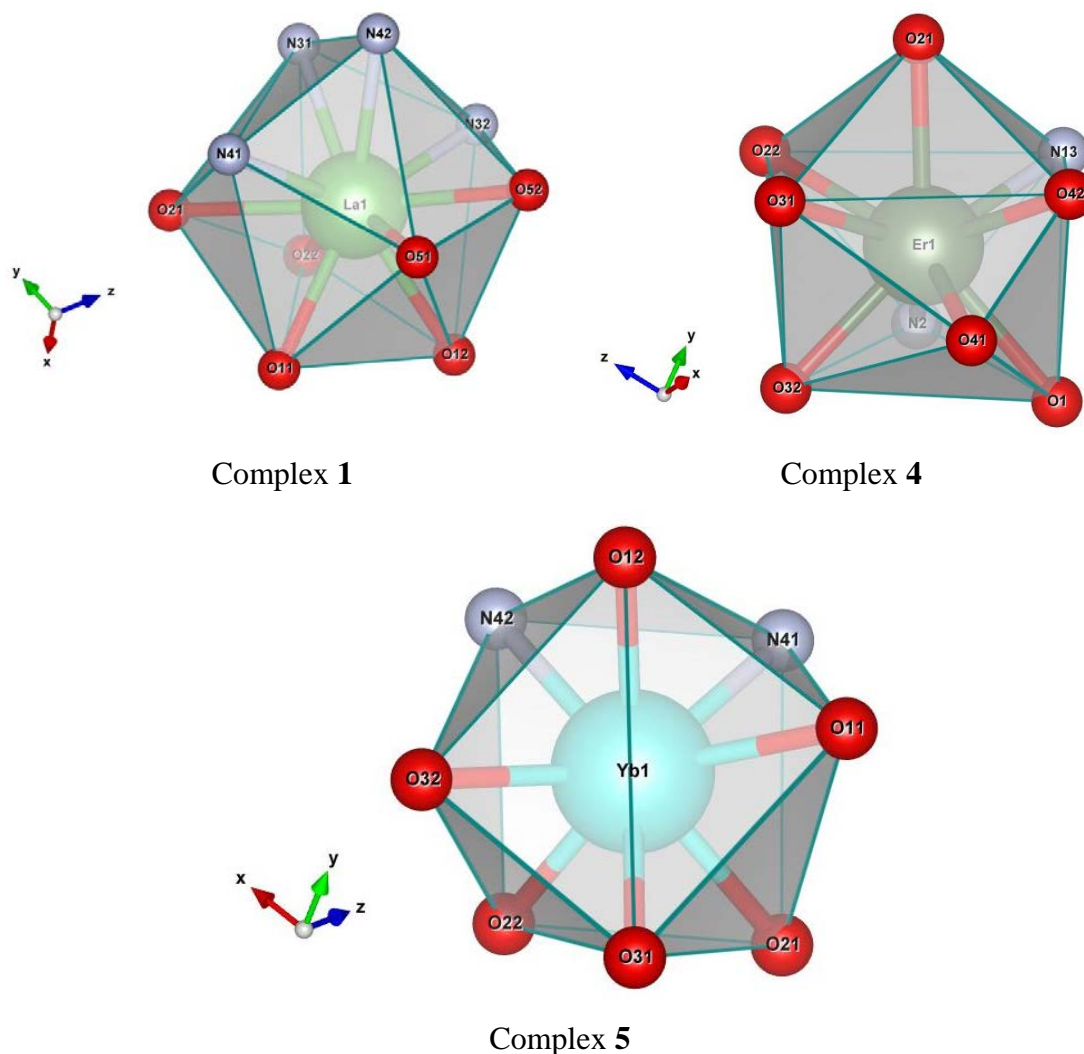
Figure 5.5: Polyhedral views of **1**, **4** and **5**.

It is observed that the CShM values are affected by the coordination number and the size of the metal ion (or bond lengths). Higher deviation parameters and coordination numbers are observed for the lighter lanthanides relative to their heavier counterparts. The lighter lanthanide coordination environments with their larger polyhedral volumes are more affected by angular distortions, resulting in higher CShM values compared to the heavier lanthanide complexes with relatively lower polyhedral volumes and shorter bond distances [45,46]. Lower coordination numbers and shorter bonds (stronger coordination) result in decreased flexibility of the coordinating ligands as well as decreased steric repulsion, thereby giving less distortions from ideal shape [49].

5.3.5 X-ray crystallography

Seven mixed-ligand lanthanide complexes derived from ethyl (2,6-dimethylphenylcarbamoyl)formate and **phen** have been prepared. Complexes with the general formula [Ln(Hpma)$_2$(phen)$_2$(OAc)]·2H$_2$O (Ln = La (**1**), Ce (**2**) and Nd (**3**)) are isostructural, and crystallise in the monoclinic system with space group *P21/c* (Figure 5.6a). The sphenocorona coordination geometry around each deca-coordinate metal centre is formed by four nitrogen atoms (N31, N32, N41, N42) of two bidentate **phen** ligands and six *O*-atoms from two bidentate **Hpma**⁻ ligands (O11, O12, O21, O22) and one bidentate acetate ion (O51, O52). The crystal structures of **1**–**4** show that the lanthanide ions exist in the +3 oxidation state, the charge of which is neutralised by two mono-anionic **Hpma**⁻ ligands and one CH$_3$COO⁻ ion (Figure 5.6a).

Single-crystal X-ray diffraction studies show that the Er(III) ion of complex **4** (triclinic system, space group *P-1*) is surrounded by nine donor-atoms provided by one bidentate **phen** ligand, two bidentate chelating **Hpma**⁻ molecules, one bidentate acetate group and one water molecule. The YbO$_6$N$_2$ distorted square antiprism coordination environment of **5** (monoclinic system, space group *P21/c*) exhibits a coordination number of eight, with the +3 charge on the metal ion being neutralised by three bidentately coordinated **Hpma**⁻ ligands (Figure 5.6a). The inner coordination sphere is completed by one bidentately coordinated **phen** molecule.

The molecular structures of the isostructural mixed-ligand complexes derived from Nd(III) and Gd(III) nitrates are presented in Figure 5.6b. The coordination compounds **6** and **7** crystallise in the triclinic space group *P-1*, and are characterised by metal ions linked to one water molecule, one **phen** and three **Hpma**⁻ ligands in similar chelating modes to **1**–**5**. This gives nine-coordinate complexes with distorted CSAPR-9 geometry. The lower coordination numbers in **6** and **7** compared to **1**–**3** can be attributed to the presence of more bulky **Hpma**⁻ ligands in **6** and **7** [8]. The presence of three chelating **Hpma**⁻ ligands enables binding of only one phenanthroline base to the Nd(III) ion in **6** instead of two **phen** ligands (as seen in **3**), due to the larger bite angle of the **Hpma**⁻ ligand compared to the acetate ligand [5].

Complex **1**   Complex **2**

Complex **3**   Complex **4**

Complex **5**
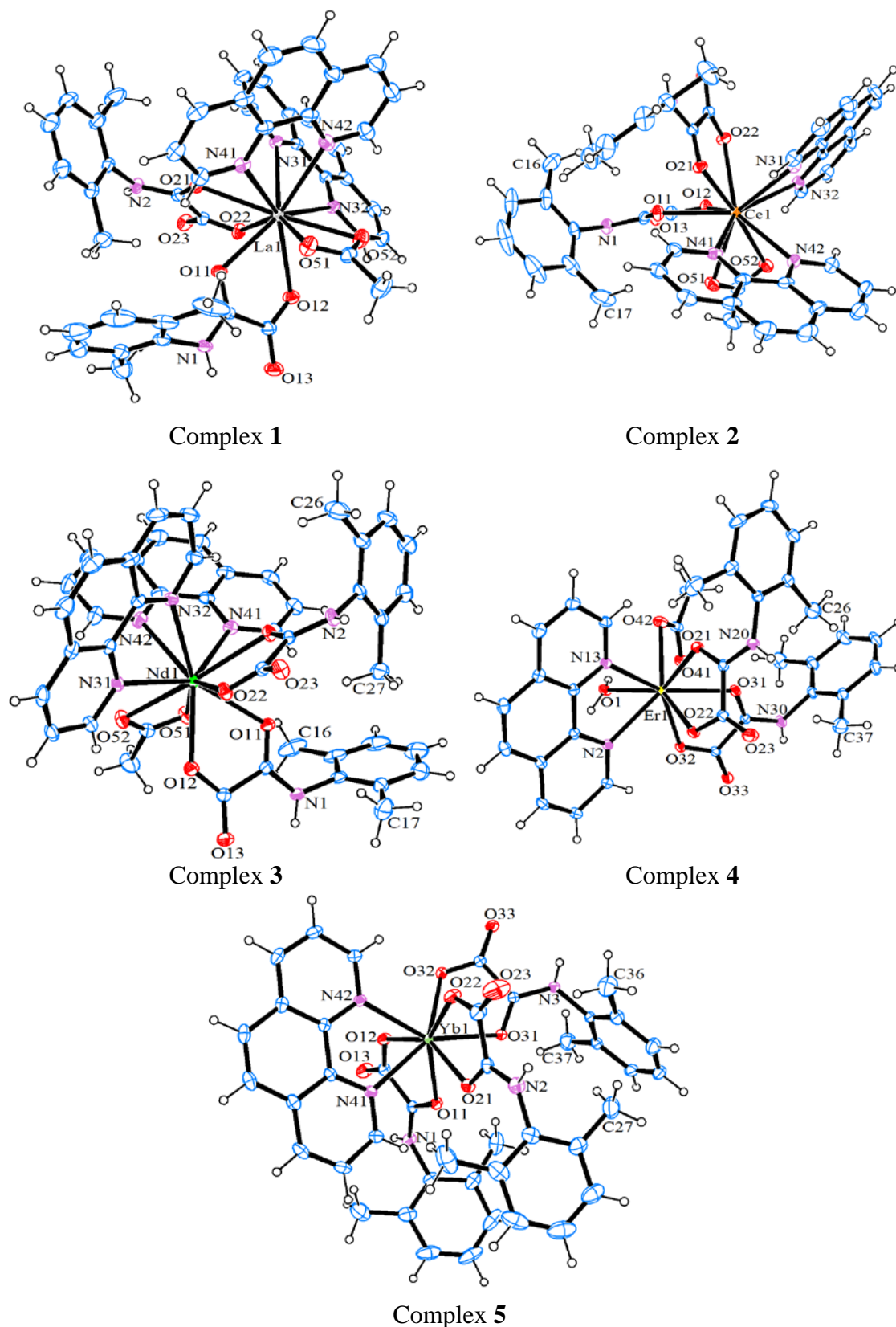
Figure 5.6a: The crystal structures of **1**–**5** displaying 30 % probability displacement ellipsoids and partial atom-numbering schemes. Outer-sphere solvent molecules are omitted for clarity.
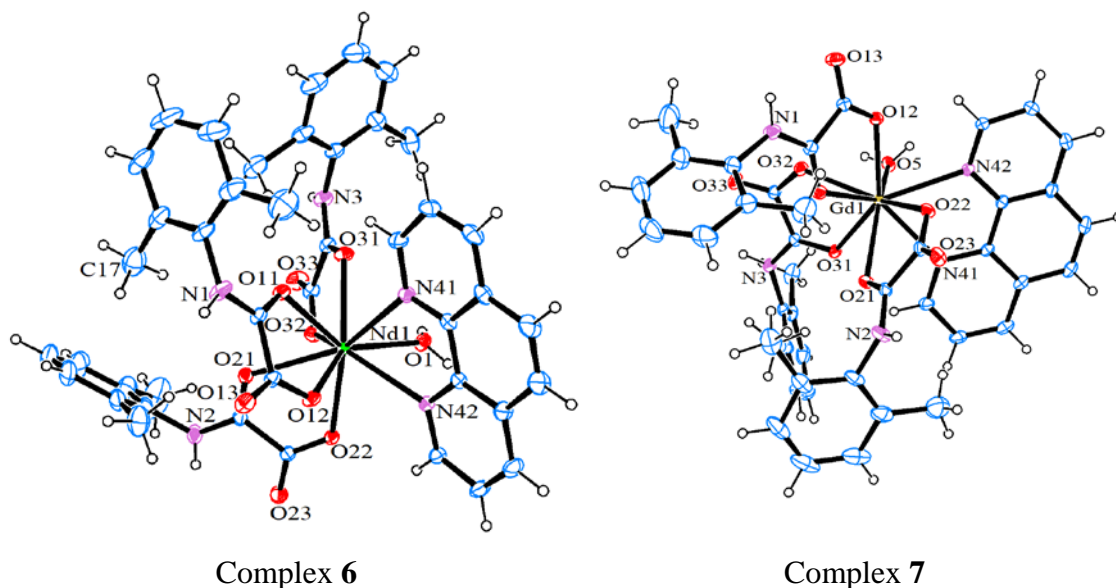
Complex **6**   Complex **7**

Figure 5.6b: *ORTEP* drawings of **6** and **7** (30 % probability level). Lattice H_2O molecules are omitted for clarity.

Selected bond lengths and angles for the complexes are listed in Tables 5.2a and 5.2b. The average Ln-N bond lengths [2.4620(19) to 2.775(3) Å] are longer than the Ln-O bonds [2.2658(18) to 2.632(2) Å] due to the stronger binding ability of the oxygen atoms [8,22]. The lanthanide contraction manifests itself by a gradual reduction in metal-oxygen and metal-nitrogen bond lengths, with increasing atomic number [8,50,51].

N-(2,6-dimethylphenyl)oxamate (**Hpma⁻**) and **phen** coordinate to the metal centres, forming five-membered rings, in which the $(O-Ln-O)_{Hpma–}$ bite angles [range: 61.65(6)° to 69.01(6)°] are larger than the $(N-Ln-N)_{phen}$ bite angles [range: 59.13(8)° to 66.21(6)°]. The average O-Ln-O and N-Ln-N bite angles decrease in the order: **5** (Yb) > **4** (Er) > **7** (Gd) > **6** (Nd) > **3** (Nd) > **2** (Ce) > **1** (La). This trend, whereby bite angles increase as the metal ionic radii decrease, is common, and is attributed to Ln-ligand bond shortening across the period [51]. The larger bite angles observed in the nine-coordinate Nd(III) complex (**6**) is an indication of less steric crowding than in the ten-coordinate Nd(III) complex (**3**), where there is increased congestion around the metal centre [52]. The four-membered chelate rings formed *via* binding of the acetate groups give an average bite angle of approximately 51.09°.

Table 5.2a: Selected bond parameters (Å, °) for lanthanide complexes **1–5**.

Compounds	[Ln(Hpma)₂(phen)₂(OAc)]·2H₂O			[Er(Hpma)₂(phen)(OAc)(H₂O)]·EtOH·H₂O		[Yb(Hpma)₃(phen)]·2 EtOH	
Bond lengths (Å)	**1** (Ln = La)	**2** (Ln = Ce)	**3** (Ln = Nd)	**4**		**5**	
Ln1-O11	2.567(2)	2.557(2)	2.5222(17)	Er1-O1	2.3841(13)	Yb1-O11	2.3553(16)
Ln1-O12	2.554(2)	2.539(2)	2.5038(18)	Er1-O21	2.4031(13)	Yb1-O12	2.2866(16)
Ln1-O21	2.632(2)	2.612(2)	2.5864(17)	Er1-O22	2.3933(14)	Yb1-O21	2.3837(16)
Ln1-O22	2.549(2)	2.523(2)	2.4998(17)	Er1-O31	2.4349(13)	Yb1-O22	2.2658(18)
Ln1-O51	2.547(2)	2.524(2)	2.4934(18)	Er1-O32	2.2868(13)	Yb1-O31	2.3266(16)
Ln1-O52	2.608(2)	2.594(2)	2.5691(19)	Er1-O41	2.6371(16)	Yb1-O32	2.2815(16)
Ln1-N31	2.772(2)	2.747(2)	2.6573(19)	Er1-O42	2.3379(16)	Yb1-N41	2.489(2)
Ln1-N32	2.716(2)	2.696(2)	2.712(2)	Er1-N2	2.5396(17)	Yb1-N42	2.4620(19)
Ln1-N41	2.744(2)	2.728(3)	2.693(2)	Er1-N13	2.5007(14)		
Ln1-N42	2.775(3)	2.758(3)	2.724(3)				
Bond angles (°)							
O11-Ln1-O12	63.20(7)	63.56(7)	64.38(5)	O21-Er1-O22	66.75(4)	O11-Yb1-O12	69.01(6)
O21-Ln1-O22	61.65(6)	62.09(7)	62.62(5)	O31-Er1-O32	68.93(4)	O21-Yb1-O22	68.93(6)
O51-Ln1-O52	50.45(7)	50.90(7)	51.30(6)	O41-Er1-O42	51.69(4)	O31-Yb1-O32	69.88(6)
N31-Ln1-N32	59.74(7)	60.30(7)	61.03(6)	N2-Er1-N13	65.10(5)	N41-Yb1-N42	66.21(6)
N41-Ln1-N42	59.13(8)	59.45(8)	60.25(6)				

Table 5.2b: Selected bond parameters (Å, °) for coordination compounds **6** and **7**.

[Nd(Hpma)₃(phen)(H₂O)]·4H₂O		[Gd(Hpma)₃(phen)(H₂O)]·4H₂O	
6		**7**	
Bond lengths (Å)		**Bond lengths (Å)**	
Nd1-O1	2.4792(18)	Gd1-O5	2.4264(15)
Nd1-O11	2.5077(18)	Gd1-O11	2.4982(14)
Nd1-O12	2.4722(18)	Gd1-O12	2.3686(14)
Nd1-O21	2.5450(18)	Gd1-O21	2.4682(14)
Nd1-O22	2.4230(18)	Gd1-O22	2.4267(14)
Nd1-O31	2.4746(18)	Gd1-O31	2.4158(14)
Nd1-O32	2.4682(19)	Gd1-O32	2.4396(15)
Nd1-N41	2.640(2)	Gd1-N41	2.5823(16)
Nd1-N42	2.6572(19)	Gd1-N42	2.6133(16)
Bond angles (°)		**Bond angles (°)**	
O11-Nd1-O12	65.32(6)	O11-Gd1-O12	67.21(5)
O21-Nd1-O22	65.71(6)	O21-Gd1-O22	66.39(5)
O31-Nd1-O32	64.78(6)	O31-Gd1-O32	65.53(5)
N41-Nd1-N42	62.25(6)	N41-Gd1-N42	63.53(5)

Crystallographic analyses reveal that the bond lengths and ligand bite angles of all the synthesised complexes do not show any anomalies and are in agreement with those of related compounds derived from oxamates and phenanthrolines [13,53-55]. An example is the dysprosium(III) complex with *N*-(2,6-dimethylphenyl) oxamic acid in which the metal-oxygen bonds lie in the range 2.340(2) − 2.407(2) Å, while the oxamate bite angles vary from 67.36(8) to 68.04(7)° [13]. Furthermore, the Ln-N

bond lengths and (N-Ln-N)$_{phen}$ bite angles of the synthesised complexes are comparable to those in Ce(III), Pr(III) and Nd(III) nitrate complexes with 1,10-phenanthroline [ranges: 0.2613(6) − 0.2719(3) nm and 61.0(1)^{o} − 62.3(2)^{o}, respectively] [54].

Besides the strong Ln(III)-ligand bonds as the main driving force for coordination, the relatively weak hydrogen bonds (O-H···O and N-H···O) are also a useful tool in the assembly of lanthanide complexes [56,57]. The crystal structures of **1**–**7** are stabilised through a variety of O-H···O networks [O···O = 2.711(6) to 2.923(4) Å] which occur between the coordinated and crystallographic H$_2$O molecules, lattice ethanol, acetate oxygens and the *O*-atoms of **Hpma**$^{-}$ (free and coordinated), as detailed in Tables 5.2c and 5.2d (see Figure 5.7a for hydrogen-bonding in complex **4**). All the complexes show N-H···O type hydrogen bonds [N···O = 2.682(2) – 2.995(3) Å] that are apparent between the N-H of **Hpma**$^{-}$ ligands and the free oxygen atoms of **Hpma**$^{-}$. Additionally, the crystal packing of the metal complexes is determined by the weak C-H···O contacts.

The crystal packing of the coordination compounds is also ensured by non-covalent parallel offset π-π interactions between the aromatic rings, with centroid-centroid (Cg-Cg) distances ranging from 3.4594(13) to 5.9882(18) Å [58,59]. A prominent example of such an interaction can be found in complex **1**, involving the 6-membered pyridyl rings of **phen**, originating from neighbouring units [Cg-Cg distance = 3.6647(17) Å; slippage = 1.479 Å] (Figure 5.7b). Moreover, the metal complexes **1**–**3** show the existence of C-H···π interactions between the partially positive methyl group hydrogens of **Hpma**$^{-}$, and the electron-rich π-cloud of **phen** (6-membered in **1**–**3** and 10-membered in **3**) and the **Hpma**$^{-}$ ring centroids (range = 2.75 – 2.97 Å) [59,60]. The other contribution of C-H···π links in **3** is from the acetate C-H groups and the 10-membered rings of **phen** (C52-H52C···Cg11). In the structure of **4**, the -N-H groups and the 6-membered rings of **Hpma**$^{-}$ of adjacent units form N-H···π interactions with a distance of 2.87(2) Å (symmetry operation: 1-*x*,1-*y*,2-*z*) [61]. In addition to influencing stabilisation of the complexes, the hydrogen bond interactions C-H···O, π-π, C-H···π and N-H···π are key in controlling the intercalation of different drugs into

DNA, as well as in protein structure and stability [61,62]. A significant number of these X-H···π interactions (X = C or N) are involved in drug recognition, enzyme action, DNA recognition and stabilisation of secondary structure of protein [61].

Table 5.2c: Hydrogen-bonding geometry (Å, °) for **1**–**5**.

Complex 1				
D-H···*A*	*D*-H	H···*A*	*D*···*A*	*D*-H···*A*
N1-H1···O13	0.80(3)	2.35(3)	2.696(3)	107(3)
N1-H1···O23	0.80(3)	2.13(3)	2.852(3)	150(3)
N2-H2···O23	0.77(4)	2.43(4)	2.730(3)	105(3)
N2-H2···O13	0.77(4)	2.14(4)	2.862(4)	155(3)
C42-H42···O23	0.95	2.50	3.340(5)	148
C323-H323···O22	0.95	2.33	3.166(3)	146
C325-H325···O52	0.95	2.50	3.055(4)	117
C415-H415···O11	0.95	2.55	3.244(4)	130
C415-H415···O21	0.95	2.53	2.863(4)	101
Complex 2				
D-H···*A*	*D*-H	H···*A*	*D*···*A*	*D*-H···*A*
N1-H1···O13	0.83(3)	2.29(3)	2.701(4)	111(3)
N1-H1···O23	0.83(3)	2.15(3)	2.859(4)	144(3)
N2-H2···O23	0.82(4)	2.45(3)	2.742(3)	102(3)
N2-H2···O13	0.82(4)	2.11(4)	2.872(4)	156(3)
Complex 3				
D-H···*A*	*D*-H	H···*A*	*D*···*A*	*D*-H···*A*
N1-H1···O13	0.83(3)	2.34(3)	2.696(3)	107(2)
N1-H1···O23	0.83(3)	2.13(3)	2.867(3)	148(2)
N2-H2···O23	0.84(3)	2.42(3)	2.738(3)	104(2)
N2-H2···O13	0.84(3)	2.11(3)	2.870(3)	152(2)
O6-H6A···O13	0.83	2.16	2.759(4)	129
O6-H6B···O7	0.83	2.13	2.862(8)	148
Complex 4				
D-H···*A*	*D*-H	H···*A*	*D*···*A*	*D*-H···*A*
O1-H1A···O6	0.83(2)	1.99(2)	2.823(2)	173(2)
O1-H1A···O41	0.83(2)	2.57(2)	2.888(2)	104.2(18)
O1-H1B···O33	0.835(17)	1.904(18)	2.729(2)	170(2)
O6-H6A···O51	0.841(19)	1.973(19)	2.809(2)	172(2)
O6-H6B···O41	0.836(16)	2.135(18)	2.840(2)	142(2)
N20-H20···O23	0.81(2)	2.41(3)	2.748(2)	106(2)
N30-H30···O33	0.78(2)	2.29(2)	2.682(2)	112(2)
O51-H51···O22	0.84	2.04	2.876(2)	171
Complex 5				
D-H···*A*	*D*-H	H···*A*	*D*···*A*	*D*-H···*A*
N1-H1···O13	0.81(3)	2.40(4)	2.736(3)	107(3)
N1-H1···O23	0.81(3)	1.97(3)	2.737(3)	160(4)
N2-H2···O23	0.81(2)	2.34(3)	2.720(4)	110(2)
N2-H2···O13	0.81(2)	2.22(2)	2.995(3)	161(3)
N3-H3···O33	0.81(3)	2.38(3)	2.714(3)	106(2)
O5-H5···O6	0.8400	1.9100	2.711(6)	159.00
O6-H6···O13	0.8400	2.1300	2.923(4)	157.00

D = donor, *A* = acceptor

Table 5.2d: Hydrogen-bonding geometry (Å, °) for **6** and **7**.

Complex 6				
D-H···*A*	*D*-H	H···*A*	*D*···*A*	*D*-H···*A*
N1-H1···O13	0.8800	2.2800	2.668(3)	107
O1-H1A···O23	0.834(18)	1.950(17)	2.761(3)	164(2)
O1-H1B···O3	0.84(2)	1.98(2)	2.812(3)	170(3)
N2-H2···O23	0.8800	2.2700	2.673(3)	108
N3-H3···O13	0.8800	2.0200	2.814(3)	150
N3-H3···O33	0.8800	2.3600	2.724(3)	105
Complex 7				
D-H···*A*	*D*-H	H···*A*	*D*···*A*	*D*-H···*A*
N1-H1···O13	0.8800	2.2700	2.675(2)	108.00
N2-H2···O23	0.8800	2.2900	2.679(2)	107.00
N3-H3···O23	0.8800	2.0200	2.812(2)	149.00
N3-H3···O33	0.8800	2.3700	2.731(2)	105.00
O5-H5A···O13	0.829(15)	1.951(14)	2.768(2)	169(2)
O5-H5B···O7	0.841(19)	2.011(18)	2.816(2)	160(2)
O6-H6A···O33	0.84(3)	1.97(3)	2.793(2)	165(3)
O6-H6B···O22	0.84(2)	1.99(2)	2.830(2)	175(2)
O7-H7A···O6	0.84(2)	1.99(3)	2.823(3)	171(3)
O7-H7B···O6	0.84(2)	2.05(2)	2.872(3)	167(2)

D = donor, *A* = acceptor
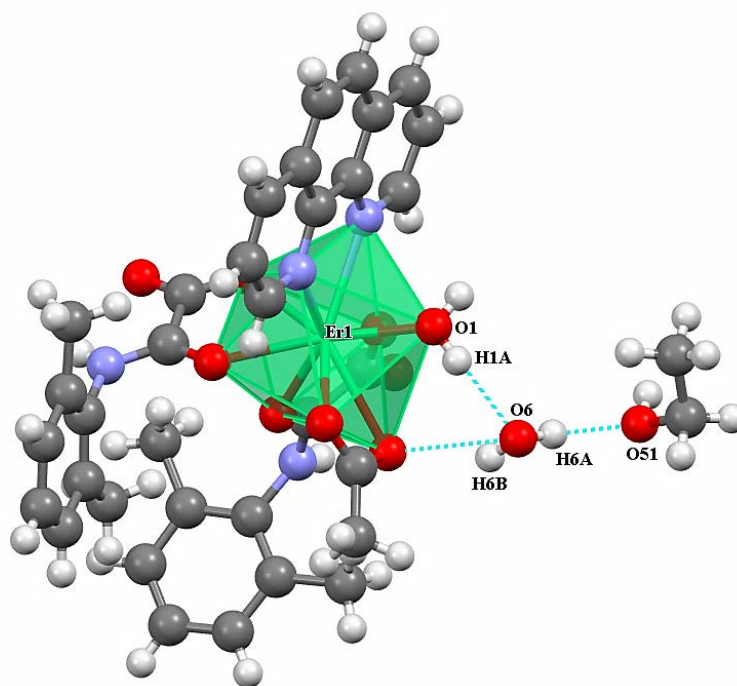
Figure 5.7a: Hydrogen bonding in the Er(III) complex.
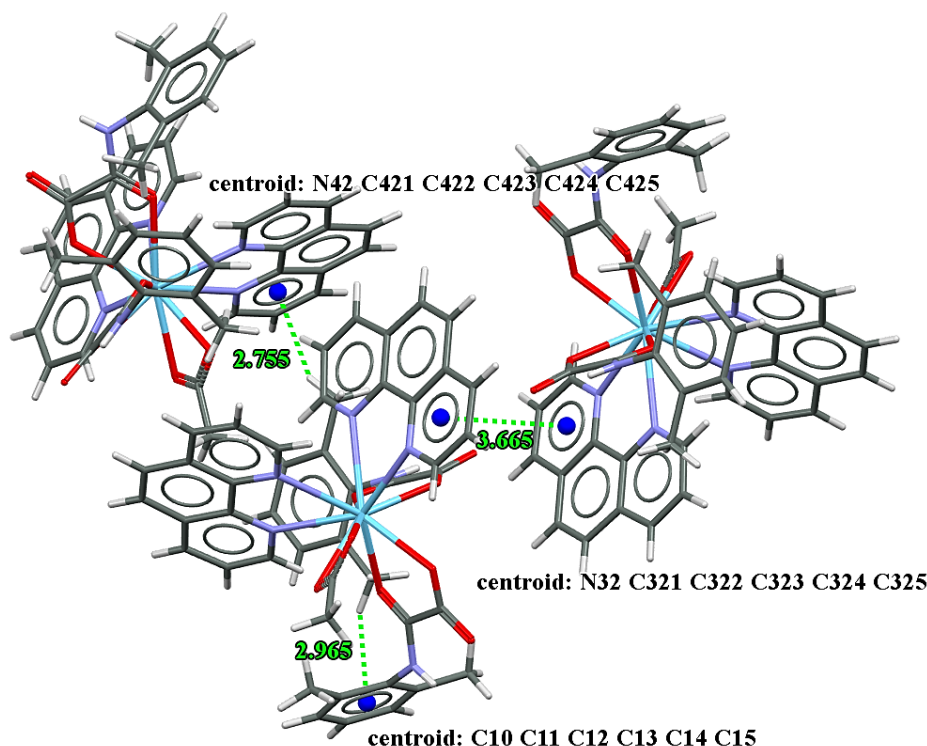
Figure 5.7b: An illustration of π-π (Symmetry: 2-*x*,1-*y*,1-*z*) and C-H···π interactions

(C-H···π = 2.755 Å: 1-*x*,1/2+*y*,1/2-*z*; C-H···π = 2.965 Å: *x*,*y*,*z*) in complex **1**.

5.3.6   Atomic charge analysis of the ligands

The natural population analysis (NPA) of **Hpma⁻** and **phen** (Figure 5.8a) were calculated using the DFT/B3LYP method, with the basis set aug-cc-pVTZ (the NPA of **Hpma⁻** has been outlined in Chapter 4) [63]. From Figure 5.8b, it is clear that all the hydrogen atoms of the **phen** molecule possess positive charges. The four carbon atoms (C7, C13, C15 and C21) linked to the electronegative nitrogen atoms are also electron deficient, with the most electropositive charge accumulated on C7 [0.28824 (DMSO) and 0.29450 (gas phase)]. The decreased population at these carbon atoms is a result of the electron-withdrawing properties of the nitrogen atoms [64]. The remaining carbon atoms exhibit negative charges. It has been found that the most electronegative charge of -0.47789 and -0.44400 (in DMSO) is accumulated over N1 and N2, respectively, thus supporting formation of *N,N*-donor bidentate systems. The natural population analysis precisely describes the distribution of electrons in different sub-shells (core, valence and Rydberg) of the atomic orbitals (Table 5.3).
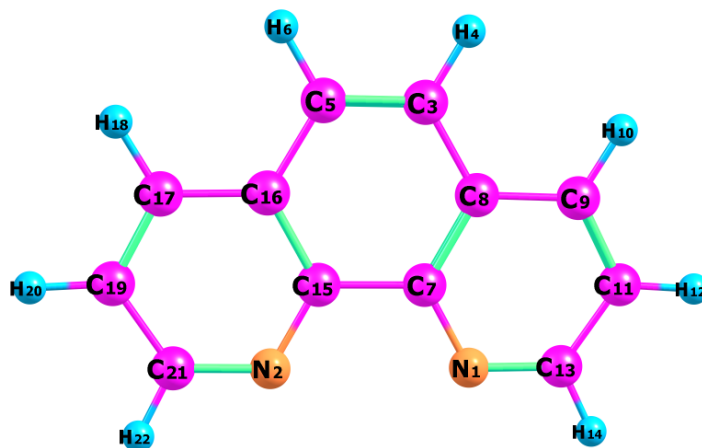
Figure 5.8a: The optimised molecular structure of **phen**, with atom-numbering scheme.
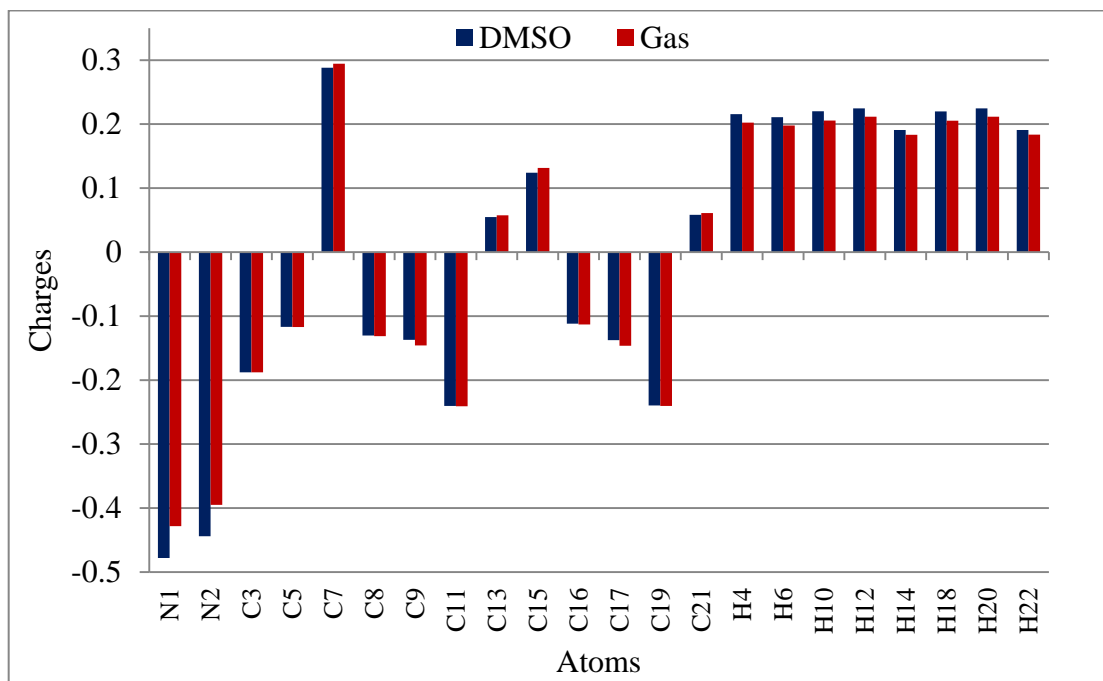
Figure 5.8b: The NPA atomic charge distribution of **phen** in the gas phase and DMSO.

Table 5.3: Natural population analysis showing the allocation of electrons between the core, valence and Rydberg orbitals for selected atoms in **phen** in DMSO.

Atom	Charge	Core	Valence	Rydberg	Total
N1	-0.47783	1.99999	5.42660	0.05130	7.47789
N2	-0.44400	1.99999	5.40857	0.03544	7.44400
C7	0.28824	1.99999	3.68581	0.02596	5.71176
C19	-0.23963	1.99999	4.22230	0.01735	6.23963
H12	0.22470	0.00000	0.77321	0.00210	0.77530
H14	0.19078	0.00000	0.80673	0.00249	0.80922

Core: 27.99983 (99.9994 % of 28)
Valence: 65.57880 (99.3618 % of 66)
Rydberg: 0.42136 (0.4483 % of 94)

The molecular electrostatic potential (MEP) maps at the DFT/B3LYP/aug-cc-pVTZ optimised geometry was calculated to reveal the reactive sites of electrophilic and nucleophilic attacks for **Hpma⁻** and **phen** (Figure 5.9a and 5.9b) [65]. The **Hpma⁻** MEP supports the bidentate chelation and/or bridging ability of the oxamate moiety due to the most negative potential observed on the three oxygen atoms. However, the presence of **phen** in the coordination sphere probably prevented complexes from polymerising through bridging, resulting in **Hpma⁻** only binding bidentately [8]. The nitrogen atoms of **phen** were identified as having the most negative potential, thus making them the most reactive part in the organic compound. The violet or blue regions, especially around the hydrogens, represent electron-poor or positive electrostatic potential sites. The former regions thus correspond to areas where the proton is attracted to the electronic density, whilst the latter surfaces (blue/violet) denote repulsion of the proton by atomic nuclei in the surface with a lower electron density [65]. Interestingly, the **Hpma⁻** and **phen** aromatic rings are electron-rich due to the delocalised π-system, while the **Hpma⁻** hydrogen atoms show electron deficiency, thus indicating the favourability of C-H⋯π and N-H⋯π interactions [66,67].
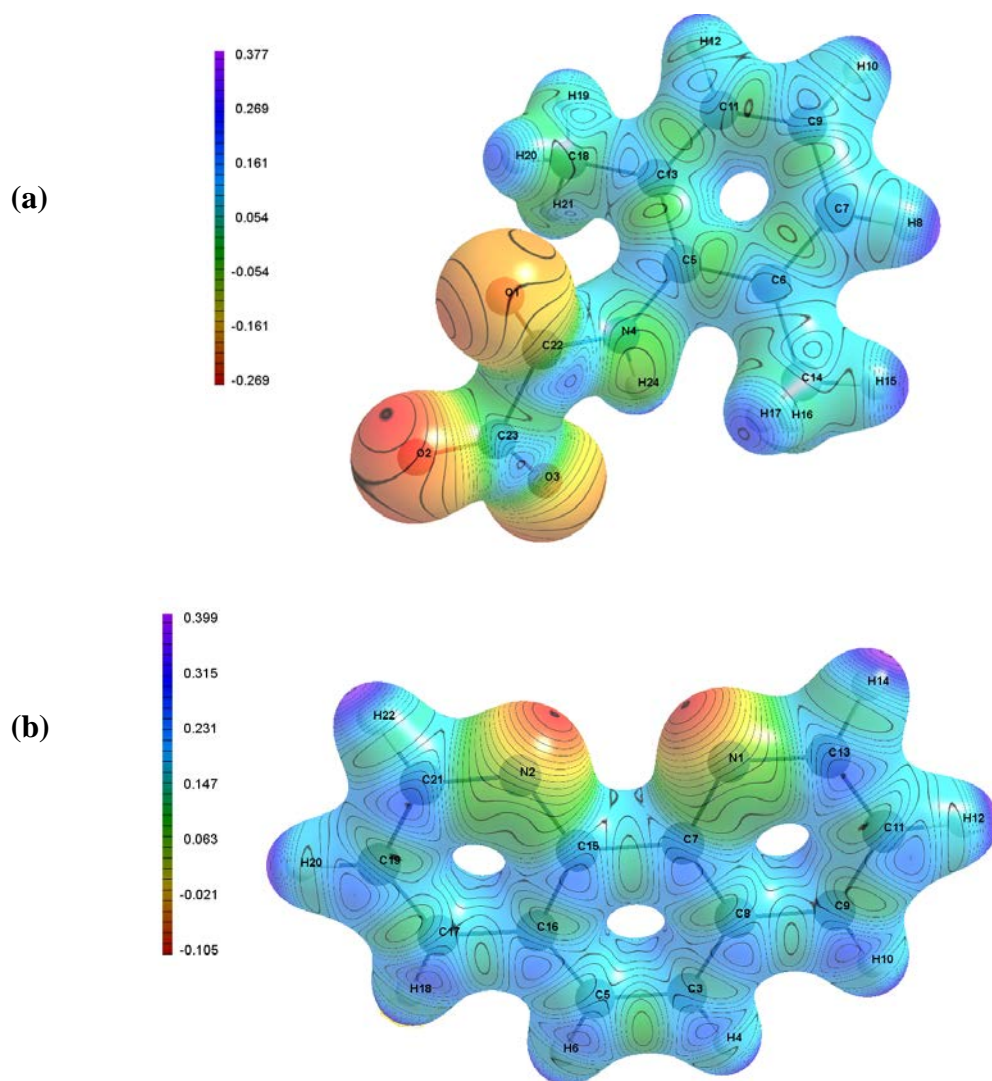
Figure 5.9: Molecular electrostatic potential maps of: **(a) Hpma⁻** and **(b) phen**.

5.3.7 Frontier molecular orbital analysis, and global and chemical reactivity descriptors

The energy values of the highest occupied molecular orbital (*HOMO*) and the lowest unoccupied molecular orbital (*LUMO*) for **phen** were computed at B3LYP/aug-cc-pVTZ level in DMSO (Figure 5.10). Generally the energies of these frontier molecular orbitals (*HOMO* and *LUMO*) and their energy gaps (ΔE) are a reflection of chemical reactivity (*e.g.* charge-transfer interactions) and stability of the molecule [68,69]. A small energy gap between the *HOMO* and *LUMO* implies high chemical reactivity, since the *HOMO* is an electron-donor, while the *LUMO* is an electron-acceptor. High kinetic stability (or hardness of the crystal), on the other hand, is

denoted by high energy gaps [68,70]. The *HOMO* and *LUMO* energies were found to be -6.662 and -1.907 eV, respectively, with an energy gap ($\Delta E = E_{LUMO} - E_{HOMO}$) of 4.755 eV. The $\pi \rightarrow \pi^*$ transition is the most probable electronic transition for the ligand [71,72]. The big energy gap might imply that the structure of **phen** is very stable [70].

$E_{LUMO+1} = -1.862$ eV

$E_{LUMO} = -1.907$ eV

$\Delta E = 4.755$ eV

$\Delta E = 5.181$ eV

$E_{HOMO} = -6.662$ eV

$E_{HOMO-1} = -7.043$ eV
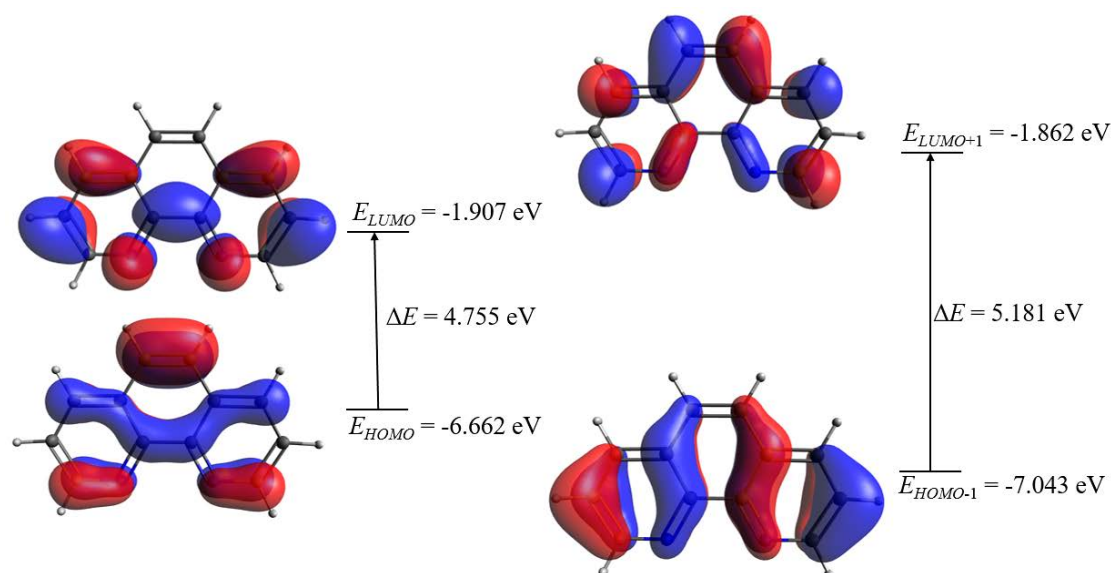
Figure 5.10: Frontier molecular orbital surfaces (*HOMO*-1 to *LUMO*+2) and energy levels for the orbitals of **phen** computed at B3LYP/aug-cc-pVTZ level.

Global reactivity indices, such as chemical potential, softness, hardness and electrophilicity, were calculated at B3LYP/aug-cc-pVTZ level to study the electronic effects of the ligand (Table 5.4) [73-75]. The global hardness value, an indication of molecular stability, was 2.378 eV, whilst the softness value (the inverse of hardness) is 0.421 eV^{-1}. Hard molecules are less polarisable compared to soft molecules, as they require higher excitation energies to achieve the excited states [69].

Table 5.4: Calculated frontier molecular orbital parameters and global reactivity descriptors for **phen** at DFT/B3LYP/aug-cc-pVTZ level in DMSO. All parameters are in eV, except for softness, which is in eV^{-1}.

Global and chemical reactivity descriptor	Symbols	Values
Energy of *HOMO*	E_{HOMO}	-6.662
Energy of *LUMO*	E_{LUMO}	-1.907
Energy of *HOMO*-1	$E_{HOMO\text{-}1}$	-7.043
Energy of *LUMO*+1	E_{LUMO+1}	-1.862
Energy of *HOMO*-2	$E_{HOMO\text{-}2}$	-7.163
Energy of *LUMO*+2	E_{LUMO+2}	-0.748
First energy gap	$\Delta E = LUMO - HOMO$	4.755
Second energy gap	$\Delta E = LUMO+1 - HOMO\text{-}1$	5.181
Third energy gap	$\Delta E = LUMO+2 - HOMO\text{-}2$	6.415
Ionisation energy (I)	$-E_{HOMO}$	6.662
Electron affinity (A)	$-E_{LUMO}$	1.907
Hardness (η)	$\dfrac{(I - A)}{2}$	2.378
Chemical potential (μ)	$\dfrac{-(I + A)}{2}$	-4.285
Softness (σ)	$\dfrac{1}{\eta}$	0.421
Electrophilicity index (ω)	$\dfrac{\mu^2}{2\eta}$	3.861
Electronegativity (χ_m)	$\dfrac{I + A}{2}$	4.285

5.3.8   Anticancer screen

For this study, the effects of the proligand **Hdmp**, **phen**, Ln(III) salts, metal complexes **1**–**7**, as well as the positive control, curcumin, were assessed for potential cytotoxicity against the MCF-7, HEC-1A and THP-1 cell lines (Figure 5.11; Table S5.3). No cytotoxic effects are observed in THP-1 cells (p>0.05) for all the target compounds, except for the positive control (21.5±0.83 % cell viability); an indication of no adverse effects exerted by the target compounds on the monocytes of the immune system [76,77]. This can be explained by the fact that the THP-1 human monocytic cell line possesses high similarities with primary monocytes and macrophages in biological function [76,78].
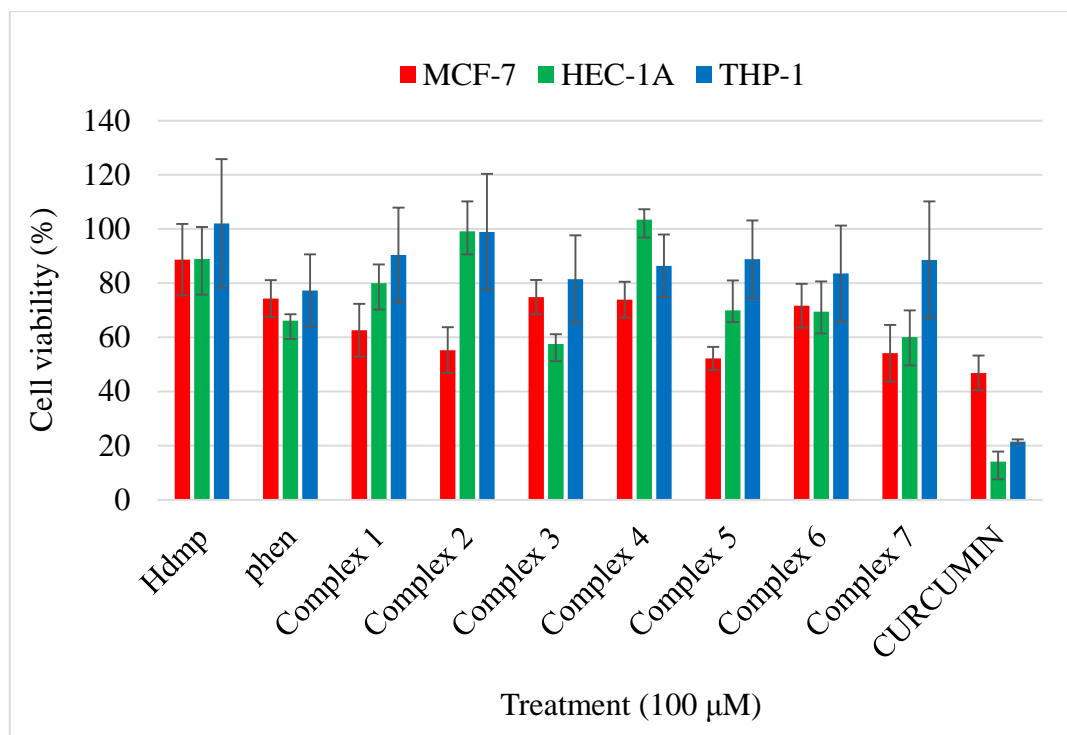
Figure 5.11: Cytotoxic effects of the free ligands and complexes **1**–**7** on MCF-7, HEC-1A and THP-1 cells using the MTT assay. Mean values of three independent experiments ± SD are shown.

Cytotoxicity studies revealed antiproliferative activity in MCF-7 cells ($p < 0.05$) after treatment with **phen**, and coordination compounds **1**–**7**. It is further observed that the cytotoxicity of **2**, **5** and **7** is similar to that of the positive control (curcumin) in MCF-7 cells ($p > 0.05$), with ~50 % inhibition at 100 µM. Nevertheless, none of the tested ligands, Ln(III) acetates, Ln(III) nitrates and complexes showed greater activity than curcumin in the cell lines tested (46.8±6.46, 14.1±3.76 and 21.5±0.83 % cell viability in MCF-7, HEC-1A and THP-1 cells, respectively). Complex **2**, however, shows selective toxicity towards MCF-7 cells, without decreasing viability in HEC-1A or THP-1 cells.

Statistically significant cytotoxic effects were exerted by [Nd(NO$_3$)$_3$·6H$_2$O], **phen**, **3**, **6** and **7** in HEC-1A cells ($p < 0.05$). The high electrophilicity index of **phen** can be related to the significant biological activity of the compound towards MCF-7 and

HEC-1A cells [79-81]. Electrophilicity is also an important electronic parameter in the stabilisation of the compounds in the active site [82]. The cytotoxicity of complex **3** against HEC-1A cells (~50 % inhibition at 100 µM) appears similar to that of the Nd(III), Er(III) and Yb(III) complexes with the hydrazone **H₂Nic** (Chapter 3). Cytotoxicity shown by **phen**, **3** and **5**–**7** in both MCF-7 and HEC-1A cells, but not in THP-1 cells suggests that hormone-responsive breast and endometrial cancer cell lines could be sensitive to these compounds [83-85]. This prompts the execution of further experiments to gain more insights into the hormone-responsive mechanisms of cell growth inhibition.

5.4   Conclusion

Octa-, nona- and deca-coordinate mixed-ligand complexes of the bidentate ligand **Hpma⁻** and **phen** were successfully prepared using lanthanide acetates and nitrates. In summary, seven novel Ln(III) complexes, [Ln(Hpma)$_2$(phen)$_2$(OAc)]·2H$_2$O (Ln = La, Ce and Nd), [Er(Hpma)$_2$(phen)(OAc)(H$_2$O)]·EtOH·H$_2$O, [Yb(Hpma)$_3$(phen)]·2EtOH and [Ln(Hpma)$_3$(phen)(H$_2$O)]·4H$_2$O (Ln = Nd and Gd) were synthesised. The crystallographic analysis revealed that **1**–**3** are isostructural, as well as **6** and **7**. The ability of 1,10-phenanthroline to prevent complexes from polymerising is revealed by the isolation of monomeric mixed-ligand complexes **1**–**7**, in contrast to the polymeric Ln(III)-Hpma coordination compounds synthesised in Chapter 4 [8]. The *O,O-* and *N,N-*donor properties of the two ligands in these coordination compounds was supported by NBO charge population analysis and electrostatic potential surfaces. The coordination fashion of the *O,O-*donor oxamate moiety is dependent on two factors: 1) the preference of lanthanide ions for oxygen-donor groups, and 2) the protonated amide *N-*atom [13]. Bond parameters do not show any anomalies and are in agreement with those of related compounds. The average Ln-O and Ln-N bond lengths decrease as the atomic number of the rare-earth elements increase, which indicates the effect of lanthanide contraction. The auxiliary ligand **phen** was effective in preventing polymerisation, as monomeric complexes were obtained.

The solid-state structures of the coordination compounds include combinations of hydrogen bonds (O-H⋯O and N-H⋯O), C-H⋯O, π⋯π, C-H⋯π and N-H⋯π interactions, with the solvents of crystallisation playing a key role in hydrogen bonding. These interactions influence the crystal packing, and it is worthwhile to further study their effects on biomolecules and drug design [66].

The effects of free ligands, metal acetates and nitrates, and Ln(III) complexes on the cell growth in MCF-7 and HEC-1A cells were evaluated by the MTT assay [86]. 1,10-Phenanthroline and complexes **1**–**7** show moderate cytotoxicity against MCF-7 cells, while [Nd(NO$_3$)$_3$·6H$_2$O], **phen**, **3**, **6** and **7** are cytotoxic against HEC-1A cells. None of the compounds were cytotoxic against the THP-1 cells. In all three cell lines, curcumin was the most active compound tested. These observations infer that different compounds show different toxic effects, whilst the selective toxicity of complex **2** towards MCF-7 cells suggest that the same complex displays varying antiproliferative effects in different cancer cells. Interestingly, a comparison of lanthanide complexes with **Hpma⁻** (Chapter 4) and mixed-ligand Ln(III) complexes of **Hpma⁻** and **phen** suggest significant reduction in cancer cell viability on introduction of **phen** into Ln(III)-oxamate complexes. The higher cytotoxicities of the mixed-ligand complexes are consistent with the DNA-binding and cleavage activity of **phen** or its metal complexes [7,87].

5.5   Supplementary information

5.5.1   Crystal data and refinements

Table S5.1a: Crystal and structure refinement data for complexes **1**–**3**.

	1	**2**	**3**
Formula	$2(C_{46}H_{39}LaN_6O_8)$, 3(O)	$2(C_{46}H_{39}CeN_6O_8)$, 3(O)	$C_{46}H_{39}N_6NdO_8$, H_2O, O
M_r (g.mol^{-1})	1933.48	1935.90	982.09
Crystal system	Monoclinic	Monoclinic	Monoclinic
Space group	*P2₁/c* (No. 14)	*P2₁/c* (No. 14)	*P2₁/c* (No. 14)
a, b, c [Å]	12.0482(4), 16.1025(5), 23.1939(8)	12.0523(5), 16.0867(7), 23.1852(10)	12.0206(6), 16.0518(8), 23.0415(11)
α, β, γ (°)	90, 104.666(2), 90	90, 104.689(2), 90	90, 104.519(2), 90
V (Å^3)	4353.2(3)	4348.3(3)	4303.9(4)
Z	2	2	4
ρ (g.cm^{-3})	1.475	1.479	1.516
μ (mm^{-1})	1.046	1.111	1.273
$F(000)$	1960	1964	1996
Crystal size (mm)	$0.09 \times 0.16 \times 0.33$	$0.04 \times 0.17 \times 0.23$	$0.16 \times 0.21 \times 0.29$
Temperature (K)	200	200	200
Mo *Kα* radiation, λ (Å)	0.71073	0.71073	0.71073
θ (min-max) (°)	1.8, 28.3	1.8, 28.3	1.8, 28.3
Data set	-16≤*h*≤16; -21≤*k*≤21; -30≤*l*≤30	-16≤*h*≤16; -20≤*k*≤21; -30≤*l*≤30	-16≤*h*≤16; -20≤*k*≤21; -30≤*l*≤30
Tot., Unique data, R_{int}	63314, 10820, 0.038	61989, 10761, 0.063	99387, 10702, 0.038
Observed [I>2σ(I)] reflections	8974	7465	8664
$N_{reflections}$, $N_{parameters}$	10820, 581	10761, 581	10702, 581
$R[F^2>2\sigma(F^2)]$, $wR(F^2)$, S	0.0348, 0.0897, 1.12	0.0373, 0.0818, 1.01	0.0281, 0.0650, 1.05
$\Delta\rho_{min}$, $\Delta\rho_{max}$ (e.Å^{-3})	-0.94, 1.23	-0.60, 0.80	-0.55, 0.72

Table S5.1b: Crystal and structure refinement data for complexes **4** and **5**.

	4	5
Formula	**$C_{34}H_{33}ErN_4O_9$, C_2H_6O, H_2O**	**$C_{42}H_{38}N_5O_9Yb$, $2(C_2H_6O)$**
M_r (g.mol^{-1})	872.99	1021.95
Crystal system	Triclinic	Monoclinic
Space group	*P-1* (No. 2)	*P21/c* (No. 14)
a, b, c [Å]	12.086(3), 13.105(3), 13.534(3)	9.5136(4), 21.6436(7), 22.3636(8)
α, β, γ (°)	92.077(9), 115.737(9), 106.619(9)	90, 93.966(2), 90
V (Å^3)	1818.1(8)	4593.8(3)
Z	2	4
ρ (g.cm^{-3})	1.595	1.478
μ (mm^{-1})	2.373	2.100
$F(000)$	882	2076
Crystal size (mm)	$0.25 \times 0.46 \times 0.53$	$0.20 \times 0.25 \times 0.64$
Temperature (K)	200	200
Mo $K\alpha$ radiation, λ (Å)	0.71073	0.71073
θ (min-max) (°)	1.9, 28.3	1.8, 28.3
Data set	-16≤h≤16; -16≤k≤17; -18≤l≤18	-12≤h≤12; -28≤k≤24; -29≤l≤29
Tot., Unique data, R_{int}	55437, 8999, 0.019	75865, 11436, 0.032
Observed [I>2σ(I)] reflections	8592	9880
$N_{reflections}$, $N_{parameters}$	8999, 501	11436, 590
$R[F^2>2\sigma(F^2)]$, $wR(F^2)$, S	0.0146, 0.0371, 1.09	0.0260, 0.0577, 1.08
$\Delta\rho_{min}$, $\Delta\rho_{max}$ (e.Å^{-3})	-0.55, 0.75	-0.51, 0.86

Table S5.1c: Crystal and structure refinement data for complexes **6** and **7**.

	6	7
Formula	$C_{42}H_{40}N_5NdO_{10}$, 4(O)	$C_{42}H_{40}GdN_5O_{10}$, 2(O)
M_r (g.mol^{-1})	983.03	1000.07
Crystal system	Triclinic	Triclinic
Space group	*P-1* (No. 2)	*P-1* (No. 2)
a, b, c [Å]	10.6660(6), 12.7949(8), 18.1096(11)	10.6087(7), 12.7117(8), 18.0422(12)
α, β, γ (°)	76.516(3), 74.850(2), 90.000(3)	76.604(3), 75.000(3), 89.978(3)
V (Å^3)	2314.9(2)	2281.6(3)
Z	2	2
ρ (g.cm^{-3})	1.410	1.456
μ (mm^{-1})	1.189	1.522
F(000)	998	1014
Crystal size (mm)	$0.06 \times 0.56 \times 0.57$	$0.08 \times 0.47 \times 0.56$
Temperature (K)	200	200
Mo *Kα* radiation, λ (Å)	0.71073	0.71073
θ (min-max) (°)	1.8, 28.4	2.0, 28.3
Data set	$-14 \leq h \leq 14$; $-17 \leq k \leq 17$; $-24 \leq l \leq 24$	$-14 \leq h \leq 14$; $-16 \leq k \leq 16$; $-24 \leq l \leq 23$
Tot., Unique data, R_{int}	141091, 11445, 0.025	59621, 11265, 0.029
Observed [I>2σ(I)] reflections	10774	10257
$N_{reflections}$, $N_{parameters}$	11445, 573	11265, 589
$R[F^2>2\sigma(F^2)]$, $wR(F^2)$, S	0.0279, 0.0775, 1.15	0.0223, 0.0539, 1.05
$\Delta\rho_{min}$, $\Delta\rho_{max}$ (e.Å^{-3})	-0.56, 1.47	-0.48, 0.75

5.5.2   Molecular modelling data

Table S5.2: Natural population analysis of 1,10-phenanthroline at the DFT/B3LYP level using the aug-cc-pVTZ basis set in the gas phase and DMSO.

Atoms	Natural charge (DMSO)	Population	Natural charge (gas)	Population
N1	-0.47789	7.47789	-0.42835	7.42835
N2	-0.44400	7.44400	-0.39485	7.39485
C3	-0.18786	6.18786	-0.18786	6.18786
C5	-0.11681	6.11681	-0.11714	6.11714
C7	0.28824	5.71176	0.29450	5.70550
C8	-0.13030	6.13030	-0.13127	6.13127
C9	-0.13696	6.13696	-0.14589	6.14589
C11	-0.24027	6.24027	-0.24099	6.24099
C13	0.05483	5.94517	0.05762	5.94238
C15	0.12397	5.87603	0.13149	5.86851
C16	-0.11171	6.11171	-0.11309	6.11309
C17	-0.13753	6.13753	-0.14635	6.14635
C19	-0.23963	6.23963	-0.24036	6.24036
C21	0.05834	5.94166	0.06108	5.93892
H4	0.21571	0.78429	0.20246	0.79754
H6	0.21086	0.78914	0.19789	0.80211
H10	0.22012	0.77988	0.20557	0.79443
H12	0.22470	0.77530	0.21166	0.78834
H14	0.19078	0.80922	0.18340	0.81660
H18	0.21986	0.78014	0.20537	0.79463
H20	0.22468	0.77532	0.21164	0.78836
H22	0.19087	0.80913	0.18349	0.81651
Total	**0.00000**	**94.00000**	**0.00000**	**94.00000**

5.5.3 Anticancer activity tests

Table S5.3: Summary of cytotoxicity of the ligands **Hdmp**, **phen** and their Ln(III) complexes.

Compound (100 µM)	Cells		
	MCF-7	HEC-1A	THP-1
	Cell viability (%)		
La(OAc)$_3$)$_3$·xH$_2$O	103.7±10.28	82.87±13.03	122.0±12.76
Ce(OAc)$_3$)$_3$·xH$_2$O	102.0±9.69	121.1±16.28	108.2±15.38
Nd(OAc)$_3$)$_3$·xH$_2$O	104.3±9.69	93.87±13.18	101.9±2.62
Er(OAc)$_3$)$_3$·xH$_2$O	93.8±1.70	95.4±18.87	105.4±18.88
Yb(OAc)$_3$)$_3$·4H$_2$O	100.5±0.65	85.8±6.85	89.9±10.16
Nd(NO$_3$)$_3$·6H$_2$O	88.6±6.99	82.4±4.77	93.7±23.98
Gd(NO$_3$)$_3$·6H$_2$O	88.8±12.26	85.7±14.64	89.4±17.70
Hdmp	88.7±13.17	88.9±11.81	102.0±23.74
phen	74.4±6.78	66.2±2.37	77.3±13.34
Complex **1**	62.6±9.75	80.0±6.89	90.4±17.49
Complex **2**	55.3±8.50	99.2±11.05	98.9±21.42
Complex **3**	74.8±6.33	57.6±3.57	81.5±16.23
Complex **4**	73.9±6.60	103.43±3.85	86.4±11.59
Complex **5**	52.2±4.29	69.9±11.08	88.8±14.34
Complex **6**	71.7±8.05	69.5±11.16	83.6±17.68
Complex **7**	54.2±10.43	60.1±9.91	88.5±21.63
CURCUMIN	46.8±6.46	14.1±3.76	21.5±0.83

5.6   References

[1]   K.M. Knopf, B.L. Murphy, S.N. MacMillan, J.M. Baskin, M.P. Barr, E. Boros and J.J. Wilson, "*In vitro* anticancer activity and *in vivo* biodistribution of rhenium(I) tricarbonyl aqua complexes", *J. Am. Chem. Soc.*, **139** (2017) 14302−14314.

[2]   American Cancer Society. *Global Cancer Facts & Figures*, 3rd Edition, Atlanta: American Cancer Society; 2015, pp 1–61.

[3]   P. Jia, R. Ouyang, P. Cao, X. Tong, X. Zhou, T. Lei, Y. Zhao, N. Guo, H. Chang, Y. Miao and S. Zhou, "Review: Recent advances and future development of metal complexes as anticancer agents", *J. Coord. Chem.*, **70** (2017) 2175–2201.

[4]   E.N. Sholikhah, J. Jumina, S. Widyarini, R. Hadanu and M. Mustofa, "*In vitro* anticancer activity of *N*-benzyl 1,10-phenanthroline derivatives on human cancer cell lines and their selectivity", *I.J. Biotech.*, **23** (2018) 68–73.

[5]   A. Hussain and A.R. Chakravarty, "Photocytotoxic lanthanide complexes", *J. Chem. Sci.*, **124** (2012) 1327–1342.

[6]   C.-H. Leung, S. Lin, H.-J. Zhong and D.-L. Ma, "Metal complexes as potential modulators of inflammatory and autoimmune responses", *Chem. Sci.*, **6** (2015) 871–884.

[7]   A. Bencini and V. Lippolis, "1,10-Phenanthroline: A versatile building block for the construction of ligands for various purposes", *Coord. Chem. Rev.*, **254** (2010) 2096–2180.

[8]   C. Huang (2010) – *Rare-Earth Coordination Chemistry – Fundamentals and Applications*. John Wiley & Sons, Asia. pp 91–232.

[9]   Y. Wang, C.-W. Jin, S.-M. He, N. Ren and J.-J. Zhang, "Five novel lanthanide complexes with 2-chloroquinoline-4-carboxylic acid and 1,10-phenanthroline: Crystal structures, molecular spectra, thermal properties and bacteriostatic activities", *J. Mol. Struct.*, **1125** (2016) 383–390.

[10]   W.X.C. Oliveira, C.B. Pinheiro, M.M. da Costa, A.P.S. Fontes, W.C. Nunes, F. Lloret, M. Julve and C.L.M. Pereira, "Crystal engineering applied to modulate the structure and magnetic properties of oxamate complexes containing the [Cu(bpca)]$^+$ cation", *Cryst. Growth Des.*, **16** (2016) 4094−4107.

[11]   F.J. Caires, W.D.G. Nunes, C. Gaglieri, André L.C.S. do Nascimento, J.A. Teixeira, G.A.C. Zangaro, O. Treu-Filho and M. Ionashiro, "Thermoanalytical, spectroscopic and DFT studies of heavy trivalent

lanthanides and yttrium(III) with oxamate as ligand", *Mater. Res.,* **20** (2017) 937–944.

[12]   N. Li, Y. Zheng, X. Jiang, R. Zhang and W. Chen, "Generation of reactive cobalt oxo oxamate radical species for biomimetic oxidation of contaminants", *RSC Adv.*, **7** (2017) 42875–42883.

[13]   F.R. Fortea-Pérez, J. Vallejo, M. Julve, F. Lloret, G. De Munno, D. Armentano and E. Pardo**,** "Slow magnetic relaxation in a hydrogen-bonded 2D array of mononuclear dysprosium(III) oxamates"**,** *Inorg. Chem.*, **52** (2013) 4777−4779.

[14]   F.R. Fortea-Pérez, D. Armentano, M. Julve, G. De Munno and S.-E. Stiriba, "Bis(oxamato)palladate(II) complexes: synthesis, crystal structure and application to catalytic Suzuki reaction", *J. Coord. Chem.*, **67** (2014) 4003–4015.

[15]   C.J. Valvona and H.L. Fillmore, "Oxamate, but not selective targeting of LDH-A, inhibits medulloblastoma cell glycolysis, growth and motility", *Brain Sci.*, **8** (2018) 1–12.

[16]   C.K.L. Lam, M. Chari, P.Y.T. Wang and T.K.T. Lam, "Central lactate metabolism regulates food intake", *Am. J. Physiol. Endocrinol. Metab*., **295** (2008) E491–E496.

[17]   P. Tang, J. Xu, C.L. Oliveira, Z.J. Li and S. Liu, "A mechanistic kinetic description of lactate dehydrogenase elucidating cancer diagnosis and inhibitor evaluation", *J. Enzyme Inhib. Med. Chem.*, **32** (2017) 564–571.

[18]   C. Ramachandran, A. Juan, K. Quirin, L. Khatib, Y. Schultz, T.L. Lampidis, E. Escalon and S.J. Melnick, "Synergistic effect of supercritical CO_2 extract of mango ginger (*Curcuma amada*- Roxb.) with glycolytic inhibitors in human glioblastoma cells *in vitro*.", *Advances in Cancer Research & Therapy*, **3** (2019) 1–11.

[19]   X. Zhai, Y. Yang, J. Wan, R. Zhu and Y. Wu, "Inhibition of LDH-A by oxamate induces G_2/M arrest, apoptosis and increases radiosensitivity in nasopharyngeal carcinoma cells", *Oncol. Rep.*, **30** (2013) 2983-2991.

[20]   Y. Yang, D. Su, L. Zhao, D. Zhang, J. Xu, J. Wan, S. Fan and M. Chen, "Different effects of LDH-A inhibition by oxamate in non-small cell lung cancer cells", *Oncotarget*, **5** (2014) 11886–11895.

[21]   E. Mungo, L. Bergandi, I.C. Salaroglio and S. Doublier, "Pyruvate treatment restores the effectiveness of chemotherapeutic agents in human colon adenocarcinoma and pleural mesothelioma cells", *Int. J. Mol. Sci.*, **19** (2018) 1–23.

[22]   G.-C. Zong, J.-X. Huo, N. Ren, J.-J. Zhang, X.-X. Qi, J. Gao, L.-N. Geng, S.-P. Wang and S.-K. Shi, "Preparation, characterization and properties of four new trivalent lanthanide complexes constructed using 2-bromine-5-methoxybenzoic acid and 1,10-phenanthroline", *Dalton Trans.*, **44** (2015) 14877–14885.

[23]   Z.A. Taha, A.M. Ajlouni, T.S. Ababneh, W. Al-Momani, A.K. Hijazi, M. Al Masri and H. Hammad, "DFT computational studies, biological and antioxidant activities, and kinetics of thermal decomposition of 1,10-phenanthroline lanthanide complexes", *Struct. Chem.*, **28** (2017) 1907–1918.

[24]   X. Wang, G. Jia, Y. Yu, Y. Gao, W. Zhang, H. Wang, Z. Cao and J. Liu, "A new homogeneous electrocatalyst for electrochemical carbonylation of methanol to dimethyl carbonate", *Quim. Nova,* **38** (2015) 298–302.

[25]   A.M. Ajlouni, Q. Abu-Salem, Z.A. Taha, A.K. Hijazi and W. Al Momani, "Synthesis, characterization, biological activities and luminescent properties of lanthanide complexes with [2-thiophenecarboxylic acid, 2-(2-pyridinylmethylene)hydrazide] Schiff bases ligand", *J. Rare Earth.*, **34** (2016) 986–993.

[26]   S.C. Bishop, R. Winefield, A. Anbanandam and J.N. Lampe, "Aqueous synthesis of a small-molecule lanthanide chelator amenable to copper-free click chemistry", *PLoS ONE*, **14** (2019) 1–16.

[27]   A.A. Ansari, "Paramagnetic NMR shift, spectroscopic and molecular modeling studies of lanthanide(III)-morin complexes", *J. Coord. Chem.*, **61** (2008) 3869–3878.

[28]   M.P.C. Campello, E. Palma, I. Correia, P.M.R. Paulo, A. Matos, J. Rino, J. Coimbra, J.C. Pessoa, D. Gambino, A. Paulo and F. Marques, "Lanthanide complexes with phenanthroline-based ligands: insights into cell death mechanisms obtained by microscopy techniques", *Dalton Trans.*, **48** (2019) 4611–4624.

[29]   P. Pitchaimani, K. Mun Lo and K.P. Elango, "Synthesis, spectral characterization, crystal structures of lanthanide(III) pyrrolidine dithiocarbamate complexes and their catalytic activity", *J. Coord. Chem.*, **68** (2015) 2167–2180.

[30]   M.D. Regulacio, M.H. Pablico, J.A. Vasquez, P.N. Myers, S. Gentry, M. Prushan, S. Tam-Chang and S.L. Stoll, "Luminescence of Ln(III) dithiocarbamate complexes (Ln = La, Pr, Sm, Eu, Gd, Tb, Dy)", *Inorg. Chem.*, **47** (2008) 1512–1523.

[31]   R.K. Agarwal, S. Prasad, R. Garg and S.K. Sidhu, "Synthesis and preliminary structural characterization of some lanthanide(III) semicarbazone complexes", *Bull. Chem. Soc. Ethiop.*, **20** (2006) 167–172.

[32]   R.K. Agarwal and A. Kumar, "Synthesis, physico-chemical and biological properties of some mixed ligand complexes of trivalent lanthanides with 4[*N*-4′-dimethylamino-benzalidene)amino] antipyrine thiosemicarbazone and pyridine", *J. Appl. Chem. Res.*, **16** (2011) 40–58.

[33]   K. Raja, A. Suseelamma and K.H. Reddy, "Synthesis, spectral properties, DNA binding interactions and DNA cleavage studies of lanthanide(III) complexes of 2-acetylpyridine acetoylhydrazone: The X-ray crystal structure of 10-coordinate Ce(III) and Sm(III) complexes", *J. Iran Chem. Soc.*, **12** (2015) 1473–1486.

[34]   N. Guskos, J. Majszczyk, J. Typek, G. Zolnierkiewicz, E. Tomaszewicz and K. Aidinis, "Relative intensities of *f-f* transitions of Erbium(III) ion studied by photoacoustic spectroscopy", *Rev. Adv. Mater. Sci.*, **23** (2010) 97–101.

[35]   L.B Su, Q.G. Wang, H.J. Li, G. Brasse, P. Camy, J.L. Doualan, A. Braud, R. Moncorgé, Y.Y. Zhan, L.H. Zheng, X.B. Qian and J. Xu, "Spectroscopic properties and CW laser operation of Nd,Y-codoped CaF_2 single crystals", *Laser Phys. Lett.*, **10** (2013) 1–4.

[36]   R. Ilmi and K. Iftikhar, "Structure elucidation by sparkle/RM1, effect of lanthanide contraction and photophysical properties of lanthanide(III) trifluoroacetylacetonate complexes with 1,10-phenanthroline", *J. Photochem. Photobiol. A: Chem.*, **325** (2016) 68–82.

[37]   S. Mohan, K.S. Thind and G. Sharma, "Effect of Nd^{3+} concentration on the physical and absorption properties of sodium-lead-borate glasses", *Braz. J. Phys.*, **37** (2007) 1306–1313.

[38]   F. Ramos-Lara, A. Lira, M.O. Ramírez, M. Flores, R. Arroyo and U. Caldiño, "Optical spectroscopy of Nd^{3+} ions in poly(acrylic acid)", *J. Phys.: Condens. Matter*, **18** (2006) 7951–7959.

[39]   K.A. Thiakou, V. Nastopoulos, A. Terzis, C.P. Raptopoulou and S.P. Perlepes, "Di-2-pyridyl ketone in lanthanide(III) chemistry: Mononuclear and dinuclear erbium(III) complexes", *Polyhedron*, **25** (2006) 539–549.

[40]   W. Ma, L. Su, X. Xu, J. Wang, D. Jiang, L. Zheng, X. Fan, C. Li, J. Liu and J. Xu, "Effect of erbium concentration on spectroscopic properties and 2.79 μm laser performance of Er:CaF_2 crystals", *Opt. Mater. Express*, **6** (2016) 409–415.

[41]   P. Martin-Ramos, M. Ramos-Silva, F. Lahoz, I.R. Martin, P. Chamorro-Posada, M.E.S. Eusebio, V. Lavin and J. Martin-Gil, "Highly fluorinated erbium(III) complexes for emission in the C-band", *J. Photochem. Photobiol. A*: *Chem.*, **292** (2014) 16–25.

[42]   W.T. Carnall, G.L. Goodman, K. Rajnak and R.S. Rana, "A systematic analysis of the spectra of lanthanides doped into single crystal LaF$_3$", *J. Chem. Phys.*, **90** (1989) 3443–3457.

[43]   R.K. Agarwal, R.K. Garg and S.K. Sindhu, "Synthesis and magneto-spectral investigations of some six and nine coordinated complexes of lanthanide(III) derived from 4[*N*-(2′-hydroxy-1′-naphthalidene)amino]antipyrinethiosemicarbazone", *J. Iran Chem. Soc.*, **2** (2005) 203–211.

[44]   M. Llunell, D. Casanova, J. Cirera, P. Alemany and S. Alvarez, *SHAPE: Program for the Stereochemical Analysis of Molecular Fragments by Means of Continuous Shape Measures and Associated Tools, User's Manual Version 2.1*, 2013.

[45]   J. Cirera, E. Ruiz and S. Alvarez, "Continuous Shape Measures as a stereochemical tool in organometallic chemistry", *Organometallics,* **24** (2005) 1556–1562.

[46]   T. Zhu, P. Chen, H. Li, W. Sun, T. Gao and P. Yan, "Structural effects on the photophysical properties of mono-β-diketonate and bis-β-diketonate Eu^{III} complexes", *Phys. Chem. Chem. Phys.*, **17** (2015) 16136–16144.

[47]   A. Ruiz-Martínez and S. Alvarez, "Stereochemistry of compounds with coordination number ten", *Chem. Eur. J.*, **15** (2009) 7470–7480.

[48]   D. Casanova, J. Cirera, M. Llunell, P. Alemany, D. Avnir and S. Alvarez, "Minimal distortion pathways in polyhedral rearrangements", *J. Am. Chem. Soc.*, **126** (2004) 1755–1760.

[49]   K. Liu, H. Li, X. Zhang, W. Shi and P. Cheng, "Constraining and tuning the coordination geometry of a lanthanide ion in metal−organic frameworks: Approach toward a single-molecule magnet", *Inorg. Chem.*, **54** (2015) 10224–10231.

[50]   A. Kovács, C. Apostolidis, O. Walter and P. Lindqvist-Reis, "'Lanthanide contraction' in [Ln(BTP)$_3$](CF$_3$SO$_3$)$_3$ complexes", *Struct. Chem.*, **26** (2015) 1287–1295.

[51]   Y. Ma, Y.-S. Yang, Y.-H. Jiang, Y.-X. Li, M. Liu, Z.-F. Li, H.-L. Han, Y.-P. Yang, X.-L. Xin and Q.-H. Jin, "Lanthanide contraction and chelating effect on a new family of lanthanide complexes with tetrakis(*O*-isopropyl)methyle-nediphosphonate: synthesis, structures and terahertz time-domain spectroscopy", *RSC Adv.*, **7** (2017) 41651–41666.

[52]   S.A. Cotton, O.E. Noy, F. Liesener and P.R. Raithby, "Unequivocal characterisation of a [Ln(terpy)(NO$_3$)$_3$·(H$_2$O)] complex: The synthesis and structure of [M(terpy)(NO$_3$)$_3$·(H$_2$O)] (M = Eu, Tb); a comparison with the

structure of [Eu(bipy)$_2$(NO$_3$)$_3$] and with other europium nitrate complexes {terpy = 2,2′:6′,2″-terpyridyl; bipy = 2,2′-bipyridyl}", *Inorg. Chim. Acta*, **344** (2003) 39–40.

[53] T.T. da Cunha, V.M.M. Barbosa, W.X.C. Oliveira, C.B. Pinheiro, E.F. Pedroso, W.C. Nunes and C.L.M. Pereira, "Slow magnetic relaxation in mononuclear gadolinium(III) and dysprosium(III) oxamato complexes", *Polyhedron*, **169** (2019) 102–113.

[54] Nibha, B.P. Baranwal, G. Singh and C.G. Daniliuc, "Synthesis, characterization and thermolysis of lanthanide metal nitrate complexes with 1,10-phenanthroline, Part-95", *J. Rare Earth.*, **32** (2014) 545–552.

[55] V. Kubat, G. Demo, L. Jeremias and J. Novosad, "Synthesis and structure of tris(dimethyldithiocarbamato) (1,10-phenanthroline)lanthanide complexes", *Z. Kristallogr.*, **228** (2013) 369–373.

[56] J. Vančo, Z. Trávníček, O. Kozák and R. Boča, "Structural, magnetic and luminescent properties of lanthanide complexes with *N*-salicylideneglycine", *Int. J. Mol. Sci.*, **16** (2015) 9520–9539.

[57] L. Puntus, K. Zhuravlev, K. Lyssenko, M. Antipin and I. Pekareva, "Luminescence and structural properties of lanthanide complexes of Schiff bases derived from pyridoxal and amino acids", *Dalton Trans.*, **36** (2007) 4079–4088.

[58] A. Husain and C.L. Oliver, "A C-shaped *p*-sulfonatocalix[4]arene-based supermolecule exhibiting mutual-inclusion and bilayer insertion of dipicolinate", *CrystEngComm*, **16** (2014) 3749–3757.

[59] R. Carballo, B. Covelo, N. Fernández-Hermida, A.B. Lago and E.M. Vázquez López, "Non-covalent interactions in a nickel(II) complex with benzilate and 1,10-phenanthroline", *J. Chem. Crystallogr.*, **41** (2011) 1949–1954.

[60] M. Nishio, "The CH/π hydrogen bond in chemistry. Conformation, supramolecules, optical resolution and interactions involving carbohydrates", *Phys. Chem. Chem. Phys.*, **13** (2011) 13873–13900.

[61] A. Anbarasu, S. Anand and R. Sethumadhavan, "N-H···π interactions: Investigations on the evidence and consequences in RNA binding proteins", *The Open Structural Biology Journal*, **2** (2008) 33–42.

[62] P. Ruíz, R. Ortiz, L. Perelló, G. Alzuet, M. González-Álvarez, M. Liu-González and F. Sanz-Ruíz, "Synthesis, structure, and nuclease properties of several binary and ternary complexes of copper(II) with norfloxacin and 1,10 phenanthroline", *J. Inorg. Biochem.*, **101** (2007) 831–840.

[63] C. Theivarasu and R. Murugesan, "Natural Bond Orbital (NBO) population analysis of an energetic molecule 1-phenyl-2-nitroguanidine", *Int. J. Chem. Sci.*, **14** (2016) 2029–2050.

[64] A. Zülfikaroğlu, H. Batı and N. Dege, "A theoretical and experimental study on isonitrosoacetophenone nicotinoyl hydrazone: Crystal structure, spectroscopic properties, NBO, NPA and NLMO analyses and the investigation of interaction with some transition metals", *J. Mol. Struct.*, **1162** (2018) 125–139.

[65] Z.-Q. Liang, Z.-Y. Zou, P. Ding, C.-Q. Ye, S.-R. Chen, X.-J. Zhao, J.-H. Chen, X.-M. Wang and X.-T. Tao, "Tailoring the sensing behaviors to Zn^{2+} and AIEE properties of phenanthroline derivatives through isomer engineering", *Dyes and Pigments*, **150** (2018) 382–389.

[66] S. Karthikeyan, V. Ramanathan and B. Kumar Mishra, "Influence of the substituents on the CH···π interaction: Benzene−Methane complex", *J. Phys. Chem. A*, **117** (2013) 6687−6694.

[67] S. Roy, M.G.B. Drew, A. Bauzá, A. Frontera and S. Chattopadhyay, "Estimation of conventional C–H···π (arene), unconventional C–H···π (chelate) and C–H···π (thiocyanate) interactions in hetero-nuclear nickel(II)–cadmium(II) complexes with a compartmental Schiff base", *Dalton Trans.*, **46** (2017) 5384–5397.

[68] S. Gatfaoui, N. Issaoui, A. Mezni, F. Bardak, T. Roisnel, A. Atac and H. Marouani, "Synthesis, structural and spectroscopic features, and investigation of bioactive nature of a novel organic-inorganic hybrid material 1*H*-1,2,4-triazole-4-ium trioxonitrate", *J. Mol. Struct.*, **1150** (2017) 242–257.

[69] N. Günay, Ö. Tamer, D. Kuzalic, D. Avc and Y. Atalay, "Theoretical investigation of *N*-methyl-*N′*-(4-nitrobenzylidene) pyrazine-2-carbohydrazide: Conformational study, NBO analysis, molecular structure and NMR spectra", *Acta Phys. Pol. A*, **127** (2015) 701–710.

[70] A. Kanaani, D. Ajloo, H. Kiyani, H. Ghasemian, M. Vakili and M. Feizabadi, "Molecular structure, spectroscopic investigations and computational study on the potential molecular switch of (*E*)-1-(4-(2-hydroxybenzylideneamino)phenyl)ethanone", *Mol. Phys.*, **114** (2016) 2081–2097.

[71] M. Ali, A. Mansha, S. Asim, M. Zahid, M. Usman and N. Ali, "DFT study for the spectroscopic and structural analysis of *p*-dimethylaminoazobenzene", *Journal of Spectroscopy*, **2018** (2018) 1–15.

[72] S. San Tan, S. Yanagisawa, K. Inagaki, M.B. Kassim and Y. Morikawa, "Experimental and computational studies on ruthenium(II) bis-diimine complexes of *N*,*N′*-chelate ligands: the origin of changes in absorption spectra

upon oxidation and reduction", *Phys. Chem. Chem. Phys.,* **21** (2019) 7973–7988.

[73] J.Y. Chen, H. Jiang, S.J. Chen, C. Cullen, C.M. Sabbir Ahmed and Y.-H. Lin, "Characterization of electrophilicity and oxidative potential of atmospheric carbonyls", *Environ. Sci.: Processes Impacts*, **21** (2019) 856–866.

[74] A. Bendjeddou, T. Abbaz, A. Gouasmia and D. Villemin, "Quantum chemical studies on molecular structure and reactivity descriptors of some *p*-nitrophenyl tetrathiafulvalenes by Density Functional Theory (DFT)", *Acta Chim. Pharm. Indica*, **6** (2016) 32–44.

[75] N.S. Babu and D. Jayaprakash, "Global and reactivity descriptor studies of cyanuric acid tautomers in different solvents by using of Density Functional Theory (DFT)", *IJSR*, **4** (2015) 615–620.

[76] L. Jin, J. Wu, G. Yuan and T. Chen, "In vitro study of the inflammatory cells response to biodegradable Mg-based alloy extract", *PLoS ONE*, **13** (2018) 1–15.

[77] H. Bosshart and M. Heinzelmann, "THP-1 cells as a model for human monocytes", *Ann. Transl. Med.*, **4** (2016) 438.

[78] H.S. Lee, S.J. Stachelek, N. Tomczyk, M.J. Finley, R.J. Composto and D.M. Eckmann, "Correlating macrophage morphology and cytokine production resulting from biomaterial contact", *J. Biomed. Mater. Res. A*", **101** (2013) 203–212.

[79] R.N. Devi, S. Israel and C. Ancline, "An analysis of structural, electronic and reactivity properties of MetforminChloride using XRD and DFT approach", *Mechanics, Materials Science Engineering Journal, Magnolithe*, **9** (2017).

[80] P.K. Chattaraj and S. Giri, "Electrophilicity index within a conceptual DFT framework", *Annu. Rep. Prog. Chem., Sect. C*, **105** (2009) 13–39.

[81] K. Bellifa and S.M. Mekelleche, "QSAR study of the toxicity of nitrobenzenes to *Tetrahymena pyriformis* using quantum chemical descriptors", *Arab. J. Chem.*, **9** (2016) S1683–S1689.

[82] A. Morales-Bayuelo, "Molecular quantum similarity, chemical reactivity and database screening of 3D pharmacophores of the protein kinases A, B and G from *Mycobacterium tuberculosis*", *Molecules*, **22** (2017) 1027.

[83] A.S. Levenson and V.C. Jordan, "MCF-7: The first hormone-responsive breast cancer cell line", *Perspectives in Cancer Research,* **57** (1997) 3071–3078.

[84] S. Ali and R.C. Coombes, "Endocrine-responsive breast cancer and strategies for combating resistance", *Nat. Rev. Cancer,* **2** (2002) 101–112.

[85]   E. Castro-Rivera and S. Safe, "Estrogen- and antiestrogen-responsiveness of HEC1A endometrial adenocarcinoma cells in culture", *J. Steroid Biochem. Mol. Biol.,* **64** (1998) 287–295.

[86]   S.-H. Liu, J.-W. Zhu, H.-H. Xu, Y. Wang, Y.-M. Liu, J.-B. Liang, G.-Q. Zhang, D.-H. Cao, Y.-Y. Lin, Y. Wu and Q.-F. Guo, "Protein-binding, cytotoxicity *in vitro* and cell cycle arrest of ruthenium(II) polypyridyl complexes", *Spectrochim. Acta, Part A*, **161** (2016) 77–82.

[87]   M. Ganeshpandian, S. Ramakrishnan, M. Palaniandavar, E. Suresh, A. Riyasdeen and M.A. Akbarsha, "Mixed ligand copper(II) complexes of 2,9-dimethyl-1,10-phenanthroline: Tridentate 3N primary ligands determine DNA binding and cleavage and cytotoxicity", *J. Inorg. Biochem.*, **140** (2014) 202–212.

CHAPTER 6

Mixed-ligand complexes of lanthanides derived from an α-hydroxycarboxylic acid (benzilic acid) and 1,10-phenanthroline

6.1   Introduction

The chemistry of lanthanide(III) carboxylates receives ongoing attention in different fields due to their fascinating physico-chemical properties, structural diversity and potential uses of the compounds, and thus have been widely studied in recent years [1]. Although much research has focused on the potential applications of lanthanide-carboxylic acid complexes as single-ion magnets (SIMs) and fluorescent sensors, carboxylic acid-derived Ln(III) complexes are of particular interest because of their biological activities, including anticancer and antimicrobial properties [1-6].

α-Hydroxycarboxylic acids are an important group of biogenic metal ion binders that are essential for biochemical processes, such as in the Krebs cycle, Cori cycle and photorespiration [7]. The α-hydroxycarboxylates are also able to mimic more complex biologically active ligands, for example sugars – a property conferred by their alcoholic and carboxylate functionalities [7]. A representative of aromatic hydroxycarboxylic acids that attracted substantial research interest over the years is benzilic acid (**H₂ben**, Figure 6.1) [7-9]. Benzilic acid and some of its derivatives are used in the production of glycolate pharmaceuticals and hallucinogenic drugs [7]. *In vitro* antitumour activities against the human tumour cell lines, MCF-7, HeLa, human colon adenocarcinoma (Colo205), human hepatocellular carcinoma (HepG2) and non-small cell lung cancer (NCI-H460), have also been observed for tri(*n*-butyl)tin carboxylate complexes derived from benzilic acid and 2-chloronicotinic acid [10]. The central tin atom of the tri(*n*-butyl)tin carboxylate complex is linked to the monodentated hydroxycarboxylate moiety *via* the deprotonated carboxylate oxygen

atom (Figure 6.1) [10]. 1,10-Phenanthroline complexes, on the other hand, have been extensively studied as bioactive and luminescent compounds [6,7,11-14]. Coordination compounds prepared from the heterocyclic chelating ligand, 1,10-phenanthroline, have potential biochemical and biological applications, such as anticancer and antimicrobial activity [13-16].
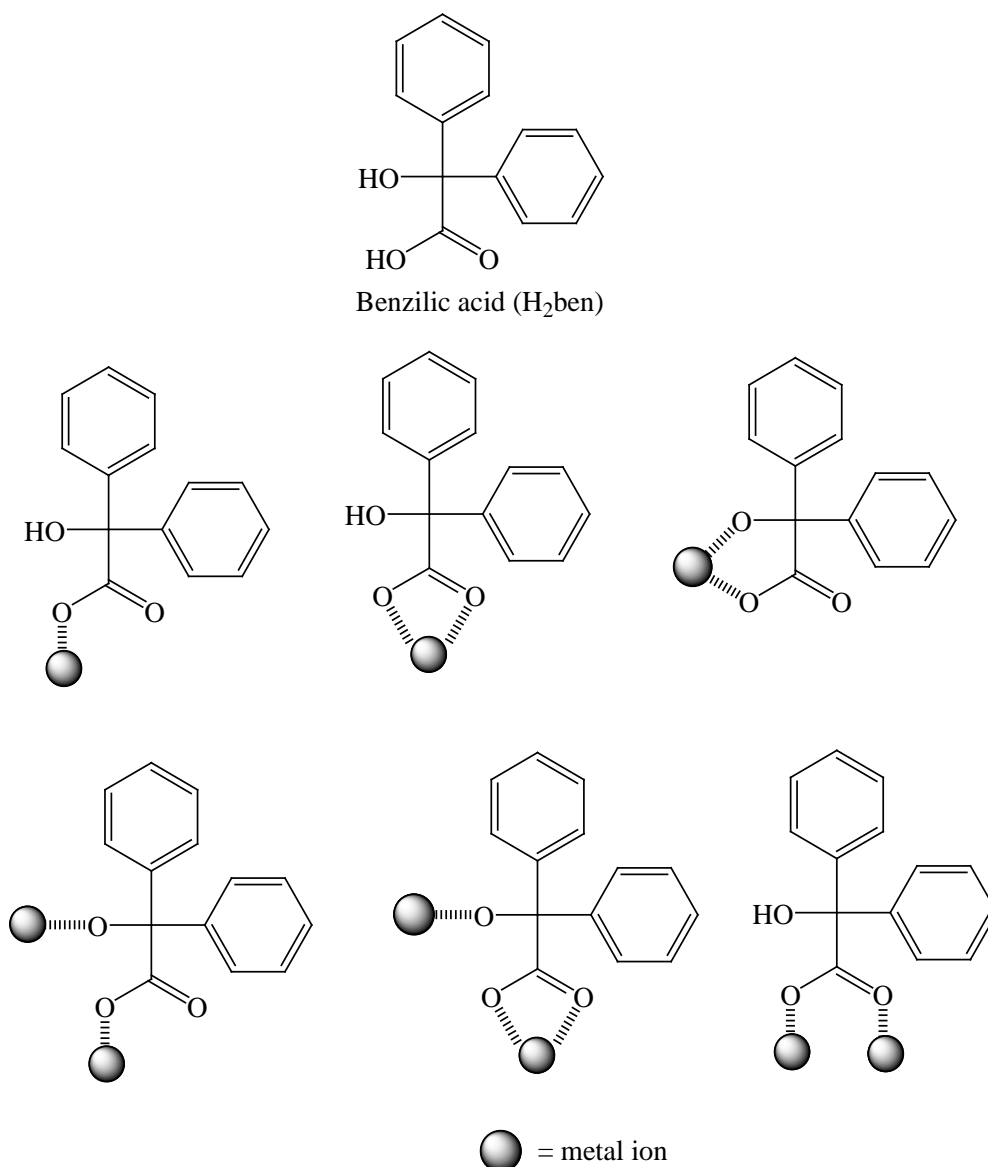
Figure 6.1: Benzilic acid structure and some of its binding modes with metal ions [7-9].

Apart from providing many biological, pharmaceutical and nutritional products, benzilic acid, as a ligand, is vital as a building block in the design and preparation of metal complexes or metal-organic frameworks (MOFs), due to its various coordination modes afforded by the *O*-atoms of the carboxylic and hydroxy groups [7,8,10]. The MOFs have interesting structural characteristics and find applications in host-guest chemistry, electrical conductivity and magnetism [8]. Some of the chelating and bridging modes of **H₂ben** with metal ions, such as Li(I), B(III), Al(III), Ga(III), In(III), Tl(I), Cd(II), Cu(II), Ni(II), Zn(II) and Pb(II), are illustrated in Figure 6.1 [7,8,17-22]. Coordinative flexibility of the α-hydroxycarboxylic acid is seen in reactions with Group 13 ions, with the B(III) centre being bidentately coordinated to doubly deprotonated benzilate ligands through the carboxylate and alcoholato oxygen atoms [7]. Coordination with Al(III), Ga(III) and In(III) occur bidentately through the carboxylate (the carboxylic acid moiety is the site of deprotonation) and the alcoholic oxygen atoms of the singly deprotonated benzilate ligands. In addition to binding through the alcoholato and one carboxylate oxygen atom, the benzilate moieties coordinate to the In(III) ions through both carboxylate oxygen atoms [7]. The investigation of the coordinative ability of benzilic acid provides potential means of elucidating and understanding structural and spectroscopic characteristics, as well as the biochemistry of the α-hydroxycarboxylic acid and its derivatives [7].

Two transition metal complexes of **H₂ben** and 1,10-phenanthroline, [Cu(Hben)₂(phen)]ₙ and [Cd(Hben)₂(phen)₂] (**Hben** = monodeprotonated benzilic acid), have been reported by Qiu *et al.* (2007) [8]. Both complexes form one-dimensional helical chains with benzilic acid – the latter having different coordination modes that results in different orientations of ligand strands. The copper helical complex comprises [phen]Cu²⁺ moieties bridged by benzilic acid. The distorted square pyramidal Cu(II) complex features benzilic acid coordinating *via* the carboxylate and hydroxylate oxygen atoms. The mononuclear cadmium complex has π-π stacking interactions that play a significant role in self-assembly. The octahedral geometry of Cd(II) is afforded by two carboxylate oxygen atoms of two monodentate benzilic acid ligands and four nitrogen atoms from two bidentately coordinated **phen** molecules [8].

Benzilic acid was considered a good candidate in this study due to its carboxylic and hydroxy group oxygen atoms which can act as coordinating and/or bridging sites for various metal ions, including the 4*f* elements [7,8,18]. In this study, benzilic acid was chosen as the primary ligand and 1,10-phenanthroline as the co-ligand to coordinate with Ln(III) ions. The ability of the ligand to bind to metal ions through the carboxylate and alcoholic moieties in monoanionic and/or dianionic form results in the synthesis of more stable assemblies than the simple carboxylic acid equivalents [7].

Since the chemical reactivity of hydroxycarboxylic acids with metals in solution, or in the solid state, rely on the reaction conditions and the influence of ancillary ligands, 1,10-phenanthroline was selected as the auxiliary ligand in this study. 1,10-Phenanthroline has a proven track record in ensuring aqueous stability and enhancing the biological activity of certain lanthanide carboxylate complexes [6,7]. Three trivalent lanthanide complexes, [Ln(Hben)$_3$(phen)$_2$(H$_2$O)]·DMF·H$_2$O (Ln = Pr, Nd, Sm; **Hben** = monodeprotonated **H$_2$ben**) were isolated and characterised by melting point, microanalyses, IR, ^{1}H NMR, UV-Vis spectroscopy and single-crystal X-ray diffraction studies. Anticancer activities of the title complexes were also investigated on breast cancer (MCF-7), the endometrial carcinoma (HEC-1A) and the human monocytic (THP-1) cell lines. This, in an effort to develop lanthanide-based chemotherapeutics which are more effective against intrinsic and acquired resistance, and possess less dose-limiting side effects compared to platinum-based drugs, such as cisplatin, oxaliplatin and carboplatin [23]. The findings of this research can enrich the studies of lanthanide coordination chemistry, as well as afford a research platform for further studies into the potential uses of these coordination compounds.

6.2   Synthesis of the mixed-ligand complexes

6.2.1   Synthesis of [Pr(Hben)$_3$(phen)$_2$(H$_2$O)]·DMF·H$_2$O   1

[Pr(NO$_3$)$_3$·6H$_2$O] (0.366 g, 0.842 mmol) and 0.303 g (1.681 mmol) 1,10-phenanthroline were dissolved in 5 mL methanol. The solution was refluxed for 1 hour, followed by addition of a mixture of benzilic acid (0.576 g, 2.524 mmol) and

1M NaOH (2.520 mL) in 4 mL distilled water. Reflux was continued for 5 hours, during which a green precipitate appeared. The precipitate was recrystallised from DMF. Green single crystals were produced after 20 days of slow vapour diffusion using diethyl ether. Yield = 0.347 g (31.9 % based on the Pr(III) salt), m.p. = 122.1 °C. Anal. *Calcd.* for $C_{66}H_{51}N_4O_{10}Pr$, C_3H_7NO, H_2O (%): C, 64.14; H, 4.68; N, 5.42. Found: C, 64.29; H, 4.39; N, 5.22. Conductivity (10^{-3} M, DMF): 14.12 ohm^{-1}cm^{2}mol^{-1}. IR (cm^{-1}): v(O-H) 3390(b), v(C=N) 1641(s), v(C=C) 1583(s), v(C-H) 752–695(s).

6.2.2   Synthesis of [Nd(Hben)₃(phen)₂(H₂O)]·DMF·H₂O   2

Preparation of the mixed-ligand complex of Nd(III) was carried out by mixing a hot aqueous solution (4 mL) of [Nd(OAc)₃·xH₂O] (0.491 g, 1.447 mmol) with a hot solution of 1,10-phenanthroline (0.574 g, 3.185 mmol). After refluxing for 2 hours, a mixture of benzilic acid (0.325 g, 1.424 mmol) and 1M NaOH (1.425 mL) in 5 mL DMF was added, and refluxed for a further 3 hours. A purple solution was filtered and left to crystallise at room temperature using the slow vapour diffusion method, with diethyl ether as solvent. Purple X-ray quality crystals of the title compound appeared after 18 days. Yield = 0.489 g (26.1 % based on the Nd(III) salt), m.p. = 123.4 °C. Anal. *Calcd.* for $C_{66}H_{51}N_4O_{10}Nd$, C_3H_7NO, H_2O (%): C, 63.97; H, 4.67; N, 5.41. Found: C, 63.64; H, 4.41; N, 5.27. Conductivity (10^{-3} M, DMF): 16.08 ohm^{-1}cm^{2}mol^{-1}. IR (cm^{-1}): v(O-H) 3390(b), v(C=N) 1641(s), v(C=C) 1583(s), v(C-H) 752–695(s).

6.2.3   Synthesis of [Sm(Hben)₃(phen)₂(H₂O)]·DMF·H₂O   3

Method 1

Complex **3** was prepared by adding a hot methanolic solution of 1,10-phenanthroline (0.189 g, 1.049 mmol) to [SmCl₃·6H₂O] (0.378 g, 1.036 mmol) dissolved in methanol (5 mL). Benzilic acid (0.472 g, 2.068 mmol) and 1M NaOH (2.068 mL) in 5 mL DMF/H₂O (1:1, v/v) was added, followed by reflux of the clear solution for a further 3 hours. The solution was filtered off, and crystallisation completed by allowing diethyl ether to slowly diffuse into the solution at room temperature. This yielded white

crystals suitable for X-ray diffraction studies after 25 days. Yield = 0.375 g (27.8 % based on the Sm(III) chloride salt), m.p. = 124.3 °C. Anal. *Calcd.* for $C_{66}H_{51}N_4O_{10}Sm$, C_3H_7NO, H_2O (%): C, 63.67; H, 4.65; N, 5.38. Found: C, 63.74; H, 4.51; N, 5.28. Conductivity (10^{-3} M, DMF): 14.07 $ohm^{-1}cm^2mol^{-1}$. IR (cm^{-1}): v(O-H) 3390(b), v(C=N) 1645(s), v(C=C) 1583(s), v(C-H) 734–690(s).

Method 2

A DMF solution (4 mL) of $[Sm(NO_3)_3 \cdot 6H_2O]$ (0.333 g, 0.749 mmol) and **phen** (0.136 g, 0.755 mmol) was refluxed for 3 h. Whilst being stirred under reflux, benzilic acid (0.343 g, 1.503 mmol) and 1M NaOH (1.503 mL) were added to the resulting mixture and refluxing continued for a further 2 h. Vapour diffusion of diethyl ether into the mother liquor afforded white single crystals of the Sm(III) complex after 2 weeks. Yield = 0.238 g (24.4 % based on the Sm(III) nitrate salt).

6.3   Results and Discussion

The reaction of a lanthanide(III)-phen solution with benzilic acid in the ratios 1:2:3, 1:2:1 and 1:1:2 in methanol, water and DMF solvent systems in the presence of NaOH, led to the isolation of complexes $[Ln(Hben)_3(phen)_2(H_2O)] \cdot DMF \cdot H_2O$ (Ln = Pr (**1**), Nd (**2**) and Sm (**3**), respectively) (Scheme 6.1). X-ray quality crystals of the complexes were grown by vapour diffusion of diethyl ether into DMF solutions of the impure solids [24,25]. The use of basic media promoted the detachment of the carboxylic proton of benzilic acid to give a hydroxycarboxylate, which then coordinated to the metal ions in mono- and bidentate fashions. This deprotonation affects the charge distribution on a vital moiety of the ligand, which leads to enhanced reactivity towards the metal ions [26].
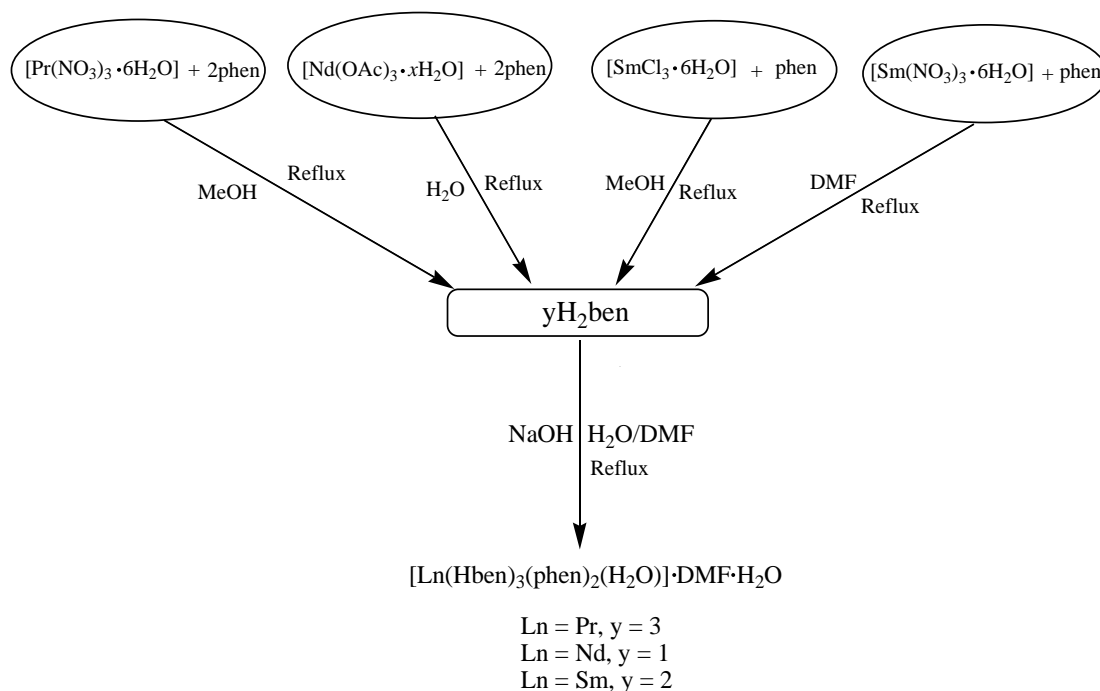
Scheme 6.1: Schematic representation of the reactions of the different Ln(III) salts with a mixed-ligand system using **H₂ben** and **phen**.

6.3.1   FT-IR spectroscopy

An overlay of the IR spectra of **H₂ben**, **phen** and coordination compounds **1**–**3** are displayed in Figures 6.2a and 6.2b. The high degree in similarity in the IR spectra of **1** and **2** is an indication of isostructurality, and a combination of peaks from two different ligands in some regions is indicative of the formation of mixed-ligand complexes [25].

In the IR spectrum of **H₂ben**, the bands peaking at 2862 and 2611 cm^{-1} are attributed to the hydroxyl stretches of the carboxylic acid moiety, while the hydroxyl and carboxylic O-H bending modes are observed as intense bands at 1345 and 1246 cm^{-1}, respectively [27]. The C=O bond gives rise to a very sharp band at 1716 cm^{-1}, whereas the C-O stretching of the hydroxyl (C-O-H) and carboxyl (–COOH) groups are identified by the peaks at 1171 and 1053 cm^{-1}, respectively [6,27,28]. Compared to the spectra of the free ligand, the strong vibrational band assigned as the v(C=O)

and carboxylic O-H bending in **H₂ben** disappeared in the complexes, hence confirming participation of the carboxylic group in coordination [29]. The peaks at 1588, 1477 and 1458 cm^{-1} in the spectrum of the free **H₂ben** are assigned to the aromatic v(C=C), while the out-of-plane C-H bending vibrations of the mono-substituted aromatic rings give an intense peak at 697 cm^{-1} [6,27]. For **phen**, the skeletal vibrational peak is found at 1426 cm^{-1}, while the v(C=N), v(C=C) and out-of-plane v(C-H) appear at 1652, 1505 and 738 cm^{-1}, respectively [6,29-31]. In the IR spectra of the metal complexes, the C=N stretches are red-shifted to about 1641 cm^{-1} (complexes **1** and **2**) and 1645 cm^{-1} (complex **3**) in comparison to that of the free **phen**. This is due to increased steric hindrance and weakening of the C=N bonds upon complexation [30,31]. The C=C vibrational peaks, on the other hand, experience blue shifts on coordination (v(C=C) = 1583 cm^{-1} for **1**–**3**). The out-of-plane vibrational bending peaks of the C-H bonds in the coordination compounds are identified in the ranges 752–695 cm^{-1} for **1** and **2**, and 734–690 cm^{-1} for **3** [6]. The presence of water molecules in the crystal structures of the complexes is confirmed by the appearance of broad peaks at 3390 cm^{-1} [30].
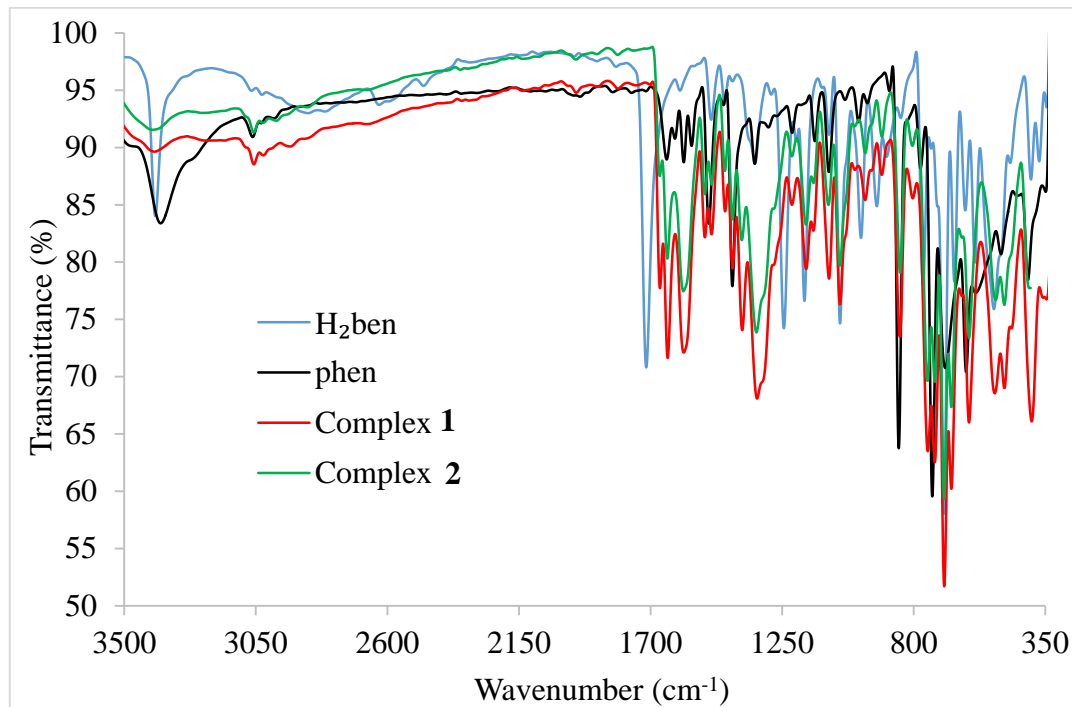
Figure 6.2a: An overlay infrared spectra of the ligands and metal complexes **1** and **2**.
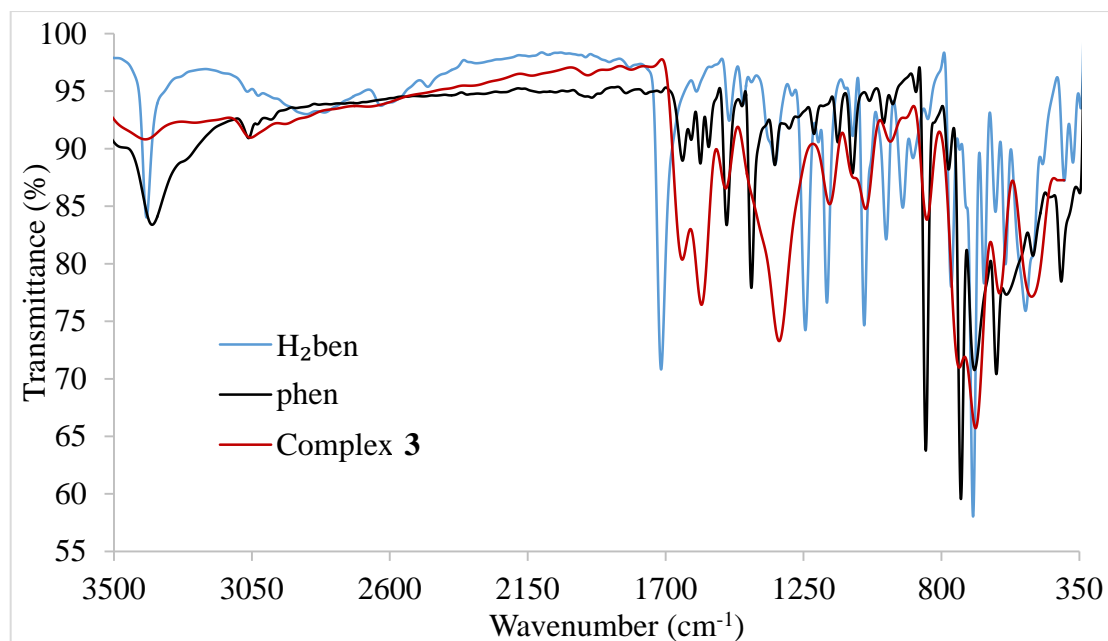
Figure 6.2b: An overlay of the IR spectra of **H₂ben**, **phen** and **3**.

6.3.2 NMR analysis

The ^{1}H NMR spectra of the free ligands (**H₂ben** and **phen**) and the three title complexes in DMSO-d_6 are shown in Figure 6.3. In the ^{1}H NMR spectrum of the free benzilic acid, the aromatic protons give a multiplet signal at 7.26–7.39 ppm, while the hydroxyl *H*-atom resonates at 6.34 ppm. The spectrum of each complex consists of two upfield methyl signals at 2.90 and 2.74 ppm, which correspond to the crystallographic solvent (DMF) peaks: the two separate signals being a result of restricted rotation about the (O)C-N bond [32,33]. The ^{1}H NMR spectrum of the free **phen** depicts four signals: a doublet (2H, aromatic) positioned at 7.77 ppm, a singlet (2H) at 7.99 ppm, a doublet corresponding to two protons (8.48 ppm) and an -N=CH- proton signal appearing at δ 9.11 ppm [30]. Chelation of **phen** to the Ln(III) ions causes signal broadening, especially in **1** and **2** as expected for the paramagnetic Ln(III) ions [34]. Furthermore, the -N=CH- proton peaks in **1** and **2** are shifted downfield to 9.87 and 9.14 ppm, respectively. The deshielding effect on these protons is ascribed to the formation of the Ln-N bonds, which leads to a decrease in electron density around the -N=CH- protons – this causes the protons to resonate at lower fields [35,36]. Paramagnetic shifts and broadening (an indication of metal

coordination) is a result of electronic coupling occurring between the unpaired resonant nuclei and the unpaired electrons of the lanthanide ions [37,38].
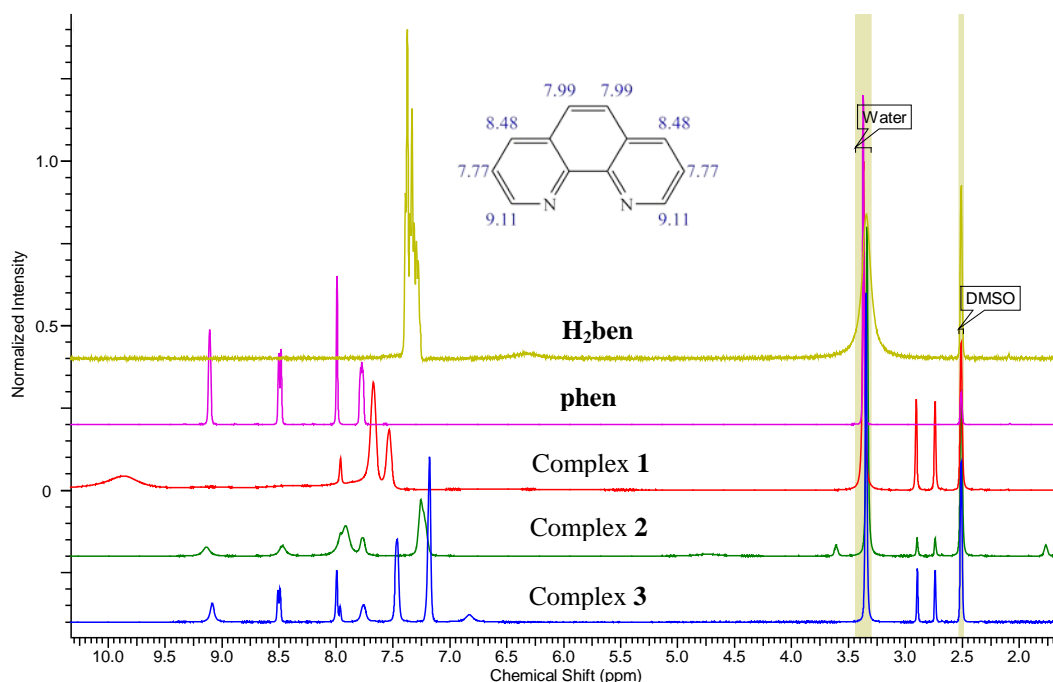
Figure 6.3: The ^{1}H NMR spectra of the ligands and complexes in DMSO-d_6.

6.3.3 UV-Vis spectroscopy

The absorption spectra of **phen** and complexes **1**-**3** are shown in Figure 6.4. No peaks were identified for **H₂ben**. The formation of complex **1** was, however, confirmed by the appearance of a short wavelength band peaking at 265 nm, which is ascribed to π-π* transitions of the bidentate aromatic **phen** (323 nm) [39,40]. The blue-shift of the π-π* transition band in **1** is due to the changes in energy levels of the ligand orbitals upon coordination, as a result of inter-electronic repulsions between the 4f electrons [41].

In addition to transitions from the coordinated ligands, the complexes exhibit a number of weak and narrow peaks that are characteristic of the Laporte-forbidden f-f transitions of the Ln(III) ions. For the Pr(III) complex, the observed absorption maxima correspond to f-f transitions from the $^3H_4$ ground state to the $^3P_2$ excited states (446 nm), $^3P_1$ (471 nm), $^3P_0$ (484 nm) and $^1D_2$ (591 nm) [39,40]. The absorption

spectrum of **2** shows absorption maxima at 527, 582, 747, 802 and 874 nm, which are assigned to transitions from the $^4I_{9/2}$ ground state to the $^4G_{7/2}$, $^4G_{5/2} + {}^2G_{7/2}$, $^4F_{7/2} + {}^4S_{3/2}$, $^4F_{5/2} + {}^2H_{9/2}$ and $^4F_{3/2}$ excited states, respectively [42-45]. On the other hand, the absorbance peaks of complex **3** at 360, 376, 392, 403, 417, 465 and 480 nm are due to transitions from the $^6H_{5/2}$ ground level to the $^4D_{3/2}$, $^6P_{7/2}$, $^4L_{15/2}$, $^6P_{3/2}$, $^4P_{5/2} + {}^6P_{5/2}$, $^4I_{13/2}$ and $^4I_{9/2} + {}^4M_{15/2}$ excited J-levels, respectively [40,46].
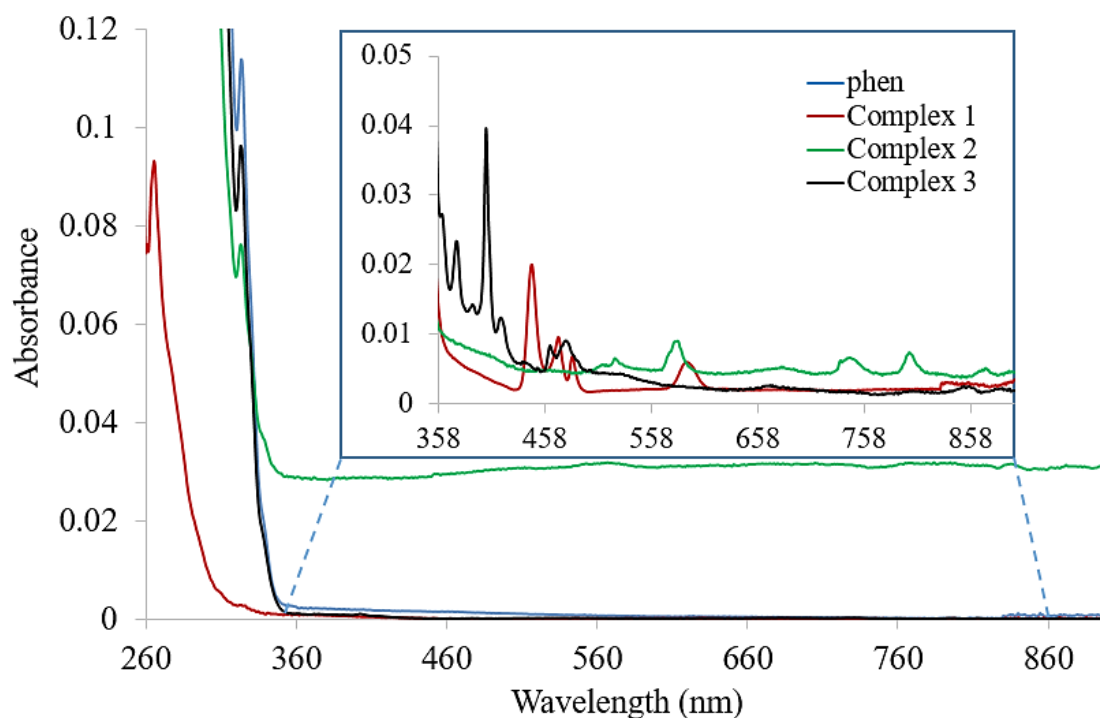
Figure 6.4: The UV-Vis-NIR spectra of DMF solutions of **phen** and **1**–**3**. The *f-f* transitions of the Ln(III) ions are indicated in the inset.

6.3.4   Coordination polyhedra determination

The coordination geometries of the nine-coordinate Ln(III) ions were calculated using *SHAPE 2.1* software, based on crystal data (Table 6.1) [47]. The Pr(III), Nd(III) and Sm(III) complexes are slightly distorted towards the spherical tricapped trigonal prism (TCTPR-9) geometry with average bond lengths, polyhedral volumes and geometry deviation parameters in the order: Pr(III) > Nd(III) > Sm(III) (Figure 6.5). It is seen that the CShM values calculated by the *SHAPE 2.1* program are less than 3, thus reflecting a small distortion from the perfect polyhedra [48,49]. Although the

geometry of the complexes was identified as TCTPR-9, the coordination environments of the compounds also display moderate deviation from the spherical capped square antiprism (CSAPR-9) and muffin (MFF-9) geometries. The differences in CShMs are attributed to the variation in bond distances and angular distortions that are determined by the Ln(III) ion size [49]. The trend reveals the highest distortion for the larger Pr(III) ion, and probably gives more angular distortions compared to Nd(III) and Sm(III) that are smaller in size, and hence possess shorter bond distances than the Pr(III) complex [48].

Table 6.1: Shape analysis of the mixed-ligand complexes **1**–**3**.

Complex	Coordination number	Shape	Symmetry	CShM	Polyhedral volume (Å^3)	Average bond length (Å)
1	9	TCTPR-9	D_{3h}	1.05300	33.4771	2.5618
2	9	TCTPR-9	D_{3h}	0.98828	32.8337	2.5440
3	9	TCTPR-9	D_{3h}	0.90604	32.0415	2.5219

Other close geometries with low CShM values

Complex **1**:   CSAPR-9 (C_{4v}); CShM = 1.20999
                      MFF-9 (C$_s$); CShM = 1.28719

Complex **2**:   CSAPR-9 (C_{4v}); CShM = 1.14318
                      MFF-9 (C$_s$); CShM = 1.24920

Complex **3**:   CSAPR-9 (C_{4v}); CShM = 1.07030
                      MFF-9 (C$_s$); CShM = 1.18161
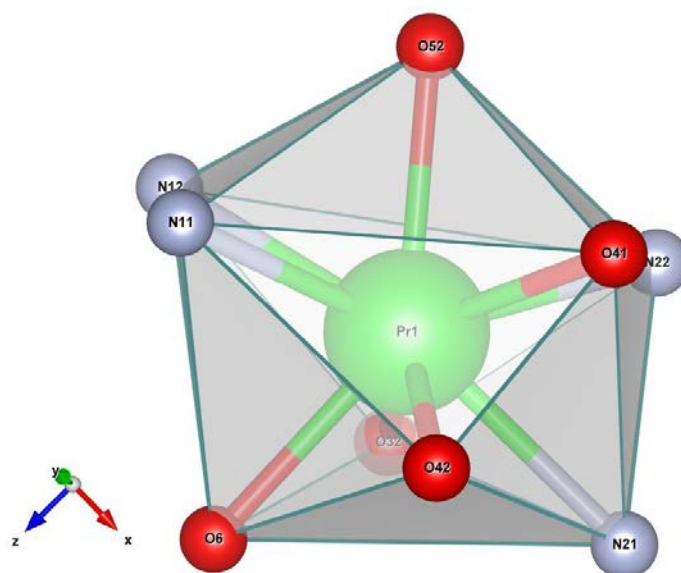
Figure 6.5: The polyhedral representation of **1** (*VESTA*).

6.3.5   X-ray crystallography

The crystal structures of **1**–**3** consist of neutral [Ln(Hben)$_3$(phen)$_2$(H$_2$O)]·DMF·H$_2$O (Ln = Pr, Nd and Sm) units in a nine coordinate environment (4N, 5O), and a DMF and a water lattice molecule in the outer coordination sphere (Figures 6.6a-c). The isostructural complexes crystallise in a monoclinic space group *P*2$_1$/n. The coordination environment around the Ln(III) ions is filled by four *N*-atoms from two bidentate **phen** molecules and five *O*-atoms provided by one bidentate monodeprotonated benzilic acid ligand, two monodentate mono-anionic benzilic acid molecules and one water molecule.
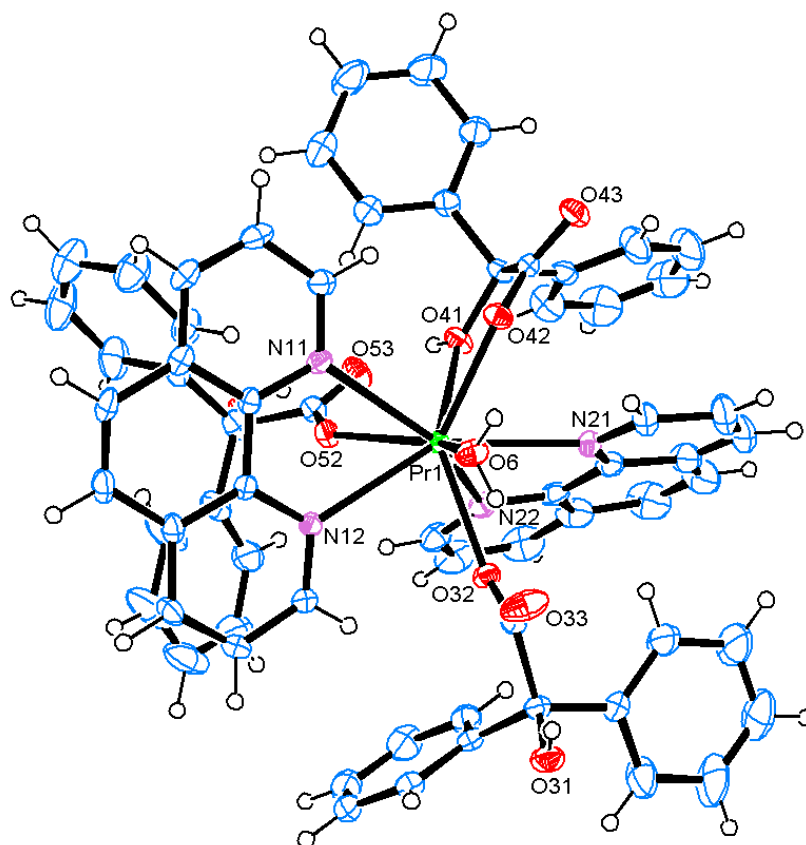
Figure 6.6a: The *ORTEP* plot of **1** with atoms represented by their 50 % probability thermal ellipsoids. Lattice DMF and H$_2$O molecules have been omitted for the sake of clarity.
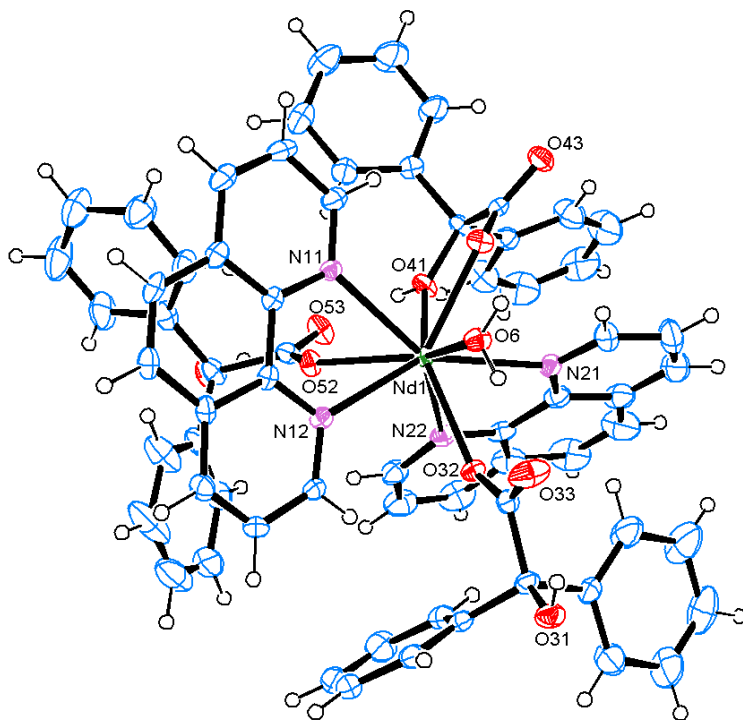
Figure 6.6b: The *ORTEP* diagram for **2** with partial atom-numbering scheme (50 % probability level). Crystallographic H_2O and DMF molecules are omitted for clarity.
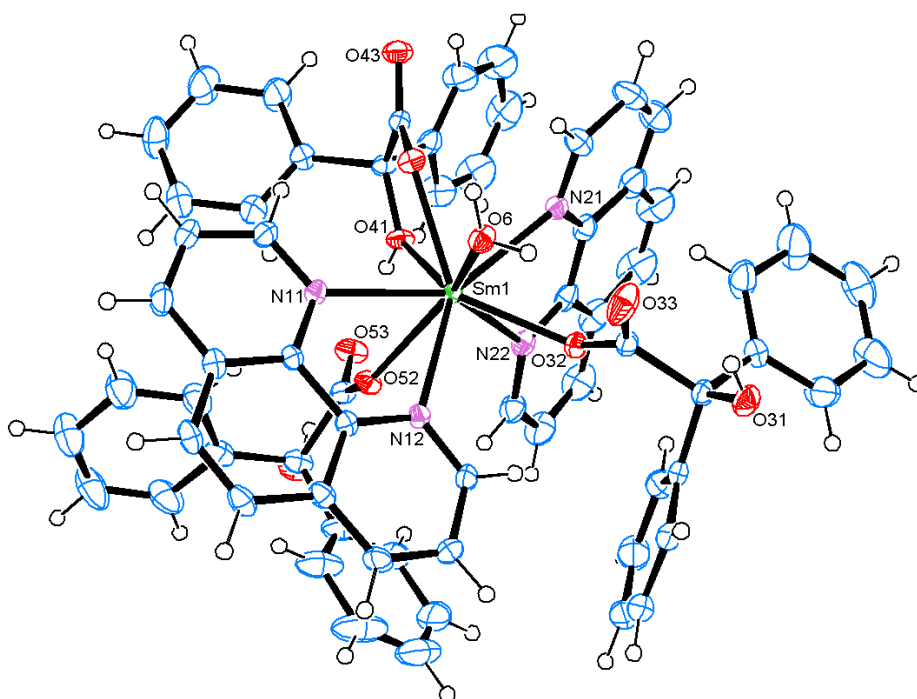
Figure 6.6c: The X-ray crystal structure of **3** with partial atom-labelling, drawn with 50 % displacement ellipsoids (crystallographic H_2O and DMF molecules are omitted for clarity).
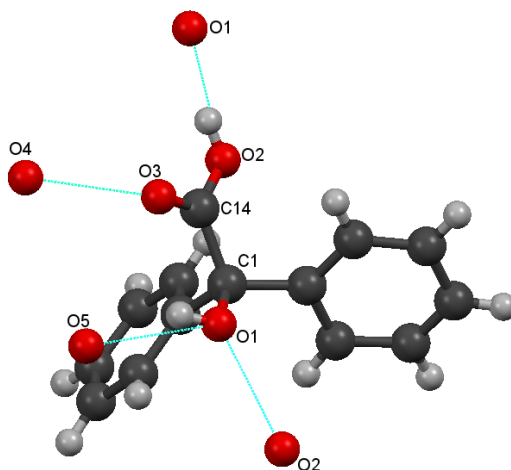
Figure 6.6d: The molecular structure of **H₂ben** illustrating partial atom-numbering scheme and hydrogen bonding [8].

A decrease in carboxylic C-O bond length upon coordination when the neutral ligand becomes negatively charged, is observed (Table 6.2a) [8]. As the carboxylic acid group becomes deprotonated, the C-O⁻ attains a partial double bond feature due to resonance, causing shorter bonds (varying from 1.252(5) to 1.276(4) Å in **1**–**3**) [50]. In contrast, the C=O (1.213(2) Å) and C-O$_{alcoholic}$ (1.411(5) Å) bonds in benzilic acid become slightly elongated after coordination (C=O = 1.230(3)–1.257(3) Å; C-O$_{alcoholic}$ = 1.420(4)–1.428(3) Å). The lengthening of the C=O results from the electron withdrawing inductive effect of complexation [36].

Bond parameters of complexes **1**–**3** illustrated in Table 6.2a show that Ln-N bond lengths lie in the range 2.6157(19) to 2.7051(19) Å, while the shorter Ln-O bonds are found between 2.4196(16) and 2.4958(17) Å. As expected, bond distances decrease with the decrease in ionic radii across the series due to the lanthanide contraction [51,52]. These values are very similar to those reported by Wang and co-workers (2016) for isostructural Ln(III) (Ln = Pr, Sm, Eu, Ho and Er) complexes with the mixed ligands, 2-chloroquinoline-4-carboxylic acid (2-ClQL) and **phen** {[Ln₂(2-ClQL)₆(phen)₂(H₂O)₂]·2H₂O} [53]. The Ln-O bond distances also compare well with those lanthanide(III) complexes of hydroxyquinoline carboxylate ligands [54]. Furthermore, the observed Ln-N bond distances with **phen** agree with those reported for tris(dimethyldithiocarbamato) (1,10-phenanthroline)lanthanide complexes in

which the average Pr-N and Nd-N bond lengths were found to be 2.66(4) Å and 2.63(3) Å, respectively [55].

Table 6.2a: Selected bond lengths (Å) and angles (°) in **H₂ben**, **1**, **2** and **3**.

H₂ben			**1** (Pr)	**2** (Nd)	**3** (Sm)
Bond lengths (Å)		**Bond lengths (Å)**			
C1-O1	1.411(5)	Ln1-O6	2.4714(14)	2.452(3)	2.4228(17)
C14-O2	1.301(1)	Ln1-O32	2.4409(16)	2.430(2)	2.4203(15)
C14-O3	1.213(2)	Ln1-O41	2.4787(17)	2.462(3)	2.4367(17)
C1-C14	1.537(5)	Ln1-O42	2.4553(16)	2.437(2)	2.4196(16)
		Ln1-O52	2.4958(17)	2.483(2)	2.4693(17)
		Ln1-N11	2.7051(19)	2.686(3)	2.6598(18)
		Ln1-N12	2.6793(19)	2.659(3)	2.6323(17)
		Ln1-N21	2.663(2)	2.644(3)	2.6157(19)
		Ln1-N22	2.666(2)	2.644(3)	2.621(2)
		C-O$_{hydroxy}$	1.427(3)	1.422(5)	1.426(3)
		C=O	1.243(3)	1.248(4)	1.244(3)
		C-O$_{carboxyl}$	1.260(3)	1.261(5)	1.260(3)
		(HO)C-C(O₂H)	1.557(3)	1.552(5)	1.557(3)
		Bond angles (°)			
		O41-Ln1-O42	60.66(5)	61.01(9)	61.49(5)
		N11-Ln1-N12	61.57(6)	62.00(8)	62.75(6)
		N21-Ln1-N22	61.99(6)	62.52(9)	63.23(6)
		Torsion angles (°)			
		N11−C111−C121−N12	0.5(3)	0.9(5)	0.5(3)
		N21−C211−C221−N22	-2.2(3)	-2.1(6)	-2.2(3)

In **1**–**3**, coordination of both the bidentate **phen** and benzilate ligands result in five membered rings, with average N-Ln-N and O-Ln-O bite angles equal to 62.34 and 61.05°, respectively. It is noticed that the ligand bite angles increase as the atomic number increases, owing to a decrease in bond distances. The O-Ln-O bite angles are typical of 5-membered chelate rings, and the **phen** bite angles are normal and fall in the same range as those obtained for Ce(III), Pr(III) and Nd(III) nitrate complexes with 1,10-phenanthroline [varying from 61.0(1) to 62.3(2)°] [12]. The 5-membered chelate rings of the *N*-atoms of **phen** and the Ln(III) ions show nearly perfect coplanarity, with N11−C111−C121−N12 and N21−C211−C221−N22 torsion angles equal to 0.5(3)° and -2.2(3)°, respectively, for complex **1** (the same trends for the torsion angles are observed in **2** and **3**). This small deviation from planarity is normal

and comparable to the torsion angles obtained for the Mn(II) complexes with **phen**: N1−C1−C9−N2 and N3−C13−C21−N4 torsion angles are -0.7(2)^o and 1.3(2)^o, respectively for [Mn(phen)$_2$(ba)(H$_2$O)](ClO$_4$) (ba = benzoic acid), and the N1−C12−C11−N2 and N3−C24−C23−N4 and N5−C35−C36−N6 torsion angles are 3.5(4)^o, 0.1(4)^o and −2.3(4)^o, respectively for [Mn(phen)$_3$](ClO$_4$)$_2$(H$_2$CO$_3$) [55,56]. The slight twisting of the rings may be a result of steric factors [57].

The crystal packing of the coordination compounds is ensured by intra- and intermolecular O-H⋯O interactions involving **Hben**$^-$ and crystallographic water molecules, which have H⋯A distances in the range 1.800(15) to 2.59(3) Å (Table 6.2b). Intramolecular O-H⋯O links are apparent between the hydroxyl group of the monodentate **Hben**$^-$ as donor and the free O-atom of the carboxylate group. The –OH (donor) of the coordinated water molecule plays an important role in the stabilisation of the crystal structure, by forming links with the free and bonded O-atoms of the η^1 **Hben**$^-$, as well as with the O-atom of the lattice water molecule. The other kind of O-H⋯O hydrogen bonds is formed by –OH of the crystallographic water molecule as a donor with the free and coordinated O-atoms of the η^2 **Hben**$^-$. Also involved in the hydrogen bonding network is the hydroxyl group of the η^2 **Hben**$^-$, which interacts with the free and coordinated O-atoms of the η^1 **Hben**$^-$. Additional stabilisation of the complexes arise from weak C-H⋯O contacts in which the crystallographic DMF molecule participates. These interactions include C-H$_{DMF}$⋯O$_{Hben-}$ and C-H$_{phen}$⋯O$_{Hben-}$ links.

Additional structural stability of the coordination compounds is provided by offset-stacked (parallel-displaced) aromatic π⋯π interactions formed by the six- and ten-membered rings of **phen** (Figure 6.6e) [58-60]. The minimum and most significant ring centroid distances (Cg-Cg) are equal to 3.5017(12), 3.503(2) and 3.5122(12) Å, with slippage values (distance between Cg(5) and the perpendicular projection of Cg(13) on ring 5) of 1.055, 1.066 and 1.103 Å obtained for **1**, **2** and **3**, respectively [**Cg(5):** C(11), C(12), C(122), C(121), C(111), C(112); **Cg(13):** N(11), C(111), C(121), C(122), C(12), C(11), C(112), C(113), C(114), C(115); symmetry code: 1-x,1-y,1-z]. Another considerable π⋯π stacking in **1**–**3** is found between the two six-

membered rings [**Cg(1):** N11, C111-115 and **Cg(5)**] of the two adjacent **phen** ligands, with Cg(1)-Cg(5) lengths of 3.6059(14), 3.612(2) and 3.6235(13) Å, and the corresponding slippages being 1.346, 1.375 and 1.406 Å [symmetry code: 1-*x*,1-*y*,1-*z*].

Table 6.2b: Hydrogen bond distances (Å) and angles (°) in **1**–**3**.

D-H···*A*	*D*-H	H···*A*	*D*···*A*	*D*-H···*A*
Complex 1				
O6-H6A···O32	0.839(17)	2.51(2)	2.894(2)	109(2)
O6-H6A···O33	0.839(17)	1.804(14)	2.625(3)	165(3)
O6-H6B···O7	0.83(2)	1.92(2)	2.709(3)	159(2)
O7-H7A···O43#1	0.83(2)	1.97(2)	2.776(3)	165(2)
O7-H7B···O42	0.838(16)	2.129(16)	2.863(3)	146(3)
O31-H31···O33	0.8400	2.070	2.579(3)	119
O41-H41···O52	0.76(3)	2.55(3)	2.833(2)	105(3)
O41-H41···O53	0.76(3)	1.87(3)	2.599(2)	163(3)
O51-H51···O53	0.84	2.02	2.551(2)	121
Complex 2				
O6-H6A···O32	0.84(2)	2.59(3)	2.885(3)	103(3)
O6-H6A···O33	0.84(2)	1.82(2)	2.623(4)	160(3)
O6-H6B···O7	0.84(3)	1.91(3)	2.711(4)	160(3)
O7-H7A···O43#1	0.83(3)	1.96(3)	2.775(4)	167(2)
O7-H7B···O42	0.83(3)	2.15(2)	2.853(4)	142(4)
O31-H31···O33	0.8400	2.0500	2.573(4)	119.00
O41-H41···O52	0.73(4)	2.55(4)	2.827(3)	105(4)
O41-H41···O53	0.73(4)	1.89(4)	2.597(4)	163(5)
O51-H51···O53	0.8400	2.0200	2.552(3)	121
Complex 3				
O6-H6A···O32	0.833(18)	2.52(2)	2.872(2)	107(2)
O6-H6A···O33	0.833(18)	1.800(15)	2.613(2)	165(3)
O6-H6B···O7	0.83(2)	1.91(2)	2.722(3)	164(2)
O7-H7A···O43#1	0.84(2)	1.97(2)	2.782(3)	166(2)
O7-H7B···O42	0.836(17)	2.133(17)	2.850(2)	144(3)
O31-H31···O33	0.8400	2.070	2.576(3)	118.00
O41-H41···O52	0.76(3)	2.54(3)	2.807(2)	103(3)
O41-H41···O53	0.76(3)	1.86(3)	2.588(2)	162(3)
O51-H51···O53	0.8400	2.0100	2.549(2)	121.00

D = donor, *A* = acceptor; symmetry code: (#1) 2-*x*,1-*y*,1-*z*.

C-H···π interactions ranging from 2.730–2.920 Å exist between the C-H groups of the aromatic moieties and the π-electrons of the aromatic **Hben⁻** and **phen** rings [symmetry code for C-H···π linking two monomeric units: *x*,1+*y*,*z*; symmetry code for interactions within the monomeric unit: *x*,*y*,*z*] (Figure 6.6f) [61-63]. These C-H···π interactions are considered short, since they are less than 3.050 Å [62]. Both the

aromatic π···π interactions and C-H···π interactions play an important role in crystal packing and influences rational drug design [8,61,62,64].

(e)

centroid: C111 C121 C122 C12 C11 C112

3.502

centroid: 10 atoms

(f)

centroid: N11 C111 C115 C114 C113 C112

centroid: C312 C313 C314 C315 C316 C311

2.913

2.899

2.736

2.907

centroid: C213 C212 C211 N21 C214 C215
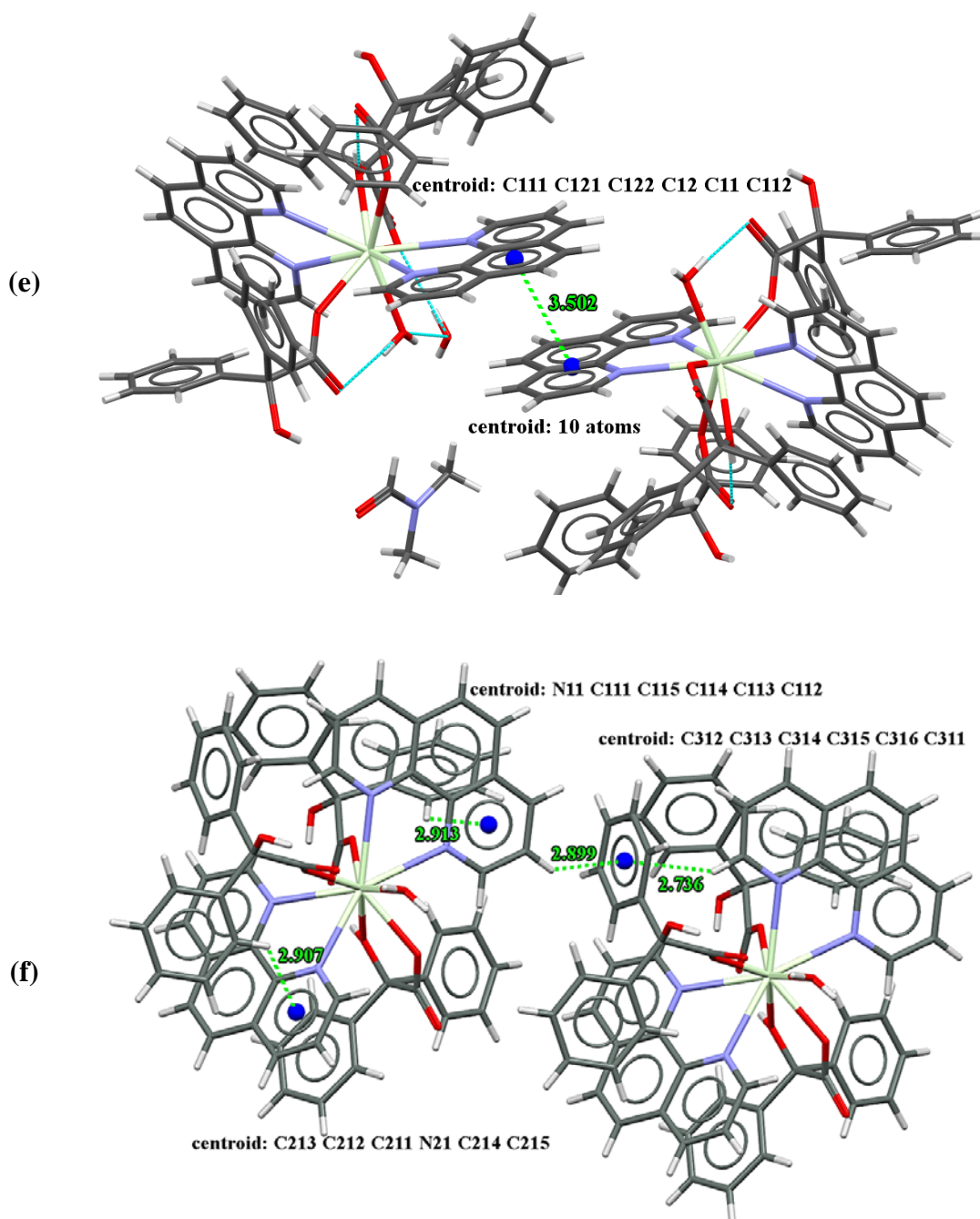
Figures 6.6e and 6.6f: Perspective view of: **(e)** hydrogen bonding and π···π interactions in **1**; **(f)** CH···π interactions in the Pr(III) complex. Hydrogen bonds are indicated by cyan dashed lines, while dashed green lines depict π···π and CH···π interactions (values are given in Å). The centroids of the aromatic rings are shown as blue spheres.

6.3.6   Atomic charge analysis of the ligands

Natural charge distribution analysis was performed to obtain the charges on individual atoms to predict the reactivity of the benzilate and the **phen** ligands (Figures 6.7a and 6.7b, and Table 6.3). The natural population analysis of **phen** was performed in Chapter 5. The natural atomic charge values were acquired from the Natural Bond Orbital (NBO) analysis [65]. The three oxygen atoms of **Hben⁻** exhibit the maximum electronegative charge values that lie in the range -0.74541 to -0.79912 in natural population analysis. It is observed that these oxygen atoms show a similar charge distribution. The negative charges on the oxygen atoms suggest the presence of hydrogen bonding interactions involving the hydroxyl and carboxylate group *O*-atoms of **Hben⁻**, which is consistent with the single-crystal XRD data [66]. The maximum positive atomic charge is accumulated on C6, which is the carbon atom of the –COOH functional group. A net positive charge is also obtained for the carbon atom bonded to the hydroxyl group, as well as all the hydrogen atoms. The withdrawal of electrons by the *O*-atoms results in decreased electron populations at C5 and C6, which leads to positive charge [65]. The negative charges on the aromatic carbon atoms and the net positive charges on the hydrogen atoms support the formation of C-H⋯π interactions in the complexes.
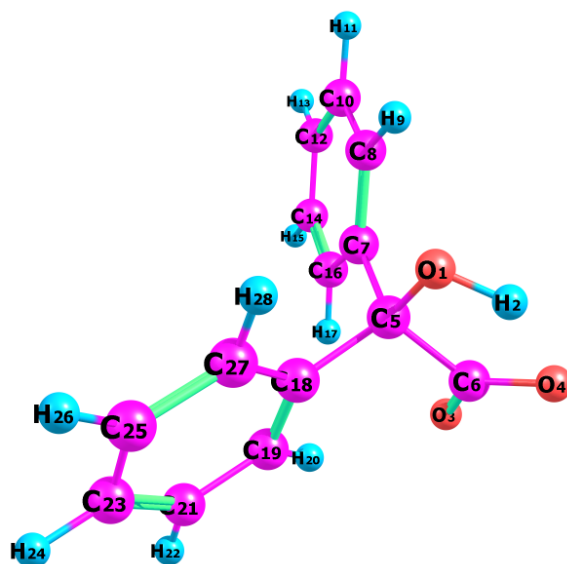
Figure 6.7a: Optimised geometry of the benzilate moiety calculated at the
B3LYP/aug-cc-pVTZ level in DMSO.
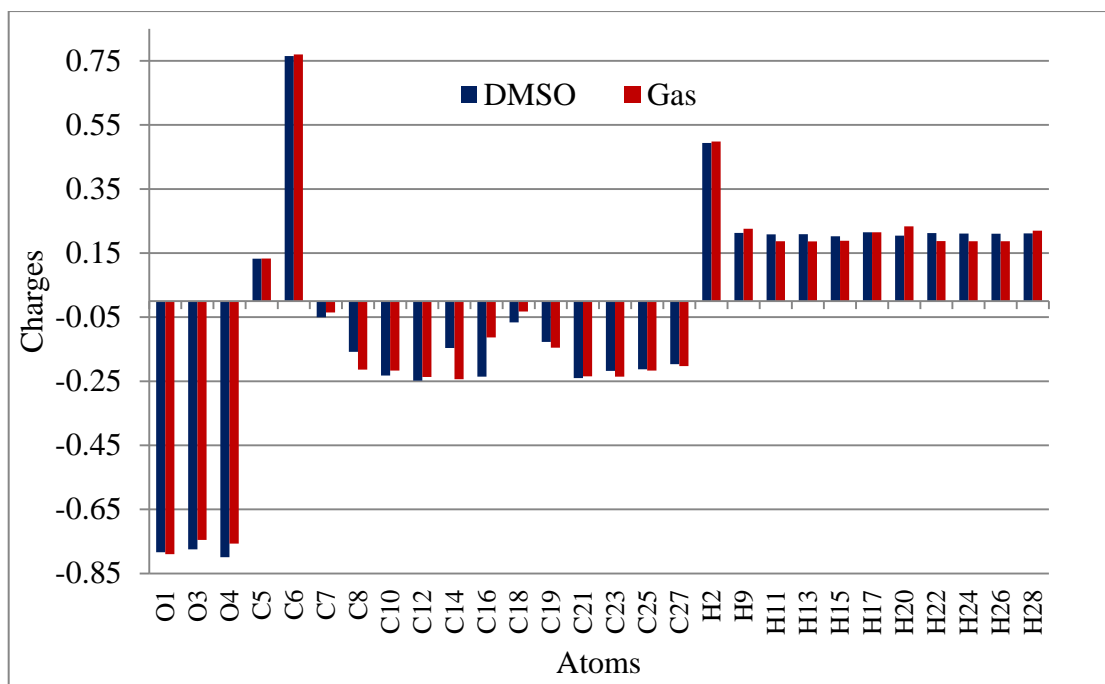
Figure 6.7b: A comparison of the charge distribution on the atoms of **Hben⁻** as obtained from NPA in the gas phase and DMSO.

Table 6.3: Natural population analysis indicating the distribution of electrons between the core, valence and Rydberg orbitals for selected atoms in **Hben⁻** in DMSO.

Atom	Charge	Core	Valence	Rydberg	Total
O1	-0.78363	2.00000	6.76189	0.02174	8.78363
O3	-0.77460	2.00000	6.74798	0.02663	8.77460
O4	-0.79912	2.00000	6.77394	0.02519	8.79912
C6	0.76496	1.99999	3.18224	0.05281	5.23504
C12	-0.24802	1.99999	4.21887	0.02917	6.24802
H2	0.49383	0.00000	0.49935	0.00682	0.50617
H15	0.20237	0.00000	0.79066	0.00697	0.79763
Core:	33.99982 (99.9995 % of 34)				
Valence:	85.46954 (99.3832 % of 86)				
Rydberg:	0.53064 (0.4422 % of 120)				

The molecular electrostatic potential (MEP) surfaces of **Hben⁻** and **phen** in Figures 6.7c and 6.7d were utilised to predict the reactive sites for nucleophilic and electrophilic attack on these ligands [67]. The red and yellow regions occupied by the three oxygen atoms of **Hben⁻** and the two nitrogen atoms of **phen** indicate maximum

negative electrostatic potential values which can thus act as electron donating or nucleophilic sites [67]. This confirms the bidentate coordination mode of **phen**, and the mono- or bidentate binding of the carboxylate ligand to the metals through its oxygen atoms. Although NPA revealed an insignificant difference on the atomic charges of O1 and the carboxylate group oxygens (O3 and O4) of **Hben⁻**, the MEP maps show more negative regions on the carboxylate oxygen atoms. This could explain why some of the **Hben⁻** ligands prefer to take the monodentate coordination mode through the carboxylate oxygen, rather than the hydroxyl oxygen atoms (apart from steric factors). The violet or blue regions have positive electrostatic potential and represent electron-poor or electrophilic sites. The maximum positive region is located on the hydrogen atoms of both ligands and C6 of **Hben⁻**. The MEP is also useful in the identification of sites for intra- and intermolecular interactions [65]. The surfaces of the ligands studied fully support the existence of O-H···O interactions apparent between the hydroxyl groups of the monodentate **Hben⁻** and the free *O*-atom of the carboxylate group, as well as the C-H$_{phen}$···O$_{Hben-}$ links. The MEP isosurface of **phen** has been discussed in Chapter 5.

6.3.7   Frontier molecular orbital analysis, and global and chemical reactivity descriptors

The highest occupied molecular orbitals (*HOMO*), lowest unoccupied molecular orbitals (*LUMO*) and the *HOMO-LUMO* energy gaps (Figure 6.8) were identified to indicate electron transfer in molecular systems, kinetic stability and chemical reactivity [65,68]. The *HOMO-LUMO* energy gap of **Hben⁻** is found to be 5.813 eV, obtained at DFT/B3LYP with aug-cc-pVTZ level, whilst the computed energy gaps between *HOMO*-1-*LUMO*+1 and *HOMO*-2-*LUMO*+2 for the benzilate ligand are 5.970 and 6.411 eV, respectively.

To obtain insights into the chemical reactivity of **Hben⁻**, global chemical concepts such as chemical potential (μ), hardness (η), softness (σ), electronegativity (χ_m) and electrophilicity index (ω), were determined (Table 6.4; see Chapter 5 for the chemical reactivity descriptors of **phen**). The chemical hardness of the ligand was formulated

using the *HOMO* and *LUMO* orbital energy gaps, using the equation: $\eta = \frac{(-E_{HOMO} + E_{LUMO})}{2}$ [65,69]. A hardness value (qualitative measure of polarisability) of 2.907 eV was obtained for **Hben⁻** – that is the extent of the distortion of the electron cloud in an electric field. The hydroxycarboxylate ligand has a softness (the inverse of hardness) of 0.344 eV^{-1} at B3LYP. Soft molecules possess small energy gaps compared to hard molecules, which makes them more polarisable due to their smaller excitation energies [69].
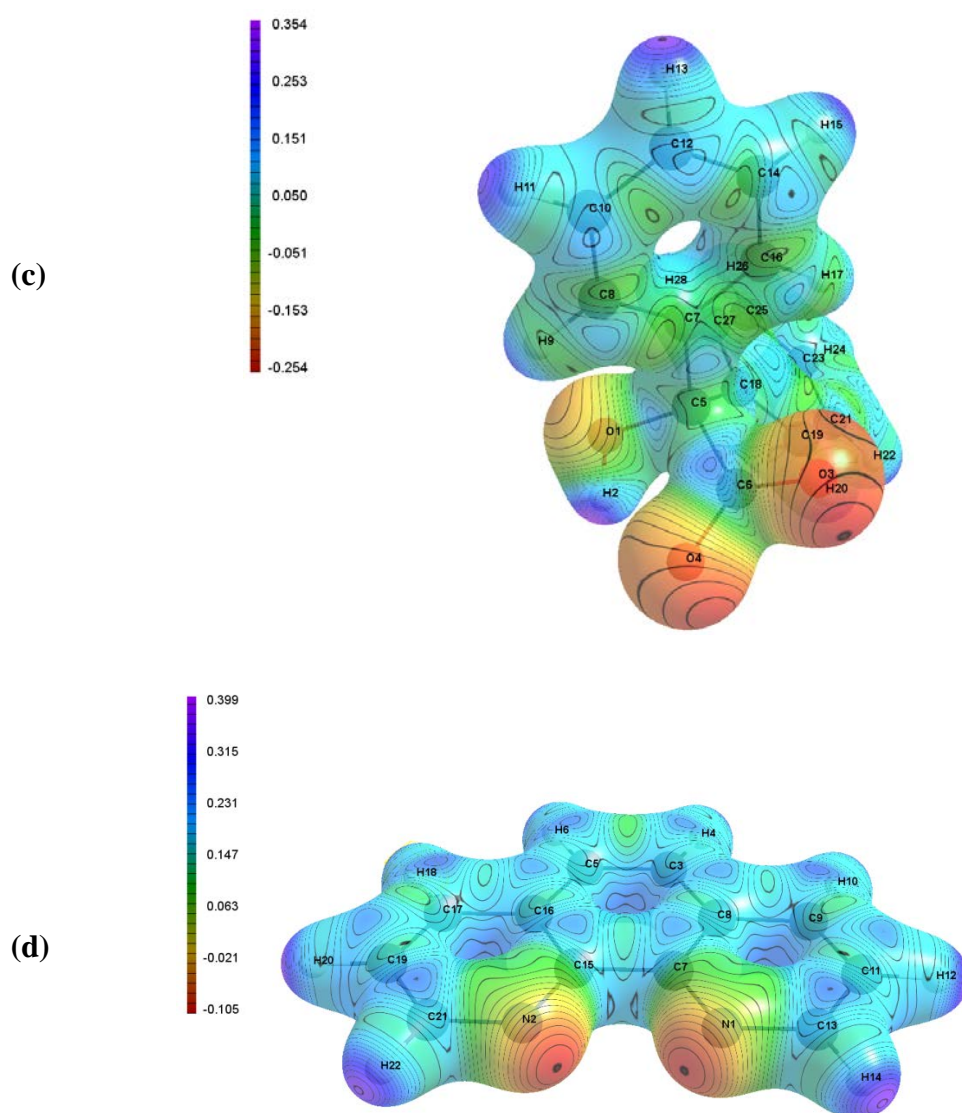
Figures 6.7c and 6.7d: Molecular electrostatic potential surfaces of: **(c) Hben⁻** and **(d) phen** in DMSO. The colour *versus* potential range for **Hben⁻** is from -0.254 (red) to 0.354 (violet). An isovalue of 0.05 was used to generate the maps.

E_{LUMO} = -0.537 eV

ΔE = 5.813 eV

E_{HOMO} = -6.350 eV

E_{LUMO+1} = -0.487 eV

ΔE = 5.970 eV

E_{HOMO-1} = -6.457 eV
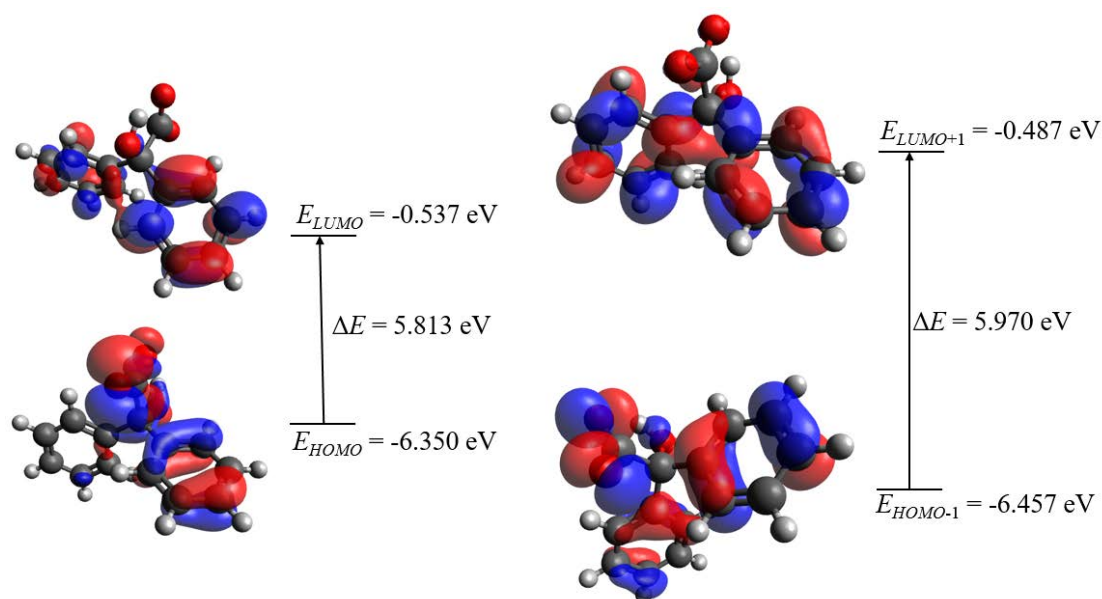
Figure 6.8: Distributions of the *HOMO* and *LUMO* molecular orbitals of **Hben⁻** calculated at B3LYP/aug-cc-pVTZ in DMSO (isovalue = 0.03).

Table 6.4: Global chemical reactivity indices for **Hben⁻**. Values are in eV, except for softness (σ) which is in eV^{-1}.

Global and chemical reactivity descriptor	Values
Energy of *HOMO*	-6.350
Energy of *LUMO*	-0.537
Energy of *HOMO*-1	-6.457
Energy of *LUMO*+1	-0.487
Energy of *HOMO*-2	-6.859
Energy of *LUMO*+2	-0.448
First energy gap	5.813
Second energy gap	5.970
Third energy gap	6.411
Ionisation energy (I)	6.350
Electron affinity (A)	0.537
Hardness (η)	2.907
Softness (σ)	0.344
Chemical potential (μ)	-3.444
Electrophilicity index (ω)	2.040
Electronegativity (χ_m)	3.444

6.3.8   Anticancer screen

Figure 6.9 illustrates the cytotoxic effects of the Ln(III) salts, the free ligands (**H₂ben** and **phen**) and the mixed-ligand Ln(III) complexes, reported in comparison to the DMSO vehicle control set at 100 %. No cytotoxic effects are observed in THP-1 cells ($p>0.05$) for all the tested compounds, except for the positive control, curcumin (21.5 ± 0.83 %). 1,10-Phenanthroline, and the Pr(III) and Nd(III) complexes significantly reduced MCF-7 cell viability (74.4 ± 6.78, 48.3 ± 12.22 and 71.6 ± 8.07 %, respectively, $p<0.05$). In addition to its activity on MCF-7 cells, **phen** exerted cytotoxic effects in HEC-1A cells ($p<0.05$). A cytotoxic effect was seen in THP-1 cells as well, indicating no selectivity of **phen** to cell type [70-72]. Further studies are therefore necessary to confirm this.
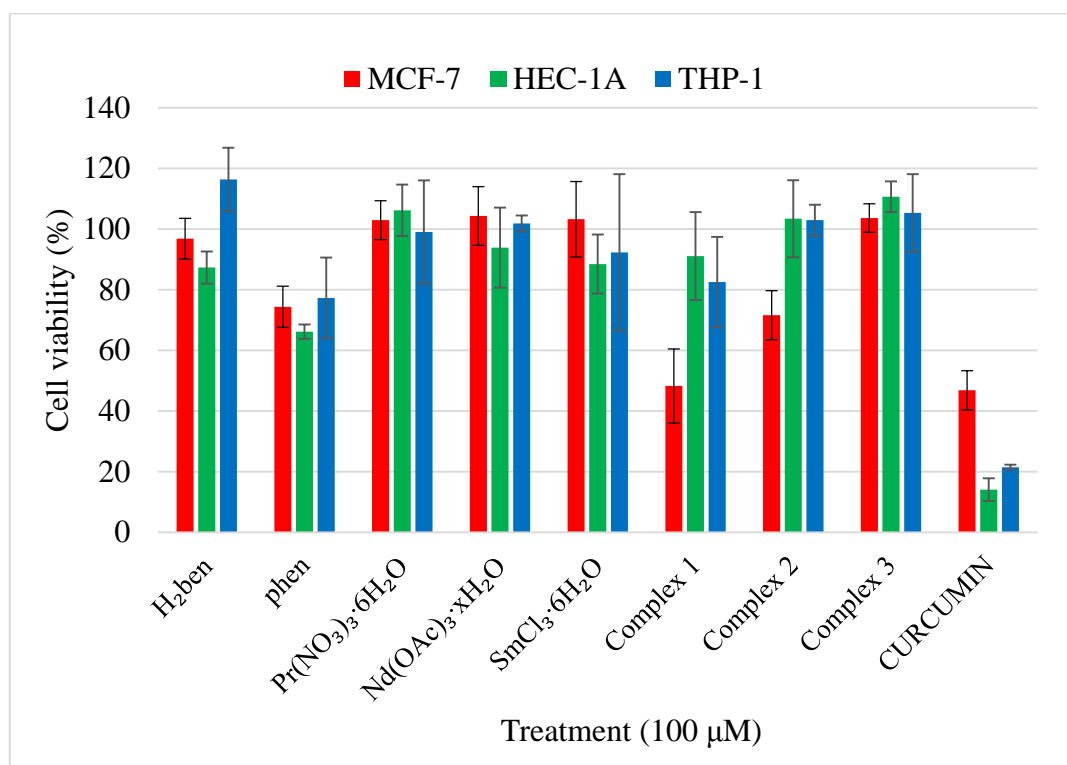
Figure 6.9: Cytotoxic effects of the compounds on MCF-7, HEC-1A and THP-1 cells using the MTT assay. Mean values of three independent experiments ± SD are shown (n = 3).

A combination of **phen** with Pr(III) gives a Pr(III) complex with enhanced cytotoxicity in MCF-7 cells compared to free **phen**, due to the synergistic effect [73].

The cytotoxicity of complex **1** is similar (48.3±12.22 % inhibition at 100 µM) to that of the positive control, curcumin (46.8±6.46 %) in MCF-7 cells (p>0.05). The Pr(III) coordination compound is, however, only toxic towards MCF-7 cells and not HEC-1A or THP-1 cells. Cell viability decreases in the order: complex **3**> complex **2**> complex **1** for MCF-7 cells. The *in vitro* studies also revealed superior potency of **phen** over **H₂ben**, which is consistent with a higher ω value for **phen** (ω = 3.861 eV) compared to the hydroxycarboxylic acid (ω = 2.040 eV) [74,75].

6.4   Conclusion

In summary, three novel isostructural complexes of Pr(III), Nd(III) and Sm(III) were prepared from benzilic acid and 1,10-phenanthroline. The Ln(III) nitrate, acetate and chloride precursors were used as starting materials in the complexation reactions with the two ligands. The structures and properties of the coordination compounds were characterised by spectroscopic techniques (IR, ^{1}H NMR and UV-Vis spectroscopy) and single-crystal X-ray diffraction analysis. Structural analysis shows that each nine-coordinate metal centre is coordinated to two bidentate **phen** ligands, three benzilate ligands (two monodentate and one bidentate) and one H_2O molecule. The occurrence of mono- and bidentate binding modes of the carboxylic acid ligand in the complexes could prompt future studies of the chelating effect on the repulsion of the ligands in the coordination sites, as well as on stability [52]. This is fundamental in ascertaining catalytic properties of different coordination patterns and in some specialised separation processes.

The importance of hydrogen bonding, weak C-H···O contacts, π···π and C-H···π interactions in crystal packing have been described. In spite of its weak nature, these non-covalent interactions are omnipresent and it is well established that they also influence the secondary, tertiary and quaternary structures of proteins, and the intercalation of various drugs into DNA [58,61]. In view of this, the study of these interactions was key in gaining an understanding on their contribution or behaviour in chemical and biological systems.

Anticancer activities of the three mixed-ligand Ln(III) complexes have been explored. It can be concluded that the inclusion of **phen** as a co-ligand contributed to the anticancer properties of the coordination compounds, in addition to providing crystal stability through facilitating the formation of $\pi\cdots\pi$ and C-H$\cdots\pi$ interactions. Anticancer efficacy of the hydroxycarboxylic acid, **phen** and metal complexes can however, be enhanced *via* the modification of the ligand systems [76,77].

6.5   Supplementary information

6.5.1   Crystallographic data

Table S6.1: Crystal and structure refinement data for **1**–**3**.

	1	2	3
Formula	$C_{66}H_{51}N_4O_{10}Pr$, C_3H_7NO, H_2O	$C_{66}H_{51}N_4O_{10}Nd$, C_3H_7NO, H_2O	$C_{66}H_{51}N_4O_{10}Sm$, C_3H_7NO, H_2O
M_r (g.mol^{-1})	1292.13	1295.46	1301.58
Crystal system	Monoclinic	Monoclinic	Monoclinic
Space group	$P2_1/n$ (No. 14)	$P2_1/n$ (No. 14)	$P2_1/n$ (No. 14)
a, b, c [Å]	14.2029(5), 13.1105(5), 32.2052(12)	14.1696(7), 13.1126(6), 32.1184(17)	14.1439(6), 13.1146(5), 32.0482(12)
α, β, γ (°)	90, 97.962(2), 90	90, 97.534(3), 90	90, 97.179(2), 90
V (Å^3)	5942.9(4)	5916.1(5)	5898.1(4)
Z	4	4	4
ρ (g.cm^{-3})	1.444	1.454	1.466
μ (mm^{-1})	0.890	0.948	1.066
$F(000)$	2656	2660	2668
Crystal size (mm)	$0.26 \times 0.36 \times 0.49$	$0.16 \times 0.24 \times 0.26$	$0.30 \times 0.41 \times 0.57$
Temperature (K)	200	200	200
Mo $K\alpha$ radiation, λ (Å)	0.71073	0.71073	0.71073
θ (min-max) (°)	1.7, 28.3	2.1, 28.4	1.7, 28.3
Data set	-18≤h≤18; -17≤k≤15; -42≤l≤42	-18≤h≤18; -17≤k≤17; -42≤l≤42	-18≤h≤18; -17≤k≤17; -42≤l≤42
Tot., Unique data, R_{int}	113196, 14776, 0.045	56275, 14748, 0.088	86529, 14705, 0.029
Observed [I>2σ(I)] reflections	12141	9088	13198
$N_{reflections}$, $N_{parameters}$	14776, 796	14748, 796	14705, 796
$R[F^2>2\sigma(F^2)]$, $wR(F^2)$, S	0.0348, 0.0710, 1.06	0.0494, 0.0894, 0.98	0.0309, 0.0657, 1.16
$\Delta\rho_{min}, \Delta\rho_{max}$ (e.Å^{-3})	-0.46, 0.69	-0.46, 0.69	-0.95, 0.73

6.5.2   Molecular modelling data

Table S6.2: Natural population analysis of **Hben**⁻ at the DFT/B3LYP level using the aug-cc-pVTZ basis set in DMSO and the gas phase.

Atoms	Natural charge (DMSO)	Population	Natural charge (gas)	Population
O1	-0.78363	8.78363	-0.78997	8.78997
O3	-0.77460	8.77460	-0.74541	8.74541
O4	-0.79912	8.79912	-0.75655	8.75655
C5	0.13234	5.86766	0.13315	5.86685
C6	0.76496	5.23504	0.76983	5.23017
C7	-0.05049	6.05049	-0.03544	6.03544
C8	-0.15829	6.15829	-0.21371	6.21371
C10	-0.23205	6.23205	-0.21657	6.21657
C12	-0.24802	6.24802	-0.23665	6.23665
C14	-0.14643	6.14643	-0.24353	6.24353
C16	-0.23585	6.23585	-0.11328	6.11328
C18	-0.06613	6.06613	-0.03251	6.03251
C19	-0.12719	6.12719	-0.14506	6.14506
C21	-0.24019	6.24019	-0.23462	6.23462
C23	-0.21786	6.21786	-0.23566	6.23566
C25	-0.21253	6.21253	-0.21686	6.21686
C27	-0.19655	6.19655	-0.20253	6.20253
H2	0.49383	0.50617	0.49795	0.50205
H9	0.21302	0.78698	0.22582	0.77418
H11	0.20825	0.79175	0.18672	0.81328
H13	0.20904	0.79096	0.18650	0.81350
H15	0.20237	0.79763	0.18850	0.81150
H17	0.21491	0.78509	0.21479	0.78521
H20	0.20450	0.79550	0.23342	0.76658
H22	0.21251	0.78749	0.18766	0.81234
H24	0.21110	0.78890	0.18684	0.81316
H26	0.21045	0.78955	0.18702	0.81298
H28	0.21165	0.78835	0.22015	0.77985
Total	**-1.00000**	**120.00000**	**-1.00000**	**120.00000**

6.5.3 Anticancer activity tests

Table S6.3: Summary of the cytotoxicity of the metal salts, free ligands, mixed-ligand complexes derived from **H₂ben** and **phen**, and curcumin.

Compound (100 μM)	Cells		
	MCF-7	HEC-1A	THP-1
	Cell viability (%)		
$Pr(NO_3)_3 \cdot 6H_2O$	102.9±6.41	106.2±8.47	99.0±17.02
$Nd(OAc_3)_3 \cdot xH_2O$	104.3±9.69	93.9±13.18	101.9±2.62
$SmCl_3 \cdot 6H_2O$	103.3±12.44	88.5±9.75	92.3±25.78
H₂ben	96.8±6.71	87.3±5.30	116.3±10.78
phen	74.4±6.78	66.2±2.37	77.3±13.34
Complex **1**	48.3±12.22	91.1±14.52	82.5±14.89
Complex **2**	71.6±8.07	103.4±12.69	103.0±5.07
Complex **3**	103.6±4.70	110.7±5.06	105.3±12.77
CURCUMIN	46.8±6.46	14.1±3.76	21.5±0.83

6.6   References

[1]   C. Huang (2010) – *Rare-Earth Coordination Chemistry – Fundamentals and Applications*. John Wiley & Sons, Asia. pp 1–500.

[2]   L. Armelao, S. Quici, F. Barigelleti, G. Accorsi, G. Bottaro, M. Cavazzini and E. Tondello, "Design of luminescent lanthanide complexes: From molecules to highly efficient photo-emitting materials", *Coord. Chem. Rev.,* **254** (2010) 487–505.

[3]   D.V. Kolechko, F.A. Kolokolov, A.I. Oflidi, A.A. Pikula, V.T. Panyushkin, I.E. Mikhailov and G.A. Dushenko, "Novel luminescent lanthanide complexes with 1,10-phenanthroline-2,9-dicarboxylic acid", *Doklady Chemistry*, **441** (2011) 374–378.

[4]   X.-X. Qi, N. Ren, S.-L. Xu, J.-J. Zhang, G.-C. Zong, J. Gao, L.-N. Geng, S.-P. Wang and S.-K. Shi, "Lanthanide complexes with 3,4,5-triethoxybenzoic acid and 1,10-phenanthroline: synthesis, crystal structures, thermal decomposition mechanism and phase transformation kinetics", *RSC Adv.*, **5** (2015) 9261–9271.

[5]   M. Hu, L-Y. Yue, E.C. Sañudo and S-M. Fang, "Three lanthanide complexes with mixed salicylate and 1,10-phenanthroline: syntheses, crystal structures, and luminescent/magnetic properties", *J. Coord. Chem.*, **69** (2016) 2164–2173.

[6]   G.-C. Zong, J.-X. Huo, N. Ren, J.-J. Zhang, X.-X. Qi, J. Gao, L.-N. Geng, S.-P. Wang and S.-K. Shi, "Preparation, characterization and properties of four new trivalent lanthanide complexes constructed using 2-bromine-5-methoxybenzoic acid and 1,10-phenanthroline", *Dalton Trans.*, **44** (2015) 14877–14885.

[7]   E. Halevas, A. Hatzidimitriou, M. Bertmer, A.A. Vangelis, A. Antzara, C. Mateescu and A. Salifoglou, "Structure lattice-dimensionality and spectroscopic property correlations in novel binary and ternary materials of Group 13 elements with α-hydroxycarboxylic benzilic acid and phenanthroline", *Cryst. Growth Des.*, **14** (2014) 4041−4059.

[8]   Y. Qiu, K. Wang, Y. Liu, H. Deng, F. Sun and Y. Cai, "Synthesis, characterization and 1D helical chain crystal structure of [Cu(DBA)$_2$(1,10-phen)]$_n$ and [Cd(DBA)$_2$(1,10-phen)$_2$] (DBA = benzilic acid)", *Inorg. Chim. Acta*, **360** (2007) 1819–1824.

[9]   W.-W. Fu, L. Xu, Y.-H. Zhang and M.-S. Chen, "Syntheses, crystal structures and luminescent properties of Ag(I) complexes with benzilic carboxylate and 2,6-pyridinedicarboxylate", *Inorganic and Nano-Metal Chemistry*, **47** (2017) 1211–1215.

[10]   D.-Z. Kuang, J.-X. Yu, Y.-L. Feng, F.-X. Zhang, W.-J. Jiang and X.-M. Zhu, "Syntheses, structures, anti-tumor activity of tri(*n*-butyl)tin carboxylates with hydrogen-bonded network", *Chinese J. Inorg. Chem.*, **31** (2015) 1112–1118.

[11]   C.-H. Leung, S. Lin, H.-J. Zhong and D.-L. Ma, "Metal complexes as potential modulators of inflammatory and autoimmune responses", *Chem. Sci.*, **6** (2015) 871–884.

[12]   Nibha, B.P. Baranwal, G. Singh and C.G. Daniliuc, "Synthesis, characterization and thermolysis of lanthanide metal nitrate complexes with 1,10-phenanthroline, Part-95", *J. Rare Earth.*, **32** (2014) 545–552.

[13]   A. Bencini and V. Lippolis, "1,10-Phenanthroline: A versatile building block for the construction of ligands for various purposes", *Coord. Chem. Rev.*, **254** (2010) 2096–2180.

[14]   A.Y. Mitrofanov, Y. Rousselin, R. Guilard, S. Brandés, A.G. Bessmertnykh-Lemeune, M.A. Uvarova and S.E. Nefedov, "Copper(II) complexes with phosphorylated 1,10-phenanthrolines: from molecules to infinite supramolecular arrays", *New J. Chem.*, **40** (2016) 5896–5905.

[15]   P. Heffeter, M.A. Jakupec, W. Korner, S. Wild, N.G.V. Keyserlingk, L. Elbling, H. Zorbas, A. Korynevska, S. Knasmuller, H. Sutterluty, M. Micksche, B.K. Keppler and W. Berger, "Anticancer activity of the lanthanum compound [tris(1,10-phenanthroline)lanthanum(III)]trithiocyanate (KP772; FFC24)", *Bio. Chem. Pharm.*, **71** (2006) 426–440.

[16]   K. Kumar, P. Meera, M. Amutha Selvi and A. Dayalan, "Tris-(1,10-phenanthroline) cobalt(III) bromide chloride hexahydrate: Synthesis, characterization, antimicrobial screening and XRD studies", *Int. J. Chem. Sci.*, **9** (2011) 1421–1428.

[17]   A. Arbaoui, C. Redshaw, D.L. Hughes and M.R.J. Elsegood, "Arylboron complexes of the acids Ph$_2$C(XH)CO$_2$H (X = O, NH)", *Inorg. Chim. Acta*, **362** (2009) 509–514.

[18]   R. Carballo, B. Covelo, N. Fernández-Hermida, A.B. Lago and E.M. Vázquez López, "Non-covalent interactions in a Nickel(II) complex with benzilate and 1,10-phenanthroline", *J. Chem. Crystallogr.*, **41** (2011) 1949–1954.

[19]   D.-Y. Ma, "Observation of a water–anion tape constructed from unusual trimeric and tetrameric water clusters embedded in a copper(II) complex", *Inorg. Chim. Acta*, **392** (2012) 440–445.

[20]   P. Halder, E. Zangrando and T.K. Paine, "Copper(II) α-hydroxycarboxylate complexes of bis(2-pyridylcarbonyl)amine ligand: From mononuclear complex to one-dimensional coordination polymer", *Polyhedron*, **29** (2010) 434–440.

[21]   R. Carballo, A. Castiñeiras, B. Covelo, E. García-Martínez, J. Niclós and E.M. Vázquez López, "Solid state coordination chemistry of mononuclear mixed-ligand complexes of Ni(II), Cu(II) and Zn(II) with α-hydroxycarboxylic acids and imidazole", *Polyhedron*, **23** (2004) 1505–1518.

[22]   U.S. Soumya Mol, R. Drisya, P.R. Satheesh Chandran, M.R. Sudarsanakumar, S. Suma and P.K. Sudhadevi Antharjanam, "Crystal growth and characterization studies of novel luminescent 2D coordination polymer of lead-benzilate possessing edge sharing PbO_6 polyhedra", *J. Mol. Struct.*, **1125** (2016) 73–78.

[23]   P. Jia, R. Ouyang, P. Cao, X. Tong, X. Zhou, T. Lei, Y. Zhao, N. Guo, H. Chang, Y. Miao and S. Zhou, "Review: Recent advances and future development of metal complexes as anticancer agents", *J. Coord. Chem.*, **70** (2017) 2175–2201.

[24]   T.K. Ronson, H. Adams, L.P. Harding, S.J.A. Pope, D. Sykes, S. Faulkner and M.D. Ward, "Polynuclear lanthanide complexes of a series of bridging ligands containing two tridentate *N,N',O*-donor units: structures and luminescence properties", *Dalton Trans.*, **14** (2007) 1006–1022.

[25]   X.-P. Yang, C.-Y. Su, B.-S. Kang, X.-L. Feng, W.-L. Xiao and H.-Q. Liu, "Studies on lanthanide complexes of the tripodal ligand bis(2-benzimidazolylmethyl)(2-pyridylmethyl)amine. Crystal structures and luminescence properties", *J. Chem. Soc., Dalton Trans.*, (2000) 3253–3260.

[26]   S.A.K. Elroby, H.A. Ewais and S.G. Aziz, "Effects of protonation and deprotonation on the reactivity of quinolone: A theoretical study", *Chinese Sci. Bull.*, **57** (2012) 1665–1671.

[27]   T. Baraniraj and P. Philominathan, "Growth and characterization of organic nonlinear optical material: Benzilic acid", *J. Cryst. Growth*, **311** (2009) 3849–3854.

[28]   M.P.C. Campello, E. Palma, I. Correia, P.M.R. Paulo, A. Matos, J. Rino, J. Coimbra, J.C. Pessoa, D. Gambino, A. Paulo and F. Marques, "Lanthanide complexes with phenanthroline-based ligands: insights into cell death mechanisms obtained by microscopy techniques", *Dalton Trans.*, **48** (2019) 4611–4624.

[29]   P. Ruíz, R. Ortiz, L. Perelló, G. Alzuet, M. González-Álvarez, M. Liu-González and F. Sanz-Ruíz, "Synthesis, structure, and nuclease properties of several binary and ternary complexes of copper(II) with norfloxacin and 1,10 phenanthroline", *J. Inorg. Biochem.*, **101** (2007) 831–840.

[30]   Z.A. Taha, A.M. Ajlouni, T.S. Ababneh, W. Al-Momani, A.K. Hijazi, M. Al Masri and H. Hammad, "DFT computational studies, biological and

antioxidant activities, and kinetics of thermal decomposition of 1,10-phenanthroline lanthanide complexes", *Struct. Chem.*, **28** (2017) 1907–1918.

[31]   X. Wang, G. Jia, Y. Yu, Y. Gao, W. Zhang, H. Wang, Z. Cao and J. Liu, "A new homogeneous electrocatalyst for electrochemical carbonylation of methanol to dimethyl carbonate", *Quim. Nova,* **38** (2015) 298–302.

[32]   G.R. Fulmer, A.J.M. Miller, N.H. Sherden, H.E. Gottlieb, A. Nudelman, B.M. Stoltz, J.E. Bercaw and K.I. Goldberg, "NMR chemical shifts of trace impurities: Common laboratory solvents, organics, and gases in deuterated solvents relevant to the organometallic chemist", *Organometallics*, **29** (2010) 2176–2179.

[33]   R.M. Pontes, E.A. Basso and F.P. dos Santos, "Medium effect on the rotational barrier of carbamates and its sulfur congeners", *J. Org. Chem.*, **72** (2007) 1901–1911.

[34]   S.B. Andrews, J.W. Faller, J.M. Gilliam and R.J. Barrnett, "Lanthanide ion-induced isotropic shifts and broadening for nuclear magnetic resonance structural analysis of model membranes", *Proc. Nat. Acad. Sci.*, **70** (1973) 1814–1818.

[35]   M.D. Regulacio, N. Tomson and S.L. Stoll, "Dithiocarbamate precursors for rare-earth sulfides", *Chem. Mater.*, **17** (2005) 3114–3121.

[36]   A.A. Ansari, "DFT and ^{1}H NMR molecular spectroscopic studies on biologically anti-oxidant active paramagnetic lanthanide(III)-chrysin complexes", *Main Group Chemistry*, **7** (2008) 43–56.

[37]   S.C. Bishop, R. Winefield, A. Anbanandam and J.N. Lampe, "Aqueous synthesis of a small-molecule lanthanide chelator amenable to copper-free click chemistry", *PLoS ONE*, **14** (2019) 1–16.

[38]   V.K. Voronov, "Principles of high-resolution NMR spectroscopy of paramagnetic molecules in solutions", *Int. J. Exp. Spectroscopic Tech.*, **3** (2018) 1–7.

[39]   P. Pitchaimani, K.M. Lo and K.P. Elango, "Synthesis, spectral characterization, crystal structures of lanthanide(III) pyrrolidine dithiocarbamate complexes and their catalytic activity", *J. Coord. Chem.*, **68** (2015) 2167–2180.

[40]   M.D. Regulacio, M.H. Pablico, J.A. Vasquez, P.N. Myers, S. Gentry, M. Prushan, S. Tam-Chang and S.L. Stoll, "Luminescence of Ln(III) dithiocarbamate complexes (Ln = La, Pr, Sm, Eu, Gd, Tb, Dy)", *Inorg. Chem.*, **47** (2008) 1512–1523.

[41] V.C. Havanur, D.S. Badiger, S.G. Ligade and K.B. Gudasi, "Synthesis, characterization and antimicrobial study of lanthanide(III) complexes of 2-anilino-*N′*-[pyridine-2-ylethylidene]acetohydrazide", *Der Pharma Chemica*, **3** (2011) 292–304.

[42] R.K. Agarwal, S. Prasad, R. Garg and S.K. Sidhu, "Synthesis and preliminary structural characterization of some lanthanide(III) semicarbazone complexes", *Bull. Chem. Soc. Ethiop.*, **20** (2006) 167–172.

[43] R.K. Agarwal and A. Kumar, "Synthesis, physico-chemical and biological properties of some mixed ligand complexes of trivalent lanthanides with 4[*N*-(4′-dimethylamino-benzalidene)amino] antipyrine thiosemicarbazone and pyridine", *J. Appl. Chem. Res.*, **16** (2011) 40–58.

[44] K. Raja, A. Suseelamma and K.H. Reddy, "Synthesis, spectral properties, DNA binding interactions and DNA cleavage studies of lanthanide(III) complexes of 2-acetylpyridine acetoylhydrazone: The X-ray crystal structure of 10-coordinate Ce(III) and Sm(III) complexes", *J. Iran Chem. Soc.*, **12** (2015) 1473–1486.

[45] L.B. Su, Q.G. Wang, H.J. Li, G. Brasse, P. Camy, J.L. Doualan, A. Braud, R. Moncorgé, Y.Y. Zhan, L.H. Zheng, X.B. Qian and J. Xu, "Spectroscopic properties and CW laser operation of Nd,Y-codoped CaF_2 single crystals", *Laser Phys. Lett.*, **10** (2013) 1–4.

[46] H.M. Ha, T.T. Quynh Hoa, L. Van Vu and N.N. Long, "Optical properties and Judd–Ofelt analysis of Sm ions in Lanthanum trifluoride nanocrystals", *J. Mater. Sci.: Mater. Electron.*, **28** (2017) 884–891.

[47] M. Llunell, D. Casanova, J. Cirera, P. Alemany and S. Alvarez, *SHAPE: Program for the Stereochemical Analysis of Molecular Fragments by Means of Continuous Shape Measures and Associated Tools, User's Manual Version 2.1*, 2013.

[48] J. Cirera, E. Ruiz and S. Alvarez, "Continuous Shape Measures as a stereochemical tool in organometallic chemistry", *Organometallics,* **24** (2005) 1556–1562.

[49] T. Zhu, P. Chen, H. Li, W. Sun, T. Gao and P. Yan, "Structural effects on the photophysical properties of mono-*β*-diketonate and bis-*β*-diketonate Eu[III] complexes", *Phys. Chem. Chem. Phys.*, **17** (2015) 16136–16144.

[50] C. Brouca-Cabarrecq, J. Dexpert-Ghys, A. Fernandes, J. Jaud and J.C. Trombe, "Synthesis, crystal structures and properties of three new lanthanide 2,6-pyridinedicarboxylate complexes with zero-dimensional structure", *Inorg. Chim. Acta*, **361** (2008) 2909–2917.

[51]   A. Kovács, C. Apostolidis, O. Walter and P. Lindqvist-Reis, "'Lanthanide contraction' in [Ln(BTP)$_3$](CF$_3$SO$_3$)$_3$ complexes", *Struct. Chem.*, **26** (2015) 1287–1295.

[52]   Y. Ma, Y.-S. Yang, Y.-H. Jiang, Y.-X. Li, M. Liu, Z.-F. Li, H.-L. Han, Y.-P. Yang, X.-L. Xin and Q.-H. Jin, "Lanthanide contraction and chelating effect on a new family of lanthanide complexes with tetrakis(*O*-isopropyl)methyle-nediphosphonate: synthesis, structures and terahertz time-domain spectroscopy", *RSC Adv.*, **7** (2017) 41651–41666.

[53]   Y. Wang, C.-W. Jin, S.-M. He, N. Ren and J.-J. Zhang, "Five novel lanthanide complexes with 2-chloroquinoline-4-carboxylic acid and 1,10-phenanthroline: Crystal structures, molecular spectra, thermal properties and bacteriostatic activities", *J. Mol. Struct.*, **1125** (2016) 383–390.

[54]   R. Feng, F.-L. Jiang, M.-Y. Wu, L. Chen, C.-F. Yan and M.-C. Hong, "Structures and photoluminescent properties of the lanthanide coordination complexes with hydroxyquinoline carboxylate ligands", *Crys. Growth Des.*, **10** (2010) 2307–2313.

[55]   V. Kubat, G. Demo, L. Jeremias and J. Novosad, "Synthesis and structure of tris(dimethyldithiocarbamato) (1,10-phenanthroline)lanthanide complexes", *Z. Kristallogr.*, **228** (2013) 369–373.

[56]   I. Kani, Ö. Atlier and K. Güven, "Mn(II) complexes with bipyridine, phenanthroline and benzoic acid: Biological and catalase-like activity", *J. Chem. Sci.*, **128** (2016) 523–536.

[57]   M. Schultz, J.M. Boncella, D.J. Berg, T. Don Tilley and R.A. Andersen, "Coordination of 2,2′-bipyridyl and 1,10-phenanthroline to substituted ytterbocenes: An experimental investigation of spin coupling in lanthanide complexes", *Organometallics*, **21** (2002) 460–472.

[58]   M.O. Sinnokrot and C.D. Sherrill, "Highly accurate coupled cluster potential energy curves for the benzene dimer: Sandwich, T-shaped, and parallel-displaced configurations", *J. Phys. Chem. A*, **108** (2004) 10200–10207.

[59]   C.R. Martinez and B.L. Iverson, "Rethinking the term ''pi-stacking''", *Chem. Sci.*, **3** (2012) 2191–2201.

[60]   Y.-C. Chang, Y.-D. Chen, C.-H. Chen, Y.-S. Wen, J.T. Lin, H.-Y. Chen, M.-Y. Kuo and I. Chao, "Crystal engineering for π-π stacking *via* interaction between electron-rich and electron-deficient heteroaromatics", *J. Org. Chem.*, **73** (2008) 4608–4614.

[61]   S. Karthikeyan, V. Ramanathan and B. Kumar Mishra, "Influence of the substituents on the CH···π interaction: Benzene−Methane complex", *J. Phys. Chem. A*, **117** (2013) 6687−6694.

[62]   S. Roy, M.G.B. Drew, A. Bauzá, A. Frontera and S. Chattopadhyay, "Estimation of conventional C–H···π (arene), unconventional C–H···π (chelate) and C–H ···π (thiocyanate) interactions in hetero-nuclear nickel(II)–cadmium(II) complexes with a compartmental Schiff base", *Dalton Trans.*, **46** (2017) 5384–5397.

[63]   S. Ullmann, P. Hahn, L. Blömer, A. Mehnert, C. Laube, B. Abel and B. Kersting, "Dinuclear lanthanide complexes supported by a hybrid salicylaldiminato/calix[4]arene-ligand: synthesis, structure, and magnetic and luminescence properties of (HNEt$_3$)[Ln$_2$(HL)(L)] (Ln = Sm^{III}, Eu^{III}, Gd^{III}, Tb^{III})", *Dalton Trans.*, **48** (2019) 3893–3905.

[64]   H. Sun, K. Ye, C. Wang, H. Qi, F. Li and Y. Wang, "The π-π stacked geometries and association thermodynamics of quinacridone derivatives studied by ^{1}H NMR", *J. Phys. Chem. A*, **110** (2006) 10750−10756.

[65]   A. Zülfikaroğlu, H. Batı and N. Dege, "A theoretical and experimental study on isonitrosoacetophenone nicotinoyl hydrazone: Crystal structure, spectroscopic properties, NBO, NPA and NLMO analyses and the investigation of interaction with some transition metals", *J. Mol. Struct.*, **1162** (2018) 125–139.

[66]   V. Meenatchi and S.P. Meenakshisundaram, "Synthesis, growth, spectral studies, first-order molecular hyperpolarizability and Hirshfeld surface analysis of isonicotinohydrazide single crystals", *RSC Adv.*, **5** (2015) 64180–64191.

[67]   A. Kanaani, D. Ajloo, H. Kiyani, H. Ghasemian, M. Vakili and M. Feizabadi, "Molecular structure, spectroscopic investigations and computational study on the potential molecular switch of (E)-1-(4-(2-hydroxybenzylideneamino)phenyl)ethanone", *Mol. Phys.*, **114** (2016) 2081–2097.

[68]   S. Gatfaoui, N. Issaoui, A. Mezni, F. Bardak, T. Roisnel, A. Atac and H. Marouani, "Synthesis, structural and spectroscopic features, and investigation of bioactive nature of a novel organic-inorganic hybrid material 1*H*-1,2,4-triazole-4-ium trioxonitrate", *J. Mol. Struct.*, **1150** (2017) 242–257.

[69]   N. Günay, Ö. Tamer, D. Kuzalic, D. Avci and Y. Atalay, "Theoretical Investigation of *N*-Methyl-*N'*-(4-nitrobenzylidene) pyrazine-2-carbohydrazide: Conformational Study, NBO Analysis, Molecular Structure and NMR Spectra", *Acta Physica Polonica A*, **127** (2015) 701–710.

[70]   Wardihan, M. Rusdi, G. Alam, M. Lukman and M.A. Manggau, "Selective cytotoxicity evaluation in anticancer drug screening of *Boehmeria virgata* (Forst) Guill leaves to several human cell lines: HeLa, WiDr, T47D and Vero", *Dhaka Univ. J. Pharm. Sci.*, **12** (2014) 87-90.

[71]   R. Mahato, W. Tai and K. Cheng, "Prodrugs for improving tumor targetability and efficiency", *Adv. Drug Deliv. Rev.*, **63** (2011) 659–670.

[72]   M.A. Musa, V.L.D. Badisa, L.M. Latinwo, J. Cooperwood, A. Sinclair and A. Abdullah, "Cytotoxic activity of new acetoxycoumarin derivatives in cancer cell lines", *Anticancer Res.*, **31** (2011) 2017–2022.

[73]   U. Ndangi, N. Mhlongo and M.E. Soliman, "Metal complexes in cancer therapy – an update from drug design perspective", *Drug Des. Dev. Ther.*, **11** (2017) 599–616.

[74]   J.Y. Chen, H. Jiang, S.J. Chen, C. Cullen, C.M. Sabbir Ahmed and Y.-H. Lin, "Characterization of electrophilicity and oxidative potential of atmospheric carbonyls", *Environ. Sci.: Processes Impacts*, **21** (2019) 856–866.

[75]   A. Morales-Bayuelo, "Molecular quantum similarity, Chemical reactivity and database screening of 3D pharmacophores of the protein kinases A, B and G from Mycobacterium tuberculosis", *Molecules*, **22** (2017) 1027.

[76]   G. Agonigi, T. Riedel, S. Zacchini, E. Păunescu, G. Pampaloni, N. Bartalucci, P.J. Dyson and F. Marchetti, "Synthesis and antiproliferative activity of new ruthenium complexes with ethacrynic-acid-modified pyridine and triphenylphosphine ligands", *Inorg. Chem.*, **54** (2015) 6504−6512.

[77]   D.-L. Ma, C. Wu, S.-S. Cheng, F.-W. Lee, Q.-B. Han and C.-H. Leung, "Development of natural product-conjugated metal complexes as cancer therapies", *Int. J. Mol. Sci.*, **20** (2019) 1–15.

CHAPTER 7

Conclusions and Future prospects

The complexation of different potentially multidentate chelating hydrazones and carboxylic acids (including an oxamate) with various lanthanides (nitrato, acetato and chlorido) was completed using different syntheses to gain insight into the bonding modes, geometrical trends adopted, as well as structural and spectral properties. Characterisation of the coordination compounds was achieved by different physicochemical methods: elemental analysis, molar conductance, IR, ^{1}H NMR and UV-Vis spectroscopy, and X-ray crystallography. In Chapters 4–5, UV-Vis spectroscopy showed that complexes exhibit characteristic Laporte-forbidden *f-f* transitions [1]. The absorption spectra of hydrazone and **phen** complexes are characterised by transition bands from the ligands.

The stereochemistry of the Ln(III)-hydrazone, Ln(III)-oxamate and Ln(III)-carboxylate complexes in Chapters 3-6 were evaluated through a continuous shape measurement method, using the *SHAPE 2.1* program. Useful information was obtained on the degree of distortion from the ideal coordinate polyhedron. These CShM parameters are useful in constraining and tuning the coordination geometries around rare-earth ions, for example, in metal-organic frameworks (MOFs) in the study of single-molecular-magnet (SMM) behaviour [2]. Eight-, nine- and ten-coordinate complexes have been reported, with the nine-coordinate spherical capped square antiprism (CSAPR-9) geometry being the most common. In summary, the geometries and deviations from reference shapes were found to depend on coordination numbers and Ln(III) ion size [3].

The effect that the ionic radii has on the coordination numbers of the complexes was elucidated, with lighter lanthanide ions such as La(III), Ce(III), Pr(III) and Nd(III) yielding nine and ten-coordinate complexes, while the heavier Yb(III) ions preferred a coordination number of eight (the heavier Er(III) ions adopt eight and nine

coordination). This variation is brought about by the lanthanide contraction, and can be useful, for example, in the separation of different 4*f* elements [4].

A total of twenty-one X-ray crystal structures for the coordination compounds have been obtained, from which the bonding parameters were determined. Crystallographic studies indicate the tridental binding of the hydrazone ligands, the bidental chelation/bridging modes of Hpma$^-$, and the monodental or bidental coordination of benzilic acid with metals, with a preference for monodeprotonated Schiff base ligands and benzilic acid, as well as monoanionic oxamate moeities. The Ln-N and Ln-O bond distances and the ligand bite angles are normal and fall within the expected ranges. The bond lengths assume shorter values as the number of 4*f* electrons increases, which is consistent with the lanthanide contraction. The bite angle is an important tool in catalysis, for instance, where it is related to catalyst efficiencies in reactions, and is thus worth investigating [5]. It was found that ligand bite angles increase as the ionic radii decrease across the period. For this reason, the parameter is useful in the explanation of rates, selectivities and in the design of ligands for biological or catalytic reactions [5]. The influence of chelate ring size on bite angles was also examined, with larger rings yielding larger bite angles.

The crystal structures of the compounds show networks supported by means of electrostatic interactions, and hydrogen bonds of the N-H⋯O, O-H⋯O, C-H⋯O and/or C-H⋯N type. Furthermore, the N-H⋯π links play a key role in crystal packing of mixed-ligand complexes of oxamates. In addition to the role of 1,10-phenanthroline in stabilisation of metal complexes through π-π stacking and C-H⋯π interactions, it was also concluded that the presence of **phen** prevents polymerisation of oxamate complexes.

Interesting physical parameters for chemical reactivity and biological activities of the coordinating ligands, such as *HOMO-LUMO* energy gaps, ionisation energies, electron affinities, softness and hardness, were obtained through DFT computational studies based on the B3LYP model and aug-cc-pVTZ basis set. Natural population analysis (NPA) and visual representations from molecular electrostatic potential

(MEP) maps show the charge distributions of the molecules, thus providing insights into electrophilic and nucleophilic reactivity [6,7]. From NPA and MEP surfaces, it was apparent that the negative charges covered the oxygen and nitrogen atoms, whilst the positive regions were over the hydrogen atoms and carbon atoms attached to electronegative oxygen and nitrogen atoms. The most preferred sites for electrophilic attack in hydrazones, *N*-(2,6-dimethylphenyl)oxamate and benzilic acid were therefore the *O*-atoms, whereas the *N*-atoms are the most reactive site in **phen**. The electron deficient carbon and hydrogen atoms being the positive potential sites, means that they are possible sites for nucleophilic attack. The MEP maps also played a key role in elucidation of ligand shape and size, in addition to predicting ligand denticity [6,8].

Anticancer screen indicated that hydrazones, **phen**, some Ln(III)-hydrazone complexes, as well as some mixed-ligand complexes with **phen**, possessed moderate cytotoxic activities against MCF-7 and HEC-1A cells. Considering the synthetic accessibility of these complexes, the findings undoubtedly show that lanthanide-based complexes have potential therapeutic application. A comparison of Chapters 4 and 5 revealed that anticancer activity can be enhanced by incorporation of **phen** as an auxiliary ligand. Based on these results, a series of new oxamate or oxamic acid derived hydrazone ligands could be designed and synthesised, and then complexed to 4*f* metal ions, with phenanthrolines as auxiliary ligands [9]. The tuning of functional groups allows further investigation of the reactivity profile, coordination, spectral characteristics and improved anticancer properties of rare-earth complexes, since oxamic acid hydrazones are known to show remarkable antiproliferative activity, for example, towards MCF-7 and MDA-MB231 breast cancer cell lines [9]. Bioactivity experiments can be expanded to include antimicrobial activities [10]. It is also worthwhile investigating the dual purpose of the oxamic acid derived hydrazone complexes in the detection of tumours (through magnetic studies) and cytotoxic effects [11-13]. The scope of the future study may also include catalytic studies, potentiometric titrimetry in aqueous solutions to investigate complex stabilities as the pH is varied, and evaluation of the relative thermal stabilities of the synthesised complexes.

References

[1]   P. Pitchaimani, K.M. Lo and K.P. Elango, "Synthesis, spectral characterization, crystal structures of lanthanide(III) pyrrolidine dithiocarbamate complexes and their catalytic activity", *J. Coord. Chem.*, **68** (2015) 2167–2180.

[2]   K. Liu, H. Li, X. Zhang, W. Shi and P. Cheng, "Constraining and tuning the coordination geometry of a lanthanide ion in metal−organic frameworks: Approach toward a single-molecule magnet", *Inorg. Chem.*, **54** (2015) 10224–10231.

[3]   A. Upadhyay, K.R. Vignesh, C. Das, S. Kumar Singh, G. Rajaraman and M. Shanmugam, "Influence of the ligand field on the slow relaxation of magnetization of unsymmetrical monomeric lanthanide complexes: Synthesis and theoretical studies", *Inorg. Chem.*, **56** (2017) 14260–14276.

[4]   Y. Koma, T. Koyama and Y. Tanaka, "Enhancement of the mutual separation of lanthanide elements in the solvent extraction based on the CMPO-TBP mixed solvent by using a DTPA-nitrate solution", *J. Nucl. Sci. Technol.*, **36** (1999) 934–939.

[5]   P. Dierkes and P.W.N.M. van Leeuwen, "The bite angle makes the difference: a practical ligand parameter for diphosphine ligands", *J. Chem. Soc.*, *Dalton Trans.*, Issue **10** (1999) 1519–1529.

[6]   Z. Demircioğlu, Ç.A. Kaştaş and O. Büyükgüngör, "Theoretical analysis (NBO, NPA, Mulliken Population Method) and molecular orbital studies (hardness, chemical potential, electrophilicity and Fukui function analysis) of (*E*)-2-((4-hydroxy-2-methylphenylimino)methyl)-3-methoxyphenol", *J. Mol. Struct.*, **1091** (2015) 183–195.

[7]   P.S. Kushwaha and P.C. Mishra, "Molecular electrostatic potential maps of the anti-cancer drugs daunomycin and adriamycin: an *ab initio* theoretical study", *J. Mol. Struct. (Theochem)*, **636** (2003) 149–156.

[8]   L. Armelao, S. Quici, F. Barigelletti, G. Accorsi, G. Bottaro, M. Cavazzini and E. Tondello, "Design of luminescent lanthanide complexes: From molecules to highly efficient photo-emitting materials", *Coord. Chem. Rev.*, **254** (2010) 487-489.

[9]   Y.A. Volkova, E.I. Chernoburova, A.S. Petrova, A.A. Shtil and I.V. Zavarzin, "Reactions of hydrazones derived from oxamic acid thiohydrazides", *Phosphorus, Sulfur, Silicon Relat. Elem.*, **192** (2017) 237–240.

[10]   K.B. Gudasi, V.C. Havanur, S.A. Patil and B.R. Patil, "Antimicrobial study of newly synthesized lanthanide(III) complexes of 2-[2-hydroxy-3-

methoxyphenyl]-3-[2-hydroxy-3-methoxybenzylamino]-1,2-dihydroquinazolin-4(3H)-one", *Metal-Based Drugs,* **2007** (2007) 1–7.

[11]   J. Goura, J.P.S. Walsh, F. Tuna and V. Chandrasekhar, "Tetranuclear lanthanide(III) complexes in a seesaw geometry: Synthesis, structure, and magnetism", *Inorg. Chem.,* **53** (2014) 3385–3391.

[12]   S. Zhang, W. Shi, L. Li, E. Duan and P. Cheng, "Lanthanide coordination polymers with "fsy-type" topology based on 4,4′-azobenzoic acid: Syntheses, crystal structures, and magnetic properties", *Inorg. Chem.,* **53** (2014) 10340–10346.

[13]   S. Wanninger, V. Lorenz, A. Subhan and F.T. Edelmann, "Metal complexes of curcumin – synthetic strategies, structures and medicinal applications", Chem. Soc. Rev., **44** (2015) 4986–5002.

LIST OF PUBLICATIONS

[1]   **Tatenda Madanhire**, Hajierah Davids, Melanie C. Pereira, Eric C. Hosten and Abubak'r Abrahams, "Synthesis, characterisation and anticancer activity screen of lanthanide(III) acetate complexes with benzohydrazone and nicotinohydrazone ligands", *Polyhedron*, 2020; accepted.

[2]   **Tatenda Madanhire**, Hajierah Davids, Melanie C. Pereira, Eric C. Hosten and Abubak'r Abrahams, "Lanthanide complexes with *N*-(2,6-dimethylphenyl)oxamate: Synthesis, characterisation and cytotoxicity", *Polyhedron*, 2020; accepted.

[3]   **Tatenda Madanhire**, Hajierah Davids, Melanie C. Pereira, Eric C. Hosten and Abubak'r Abrahams, "Mixed-ligand complexes of lanthanides derived from an α-hydroxycarboxylic acid (benzilic acid) and 1,10-phenanthroline: Physicochemical properties and anticancer activity", *Polyhedron*, 2020; submission being processed.

[4]   **Tatenda Madanhire**, Bernardus Van Brecht and Abubak'r Abrahams, "Synthesis and crystal structure of a mixed-ligand zinc(II) complex derived from ethyl (2,6-dimethylphenylcarbamoyl)formate and 1,10-phenanthroline", *Bull. Chem. Soc. Ethiop.*, 2020; submission being processed.

[5]   **Tatenda Madanhire**, Melanie C. Pereira, Hajierah Davids, Eric C. Hosten, Abubak'r Abrahams, "Lanthanide(III) complexes with *N*-(2,6-dimethylphenyl)oxamate and 1,10-phenanthroline: Synthesis, characterisation and cytotoxicity against MCF-7, HEC-1A and THP-1 cell lines", *J. Rare Earth.*; in preparation.